博士論文

Development of Small and Light-Weight Electro-Hydrostatic Actuators and their Integration to the Whole-Body Drive System of Humanoid Robots

(小型軽量電気静油圧駆動系の開発と
それを用いたヒューマノイドロボット全身駆動系の実現)

A dissertation presented by

康 天毅
Tianyi Ko

The Department of Mechano-Informatics
Graduate School of Information Science and Technology

THE UNIVERSITY OF TOKYO

June 2018

Thesis advisor
Yoshihiko Nakamura

Author
Tianyi Ko

Development of Small and Light-Weight Electro-Hydrostatic Actuators and their Integration to the Whole-Body Drive System of Humanoid Robots

Abstract

For the next generation of robots which try to move from the well-defined environments such as factories or labs to an unstructured environment closer to or extremely far from our lives, the backdrivability of the actuators has been an important requirement. While actuation by the servovalve controlled hydraulic systems or the combination of electric motors and high reduction ratio gear train have high performance on the response and torque density, their backdrivability is limited by the large friction in the force transmission process. For the intrinsically backdrivable actuators, which are the direct driven systems, pneumatic actuators, and series elastic actuators, it is still difficult to simultaneously realize both of the high torque density and control bandwidth. Actuation by Electro-Hydrostatic Actuators(EHA) has the possibility to solve the problem since its high backdrivability is realized by the low friction property of the transmission and not relying on the series elasticity. However, while its property of high backdrivability and energy efficiency was studied in the previous works, both of the torque density and response were not deeply discussed and the performance presented in the existing works was not advantageous compared to other types of backdrivable actuators. Its integration into an articulated robot was also not accomplished. In this dissertation, we establish a generalized hardware design, control, and system integration framework to realize a hydrostatically driven

humanoid robot and evaluate its whole body control and locomotion performance.

In most case the hardware development of an actuator and its controller design are conducted separately. The fundamental improvement of the control performance, however, is achieved by the hardware improvement. The effect of a hardware modification on the control performance, on the other hand, should also be evaluated from the control perspective in advance. Therefore, we first derive a simplified linear model of EHA from the fluid dynamical and material mechanical principle in chapter 2. This approximation was possible with the assumption that the flow inside the pump is laminar, the pump is a rotary one, and all values such as pump torque/velocity and fluid pressure/flow-rate are expressed in the equivalent value seen from the actuator. From the model, it is made clear that the actuator output force is affected by both the motor torque and the actuator output velocity, as the second order lag system. The output velocity of the actuator is a third order lag system from the motor torque input.

The currently available miniature backdrivable actuators have only limited torque density, therefore, they are difficult to be adopted in legged robots, which need to support their own bodyweight with the active torque. In chapter 3, we propose a systematic mechanical design approach to improve it. It is made clear that the miniaturization of the system size has the effect of increasing internal leakage and therefore impair the output force. To encounter it, the key is to attain a small internal gap and high fluid viscosity, while maximizing the effective pressure receiving surface in the limited overall weight or size. To reduce the gap inside the pump, we experimentally show that the optimization of bearing arrangement or type, and

reinforcement of the pump casing are effective. To reduce the gap in the actuator, we present the design of a light-weight cylinder and a vane motor with reinforced casing rigidity. To maintain the fluid viscosity, we propose a direct pump casing water cooling approach. Lastly, we show the integrated tie rod cluster cylinder to maximize the effective pressure receiving surface.

To maintain or even improve the backdrivability of the torque-enhanced EHA, in chapter 4 we present the approach from both the mechanical design and measurement perspective. To minimize the viscous friction, double rod cylinders are more suitable since the closed circuit volume is invariant. We proposed a double rod cylinder design with the beam structure to minimize the piston rod diameter, therefore minimize the friction due to the piston rod oil seal. We also presented an active friction compensation of the rod oil seal with the merged information of the pressure sensor and strain gauge by a complementary filter.

While the possibility of fast response is a key property of EHA compared with other elastic actuators, little attention was paid to it in the existing works. In chapter 5, from both the hardware and control perspective, we present the enhancement of the fast response property of EHA, proving their superiority over elastic actuators in the sense of the closed-loop control bandwidth. From the hardware side, to reduce the series elasticity between the pump and the load, we filled the dead volume in the chamber and selected the high bulk-modulus fluid since the fluid compressibility is a large source of elasticity. We also applied the reinforcement on the force transmission structure, with which a clear improvement in the response was seen. From the control side, we introduced the current-pressure-position triple-loop feedback controller. The

idea is to distribute the controller in three layers with different framerate processing device and control faster behavior in a faster device, instead of treating the large number of internal parameters as a single state vector. The pressure control bandwidth in the fixed piston configuration was 100 Hz, which is a higher value compared with those by the existing works on EHA and series elastic actuators.

With the actuators developed above, in chapter 6, we present our approach to integrate the complex EHA system into a whole-body humanoid, in each of the hardware, electronics and software level. The hydrostatically driven humanoid "Hydra" has 40 joints driven by 24 double rod linear cylinders with the beam structure and eight casing-reinforced vane motor, powered by 36 water cooled trochoid pump in addition to the two five-DoF cluster EHAs for the hand. The full version robot has 130 kg weight and is 180 cm tall. Due to its high joint control bandwidth, Hydra can be controlled to be stiff enough for a position control based locomotion. With the Capture Point Tracking control, Hydra could conduct a walking motion with 0.2 m stride, 30 mm step height and 1 second stepping time. With its high joint backdrivability, Hydra can be compliantly controlled to prevent a disturbance force applied on a distal link to be transferred to other links. Simultaneously realizing both of the moderate stiffness of the COM and compliant motion in the nullspace by the resolved viscoelasticity controller, it was experimentally confirmed that Hydra could conduct a stable balancing and locomotion while absorbing external force by the nullspace motion.

Contents

Title Page i
Abstract iii
Table of Contents vii
List of Figures x
List of Tables xxiv

1 Introduction **1**
1.1 Background 1
1.2 Objective of this Dissertation 5
1.3 Outline of this Dissertation 7

2 Mathematical Description of EHA to Design a High Performance Servo System **8**
2.1 Introduction 8
2.2 Internal Leakage, Fluid Compressibility and Pipeline Expansion . . . 9
2.3 A Simplified Linear EHA Model 15
2.4 Comparison with the Experiment Data 20
2.4.1 Experiment Setup 20
2.4.2 Parameter Identification 22
2.4.3 Comparison of the Dynamic Behavior 27
2.5 Conclusion 29

3 Key Design Parameters of a Few Types of Electro-Hydrostatic Actuators for Humanoid Robots **35**
3.1 Introduction 35
3.2 Effect of the Internal Gap, Fluid Viscosity and Effective Pressure Receiving Surface 36
3.3 Minimization of the Internal Gap 38
3.3.1 Gap Control of a Gear Pump 38
3.3.2 Gap Control with a Linear Cylinder 41
3.3.3 Gap Control of a Rotary Vane Motor 46
3.4 Fluid Viscosity Control by the Direct Water Cooling 48
3.5 Maximization of Effective Pressure Receiving Surface by an Integrated Tie Rod Cluster Cylinder Structure 52
3.6 Conclusion 55

4 Enhancement of Backdrivability and Force Control Accuracy of a Large Force Linear EHA 58
4.1 Introduction . . . 58
4.2 A Low Friction Lightweight Trochoid Pump with Reinforced Structure and Water Cooling . . . 59
4.3 A Double Rod Cylinder with the Beam Structure . . . 65
4.4 Active Seal Friction Compensation with a Strain Gauge . . . 67
4.5 Conclusion . . . 77

5 Current-Pressure-Position Triple-Loop Feedback Control of Electro-Hydrostatic Actuators for Humanoid Robots 79
5.1 Introduction . . . 79
5.2 Reduction of the Hydraulic Elasticity to Achieve a High Control Bandwidth . . . 81
5.3 Force Control of EHA by Fast Motor Current Feedback . . . 82
5.4 High Mechanical Stiffness Structure to Transfer the High Bandwidth Force . . . 90
5.5 Current-Pressure-Position Triple-Loop Feedback for Parallel Joints . . . 96
5.6 Conclusion . . . 99

6 Integration of Electro-Hydrostatic Actuators to a Humanoid Robot and its Whole-Body Motion Control Performance Evaluation 101
6.1 Introduction . . . 101
6.2 Joint Actuation by Electro-Hydrostatic Actuators . . . 103
6.2.1 Parallel Joint Driving Mechanism with Slider Cranks . . . 103
6.2.2 Modular Designed Kinematic Structure of the Humanoid Hydra 107
6.2.3 Underactuated Four-fingered Hand with Five EHA in Cluster 121
6.3 Distributed Multilayered System of the Humanoid Hydra . . . 127
6.3.1 Sensory and Electronics Architecture . . . 127
6.3.2 Software Architecture . . . 137
6.4 Compliant Whole-Body Locomotion Evaluation . . . 139
6.4.1 Independent Joint Control Bandwidth Evaluation . . . 139
6.4.2 While-body Joint Torque Control Performance Evaluation with a Gravity Compensation Experiment . . . 140
6.4.3 Stiff Control Realized by the High Control Bandwidth . . . 147
6.4.4 Compliant Control Realized by the Backdrivability . . . 156
6.5 Conclusion . . . 174

7 Conclusion 177
Acknowledgments . . . 181

Bibliography 186

List of Publications **198**

List of Figures

2.1 Schematic of an EHA with internal leakage. 10
2.2 Effect of the pipeline expansion and fluid compressibility on the behavior of an EHA. 13
2.3 Simplified model of an EHA as two inertias connected with a series damper and elasticity. The key is to treat all values such as the pump's torque/angular velocity or fluid pressure/flow-rate as the equivalent value seen from the actuator. 16
2.4 T-N curve (top left), input power (top right), output power (middle left), volumetric efficiency (middle right), torque efficiency (bottom left), and total energy efficiency (bottom right) of the developed EHA when a constant motor q-axis current of 18 A is applied. The volumetric efficiency represents the ratio of the piston displacement to the theoretical pump discharge volume. The torque efficiency is the ratio of piston force to the input force. 19
2.5 Common setup of the testbed experiment. The actuator is placed horizontally. A movable cart supported with a pair of linear guides is aligned with the actuator. The cart and the actuator can be connected with a connecting rod, on which a strain gauge is attached. On the connection between the connecting rod and the cart, a force gauge is attached. The cart can be either fixed on the basement, free to move, or disconnected from the actuator so that the actuator has no load. . 21
2.6 Time transition of the experiment to identify d_p and d_s. The top graph shows the value of τ_p (motor input torque) in green color and τ_q (pressure) in red color. The lower graph shows the pump velocity $\dot{\theta}_p$ seen from the piston. 23
2.7 Plot of the pump pressure and pump friction against pump velocity. All values are converted to the equivalent value seen from the cylinder. The red markers shows the pressure acquired from the pressure sensor and the blue markers shows the friction, calculated from the difference between the pressure and motor current. 24

2.8 Time transition of the experiment to identify d_c. The piston position, velocity, acceleration and friction is shown. 25

2.9 Relationship between piston velocity and friction. Blue color dots represent viscosity friction in the piping. Green color dots represent friction due to the contact oil seal. Red color is the total friction. 26

2.10 Time transition of the experiment to acquire the open loop frequency response between the pump torque τ_p as the input and the pressure τ_q as the output, under the condition that the piston is fixed. 30

2.11 Open loop frequency response between pump torque τ_p as the input and pressure τ_q as the output, under the condition that the piston is fixed. The blue markers show the experiment data, while the red line shows the theoretical value of $d_s k_s/\mathrm{G}_1$. 31

2.12 Time transition of the experiment to acquire the open loop frequency response between the pump torque τ_p as the input and the piston velocity $\dot{\theta}_c$ as the output, under the condition that the piston free to move. 32

2.13 Open loop frequency response between pump torque τ_p as the input and piston velocity $\dot{\theta}_c$ as the output, under the condition that the piston is free to move. The blue markers show the experiment data, while the red line shows the theoretical value of $d_s k_s/\mathrm{G}_3$. 33

3.1 Simulated energy efficiency of an EHA when the piston force, velocity and the total reduction ratio are fixed, while the internal gap, pressure receiving surface, and fluid viscosity varies. The graph suggests that smaller pressure receiving surface has the same effect of larger internal gap or lower fluid viscosity. 37

3.2 Three forces due to the pressure cause deformation and unexpected internal leakage. The radial force on the pump rotor due to the differential force, the axial force on the pump rotor due to the mean internal pressure, and the expansion force on the pump casing is handled with higher stiffness in the modified design. 40

3.3 Comparison of the internal leakage of the initial and modified pump. The y-axis represents leakage and the x-axis represents the pressure. The experiment was done with the discharging port of the pump closed. The leak is calculated from the rotor speed and the geometric parameters of the pump. The pressure is acquired from the attached pressure sensor. To prevent the heat effect on the amount of leak, the experiment was done in a short time. This graph shows that the new pump has more than 92 % less leak for the same pressure. 41

3.4 Low friction double rod cylinder with the beam structure. 44

3.5 Schematic of the dual-use screw hole on the cylinder body. When no inserts are attached, the holes work as normal through holes. When tongueless inserts are attached, they work as tapped screw holes. . . 45

3.6 Picture and schematic of the developed double vane motor. The expansion force due to the internal pressure, applied to the casing, is supported by a pair of thrust bearings held by the output shaft, therefore the strength of the pump casing can be reduced to save the total weight. 47

3.7 3D printed integrated coolant flow channel in the pump casing. . . . 49

3.8 Time transition of the pump discharging pressure (top), amount of internal leakage (middle), and input power to the pump (bottom). The red line represents the case without water cooling and the blue line shows the case with water cooling. The discharging port of the pump is closed, the inlet port is connected to an oil reservoir in the atmosphere, and the pump is under a pressure feedback control. While in the case without the cooling, the internal leakage and the input power diverges. With the cooling, on the other hand, the values converge to a certain value. 50

3.9 Schematic and picture of the developed cylinder cluster with casted cylinder manifold (left), and tie rod cylinder cluster (right). 53

3.10 Comparison of piston force that the initial and modified actuator can output. Force is calculated through the discharging pressure and the piston diameters. The rising edges of two graphs are different because smoother pressure reference was given to the modified pump. In both cases, same electric motor and motor driver is used to drive the pump. The graph shows that with lower energy loss, the new actuator can exert 300 N force for a long time, which was impossible for the initial version. 54

4.1 Schematic of a valve plate type axial piston pump. Rotational mechanical input into the pump is converted to prismatic piston motion by a swash plate. The valve plate rectifies the reciprocating motion of pistons into a single direction of flow. The valve plate is fixed on the pump casing and the cylinder barrel rotates with the input shaft, therefore the cylinders are automatically connected to the proper (inlet or discharging) port according to its phase. 60

4.2 Three types of gear pumps. External gear pumps (left) are the most common type of gear pumps. They consist of two external spur gears. The fluid is captured between the tooth and the sidewall. While they have a simpler structure and higher discharging pressure, they tend to have larger outer size compared to the two following other types. Internal gear pumps (middle) have a pair of an external and internal spur gear. The fluid is captured between the teeth and a crescent separator. They have smaller outer size than external gear pumps, while they need high machining accuracy. Trochoid pumps (right) have trochoid gears and the internal gear (outer rotor) has exactly one more teeth than the external gear (inner rotor). This configuration can trap the fluid and convey them without help of the crescent separator. 61

4.3 Comparison of the original design (left) and our modified design (right) of the pump. The pump casing is integrated with the 3D printed water cooling jacket. The pulley side casing is also reinforced to have higher stiffness. The electric motor is also modified to be cooled by a water jacket. 63

4.4 Comparison of an EHA hydraulic circuit with a single rod cylinder (left) and with a symmetric double rod cylinder (right). In the case of double rod cylinders, only a small capacity accumulator and simple check valves are needed since they work only to compensate the small amount of external leakage and avoid cavitation. In the case of single rod cylinders for closed circuits, the accumulator need to have at least larger capacity than the volume of the piston rod. The check valves need be pilot check valves. When the cylinder retracts, larger volume of the fluid moves out from the cylinder than the volume moves in. The differential volume need to be stored in the accumulator through the force cracked pilot check valve. When the cylinder extends, more fluid need to be sent to the cylinder than the fluid moves out. The differential volume is supplied from the accumulator. While in such case the check valve does not necessary to be a pilot one, a pilot check valve is advantageous in smooth operation and avoidance of cavitation. 64

4.5 Low friction double rod cylinder with the beam structure. 66

4.6 Common setup of the testbed experiment (Same figure as Fig.2.5). The actuator is placed horizontally. A movable cart supported with a pair of linear guides is aligned with the actuator. The cart and the actuator can be connected with a connecting rod, on which a strain gauge is attached. On the connection between the connecting rod and the cart, a force gauge is attached. The cart can be either fixed on the basement, free to move, or disconnected from the actuator so that the actuator has no load. 68

4.7 Time transition of the parameters in the experiment to confirm the quasi-static force controllability of the EHA without strain gauge feedback. The actuator is under a low gain control and the piston is manually moved by human. The red line shows the force acquired from the strain gauge on the connecting rod, which we treat as the actually exerted force by the actuator. The black line shows the error between the measured force (red line) and the desired force generated by the measured piston position (green line). The blue line shows the force estimated from the pressure sensors. 70

4.8 Time transition of the parameters in the experiment to confirm the quasi-static force controllability of the EHA with the strain gauge feedback. The actuator is under a low gain control and the piston is manually moved by human. The red line shows the force acquired from the strain gauge on the connecting rod, which we treat as the actually exerted force by the actuator. The black line shows the error between the measured force (red line) and the desired force generated by the measured piston position (green line). The blue line shows the force estimated from the pressure sensors. 71

4.9 Relationship between the piston position and actuator force, when the actuator is under a low gain position control and the piston is manually moved by human. The red line shows the desired relationship between the two. The blue markers represent the case without strain gauge feedback and the green markers show the case with. The time transition of the value is shown in Fig.4.7, Fig.4.8respectively. The RMS force tracking error of the former case was 12.1 N and 1.3 N for the latter. 72

4.10 Variation the force value acquired from the pressure sensor (red markers) and the strain gauge (blue markers) against temperature variation. While the thermal effect on the pressure sensor is small, the one on the strain gauge is as high as 2.5 N/°C gradient. 74

4.11 Time transition of the actuator force measured by the external force gauge, the strain gauge on the connecting rod, the pressure sensor on the cylinder, and the complementary filtered value. The system is heated up by an external heat gun. The temperature is represented by the orange dot line. The black thick line is the force gauge value, which is the grand truth. The blue line represents the force measured from the strain gauge. While it has the best accuracy at the beginning, a clear drift can be seen when the temperature rises. The RMS force measurement error is around 15.1 N. The green line represents the force estimated from the pressure sensor. While there is no clear drift, it has a constant offset error. The RMS error is around 6.58 N. This is 0.46% of the maximum actuator force 1500 N. With the complementary filter, which is represented by the red line, the error is smaller to be 4.18 N, which is 0.28% of the maximum force. 76

5.1 Pressure controller based on motor velocity controller. A velocity controlled motor/electronic system can realize the force control of an EHA, since the input and output side of the system is decoupled with the series damper and elasticity. This is advantageous in the cost and system simplicity since most of the industrial motor/electronic systems (even not a DC motor), especially in the low cost or small size region, support velocity command. 83

5.2 Pressure controller based on motor current controller. The motor current controller consists of a proportional feedback controller and a back EMF compensator. The former is implemented on an FPGA with 20 kHz control frequency, with the field oriented control of the brushless DC motor. The latter is implemented on a microcontroller running in 5 kHz frequency. The pressure feedback controller has a feed forward term, a PD feedback controller, and a momentum based friction observer. 84

5.3 Step response of the pressure controller based on the motor velocity controller (blue) and the motor current controller (red). The command pressure is equivalent to 550 N piston force. In the former case, the rise time is 40 ms, while in the latter case the rise time is 5 ms, which is 8 times faster. 85

5.4 Plot of the pressure tracking error against the pump rotor's angle. Clear four pulsations per rotation can be seen in the both of the velocity control based case (blue) and current control based case (red). In the former case, the peak-to-peak tracking error is 0.63 MPa, which is 74% reduced to 0.16 MPa with the latter case. 86

5.5 Time transition of the parameters in the experiment to acquire the frequency response between the command pressure and the measured pressure, with the pressure controller based on the motor velocity controller. 87

5.6 Time transition of the parameters in the experiment to acquire the frequency response between the command pressure and the measured pressure, with the pressure controller based on the motor current controller. 88

5.7 Closed-loop pressure control bode plot of the developed EHA, under the condition that the piston is fixed on the end of the cylinder. The blue markers represent the one based on the pump velocity control and the red markers represent the one based on the current control. In the latter case, the bandwidth is 100 Hz, which shows the high bandwidth property of EHAs compared with other backdrivable actuators. . . . 89

5.8 Time variation of the experiment to acquire the frequency response shown in Fig.5.9. The red line represents command force. The blue lines represent the force estimated from the pressure sensor. The green lines show the force from the strain gauge, which we treat as the force actually the actuator exerts. 92

5.9 Bode plot between force command and force from strain gauge (red), between force command to the pressure (blue), and between pressure to the strain gauge force (green). The force control bandwidth is around 15 Hz. The delay between the pressure and the force is small. The dominant one is that the pressure no longer tracks the reference as fast as the case when the piston is fixed on the end of the cylinder, which is shown in Fig.5.7. 93

5.10 Deformation of the beam structure when 500 N piston force is applied. The arrows show that both of the linear slider deformation and the beam deformation occurs. With an additional linear guide constraining the radial direction motion of the piston rod, the deformation is suppressed from the original black arrows to the red arrows. On the tip of the piston rod, the deformation is suppressed from the original 330 μm to 86 μm, which is 74% decrease. 94

5.11 Closed-loop force control bandwidth of the developed EHA when the load side of the connecting rod is fixed. With the additional linear guide, we can improve the stiffness of the force transmission structure, resulting the improvement of the control bandwidth from the original 22 Hz to 53 Hz, which is 2.4 times larger. 95

5.12 Controller architecture of the current-pressure-position triple feedback loop. The joint level position controller is implemented on the onboard PC with 1 kHz frequency. The conversion between cylinder position/force and joint angle/torque is also done on the onboard PC. The joint position controller outputs command joint torque, which is converted to the command cylinder force and sent to the MCU board through the EtherCAT bus. On the MCU board, the actuator level force feedback control is done in 5 kHz frequency and resulted command motor current is sent to the lower level driver board, where the current feedback loop is done in 20 kHz frequency. 97

5.13 Bode plot between command joint position of the hip pitch joint of Hydra and actual position (blue markers), and between command joint torque and actual torque (red markers). The closed-loop control bandwidth in both of the position and torque control was around 30-40 Hz. For the reference, the case without the reinforcement shown in the previous section is overlaid, which proves the effectiveness of the reinforcement. 98

6.1 Schematic of a two DOF universal joint driven by two linear EHAs. 105

6.2 Parameter definition of the two DOF universal joint driven by two linear EHAs. 106

6.3 Joint arrangement of the humanoid robot Hydra. 109

6.4 CAD model of the body of Hydra. Thin grey color shows backpack, yellow color shows vane motor EHA for the shoulder additional joint, purple color shows torso link structure, pink color shows linear EHA for the waist pitch and roll joint, blue color shows the waist link frame and the orange color shows vane motor EHA for hip yaw joint. . . . 110

6.5 CAD model of the left thigh link. Green color shows the intermediate hip link connecting the output flange of the hip yaw vane motor. Purple color shows the link structure of the thigh. Hip joint pitch/roll universal joint is driven by pink colored linear EHAs. Shank link in blue color is driven by one standard linear EHA in yellow and one stage pump EHA in orange. 112

6.6 CAD model of the thigh link. Purple color shows the structure of shank link. Orange color linear EHAs drive blue colored fool link. 114

6.7 CAD model of the left shoulder link. Structure of shoulder link is shown in purple. The shoulder link is fixed on the output flange of the additional joint, which is not shown in this figure. Orange colored linear EHAs drive blue intermediate shoulder roll link. The link rotates around the red colored universal joint to pitch/roll direction. Yellow colored vane motor drives yaw direction of shoulder. 115

6.8 CAD model of the left upper arm link. The link is attached on the output flange of the shoulder yaw vane motor. Orange colored stage pump EHA fixed on the purple link structure drives blue colored intermediate elbow link. 117

6.9 CAD model of the left lower arm link with hand. Yellow colored vane motor EHA is to drive yaw joint of the wrist. Its output flange is attached on the elbow intermediate link, which is not shown here. Orange colored linear EHAs fixed on the purple link structure drive the blue colored hand. Green colored cluster EHA to tendon drive the hand is packed inside the arm link structure. Thin green color shows the actuator itself while thick green shows tendon guiding structures. 118

6.10 Whole body picture of the humanoid robot Hydra. The outer cover (in white color) is designed by Professor Satoru Kitagou, Tokyo University of the Arts. 120

6.11 Picture of the developed four-fingered hand. The thumb has two DoF and each of the index, middle, and ring finger has one underactuated DoF. 124

6.12 Time transition of the finger joint angles during the drill grasping experiment. Four graphs correspond to four fingers and the three lines represents the three joints on each finger. 126

6.13 Picture and block diagram a MCU board and a driver board. 130

6.14 Outlook of the IMU, consisted with three independent fiber-optical gyroscopes and three servo accelerometers. 134

6.15 Outlook of a joint driver box. A box typically consists of an MCU board and three driver boards, which can drive three joints simultaneously. The boards are packed in an aluminum box to be protected against mechanical damage. 135

6.16 Software architecture of Hydra. 138

6.17 Time transition of the command(red) and measured(blue) joint position of the hip pitch joint to acquire the bode plot shown as the blue line in Fig.6.19. 141

6.18 Time transition of the command(red) and measured(blue) joint torque of the hip pitch joint to acquire the bode plot shown as the red line in Fig.6.19. 142

6.19 Bode plot between command joint position of the hip pitch joint of Hydra and actual position (blue markers), and between command joint torque and actual torque (red markers) (same figure with Fig.5.13). The joints were under the position control and a sine-wave shape signal with 0.25 ° amplitude was given to the target joint. The position bandwidth is acquired from the command and measured joint angle. Since the position controller is based on the minor joint level torque controller, the command and actual joint torque could be also acquired, with which we get the torque bandwidth. The closed-loop control bandwidth in both of the position and torque control was around 30-40 Hz. For the reference, the case without the reinforcement shown in the previous section is overlaid, which proves the effectiveness of the reinforcement. 143
6.20 Time transition of the command(red) and measured(blue) joint position of the hip roll joint to acquire the bode plot shown as the blue line in Fig.6.22. 144
6.21 Time transition of the command(red) and measured(blue) joint torque of the hip roll joint to acquire the bode plot shown as the red line in Fig.6.22. 145
6.22 Bode plot between command joint position of the hip roll joint of Hydra and actual position (blue markers), and between command joint torque and actual torque (red markers). The joints were under the position control and a sine-wave shape signal with 0.25 ° amplitude was given to the target joint. The position bandwidth is acquired from the command and measured joint angle. Since the position controller is based on the minor joint level torque controller, the command and actual joint torque could be also acquired, with which we get the torque bandwidth. The torque gain decreased before 30 Hz, unlike the case of the pitch direction. However, the delay property was almost the same. This means that the stability margin was still kept, therefore we can increase the position feedback gain. As the result, the torque gain drop was covered by the higher level position feedback loop and the position control bandwidth was around 30-40 Hz, similarly as the case of the pitch direction. For the reference, the case without the reinforcement shown in the previous section is overlaid, which proves the effectiveness of the reinforcement. 146
6.23 Gravity compensation experiment to evaluate joint torque control performance of the developed robot. The gravity torque was calculated on the on-board PC, converted to the actuator force, and then commanded to each actuator. The joints were easy to be moved by human hand and kept the same position when there were no external force, showing their high torque control performance. 147

6.24 Time transition of the joint angle and command/measured joint torque during the gravity compensation experiment. The graph shows that the joint torque tracks the command value rapidly and smoothly. The RMS tracking error was 0.73 Nm. 148

6.25 Block diagram of the Capture Point Tracking controller. The footstep and CP trajectory are pre-planned. To drive the actual CP to converge to the preferred trajectory, the CP Tracking controller generates the desired ZMP. The command COM acceleration is then generated for the actual ZMP to track the desired one. The command COM acceleration is integrated to be the command COM velocity and projected to the command joint velocity, with the task priority. The command joint velocity is integrated as the command joint position and sent to the joint level position feedback controller. 151

6.26 The balancing experiment based on the capture point tracking control. Horizontal disturbance, both pushing and pulling, in both x and y direction, was given. The robot could successfully move its body to the direction to avoid the disturbance. 152

6.27 The time transition of the command/measured CP, command/measured ZMP, and position of the COM during the balancing experiment. As the disturbance is given, the actual CP shifts from the desired position. The command ZMP, therefore, varies to push the CP back. The middle graph shows that the actual ZMP successfully tracks the command one. The RMS tracking error is 8.7 mm. 153

6.28 Outlook of the walking experiment based on the Capture Point Tracking control. The robot could successfully conduct the walking motion with 20 cm stride and 30 mm step height. The step time was set as 1 second. 154

6.29 Time transition of the command/measured CP, command/measured ZMP, and the COM position. The actual CP varies earlier than the command one since the controller tries to follow the dT time future point. In this case dT is set as 0.2 second. The actual ZMP follows the command one with 47 mm RMS error. 155

6.30 Block diagram of hydra's resolved viscoelasticity controller. The RVC module updates the gain matrix, according to the current joint position. The joint position feedback controller receives the gain matrix and conduct position control. Since the joint gain matrix is not diagonal, this feedback is done as the whole body and the resulted whole body torque is sent to the robot. To achieve dynamic motions with low feedback gain, feed forward torque calculated from the inverse dynamics plays an important role. 158

6.31 Experiment to examine the disturbance rejection performance of the backdrivable joints. The robot is standing by the left leg and a disturbance is manually applied on the right foot. The robot is under a joint level position control, without whole-body feedback. Two experiments were conducted: one with high joint stiffness and another with low joint feedback gain on the right leg therefore it can absorb disturbance. 160

6.32 Displacement against the disturbance in the operational space and configuration space, and variation of ZMP during the initial 0.8 second after the disturbance happens. The green makers show the case with high gain (stiff configuration) and the blue markers show the case with the low gain (compliant configuration). On the top left is the right foot displacement against the force in the x (sagittal) direction. On the top right is the relationship between the joint angle displacement and joint torque of the right hip pitch joint. On the bottom of the figure, the time transition of the ZMP on the left foot is shown. 161

6.33 Setup of the impulsive experiment to quantitatively evaluate that the robot is more compliant in the distal part. The robot is pulled by a horizontal wire, which is guided by a pulley to the vertical direction. On the other side of the wire from the robot, a linear guide with a stopper is attached. A weight, constrained by the linear guide, is dropped from a constant height from the stopper. When the weight falls by the gravity and collide with the stopper, we can apply a constant momentum to the robot. The impact was applied on two points on the robot, namely the distal disturbance point and the proximal disturbance point, as shown in the figure. The mass of the weight was 1.25 kg and the drop height was set as 45 cm, resulting in 3.71 kg·m/s momentum. 163

6.34 Time transition of the X direction displacement of the two points. The apparent operational space stiffness, which can be estimated from the constant displacement due to the gravity on the weight after the impact, was 378 N/m for the distal point. This is 34% value of the 1110 N/m stiffness for the proximal point. The apparent operational space mass, which can be estimated from the conservation of the momentum, taking the average velocity during the initial 80 ms after the impact, was 11.8 kg for the distal point. This is 18% of the value of the 65.5 kg of the proximal point. 164

6.35 Relationship between the disturbance and displacement of the COM when a quasi-static external force was applied. The graph shows that the measured relation between the COM displacement and external force, which is shown in the blue markers, is actually linear and close to the predefined property which is shown as the red line. 166

6.36 Different parts of Hydra are manually moved in different directions. When the robot was moved in the direction that COM also moves (left figure), the reaction force was relatively high. When the robot was moved in the yawing direction (middle), the reaction force was low and it was observed that the joints cooperate to maintain the COM position while allowing yawing direction displacement. When the force was applied on the top of the backpack (right), the robot bent the waist compliantly while moving the pelvis link to the opposite direction to maintain the COM position. 168

6.37 Outlook of the balancing experiment with the Resolved Viscoelasticity Control. It was observed that when the disturbance was applied close to the COM, the robot behaved similarly to a stiff robot with a stabilizer, while when the disturbance was on the edge of the body, the robot tries to absorb it compliantly moving the whole body in the direction that does not affect the COM position. 169

6.38 Time transition of the COM and ZMP in the X and Y direction, and the joint angle of the waist joint when an impulsive disturbance was given on the different part of the body. The top two graphs show that the ZMP properly moved to push the COM to the initial position, similar to the case with an explicit balancer with the ZMP manipulation. In the timing of around 13 seconds and 27 seconds, the disturbance was given on the highest part of the backpack attached on the torso. The third graph shows that while the waist joint largely moved, the motion of the COM and ZMP were kept as the same as the other cases. This can be interpreted as that the robot absorbed disturbance in the nullspace therefore minimize the effect on the COM motion. 170

6.39 Outlook of the walking experiment based on the resolved viscoelasticity control. During the walking it kept compliant in the nullspace therefore even though a disturbance force was manually applied on the top of the backpack, its effect on the locomotion was suppressed by the compliant motion of the waist joints. 171

6.40 Time transition of the command/actual COM position and the joint displacement of the waist joint. A large disturbance was applied on the top of the backpack when the time was 2 - 2.5 second. The bottom graph shows that the waist joint largely moved according to the disturbance. From the COM trajectory, however, it is difficult to see its effect. This shows that the controller successfully separated the motion of the COM and nullspace and absorbed the disturbance by the nullspace compliance. 172

6.41 Since the whole-body stabilization is realized by the joint compliance, the failure mode is a stable and compliant one. In this figure case the robot failed to step forward due to uncleaned oil on the floor. Nevertheless, it still kept stability and did not fall down. 173

List of Tables

2.1 Parameter value in Fig.2.3. 28

3.1 Specification of the Developed Double Rod Cylinder with Beam Structure. The maximum force and velocity shows the case with the pump described in 4.2. 42
3.2 Specification of the Developed Double Vane Motor. The maximum torque and speed shows the case with the pump described in 4.2. . . 46

4.1 Specification of the Developed Trochoid Pump 64

6.1 Mechanical specification of Hydra (lower body). The link name is of the link whose parent joint has the ID and name. 119
6.2 Mechanical specification of Hydra (upper body). 122
6.3 Sensors on a single developed EHA unit. 131
6.4 Arrangement of the joint driver box. 136

Chapter1

Introduction

1.1 Background

Modern framework of the actuation of articulated robot systems, initiated from the radioactive material handling in the field of nuclear research [1], has met a large variety of mechanical approaches in addition to the theoretical investigation on their nature. Starting from the works by Goertz [2], tendon-driven systems were widely studied since the actuator can be remotely placed from the joints with limited space. The Stanford-JPL hand by Salisbury et al. [3, 4] is an early example. Tendon-drives are also introduced to the surgery robot da Vinci [5]. Recently, Mizuuchi et al. developed the series of musculoskeletal humanoid robots [6, 7, 8, 9, 10]. Hydraulic actuators have been widely adopted in robot systems thanks to the advancement in the servo-valves, since the first two-stage servovalve patent by Gall et el. [11] filled in 1946 and the breakthrough by Moog et al. [12] filled in 1950. In addition to the numerous industrial robots, servovalve controlled hydraulic systems also drive quadruped robots such as the Bigdog [13] by Raibert et al. and HyQ [14] by Semini et al., and humanoid robots such as the petman [15] followed by atlas [16] by Boston Dynamics, and CB [17, 18] by Sarcos. A large part of the initial hydraulic systems was taken place by electric

motor driven ones since 1970's, due to the technical advancements in the magnetic materials, power electronics, and motor control theories. The commercial success of the harmonic drive since 1980's, originally patented in 1955 [19] by Musser, also helped it [20]. While common electric motor driven systems have a large reduction ratio gear train to magnify the weak torque of the motor, Asada et al. developed the direct-drive manipulator, whose motor is directly implemented in the joint without a gear transmission [21]. Recently Seok et al. enabled highly dynamic motions with the combination of a large torque motor and low reduction ratio gear [22, 23, 24]. Pneumatic actuation also has a long history in the robot actuation. The early works include the Utah-MIT hand by Jacobson et al. [25] in 1986. Pneumatic systems are widely combined with artificial muscles, which is firstly patented in 1955 [26] and then commercialized by Bridgestone in 1980's. The shadow dexterous hand [27] is an example of commercially successful pneumatic artificial muscle driven hand. Examples of pneumatically driven humanoid robots include the Lucy by Verrelst et al. [28] and the athlete robot by Niiyama et al. [29]. To exert impulsive high joint power, insertion of series elasticity, with which the kinetic energy is stored, is a natural approach since the model of muscles by Hill [30]. Hyodo et al. developed an antagonistically tendon driven joint with nonlinear series elasticity [31]. Pratt et al. developed a series elastic actuator for legged robots [32]. Recent outstanding works as a system includes COMAN by Tsagarakis et al. [33], WALK-MAN by Negrello et al. [34], and THOR by Knabe et al. [35].

For the next generation of robots which try to move from the well-defined environments such as factories or labs to an unstructured environment closer to or extremely

far from our lives, backdrivability of the actuators has been an important requirement. While actuation by the servovalve controlled hydraulic systems or the combination of electric motors and high reduction ratio gear train have high performance on the response and torque density, their backdrivability is limited by the large friction in the force transmission process. For the intrinsically backdrivable actuators, which are the direct driven system (including the low geared ones), pneumatic actuators, and series elastic actuators, there still exists tradeoff between limited torque density (for direct driven systems) and limited control bandwidth (for those with series elasticity). To overcome this problem, various approaches have been taken. One approach is to actively adjust the stiffness of the elastic components of series elastic actuators [36]. This can be achieved by the antagonistic tendon drive with non-linear springs (such as the work by Hyodo et al. [31], and Grebenstein et al. [37]), the cam disk and roller (the Floating Spring Joint by Wolf et al. [38]), and adjustable length plate spring (the knee joint by Otani et al. [39]). While the variable stiffness actuators can select the proper elasticity according to the task, such as to adjust the joint in a stiff configuration for high accuracy positioning and adjust in a compliant configuration for force-sensitive tasks, the different property cannot be achieved simultaneously. Zinn et al. [40] proposed parallel actuation of a manipulator with a large-torque series elastic actuator and a small size low geared direct drive mechanism to cover the late response of the elasticity. The spiral motor by Fujimoto et al. [41] is another approach merging the reducer and rotation/linear motion conversion function into the structure of a large-torque motor.

Electro-Hydrostatic Actuators (EHA) [42] is a distributed and stand-alone hy-

draulic system, where each actuator has its exclusive pump nearby, connected with a closed hydraulic circuit. For the transmission part, it is also called Hydrostatic Transmission (HST) [43]. The pump is driven by a servo motor and control of the actuator is done by the control of the motor, rather than a servovalve. Since each EHA has an independent circuit, a multi-DoF system with EHA does not have complex pipeline and manifold. They are also advantageous in energy efficiency since the necessary pressure is generated on-demand, rather than to regulate the high source pressure into the desired one by servovalve. Recently, they are widely adopted in aerospace industry, replacing the traditional centralized hydraulic system to drive the ladders [44, 45]. The early works to adopt hydrostatic transmissions to robot actuation includes the HST rotary robot joint by Bobrow et al. [46] and the linear actuator by Habibi et al. [47]. Kaminaga [48] pointed out that due to the simple structure of their hydraulic circuit, EHA can be designed to have high backdrivability and therefore suitable for force-sensitive actuation. Based on this idea, they developed a series of EHA driven hand [49, 50], robot knee joint [51] and human knee power assist device [52]; and they experimentally showed their high backdrivability [53]. Different examples of the adaptation of EHA to robot actuation includes the work by Alfayad et al. [54, 55, 56], while the focus was on the energy efficiency and the backdrivability was not discussed in detail.

Actuation by EHA has the possibility to resolve the tradeoff between the torque density and response of the intrinsically backdrivable actuators, since the force magnification is done by the principle of Pascal and its backdrivability does not rely on the explicit series elasticity. However, while its property of high backdrivability and

energy efficiency was studied in the previous works, both of the torque density and response were not deeply discussed and the performance presented in the existing works was not advantageous compared to other types of backdrivable actuators. Its integration into an articulated robot was also not accomplished. Currently existing systems only include the two-joints manipulator [57] and robot hands [49, 50]. While there was a trial to integrate EHA into a humanoid robot [58, 59], it is still not successful and the prototype is working with the common servovalve controlled system. Therefore, the property of hydrostatically driven large DoF robots, or especially humanoid robots, is not experimentally studied yet.

1.2 Objective of this Dissertation

The objective of this dissertation is to establish a generalized hardware design, control, and system integration framework to realize a hydrostatically driven humanoid robot and evaluate its whole body control and locomotion performance. The difficulty is that currently there do not exist any biped robot driven by EHA, therefore it is not clear whether it is possible to realize a hydrostatically driven humanoid with a locomotion capability, and whether a hydrostatically driven humanoid has an advantageous property compared with the robots with other actuation systems.

Before to integrate EHA to a humanoid and evaluate it, there are two main challenges. The first one is to enhance the torque density of the small and light-weight EHA. This is necessary because the currently available EHA with compatible size and weight for a humanoid robot do not have enough torque to support the body weight of the robot. This does not match the fact that the EHA for aerospace applications

have a superior torque density compared with actuators with mechanical transmissions. Therefore, by extracting the difference between the small and light-weight EHA for robot applications and those for aerospace applications, we present a systematic approach to realize EHA with enough torque density for a humanoid robot.

Backdrivability is our very motivation to select EHA as the actuator for a compliant humanoid robot. Therefore, its highly backdrivable property should not be harmed by the improvement of the torque density. In fact, EHA for the aerospace applications are not highly backdrivable actuators. In this dissertation, we also discuss the method to enhance the backdrivability of the torque-density-enhanced EHA.

The second challenge is to enhance the control bandwidth of EHA. For legged robots, the manipulation of the COM or swinging leg is a hard real-time task. Even for an intrinsically compliant robot, a selectively stiff control is partially required. While EHA are advantageous in the control bandwidth since its backdrivability is not relying on the elasticity, few attentions were paid in the existing works and the actually reported control bandwidths were not higher than the series elastic actuators. From both of the mechanical design and control perspective, we present the enhancement of the control bandwidth of the developed EHA.

In a large number of study on actuators the development of the hardware and its controller are performed independently. However, they are closely related: a fundamental improvement of the control performance is achieved by the modification of the hardware, and the development of the hardware need to take its effect on the control property into account. Therefore, before all of the discussion above, we first derive a simplified EHA model for the controller design from a complicated mechanical

model, relating the parameters of the two models.

1.3 Outline of this Dissertation

This dissertation consists of seven chapters. The initial part of this dissertation is on the realization of high torque density, highly backdrivable, and fast response miniature backdrivable EHA capable to actuate humanoid robots. Chapter 2 provides the modeling and analysis of EHA's behavior. Chapter 3 provides mechanical design approaches to improve the miniature backdrivable EHA's torque density, Chapter 4 provides enrichment of EHA's backdrivability. Chapter 5 provides hardware and control approaches to enhance EHA's closed-loop position/torque control bandwidth. The latter of this dissertation, which is chapter 6, is on the integration of developed EHA to the whole-body actuation system of a humanoid robot and evaluation of its whole-body control property, including the walking performance. Chapter 7 concludes the dissertation.

Chapter2

Mathematical Description of EHA to Design a High Performance Servo System

2.1 Introduction

Improvement of the performance of an actuator should be approached from both of the hardware and control aspects. While in most cases the development of the hardware and controller are conducted independently, the effect of hardware design parameters on the control performance should always be taken into consideration. In other words, the hardware should be designed according to the requirement of the controller side and for any modification of the hardware, its effect on the control property should be evaluated in advance.

EHA can be expressed as a linear system with a damper corresponding to the internal leakage and spring corresponding to the fluid compressibility [60], and therefore expressed as two inertias connected by a serial damper and serial spring [61]. Tsuda et al. [62] pointed out that an EHA driven joint with long pipeline can be modeled

as a two-inertia resonance system and adopted the self-resonance suppression control [63]. Kaminaga et al. [53] proposed a simple and symmetric (between input and output side) state space explanation and formulation of EHA, targeting the backdrivable EHA driven robot joints.

In a simplified EHA model, each parameter is the result of a complex combination of the hardware design parameters. In most of the models, however, their values are directly identified through experiments therefore it is not clear which property of the hardware is actually governing it and how to modify the hardware to fundamentally improve the performance. In this chapter, for the use of the discussion on both of the hardware design and control of EHA in the following chapters, we derive a simplified linear EHA model from a detailed model with mechanical parameters such as gaps or cylinder bore, and discuss their effect on the control performance. Furthermore, we identify the parameters of our developed EHA from FEM analysis and quasi-static experiments to discuss which parameters are dominant and require careful design.

2.2 Internal Leakage, Fluid Compressibility and Pipeline Expansion

We first consider the model shown in Fig.2.1. In the figure, the pump on the left is connected to the actuator on the right, with the pipelines. The pump receives an external force/torque input of $\tilde{\tau}_p$, and the actuator's output force/torque is τ_c. The unit is [N] in the case of a linear pump/actuator, and [Nm] in the case of a rotary pump/actuator. The position of the pump is $\tilde{\theta}_p$ and the position the actuator is θ_c,

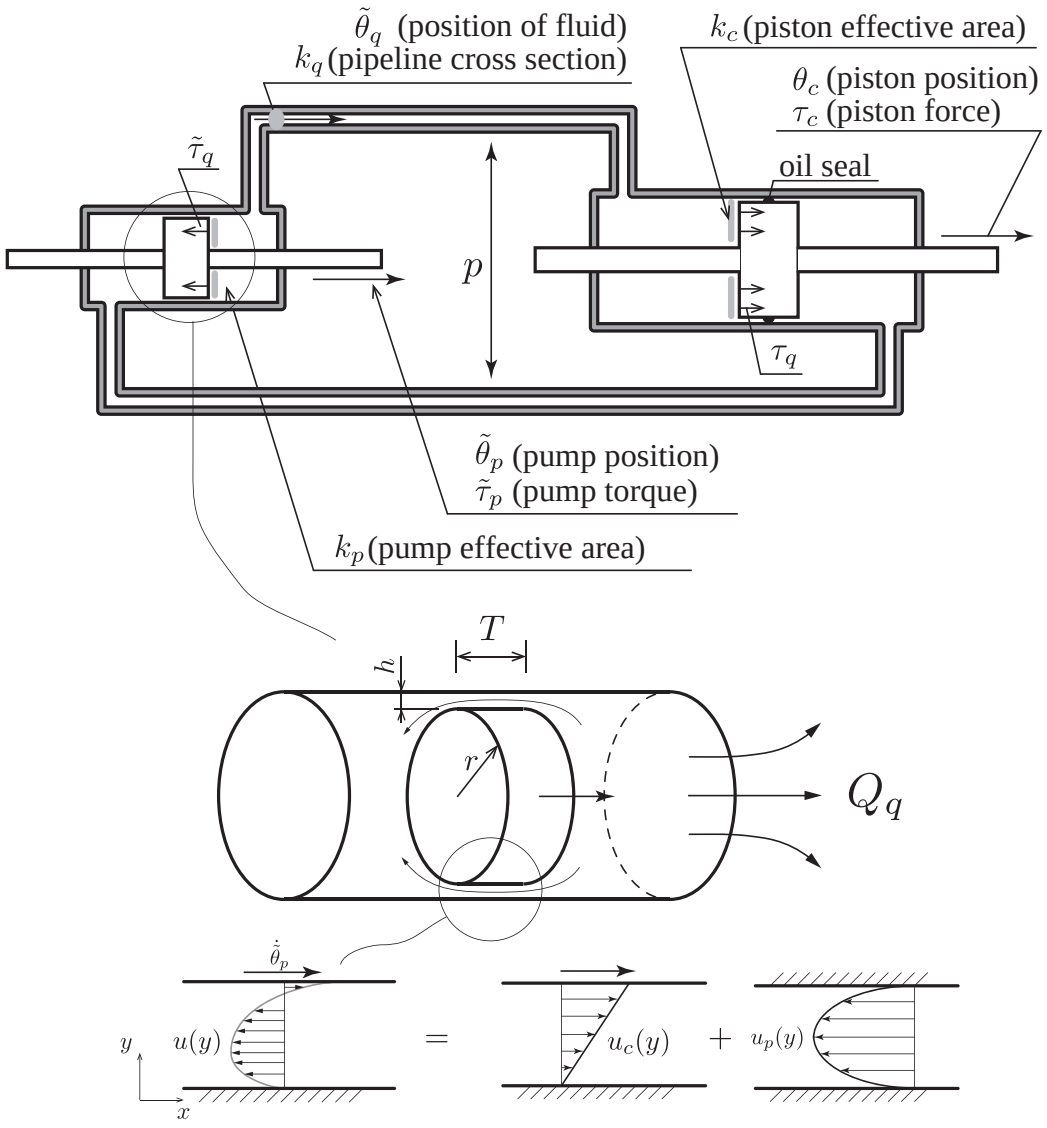

Figure 2.1: Schematic of an EHA with internal leakage.

with the unit of [m] for a linear and [rad] for a rotary version. The constants k_p and k_c are the effective pressure receiving surface of the pump and actuator, with the unit of [m^2] for the linear and [m^3] for the rotary one. With the differential pressure of the system, which is denoted as p [Pa], the pump and the actuator receive the pressure-induced force of $\tilde{\tau}_q$ and τ_q ([N] or [Nm]) respectively:

$$\tilde{\tau}_q = k_p p \tag{2.1}$$

$$\tau_q = k_c p \tag{2.2}$$

Internal leakage is a leak of fluid from the high-pressure side to the low-pressure side in a hydraulic system. In the following, we treat the actuator as a linear cylinder, which has almost zero internal leakage due to the piston seal, therefore we only consider the leak inside the pump. When the Reynolds number is low, the flow of the internal leakage is laminar, or more specifically the Couette-Poiseuille flow, which is a linear sum of the Couette flow and the Poiseuille flow. The former is the drag flow between two surfaces moving tangentially, and the latter is the pressure-induced flow through a channel. When we treat the pump as a linear cylinder shown in the bottom of Fig.2.1, the flow velocity distribution in the gap is expressed as

$$u(y) = \frac{\dot{\theta}_p}{h} y + \frac{p}{2\mu T}(y^2 - hy) \tag{2.3}$$

where μ [Pa·s] is the fluid viscosity and h [m] is the internal gap between the moving part and the casing. The actual discharging flow rate of the pump Q_q [m^3/s] and the pump input force $\tilde{\tau}_p$ can be then expressed as follows:

$$Q_q = k_p \dot{\theta}_p + \pi h r^2 \dot{\theta}_p - \frac{\pi r h^2}{6\mu T} p \tag{2.4}$$

$$\tilde{\tau}_p = \tilde{\tau}_q + \frac{2\pi\mu r T}{h} \dot{\theta}_p + \frac{\pi h r}{\mu} p \tag{2.5}$$

where r [m] and T [m] is the radius and thickness of the pump's piston, respectively. In Eq.(2.4), the first term is the theoretical flow. The second term is the drag flow (the Couette flow corresponding to the first term of Eq.(2.3)) and the last term is the internal leakage (the Poiseuille flow corresponding to the second term of Eq.(2.3).) Similarly, in Eq.(2.5), the second term is the viscous friction by the drag flow and the third term is the drag by the internal leakage flow.

For rotational pumps, such as gear pumps or rotational piston pumps, we can make a further approximation to ignore the second term of Eq.(2.4) and the third term of Eq.(2.5), since their effect is canceled through the rotation. [1] With the definition of the internal leakage resistance k_l [Pa/(m^3/s)] and pump's damper $\tilde{d}_p$ [Nm/(rad/s)] as follows,

$$k_l \triangleq \frac{6\mu T}{\pi r h^2} \tag{2.6}$$

$$\tilde{d}_p \triangleq \frac{2\pi\mu r T}{h} \tag{2.7}$$

we can simplify Eq.(2.4) and Eq.(2.5) as follows:

$$Q_q \approx k_p\dot{\tilde{\theta}}_p - \frac{1}{k_l}p \tag{2.8}$$

$$\tilde{\tau}_p \approx \tilde{\tau}_q + \tilde{d}_p\dot{\tilde{\theta}}_p \tag{2.9}$$

To eliminate Q_q, we define a point on the piping which is close to the pump so that there is no elasticity between them (see Fig.2.1.) The flow rate can be expressed by the product of the cross-section of the pipeline k_q [m^2] and the mean flow velocity $\dot{\tilde{\theta}}_q$ [m/s]:

$$Q_q = k_q\dot{\tilde{\theta}}_q \tag{2.10}$$

[1] The summation of the drag flow is zero in the discharging direction, since the motion is cyclic. The torque due to the drag of the internal leakage flow balances in the pump torque direction.

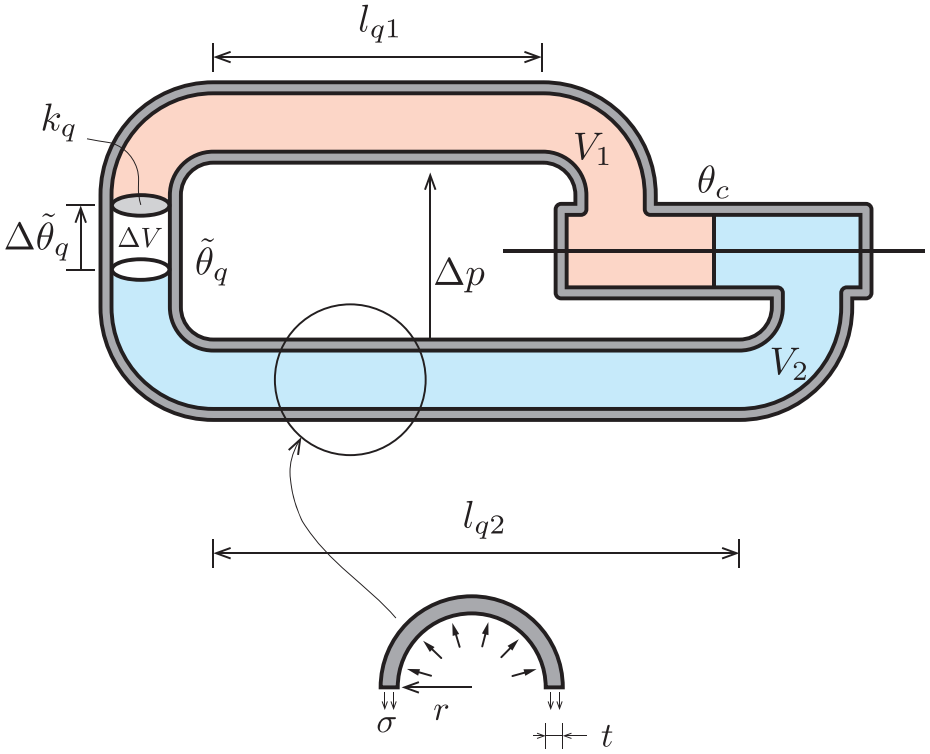

Figure 2.2: Effect of the pipeline expansion and fluid compressibility on the behavior of an EHA.

The transmission of EHA includes speed reduction and conversion between the rotary and linear motion. The values such as pump's rotational velocity or flow velocity can be converted to the equivalent value seen from the actuator. If we denote the actuator equivalent value of $\tilde{\theta}_p$, $\tilde{\theta}_q$ as θ_p, θ_q, they are

$$\theta_p \triangleq \frac{k_p}{k_c}\tilde{\theta}_p \tag{2.11}$$

$$\theta_q \triangleq \frac{k_q}{k_c}\tilde{\theta}_q \tag{2.12}$$

From Eq.(2.2), Eq.(2.8), Eq.(2.10), Eq.(2.11), Eq.(2.12), we get a series linear damper:

$$\tau_q = k_l k_c^2(\dot{\theta}_p - \dot{\theta}_q) \triangleq d_s(\dot{\theta}_p - \dot{\theta}_q) \tag{2.13}$$

While there is a series damper between θ_p and θ_q due to the internal leakage,

there is a series elasticity between θ_q and θ_c due to the pipeline expansion and fluid compressibility. We consider a case that the piston is fixed, as shown in Fig.2.2. If the pump generates Δp [Pa] pressure in addition to the original differential pressure p, the fluid inside the pipeline moves $\Delta\tilde{\theta}_q$ [m].

We first discuss the effect of pipe expansion, taking the fluid as incompressible. In that case, the conservation of the fluid volume can be written as

$$\Delta\tilde{\theta}_q k_q = \Delta k_{q1} l_{q1} \tag{2.14}$$

$$-\Delta\tilde{\theta}_q k_q = \Delta k_{q2} l_{q2} \tag{2.15}$$

where l_{q1}, l_{q2} [m] is the length of pipeline on the high and low pressure side and Δk_{q1}, Δk_{q2} [m^2] is the variation of the pipeline cross section due to Δp. When the pipeline is approximated as a thin cylinder with the inner radius r [m], thickness t [m] and the Young's modulus E [Pa], variation of the inner cross section can be expressed as

$$\Delta k_{qi} = \pi(r + \Delta r_i)^2 - \pi r^2 \tag{2.16}$$

$$\approx 2\pi r \Delta r_i \tag{2.17}$$

$$= \frac{2\pi r^3}{Et}\Delta p_i \tag{2.18}$$

where Δp_i $(i = 1, 2)$ denotes the absolute pressure variation on the both side. The differential pressure variation due to the pipe expansion Δp_{pipe} is therefore expressed by $\Delta\theta_q$, which is the cylinder equivalent value of $\Delta\tilde{\theta}_q$.

$$\Delta p_{\text{pipe}} = \Delta p_1 - \Delta p_2 \tag{2.19}$$

$$= \frac{Etk_c}{2\pi r^3}\left(\frac{1}{l_{q1}} + \frac{1}{l_{q2}}\right)\Delta\theta_q \tag{2.20}$$

Secondly, we treat the pipe has no deformation and see the effect of the fluid

compressibility. The invariant chamber volume results

$$-\Delta\tilde{\theta}_q k_q = \Delta V_1 \tag{2.21}$$

$$\Delta\tilde{\theta}_q k_q = \Delta V_2 \tag{2.22}$$

where V_i [m^3] $(i = 1, 2)$ is the fluid volume on the two sides. The relation between the pressure variation Δp_i and volume variation ΔV_i of the fluid is dependent on the fluid volume:

$$\Delta V_i = -\frac{V_i}{\kappa}\Delta p_i \qquad (i = 1, 2) \tag{2.23}$$

where κ [Pa] is the bulk module. The variation of the differential pressure due to the fluid compressibility Δp_{fluid} is then

$$\Delta p_{\text{fluid}} = \kappa k_c \left(\frac{1}{V_1} + \frac{1}{V_2}\right)\Delta\theta_q \tag{2.24}$$

If we ignore the small mutual effect of the piping expansion and fluid compressibility, the total series elasticity is a parallel connection of them:

$$\tau_q = \frac{k_s^{\text{pipe}} k_s^{\text{fluid}}}{k_s^{\text{pipe}} + k_s^{\text{fluid}}}(\theta_q - \theta_c) \triangleq k_s(\theta_q - \theta_c) \tag{2.25}$$

$$k_s^{\text{pipe}} \triangleq \frac{Etk_c^2}{2\pi r^3}\left(\frac{1}{l_{q1}} + \frac{1}{l_{q2}}\right) \tag{2.26}$$

$$k_s^{\text{fluid}} \triangleq \kappa k_c^2\left(\frac{1}{V_1} + \frac{1}{V_2}\right) \tag{2.27}$$

2.3 A Simplified Linear EHA Model

From Eq.(2.13), Eq.(2.25), we can simplify EHA as a model shown in Fig.2.3, where J_p is the pump's effective inertia and J_c is the inertia of the piston. The key is to treat all values such as the pump's torque/angular velocity or fluid pressure/flow-rate as the equivalent value seen from the actuator.

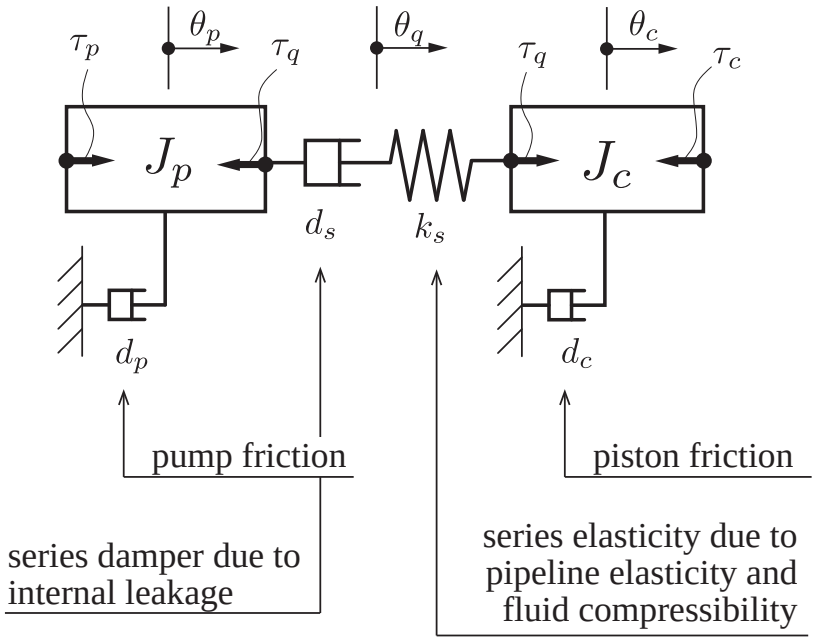

Figure 2.3: Simplified model of an EHA as two inertias connected with a series damper and elasticity. The key is to treat all values such as the pump's torque/angular velocity or fluid pressure/flow-rate as the equivalent value seen from the actuator.

The behavior of the pump, series damper, series elasticity, and piston can be written as follows:

$$J_p s^2 \theta_p + d_p s \theta_p + \tau_q = \tau_p \tag{2.28}$$

$$\tau_q = d_s s(\theta_p - \theta_q) \tag{2.29}$$

$$\tau_q = k_s(\theta_q - \theta_c) \tag{2.30}$$

$$J_c s^2 \theta_c + d_c s \theta_c + \tau_c = \tau_q \tag{2.31}$$

Eliminating intermediate variables θ_p, θ_q, we get the following transfer functions:

$$\tau_q = \frac{d_s k_s}{\mathrm{G}_1(s)}\tau_p - \frac{\mathrm{G}_2(s)}{\mathrm{G}_1(s)}s\theta_c \tag{2.32}$$

$$\tau_c = \frac{d_s k_s}{\mathrm{G}_1(s)}\tau_p - \frac{\mathrm{G}_3(s)}{\mathrm{G}_1(s)}s\theta_c \tag{2.33}$$

$$s\theta_c = \frac{d_s k_s}{\mathrm{G}_3(s)}\tau_p - \frac{\mathrm{G}_1(s)}{\mathrm{G}_3(s)}\tau_c \tag{2.34}$$

$$\tag{2.35}$$

where $\mathrm{G}_1(s)$, $\mathrm{G}_2(s)$, $\mathrm{G}_3(s)$ is defined as follows:

$$\mathrm{G}_1(s) \triangleq J_p d_s s^2 + (J_p k_s + d_p d_s)s + (d_p + d_s)k_s \tag{2.36}$$

$$\mathrm{G}_2(s) \triangleq J_p d_s k_s s + d_p d_s k_s \tag{2.37}$$

$$\begin{aligned}\mathrm{G}_3(s) \triangleq\ & -J_p J_c d_s s^3 - (J_p J_c k_s + J_c d_p d_s + J_p d_s d_c)s^2 \\ & -(J_c d_p k_s + J_c d_s k_s + J_p d_c k_s + d_p d_s d_c - J_p d_s k_s)s \\ & -d_p d_c k_s - d_s d_c k_s + d_p d_s k_s\end{aligned} \tag{2.38}$$

In Eq.(2.32) and Eq.(2.33), the first term shows that it is a second order lag system between the pump input torque and the pressure or actuator force. The second term denotes the effect of piston velocity on the actuator force. In the case that J_c and d_c is small, $\mathrm{G}_2 \approx \mathrm{G}_3$, therefore the pressure and the piston force are almost the same. Eq.(2.34) shows that there is a third order lag between pump torque and piston velocity.

From the model, we can also derive the T-N curve and efficiency of the system. Here, we take an example of the actuator set expressed in the following section 2.4. The T-N curve illustrates the relationship between the output force and velocity, with a fixed input. In the case of electric motors, the fixed input is the voltage and the

relationship is a straight line. In the case of EHAs, multiple types of the fixed input is possible, such as motor voltage, motor current, or motor velocity. When we are in the context of robot actuation, the largest constraint is mostly the motor torque, or the motor current, which is limited by the heat problem. This leads us to select the maximum motor current, which is set as 18 A q-axis current in our system, as the constant input.

Based on the parameters identified in 2.4.2, when the friction and internal leakage do not exist, the 18 A q-axis current corresponds to 2150 N piston force. In other words, $\tau_p = 2150$ in the model shown in Fig.2.3. For each given value of the piston force τ_c or the piston velocity $\dot{\theta}_c$, the other value is calculated. The calculated T-N curve is shown in the top left graph of Fig.2.4. As the same case with the electric motor, the T-N curve with a fixed motor torque also has a straight line shape. The stall piston force is around 1700 N and the maximum piston velocity is around 150 mm/s. This corresponds well with the maximum force and velocity experiment in the previous work [64].

The upper right graph shows the input energy of each point on the T-N curve, while the middle left graph shows the output energy. On the middle right is the volumetric efficiency, which represents the ratio of the piston displacement to the theoretical pump discharge volume. On the bottom left is the torque efficiency, which is the ratio of piston force to the input force. Lastly, the bottom right is the total energy efficiency, which is the ratio of the output energy to the input energy, and also equals to the product of the volumetric efficiency and torque efficiency. The highest efficiency of the transmission is estimated to be 40 %. A difference from electric motors is that

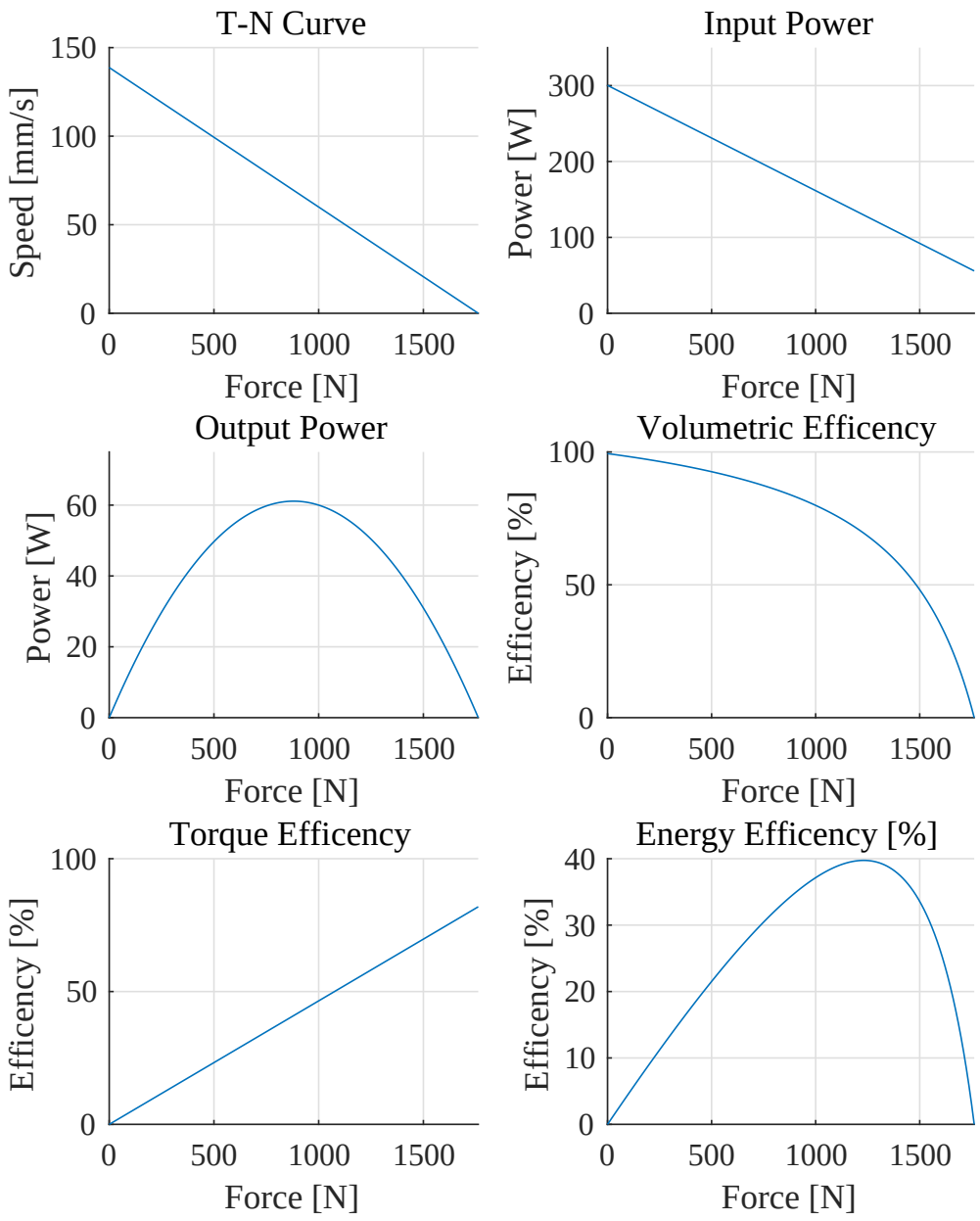

Figure 2.4: T-N curve (top left), input power (top right), output power (middle left), volumetric efficiency (middle right), torque efficiency (bottom left), and total energy efficiency (bottom right) of the developed EHA when a constant motor q-axis current of 18 A is applied. The volumetric efficiency represents the ratio of the piston displacement to the theoretical pump discharge volume. The torque efficiency is the ratio of piston force to the input force.

the peak of the efficiency exists on the high torque side, while the electric motors have it on the low torque side. This is because of the difference of the "resistance". In the case of electric motors, the torque is low in the high speed region due to the back-EMF. This simply caused less current and do not generate loss by itself. In EHAs, the force is low in the high speed region because of the friction in the pump, which is an energy loss. This suggests that the EHA is more suitable for large torque and slow motion applications.

2.4 Comparison with the Experiment Data

2.4.1 Experiment Setup

In this section the dynamic behavior of the real actuator and the presented model is compared. The experiment setup is shown in Fig.2.5. The actuator is our developed high force to weight ratio linear EHA, the detail of which is shown in the following chapters. The actuator is placed horizontally. This testbed experiment setup is a common one in this thesis. A movable cart supported with a pair of linear guides is aligned with the actuator. The cart and the actuator can be connected with a connecting rod, on which a strain gauge is attached. On the connection between the connecting rod and the cart, a force gauge is attached. The cart can be either fixed on the basement, free to move, or disconnected from the actuator so that the actuator has no load.

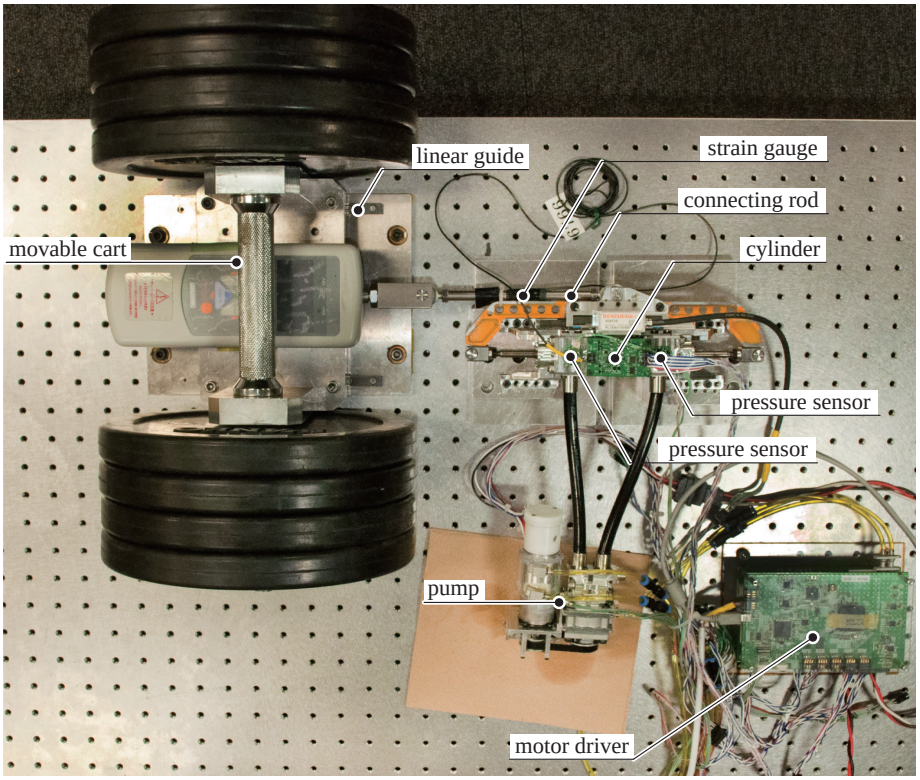

Figure 2.5: Common setup of the testbed experiment. The actuator is placed horizontally. A movable cart supported with a pair of linear guides is aligned with the actuator. The cart and the actuator can be connected with a connecting rod, on which a strain gauge is attached. On the connection between the connecting rod and the cart, a force gauge is attached. The cart can be either fixed on the basement, free to move, or disconnected from the actuator so that the actuator has no load.

2.4.2 Parameter Identification

We first decide the values of each variable by either calculation or experiments. The pump inertia J_p [kg] is the equivalent value seen from the piston. If we write the original inertia of the pump rotor and motor rotor as $\tilde{J}_p$ [kg·m^2], we acquire J_p from the preservation of kinetic energy:

$$\frac{1}{2}\tilde{J}_p\dot{\tilde{\theta}}_p^2 = \frac{1}{2}J_p\dot{\theta}_p^2 \tag{2.39}$$

We get J_p as 118 kg from the 6.23×10^{-6} [kg m^2] $\tilde{J}_p$ from the CAD model and motor catalogue. The piston inertia J_c is acquired from the CAD model as 295 g.

The elasticity due to the pipeline, which the one in Eq.(2.26), is acquired through a FEM analysis with a simplified tube model. The piping is Bridgestone's SPL04 plastic hose with 6.3 mm inner bore and 10.6 mm external diameter. It is made of the polyester main layer, polyester fiber reinforcement layer, and polyurethane cover layer, from the inner to outer order. We approximate it as a simple polyester tube with the same dimension. We take a typical case of an EHA which has 150 mm length pipeline on each side. When we apply 5.25 MPa differential pressure which corresponds 1500 N piston force τ_c, we get 19.8×10^{-9} m^2 cross section variation Δk_q, therefore k_s^{pipe} is estimated as 144×10^6 N/m.

For the elasticity due to fluid compressibility, we consider the maximum case and the minimum case, since the value varies depending on the position of the piston (see Eq.(2.27).) When the piston is at the end of the cylinder, the dead volume between the piston and the cylinder head is 1750 mm^3, calculated from its CAD model. The fluid in each pipeline is 4680 mm^3, assuming that they have 150 mm length on each side. The piston swept volume, or the cylinder displacement, is 14300 mm^3. Assuming

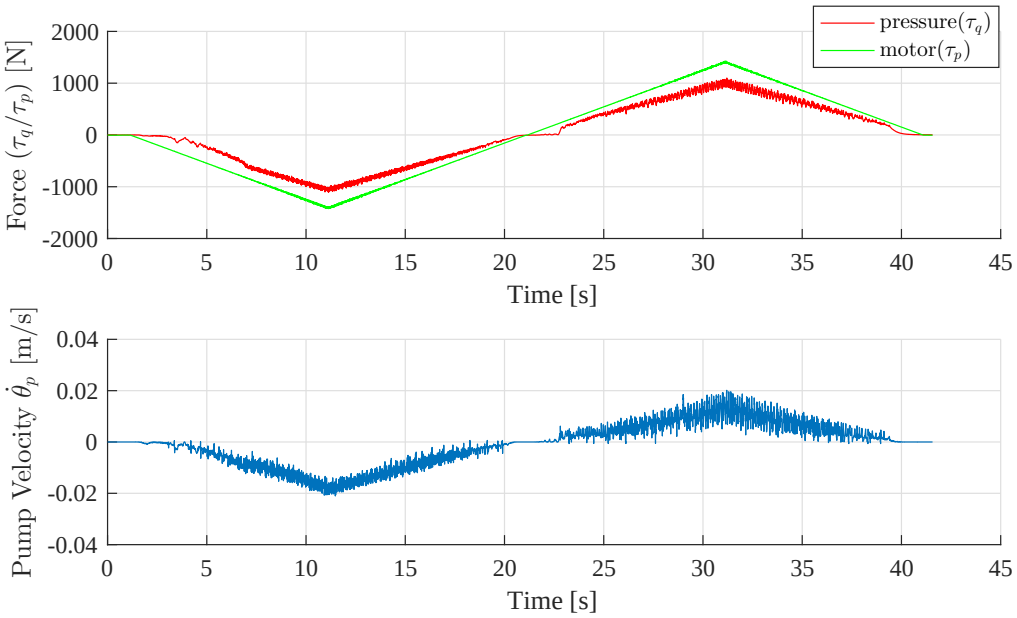

Figure 2.6: Time transition of the experiment to identify d_p and d_s. The top graph shows the value of τ_p (motor input torque) in green color and τ_q (pressure) in red color. The lower graph shows the pump velocity $\dot{\theta}_p$ seen from the piston.

the bulk module κ is 1.85 GPa [60], we get the maximum elastic coefficient ${}_{\max}k_s^{\text{fluid}}$ as 3.08×10^7 N/m (when the piston is in the middle of the cylinder) and the minimum ${}_{\min}k_s^{\text{fluid}}$ as 2.23×10^7 (when the piston is at the end of the cylinder.)

As the total, the series elasticity coefficient k_s varies from 2.54×10^7 N/m to 1.93×10^7 N/m depending on the piston position. Their variation from the average value 2.24×10^7 N/m is less than 14%, which justify our approximation of it as a constant linear elasticity.

To acquire damper factors, we conducted a series of identification experiments. The first experiment is to fix the piston and apply a ramp input to the pump. τ_p can be measured through the motor current and τ_q is measured by the pressure sensor. With the pump velocity acquired from the motor encoder, we can identify d_p and d_s. The

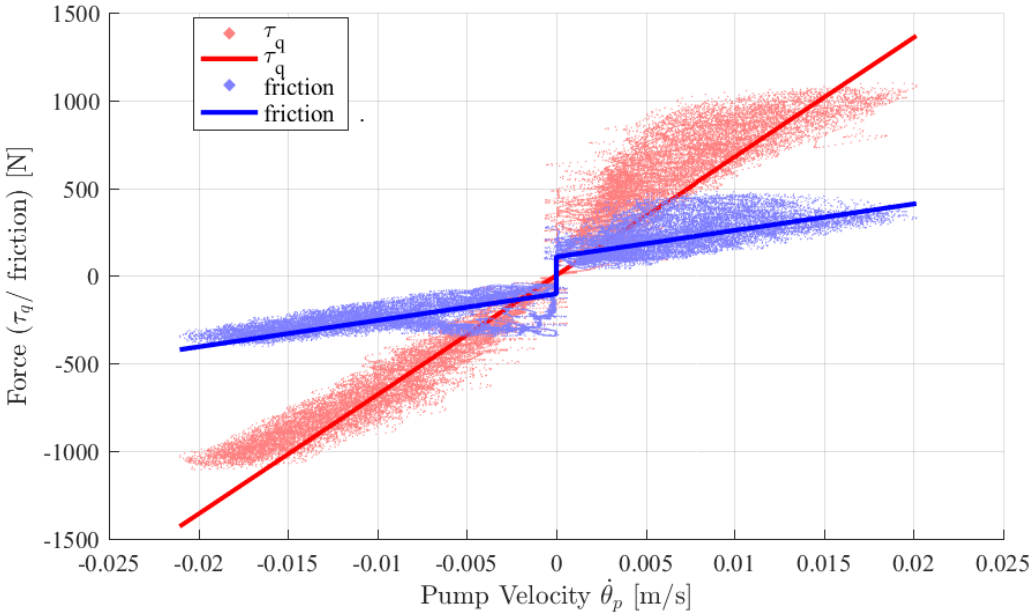

Figure 2.7: Plot of the pump pressure and pump friction against pump velocity. All values are converted to the equivalent value seen from the cylinder. The red markers shows the pressure acquired from the pressure sensor and the blue markers shows the friction, calculated from the difference between the pressure and motor current.

second experiment is to free the piston and control the motor to generate a variety of piston velocity. Data is trimmed to eliminate those when the piston is accelerating. Since the external force τ_c is zero, τ_q equals to the friction force.

Fig.2.6, Fig.2.7 shows the result of the first experiment, while the former graph shows its time transition and the latter shows the relationship between pump friction and τ_q against $\dot{\theta}_p$. In Fig.2.6, the top graph shows the value of τ_p (motor input torque) in green color and τ_q (pressure) in red color. The lower graph shows the pump velocity $\dot{\theta}_p$ seen from the piston. In Fig.2.7, blue color dots represent viscosity friction in the pipeline. The green color dots represent the friction due to the contact oil seal. and the red color ones is the total friction. The property of d_s (shown in red markers) is

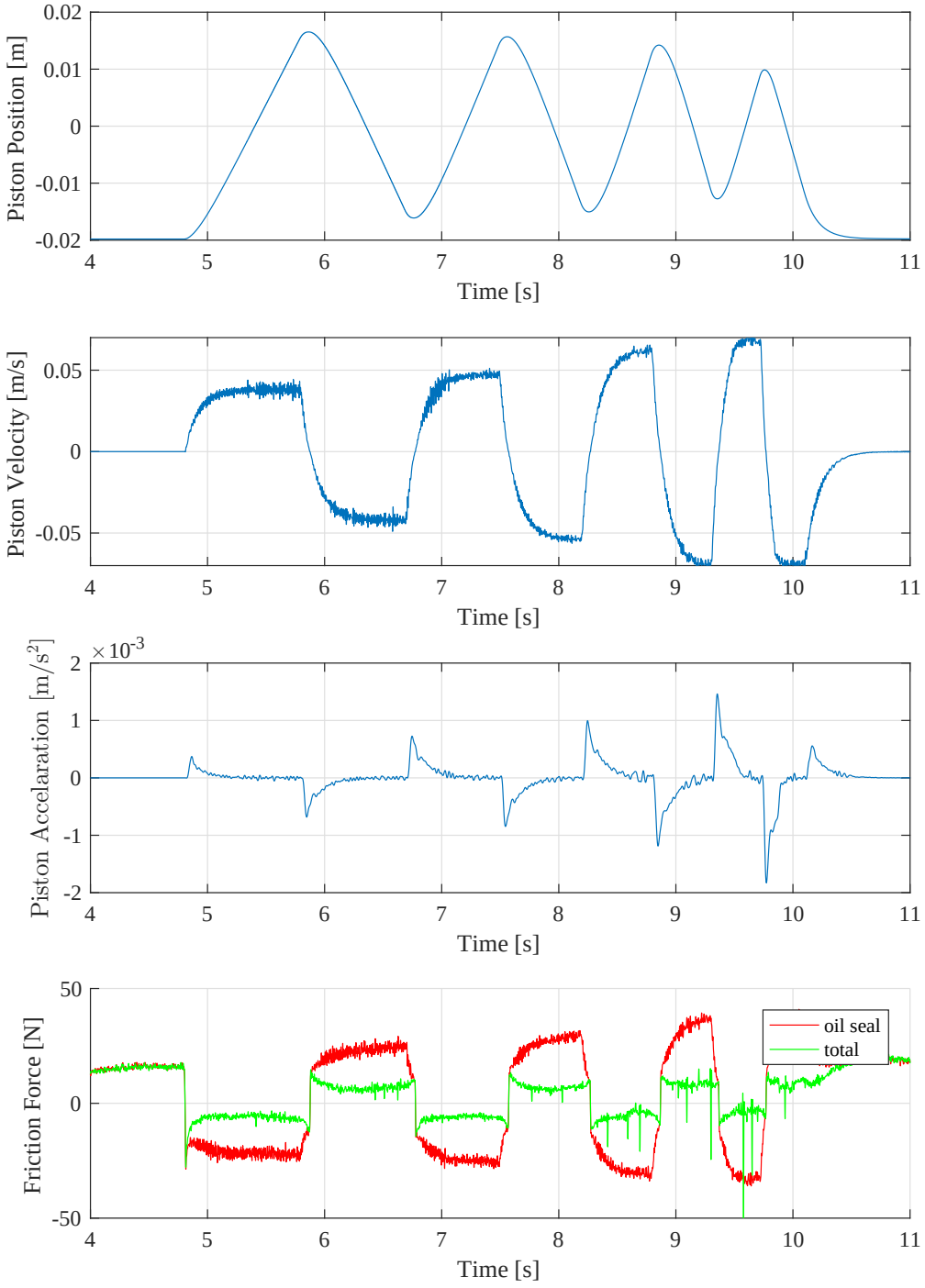

Figure 2.8: Time transition of the experiment to identify d_c. The piston position, velocity, acceleration and friction is shown.

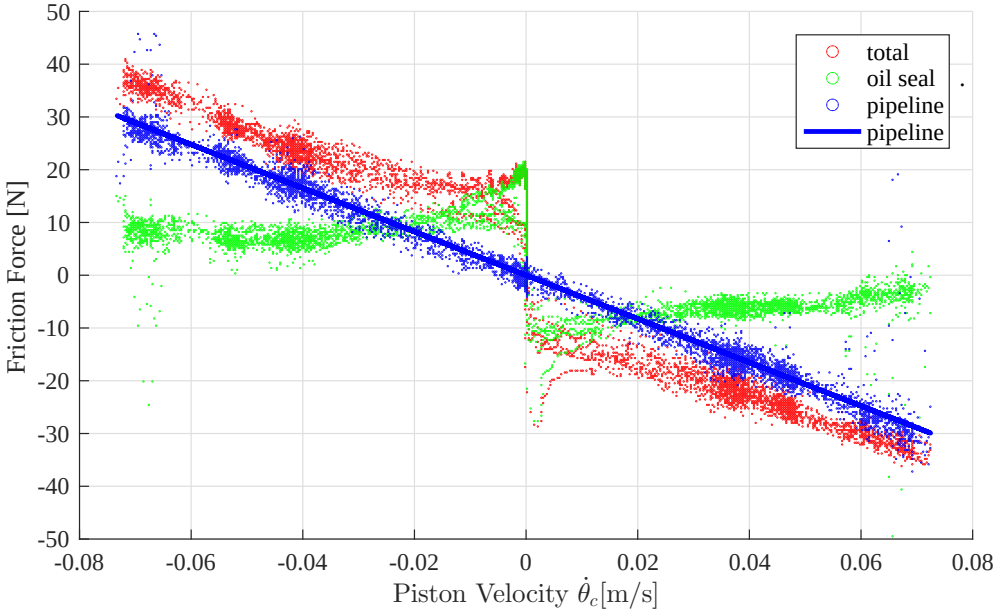

Figure 2.9: Relationship between piston velocity and friction. Blue color dots represent viscosity friction in the piping. Green color dots represent friction due to the contact oil seal. Red color is the total friction.

quite linear, since its behavior is described in a framework of hydrodynamics in the previous section. From the graph we get the value of 6.79×10^4 N/(m/s) as d_s. The pump friction d_p has a nonlinearity when the direction of the pump switches. This is because it is a combination of viscosity friction and oil seal's mechanical friction. If we linearize it, we get the value of 2.48×10^4 N/(m/s) as d_p.

Fig.2.8, Fig.2.9 shows the result of the second experiment, while the former graph shows the time transition and the latter shows the values against piston velocity. Fig.2.8 shows the value of pump position, velocity, acceleration and friction, respectively. The friction due to d_c includes viscosity friction in the pipeline and the mechanical friction of the oil seals and bushings. The developed EHA has two pairs of pressure sensors, which measure the differential pressure on both the pump and

cylinder. In the case of this experiment, the piston is free ($\tau_c = 0$) therefore the force acquired from the pump pressure sensor equals to the friction. With the pressure sensors on the cylinder, we can get additional information with which we can separate the viscosity and mechanical friction. The pump pressure is shown in the red and the cylinder pressure is shown in green line. In Fig.2.9, the red markers show the total friction from the pump pressure sensors, the green line shows the mechanical friction measured from the cylinder sensors, and the blue line shows the viscosity friction acquired from the difference between the two pressure sensor pairs. The viscosity friction is linear, from where we can get the damper coefficient of 414 N/(m/s). The total friction coefficient d_c is linearized as 549 N/(m/s). Table 2.1 summarizes the parameters.

2.4.3 Comparison of the Dynamic Behavior

To validate the model against real experiment data, we conducted several open loop frequency response experiments. The first experiment is to fix the piston and apply sine wave τ_p input to the pump and see the relationship between τ_p and τ_q. This corresponds to Eq.(2.32) with $s\theta_c = 0$, therefore we can see the effect of $G_1(s)$. The time transition of the values is shown in Fig.2.10. To acquire the frequency response with less noise, the sine wave reference, or the excitation signal, has a constant frequency. The actually applied excitation signal is a simple connection of multiple "constant frequency sine wave" with different frequency. The acquired experiment data is then cut into independent zones with a constant excitation frequency. In each of them, we apply FFT to both the input signal and the output signal. The gain

Table 2.1: Parameter value in Fig.2.3.

Parameter	Value	Unit	Description
$\tilde{\theta}_p$	-	rad	position of pump
θ_p	-	m	piston equivalent value of $\tilde{\theta}_p$
$\tilde{\theta}_q$	-	m	position of fluid on pump discharging port
θ_q	-	m	piston equivalent value of $\tilde{\theta}_q$
k_p	66.5×10^{-9}	m^3	pump effective pressure receiving surface
k_q	31.1×10^{-6}	m^2	piping cross section
k_c	286×10^{-6}	m^2	piston effective pressure receiving surface
$\tilde{J}_p$	6.23×10^{-6}	kg·m^2	inertia of pump rotor
J_p	118	kg	inertia of pump rotor seen from piston
J_c	295×10^{-3}	kg	inertia of piston and beam structure
d_p	1.50×10^{4}	N/(m/s)	pump friction damper coefficient
d_c	413	N/(m/s)	piston friction damper coefficient
d_s	6.79×10^{4}	N/(m/s)	internal leakage serial damper coefficient
k_s^{pipe}	1.44×10^{8}	N/m	elasticity due to piping expansion
${}_{\max}k_s^{\text{fluid}}$	3.08×10^{7}	N/m	elasticity due to fluid compression (maximum)
${}_{\min}k_s^{\text{fluid}}$	2.23×10^{7}	N/m	elasticity due to fluid compression (minimum)
${}_{\max}k_s$	2.54×10^{7}	N/m	total series elasticity (max)
${}_{\min}k_s$	1.93×10^{7}	N/m	total series elasticity (min)
${}_{\text{ave}}k_s$	2.24×10^{7}	N/m	total series elasticity (average)

and the phase delay on the frequency with the largest amplitude is treated as the data point, while the data points of each zone are gathered to shape a bode plot. The acquired bode plot is shown in Fig.2.11, with the measured data plot in blue circle markers. The plot of $d_s k_s/\mathrm{G}_1$ is shown as a red line. The experiment data and the model roughly correspond to each other, while the former has a resonance point around 25 Hz, where in the case of the model there is a small one around 60 Hz. The cause for this difference is presumed to be the nonlinearity of the pump friction.

The second open loop response experiment is done with the piston free to move. As the same with the previous experiment, we input sine wave τ_p to the pump and see the relationship between τ_p and this time the piston velocity $\dot{\theta}_c$. This corresponds to Eq.(2.34) with $\tau_c = 0$, therefore we can see the difference of $\mathrm{G}_3(s)$ The time transition of the values in the experiment is shown in Fig.2.12. The Bode plot is shown in Fig.2.13, where the experimental data is shown in blue markers and the value from the $d_s k_s/\mathrm{G}_3 s$ is shown in red line. The gain of the experimental data and model corresponds well, while the phase latency is smaller in the case of experimental data.

2.5 Conclusion

In this chapter, for the use of the discussion on both of the hardware design and control of EHA in the later chapters, we derived a simplified linear EHA model from a detailed model and discussed their effect on the control performance. The specific conclusion is as follows:

1. An EHA can be simplified as a mass-spring-damper model if all values such as

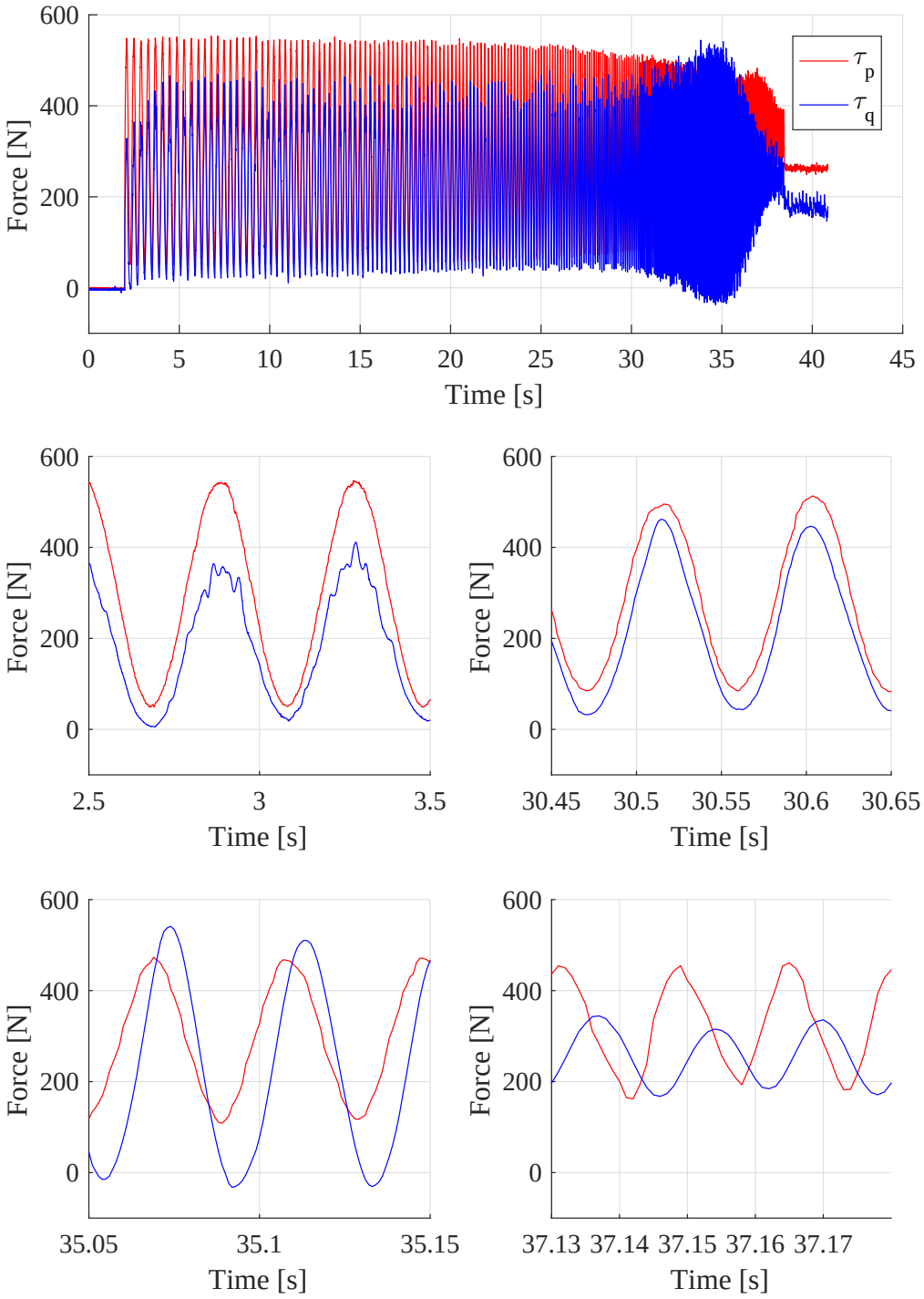

Figure 2.10: Time transition of the experiment to acquire the open loop frequency response between the pump torque τ_p as the input and the pressure τ_q as the output, under the condition that the piston is fixed.

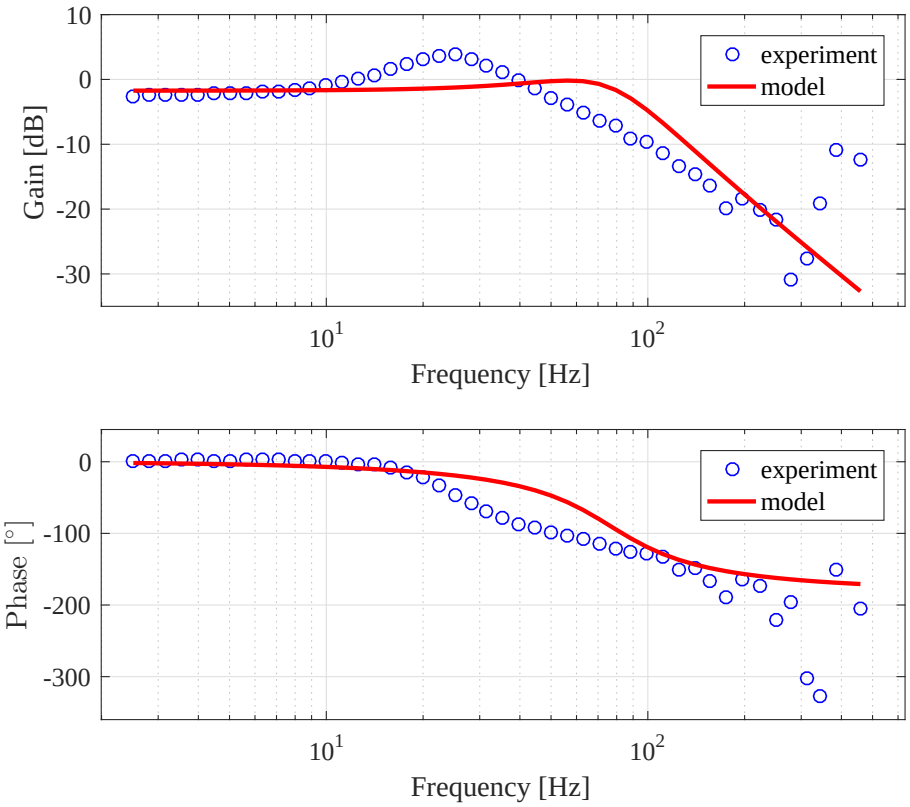

Figure 2.11: Open loop frequency response between pump torque τ_p as the input and pressure τ_q as the output, under the condition that the piston is fixed. The blue markers show the experiment data, while the red line shows the theoretical value of $d_s k_s / \mathrm{G}_1$.

pump torque/velocity and fluid pressure/flow-rate are expressed in the equivalent value seen from the actuator. The flow of the internal leakage in the pump can be modeled as a serial damper between the pump and the fluid. The elasticity due to the pipeline expansion and fluid compressibility can be modeled as a linear series elasticity between the fluid and the load.

2. The actuator output force is affected by both the motor torque and the actuator output velocity, as the second order lag system. The output velocity of the

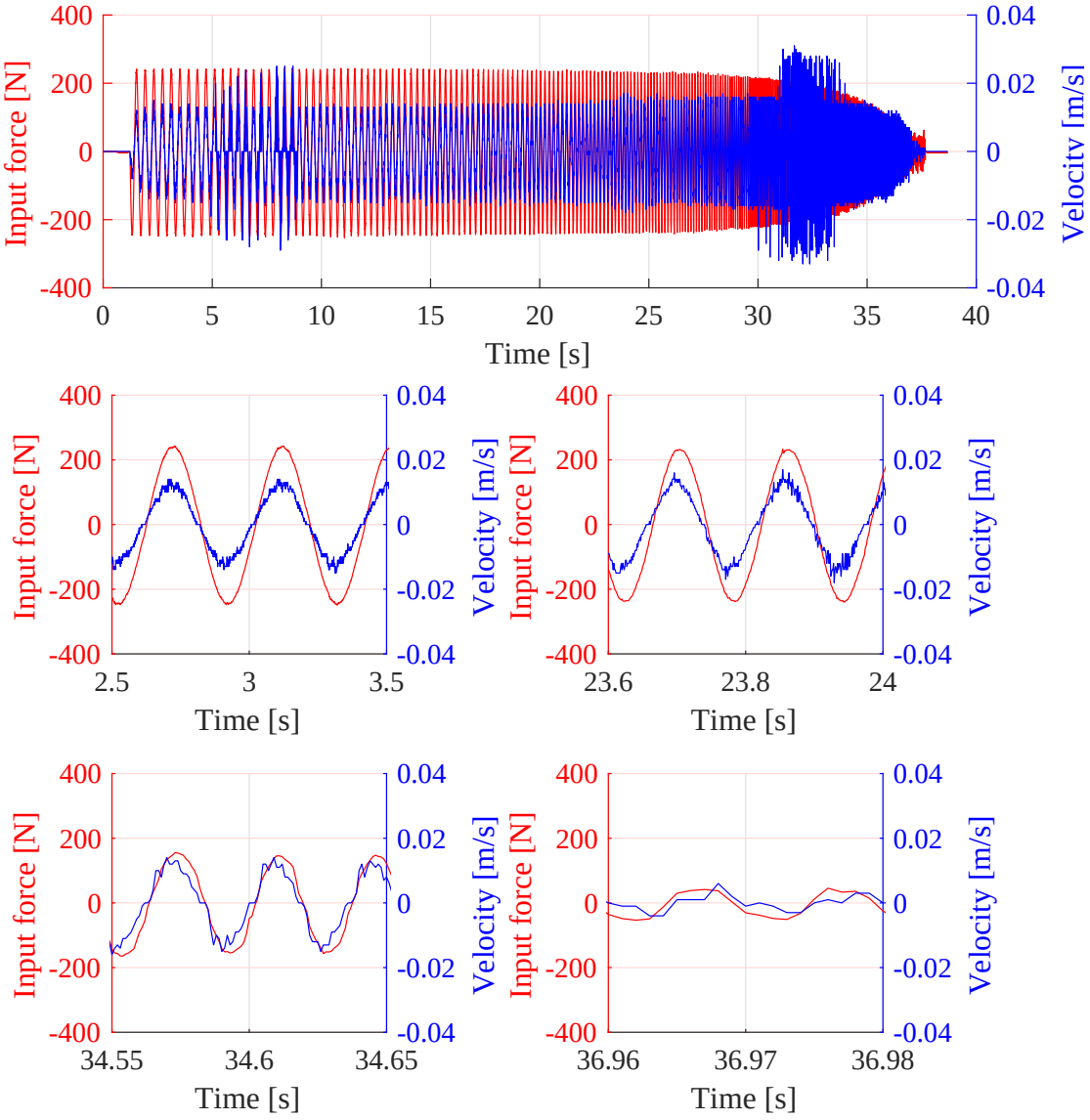

Figure 2.12: Time transition of the experiment to acquire the open loop frequency response between the pump torque τ_p as the input and the piston velocity $\dot{\theta}_c$ as the output, under the condition that the piston free to move.

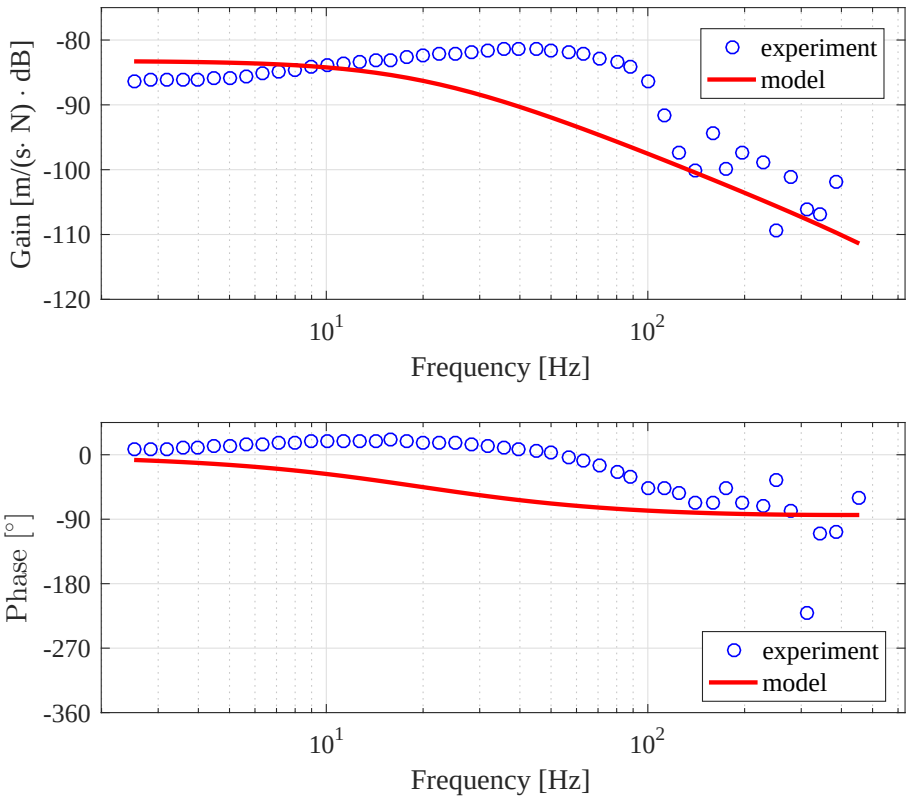

Figure 2.13: Open loop frequency response between pump torque τ_p as the input and piston velocity $\dot{\theta}_c$ as the output, under the condition that the piston is free to move. The blue markers show the experiment data, while the red line shows the theoretical value of $d_s k_s / \mathrm{G}_3$.

actuator is a third order lag system from the motor torque input.

3. In our developed actuator, the compressibility of the fluid has around two times larger effect on the series elasticity than the effect of piping expansion. The elasticity due to the fluid compression varies depends on the piston position. The total elasticity varies at maximum 14 % from the average elasticity, depending on the piston position, which is small enough to be assumed as a constant value.

4. When the motor current is fixed, the T-N curve of EHAs has the same straight line shape with electric motors. Unlike electric motors, though, the highest energy efficiency point is on the high torque side, which suggests that EHAs are more suitable for large torque slow motion applications. In the case of the developed actuator, the maximum efficiency is estimated to be 40 %.

5. We experimentally showed that our simplified model, with parameters identified in the quasi-static conditions, had similar dynamic behaviors with the one of the real actuator.

Chapter3

Key Design Parameters of a Few Types of Electro-Hydrostatic Actuators for Humanoid Robots

3.1 Introduction

Torque density of the actuator is one of the most critical property for legged robots, due to the requirement of limited size and weight in contrast with the need of supporting the body weight with the active actuator torque and conduct dynamic motions. Servovalve controlled hydraulic system has the largest torque density therefore the robots with them, either quadruped [13] or humanoid [16], have high dynamic performance. Robots with highly geared electric motors have the secondary torque density. Honda ASIMO [65] is a famous electrically driven humanoid that can perform running motions. Urata et al. [66] proposed the thermal control technique to overpower the electric motors, enabling the dynamic jumping motion [67]. Series elastic actuators have the following torque density, since they are heavier due to the large capacity elastic elements. Still, they are forceful enough to drive a humanoid robot, such

as COMAN [33], WALKMAN [34] and THOR [35]. When the property of elasticity matches the motion, they can enable highly efficient motion [32]. Direct driven robots still have difficulty in the torque density and limited in quadruped robot [24].

Compared with the established actuators above, electro-hydrostatic actuators for robot applications still suffers from lack of torque density. This contradicts with the fact that the industrial grade EHA for aerospace applications overwhelm electric-mechanical actuators in torque capacity [42]. While Kaminaga et el. [51] suggested that the unexpected low output torque may be originated from unexpectedly large internal leakage, there is still no discussion on its mechanism, methodology to improve, and whether there is other factors resulting in the low torque. In this chapter, we analyze the factors that harm the output force of an EHA and discuss their countermeasures. On each approach, we present a practical design solution and experimentally evaluate its effect.

3.2 Effect of the Internal Gap, Fluid Viscosity and Effective Pressure Receiving Surface

When constructing a robot system, many parameters need to be decided at the beginning, such as joint torque, joint maximum velocity, and specification of the electric motors. For the transmission, the total reduction ratio and the torque capacity is decided in the initial requirement definition. In the case of EHA, after the torque capacity and the reduction ratio are given, there are still internal parameters to decide, such as the type of the pump, the fluid viscosity, the capacity of the pump, and the

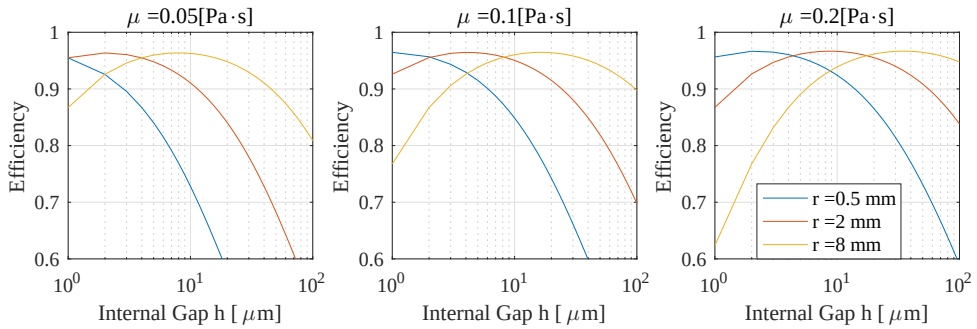

Figure 3.1: Simulated energy efficiency of an EHA when the piston force, velocity and the total reduction ratio are fixed, while the internal gap, pressure receiving surface, and fluid viscosity varies. The graph suggests that smaller pressure receiving surface has the same effect of larger internal gap or lower fluid viscosity.

size of the actuator. In this section, we clarify the parameters that are needed to be decided and their effect on the behavior of EHA.

From the model shown in Fig.2.1, we can see three design parameters that affect the performance: the pump internal gap h, the fluid viscosity μ, and the pressure receiving surface k_q or r. [1] To see their effect, we conducted a series of simulations with a fixed cylinder force (1500N), velocity (10mm/s), and reduction ratio($k_c/k_p = 30$), and different variation of h, μ, r. From Eq.(2.4), Eq.(2.5), we get the pump input force and velocity and therefore efficiency, which is plotted in Fig.3.1. The graph suggests that there is an optimal point, on the balance between viscous loss and internal leakage loss. While it is a matter of course that lower viscosity or larger internal gap results in smaller viscous friction and larger internal leakage, it is worth to notice that smaller size also has the same effect. Minimization of the actuator size or weight, therefore, relies on how to reduce the internal leakage. In other words, to

[1] Here we treat the overall reduction ratio is given, therefore the cylinder surface k_c is automatically decided according to k_q.

improve the force-to-weight ratio of EHA, the key is how to attain small internal gap and high fluid viscosity, while maximizing the effective pressure receiving surface in the limited overall weight or size. In the following sections, we show approaches for each of them.

3.3 Minimization of the Internal Gap

3.3.1 Gap Control of a Gear Pump

Minimization of the pump's internal gap plays an important role to improve the force-to-weight ratio or force-to-size ratio of an EHA. In the case of gear pumps, the key is how to reduce the distance between the pump casing and the gears. In our previous work, we saw an unexpectedly large internal leakage and therefore we could not attain the required force. The actuator was an integrated miniature cluster EHA to drive robot hands [68]. We hypothesized that the unexpected large internal gap is because of the mechanical deformation of the pump components. To confirm this, we developed a reinforced version of the pump. The new pump has the same gear with the initial version (The thickness of the gear is doubled, to keep the same reduction ratio when combined with a larger cylinder described later. Their outlook is shown in Fig.3.9.) Fig.3.2 shows the cut model of the initial and the modified pump. Their basic structures are the same: the pumps are internal gear pumps with a crescent separator and the pump shafts are driven by an external electric motor. The pump shaft and the inner rotor is supported by ball bearings. The outer rotor is not shown in the figures. The inlet/discharging ports are placed on the opposite side of the

pump shaft.

When the pump generates pressure, there are three major forces that result in the deformation. They are shown in red arrows in the figure. Firstly, the radial force is applied to the pump rotor, since the rotor separates the high-pressure fluid and the low-pressure one inside the pump. As shown in the cut model, in the initial pump the rotor was single supported by the bearings. The deformation of the bearings and the pump shaft resulted unexpectedly large inner gap. In the reinforced version, the rotor is modified to be double supported. The second force is the axial force on the rotor. Since only one side of the pump shaft is exposed to the atmosphere, the force which is the product of the internal mean pressure and the shaft's cross-section tries to push the shaft out of the pump. This is supported by the axial stiffness of the bearings. To have higher axial stiffness, the initial deep groove bearing is replaced by a larger angular bearing. The third force is the expansion force on the pump casing due to the internal mean pressure. The modified pump has a thicker structure with FEM deformation analysis.

Fig.3.3 shows the internal leakage evaluation of the initial and modified pump. The evaluation was done under a condition that the discharging port of the pump was closed. In that case, the amount of the internal leakage equals to the theoretical displacement of the pump, so that we could acquire the value from the pump's geometric specification and the rotational speed. In the graph, the horizontal axis represents the pump pressure and the vertical axis represents the amount of the internal leakage. The comparison shows that the modified pump has more than 92 % less internal leakage than the initial version. From the evaluation here, it was made

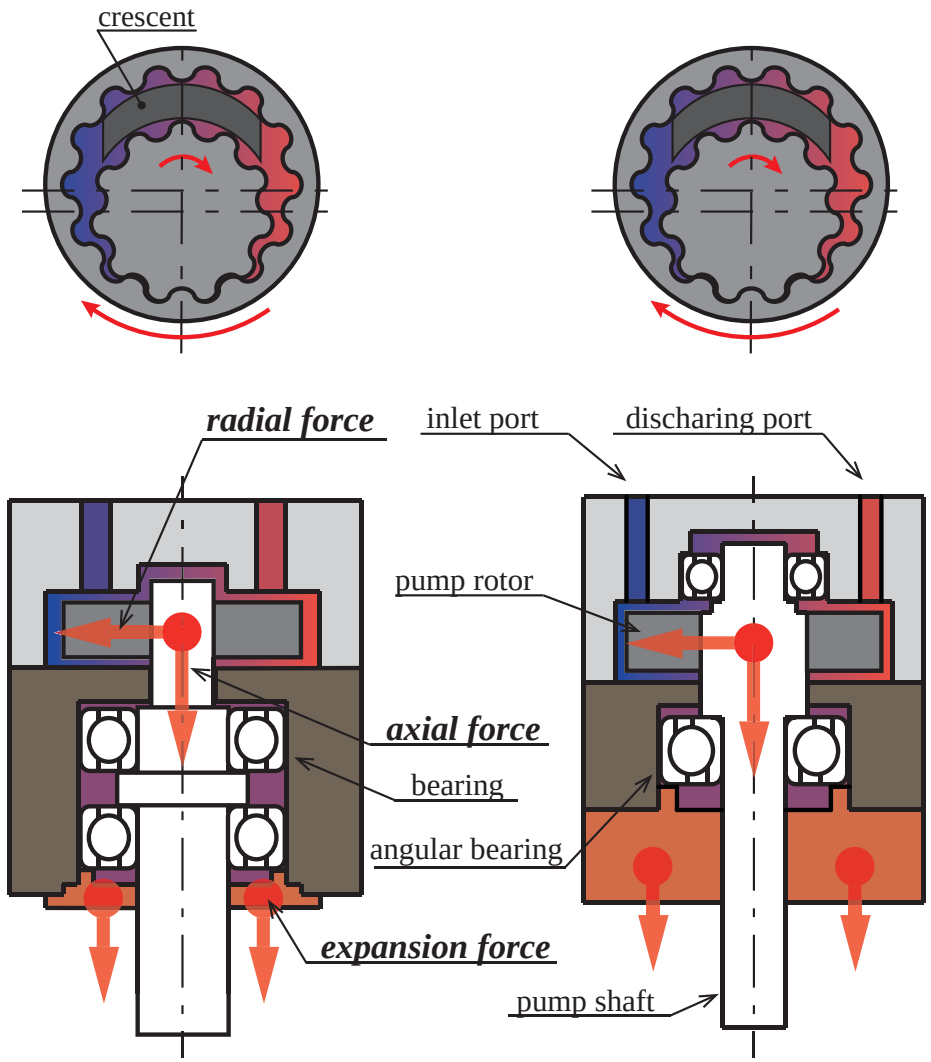

Figure 3.2: Three forces due to the pressure cause deformation and unexpected internal leakage. The radial force on the pump rotor due to the differential force, the axial force on the pump rotor due to the mean internal pressure, and the expansion force on the pump casing is handled with higher stiffness in the modified design.

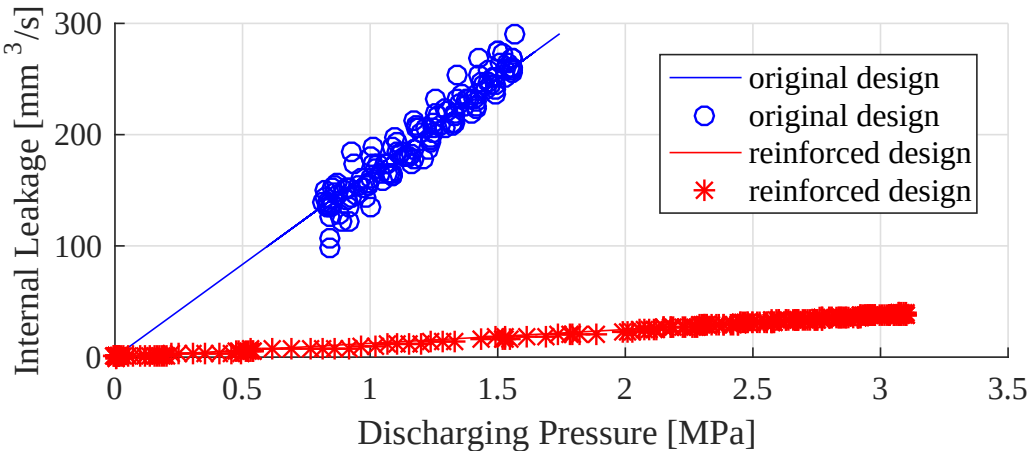

Figure 3.3: Comparison of the internal leakage of the initial and modified pump. The y-axis represents leakage and the x-axis represents the pressure. The experiment was done with the discharging port of the pump closed. The leak is calculated from the rotor speed and the geometric parameters of the pump. The pressure is acquired from the attached pressure sensor. To prevent the heat effect on the amount of leak, the experiment was done in a short time. This graph shows that the new pump has more than 92 % less leak for the same pressure.

clear that the effect of the pump's deformation due to the pressure consists a large part of the effective internal gap, and an extra consideration should be taken in the design process.

3.3.2 Gap Control with a Linear Cylinder

Gap control on the actuator side is also important to improve the force-to-weight ratio of EHA. In the sense of internal leakage reduction, cylinders are advantageous since it is easy to install piston rings to completely avoid the internal leakage around the piston. Based on this idea, we developed a light weight cylinder shown in Fig.3.4. The cylinder has 600 g weight, 240 mm length, 20 mm cylinder bore, and 50 mm stroke. With its 6mm diameter piston rod, it converts the 5.3 MPa pump pressure to

Table 3.1: Specification of the Developed Double Rod Cylinder with Beam Structure. The maximum force and velocity shows the case with the pump described in 4.2.

weight	600 g
inner bore	20 mm
piston rod diameter	6 mm
full stroke	50 mm
maximum force	1500 N
maximum speed	200 mm/s

1500 N piston force. Table 3.1 summarizes its specification.

The cylinder has a double rod piston, with which the hydraulic circuit is symmetric and does not have chamber volume variation that occurs in the case of single rod cylinders. This is advantageous in the perspective of backdrivability, which is discussed later in Chapter 4. Both ends of the piston rod are held by the beam. The beam is attached to a linear slider, whose rail is fixed on the cylinder body. The connecting rod between the load and the actuator is attached to the beam, rather than the piston rod itself. The linear guide holds constraint forces and only transfer the force parallel to the piston rod, avoiding radial force on the piston rod. This prevents buckling of the piston rod and therefore minimizes the rod diameter and friction due to the rod oil seal, which is also advantageous for the backdrivability.

Another advantage of this structure is that thanks to the linear guide, we can fix the cylinder body on the link when the other end of the connecting rod is attached on a rotational joint. In the common type of rotational joints driven by cylinders, the cylinder need to swing according to the joint angle. In our fixed cylinder arrangement, in addition to that we can save the space for the swinging, we can minimize the distance between the pump and cylinder with short and stiff piping. This is advanta-

geous in the enhancement of its response, which is discussed in the following chapter 5.

The cylinder has a tie rod basic structure. Main material for the cylinder is 7000 series aluminum alloy. To support its large force, the beam is made of carbon steel and the piston rod is made of chrome steel. The tie rods are made of titanium alloy to reduce the weight. Sliding parts between the cylinder and the piston, and between the cylinder head and the piston rod are coated by Ni-PTFE compound plating to reduce friction. Differential pressure applied on the piston surface is measured by two pressure sensor mounted on the cylinder heads. The pressure sensors are Measurement Specialties inc's Model 89 PCB mount sensor. A custom made amplifier PCB board is directly mounted on the sensor, which has analogue output. Piston position is measured by a Renishaw plc's RESOLUTE series optical linear encoder with 5 nm resolution. The encoder sensor is mounted on the cylinder body, while the encoder scale is attached on the linear slider.

A special effort is paid to improve its modularity to adapt different fixing condition. While in our case the cylinder body is fixed on the link, there are two ways to tight the screws: from the cylinder side which means the cylinder has through holes and the link side has tapped holes, or from the link side which means the link has through holes and the cylinder side has tapped holes. The cylinder parts should not have different versions to adapt this difference. We solved this problem by introducing tongueless inserts to the cylinder. Tongueless inserts are a type of screw hole inserts. Screw hole inserts are coil spring shaped steel parts to reinforce female screw holes, especially for soft materials such as aluminum or plastic. While in most case the

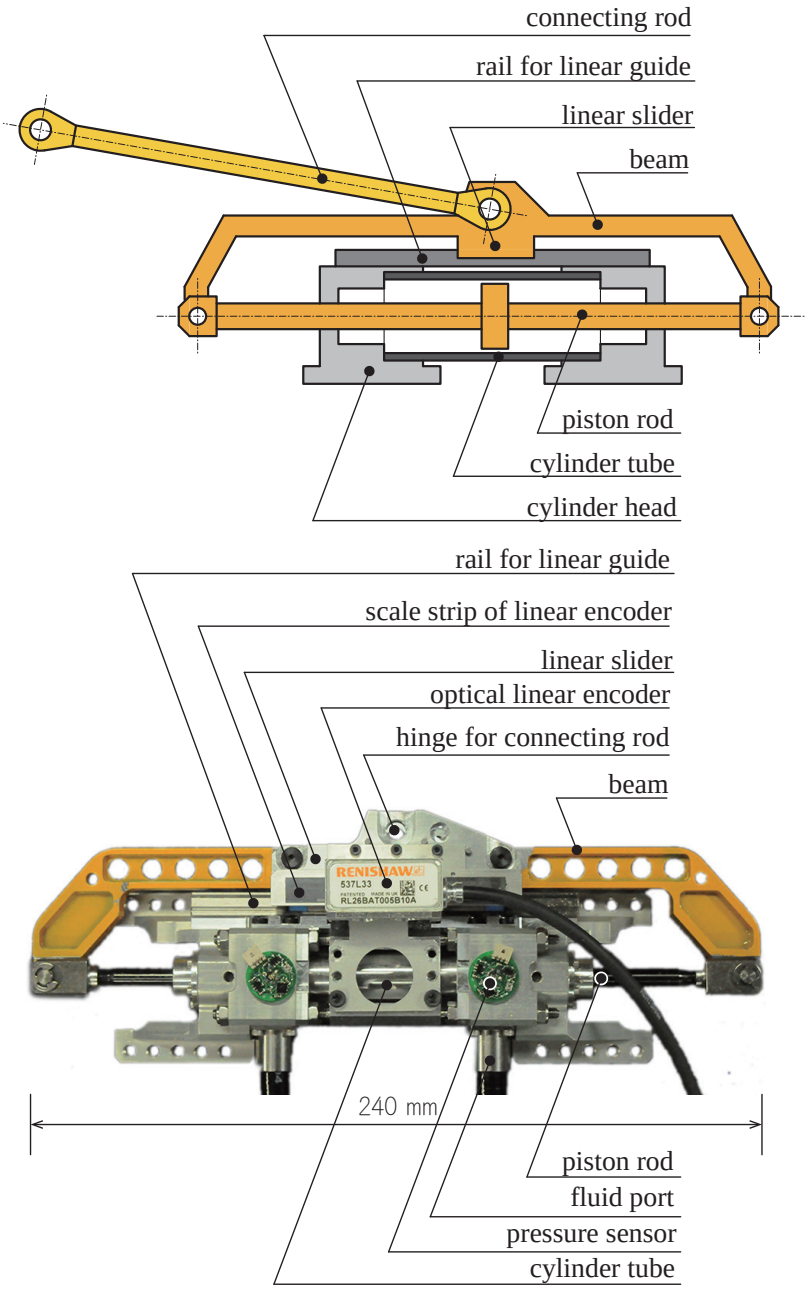

Figure 3.4: Low friction double rod cylinder with the beam structure.

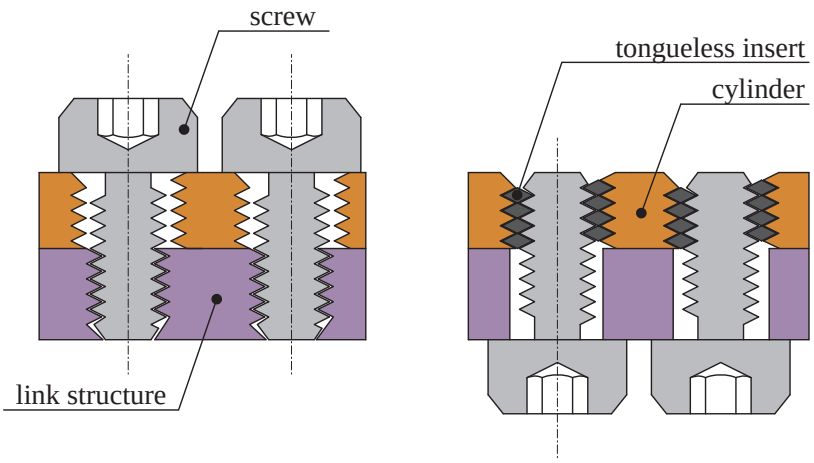

Figure 3.5: Schematic of the dual-use screw hole on the cylinder body. When no inserts are attached, the holes work as normal through holes. When tongueless inserts are attached, they work as tapped screw holes.

inserts have a "tongue", which is a straight part of the coil to be grabbed to insert them into the screw holes and removed after the inserting is done, tongueless inserts have special fixture mechanism to avoid the use of "tongue". This make it possible to attach and remove the inserts freely. For the space of inserts, the screw holes designed for inserts have larger bore than normal screw holes. If we do not attach the inserts, the screw hole is wide enough as through holes for the screws, and when we attach the inserts, they work as normal screw holes. Fig.3.5 explains the idea. We use M4 cap screws to tight the cylinder on the link. The inner diameter of a screw hole for M4 tongueless inserts is 4.2 mm, which is enough to let M4 screws to go though. The reason that we do not simply place M5 screw holes on the cylinder instead of the inserts is that the minimized design of cylinder do not have space for M5 screws with their heads not colliding with each other.

Table 3.2: Specification of the Developed Double Vane Motor. The maximum torque and speed shows the case with the pump described in 4.2.

weight	780 g
range of motion	120°
maximum torque	60 Nm
maximum speed	290°/s

3.3.3 Gap Control of a Rotary Vane Motor

While linear cylinders are advantageous in the reduction of the internal leakage, they are difficult to be applied for joints whose axis is parallel to the longitudinal direction of the link. In such case, rotary vane motors are a solution, while they are costly in the sense of the complex structure, heavy weight, and limited efficiency/torque due to the internal leakage. To overcome the problem, we took a unique structure shown in Fig.3.6. In the developed vane motor, the expansion force due to the internal pressure, applied to the casing, is supported by a pair of thrust bearings held by the output shaft. Thanks to this support, the strength of the pump casing can be reduced to save the total weight, while keeping the constant small gap between the vane and the casing.

Table 3.2 summarize the specification. It has 780 g weight and 120 ° range of motion. The vane converts 5.3 MPa pump pressure to a 60 Nm torque through the flanged output, which is held by a cross roller bearing. The vane shaft and the flange is connected through a friction coupling to transfer the torque. The developed vane motor has two minor versions: single supported and double supported version. The single supported version is designed to drive a joint whose axis is parallel to the longitudinal direction of the link, such as yaw joints of the arm of a humanoid robot.

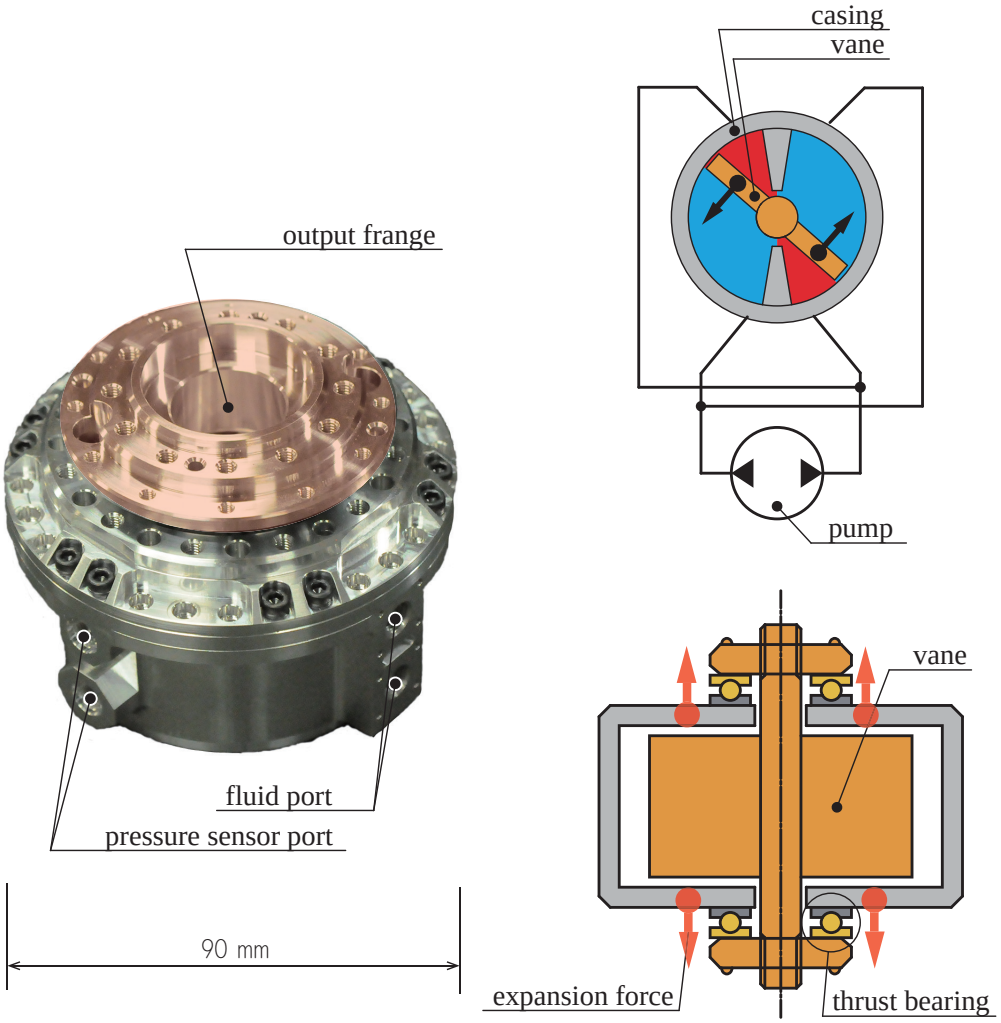

Figure 3.6: Picture and schematic of the developed double vane motor. The expansion force due to the internal pressure, applied to the casing, is supported by a pair of thrust bearings held by the output shaft, therefore the strength of the pump casing can be reduced to save the total weight.

In this case the output flange transfers all of the constraint force and driving torque. The child link is fixed on the output flange and the other side of the vane motor is fixed on the parent link. The vane motor itself works as a part of the parent link. Due to the torque capacity of the friction coupling, the output torque of the vane motor is limited to under 40 Nm. The double supported version has longer vane shaft on the opposite side of the output flange. While all of the constraint force is supported by the cross roller bearing of the output flange as the same case of single supported version, the output torque is transferred by two friction couplings on both sides of the vane motor. This allows it to exert the maximum designed torque of 60 Nm. This version is developed under the expectation of a usage where the axis of the driven joint is orthogonal to the longitudinal direction of the link but the space is limited (especially, not long enough) to adopt a linear EHA.

As the same with the case of the cylinder, two pressure sensors measure the differential pressure and a rotary optical encoder acquires the vane position. In the case of single supported version, the encoder scale disk is attached to the output flange. In the case of double supported version, the disk is attached to the other side of the flange to minimize the overall size.

3.4 Fluid Viscosity Control by the Direct Water Cooling

In the sense of the enhancement of force-to-weight ratio of EHA, high fluid viscosity is preferable since it allows us to minimize the actuator size or relax the internal gap

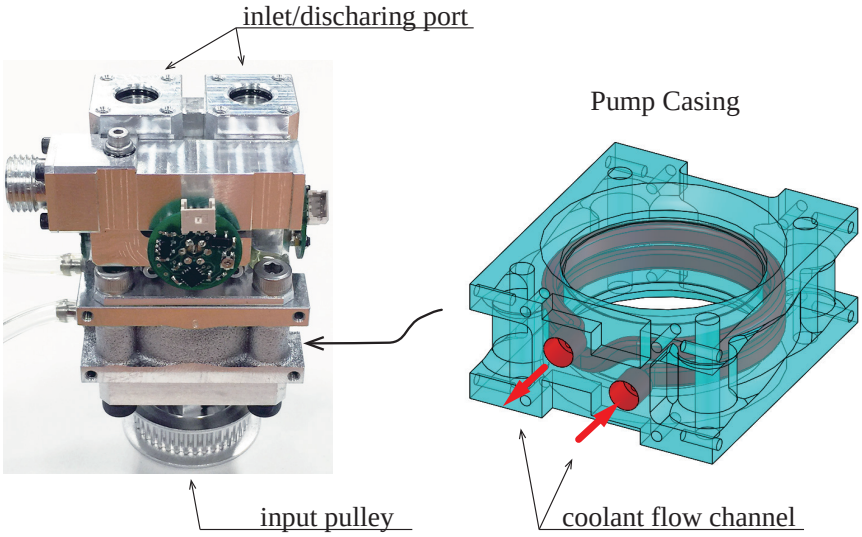

Figure 3.7: 3D printed integrated coolant flow channel in the pump casing.

requirement. The problem is that the fluid viscosity becomes smaller when the the fluid temperature is higher. The energy loss due to the friction or internal leakage is converted to the heat. When the transmission is already in the "too much internal leakage" side from the optimal condition, it results in a positive feedback: energy loss causes higher fluid temperature, then less viscosity and less efficiency, therefore even more energy loss.

An effective cooling of the fluid is crucial to avoid the decrease of performance. The problem is that unlike the servo valve hydraulics with an open hydraulic circuit, the closed and independent circuit of an EHA is difficult to cool the fluid by commonly used oil coolers. Since the heat is mostly generated in the pump, we take a straightforward approach: directly water cool the pump by introducing a 3D printed coolant channel into the pump casing. Fig.3.7 illustrates the implementation of the cooling mechanism.

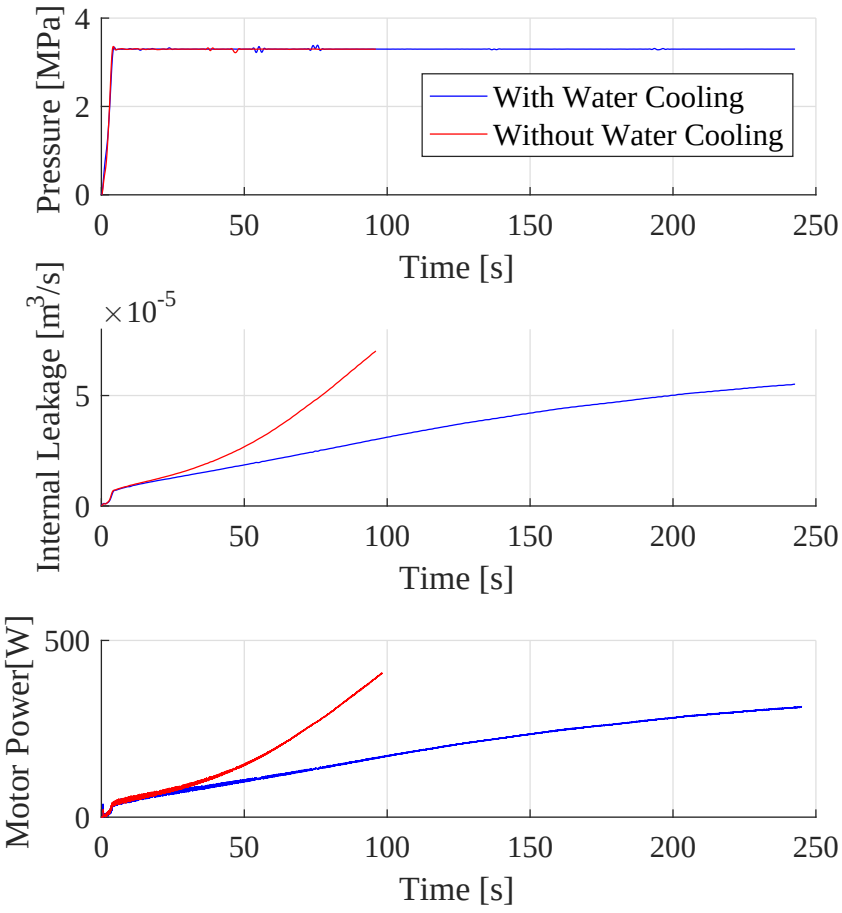

Figure 3.8: Time transition of the pump discharging pressure (top), amount of internal leakage (middle), and input power to the pump (bottom). The red line represents the case without water cooling and the blue line shows the case with water cooling. The discharging port of the pump is closed, the inlet port is connected to an oil reservoir in the atmosphere, and the pump is under a pressure feedback control. While in the case without the cooling, the internal leakage and the input power diverges. With the cooling, on the other hand, the values converge to a certain value.

To confirm the effect of the water cooling mechanism, we conducted a comparative experiment. The discharging port of the pump is closed and the inlet port is connected to an oil reservoir exposed to the atmosphere. The pump is pressure controlled with a constant command pressure of 3.5 MPa. In one trial the coolant does not flow into the pump, while the other trial the coolant flows. The same pump is used for both trials to avoid the individual pump difference. The result is shown in Fig.3.8. In the graph, the red line represents the case without coolant flow and the blue line represents the case with the flow. The graph on the top shows the time transition of the measured pump pressure. The middle shows time transition of the amount of the internal leakage. A clear difference can be seen from the graph. The amount of leakage in the case without cooling has a diverging behavior due to the positive feedback. With the cooling, on the contrary, the leakage is converging to a stable value. When 90 seconds after the beginning of the experiment, the water cooling suppressed 55 % of the leakage compared with the case without cooling. The bottom graph shows the energy input to the pump from the motor. Since the discharging port of the pump is closed, all of the input energy is lost and converted to heat. The loss is the summation of the loss due to the friction and due to the internal leakage. While the loss in the case without cooling diverges, the case with the cooling converges to the value of around 350 W.

3.5 Maximization of Effective Pressure Receiving Surface by an Integrated Tie Rod Cluster Cylinder Structure

When the loss due to the internal leakage is dominant, a larger pressure receiving surface can improve the output force of EHA. The key is how to maximize the usage of space in the limited outer size and overall weight. In this subsection, we show an enhancement of cylinder force by a design with high space usage efficiency. The target cylinder is the one for the hand [68], whose pump is already discussed in the previous section 3.3.1. In its original design [69], multiple cylinders are integrated as a manifold, which is aluminum casted with a 3D printed plaster mold. While the distance between the pistons was 21 mm, the cylinder bore was limited to be 9 mm. Rather than the cylinder body itself, the main factor that restricts the cylinder bore is the termination part of the cylinder, such as the cone-shaped region to protect piston seal in the assembling process, and the cap to close the cylinder end.

In the modified design, instead of the original merged cylinder body and separate termination part structure, we merge the termination parts (cylinder head) as a single piece, which closes multiple ends of the independent cylinder tubes. The fluid ports are also merged into the integrated cylinder head. The cylinder heads on the both ends are connected with tie rods. Since the manifold is a shared single piece, its high strength and stiffness allows free arrangement of the connecting rods according to the arrangement of cylinders. The components between each cylinder are now only O-rings to seal the gap between the cylinder head and cylinder tube. With this setup

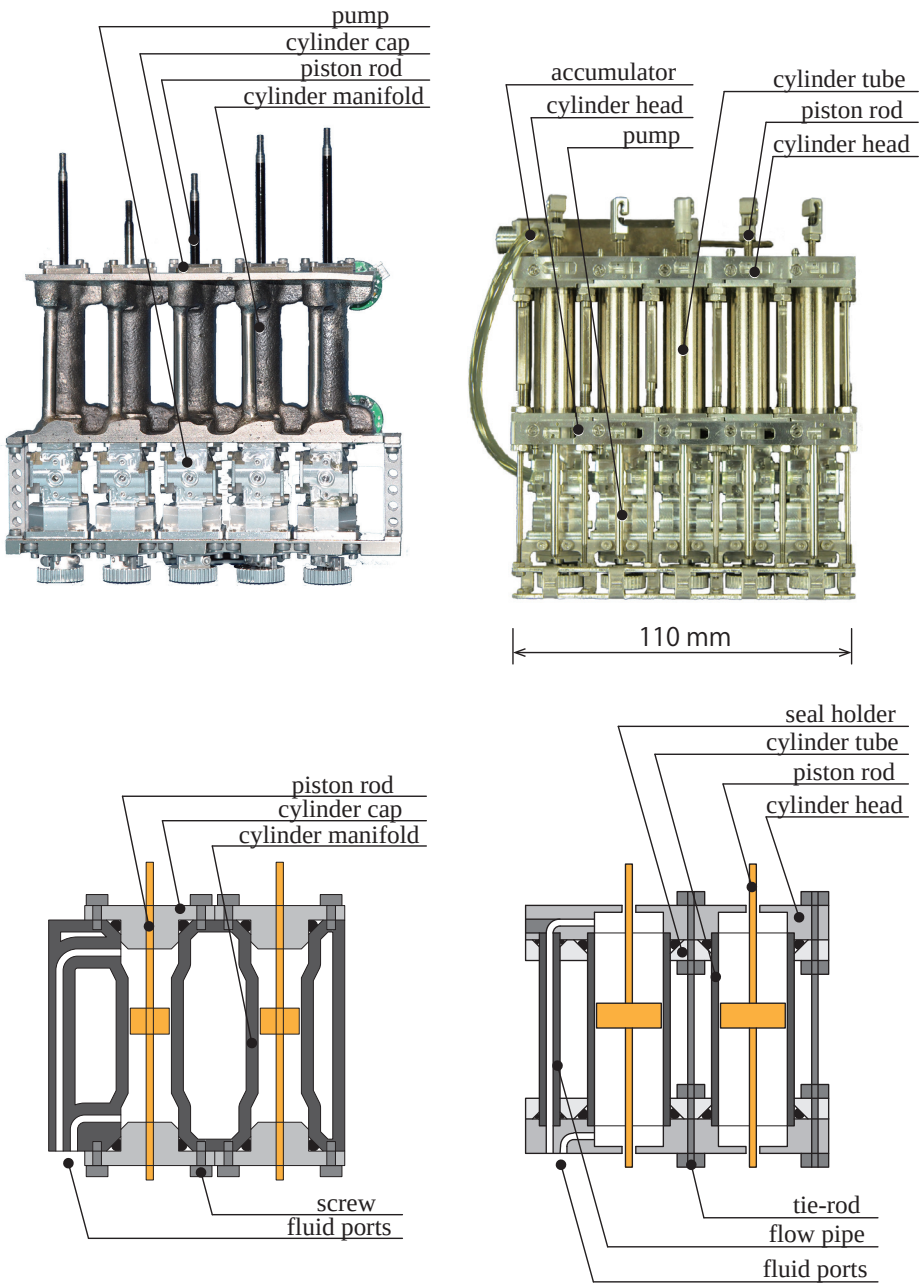

Figure 3.9: Schematic and picture of the developed cylinder cluster with casted cylinder manifold (left), and tie rod cylinder cluster (right).

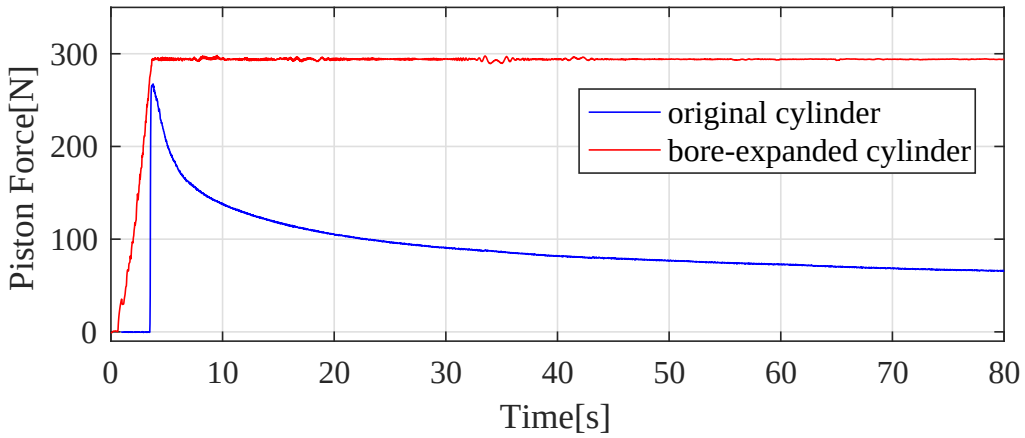

Figure 3.10: Comparison of piston force that the initial and modified actuator can output. Force is calculated through the discharging pressure and the piston diameters. The rising edges of two graphs are different because smoother pressure reference was given to the modified pump. In both cases, same electric motor and motor driver is used to drive the pump. The graph shows that with lower energy loss, the new actuator can exert 300 N force for a long time, which was impossible for the initial version.

we can increase the cylinder bore from the previous 9 mm to 13 mm, keeping the same outer size of the cylinder cluster and the distance between each piston. This means 222 % larger cylinder cross-section. (The total reduction ratio is almost the same since the pump's displacement is also doubled, as explained in section 3.3.1.) The approach also reduced 10 % of the weight, from 224 g to 200 g. This is the result of the optimization of the materials: the cylinder head is made of 7000 series aluminum alloy, the cylinder tube is made of 0.5 mm thickness chrome-molybdenum steel, while the tie rods are titanium. Fig.3.9 shows the comparison of the original design and modified design.

Fig.3.10 shows a comparison of the force output of the initial actuator and the modified actuator. The pistons were fixed on the end of the cylinder. The com-

mand force was converted to the command pressure and the pumps were pressure controlled. The actuator forces are estimated from the pressure sensors. In both case 300 N command force, which was the initial requirement, was commanded to the actuator. In the case of the initial design, the force saturated from the beginning and it dropped with the time, since the poor energy efficiency result in a larger increase of the fluid temperature, which leads less fluid viscosity and larger internal leakage. In the modified version, on the contrary, the actuator could successfully keep the force for more than 70 seconds.

3.6 Conclusion

In this chapter, we introduced a systematic mechanical design approach to improve the torque density of miniature EHA. The conclusion is as follows:

1. Even after the total reduction ratio between the actuator output and the electric motor is given, there still exists hydraulic design freedom such as the internal gap, fluid viscosity, and effective pressure receiving area. For each output force and velocity condition, the best transmission efficiency is realized on the balance of the loss due to viscous friction and the loss due to internal leakage. While it is straightforward that larger internal gap or lower viscosity results in larger internal leakage loss and lower viscous loss, the important feature is that smaller effective pressure receiving surface of the pump or actuator also has the same effect. Therefore, to improve the force-to-weight ratio of EHA, the key is how to attain small internal gap and high fluid viscosity, while maximizing the effective pressure receiving surface in the limited overall weight or size.

2. We proposed the way to reduce the internal gap of the actuator on both of the pump and actuator side. On the pump side, we experimentally showed that with a modification of the bearing arrangement, bearing type and reinforcement of the pump casing, we can suppress the amount of internal leakage by more than 92%. On the actuator side, we first presented the design of a light weight cylinder with no internal leakage. The developed cylinder had 600 g weight, 240 mm length, 20 mm cylinder bore, and 50 mm stroke. With its 6mm diameter piston rod, it converts the 5.3 MPa pump pressure to 1500 N piston force. While cylinders are advantageous in the improvement of the force-to-weight ratio, to accommodate the situation that they are not available, we also presented a design of vane motor with special structure to attain both low internal leakage and light weight. The developed vane motor had 780 g weight and 120 ° range of motion. The vane converts 5.3 MPa pump pressure to a 60 Nm torque through the flanged output.

3. We proposed the direct pump casing water cooling approach to effectively suppress the positive feedback loop of that higher fluid temperature results in lower viscosity, then lower efficiency and the even more energy loss. We experimentally showed that the water cooling could suppress the internal leakage by 55%.

4. We showed the way to maximally utilize the space to increase the effective pressure receiving surface of a cluster actuator. It was experimentally shown that the modification of an EHA, which is to double both the piston surface and the pump displacement, drastically improved the performance. Combined with the higher stiffness pump, the modified actuator could output 300 N force

for more than 70 s, which was not possible for even a short time in the initial design.

Chapter4

Enhancement of Backdrivability and Force Control Accuracy of a Large Force Linear EHA

4.1 Introduction

The possibility of high backdrivability is a key property of EHA as a robot actuator. In the other applications such as hydrostatic transmissions for ground drive propulsion [43] or EHA for airplanes [45], on the other hand, backdrivability was rarely concerned. In those case, the backdrivability is significantly reduced due to the mechanical contact, oil seal, and valve system. To improve EHA's backdrivability for a force sensitive robot joint, Kaminaga et al. [57] developed a joint with the combination of a trochoid pump and a double vane motor. Whitney et al. [70] developed a master slave robot system with low friction rolling diaphragm cylinders.

The underlying challenge in the development of EHA for robot applications is to maintain both of the high torque density and high backdrivability simultaneously. The previous highly backdrivable works had difficulties on the large torque performance,

due to either the intentionally enlarged internal gap or the low pressure-endurance property of the diaphragm cylinder. As mentioned in the previous chapter, due to the scale effect, a miniaturized EHA has strict requirement on the low internal leakage property to have enough torque for a legged robot. In this chapter, we discuss the approach to maintain and even improve the high backdrivability property of EHA while adopting the torque density improvement approach in the previous chapter. We first discuss the effect of multiple common types of hydraulic pumps on the system backdrivability, then propose a double rod cylinder structure with the special beam structure, with which we can drastically reduce the friction. On the last, we present the active friction compensation technique to furthermore improve the property.

4.2 A Low Friction Lightweight Trochoid Pump with Reinforced Structure and Water Cooling

To improve backdrivability of EHA, reduction of friction is crucial. In a large number of the hydraulic systems, piston pumps are commonly adopted. Fig.4.1 illustrates a typical axial piston pump. Piston pumps discharge the fluid with the prismatic motion of a piston in a cylinder. In spite that a single pair of piston and cylinder can only intermittently discharge the fluid, combination of multiple pairs can generate a continuous flow. Rotational mechanical input into the pump is converted to prismatic piston motion by a swash plate or a crankshaft. To rectify the reciprocating motion of pistons into a single direction of flow, a proper valve system synchronized with the pump motion, such as the valve plate, is required. While their advantage

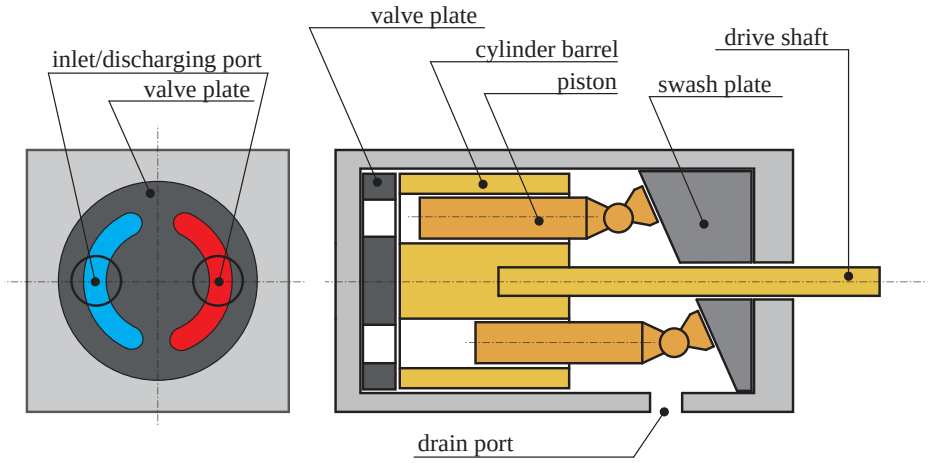

Figure 4.1: Schematic of a valve plate type axial piston pump. Rotational mechanical input into the pump is converted to prismatic piston motion by a swash plate. The valve plate rectifies the reciprocating motion of pistons into a single direction of flow. The valve plate is fixed on the pump casing and the cylinder barrel rotates with the input shaft, therefore the cylinders are automatically connected to the proper (inlet or discharging) port according to its phase.

is the capability of high discharging pressure, they have a large number of sliding parts such as the one between the pistons and the cylinder barrel, between the cylinder barrel and pump casing [1] , between the cylinder barrel and the valve plate, and between the piston shoe and the swash plate. They also have large viscous friction since the drain port side chamber is filled (not fully but almost) with the drained fluid and the rotating pistons need to go through it. They are also not advantageous in the sense of inertia, since the heavy cylinder barrel also turns according to the input shaft. Therefore, while piston pumps are suitable as a high pressure constant pressure source, they are not necessarily suitable for a force-sensitive servo system.

In gear pumps, fluid is trapped between the tooth of a pair of gears to be conveyed

[1]In the valve plate type piston pumps, the cylinder barrel also rotates according to the pump shaft therefore the cylinders are automatically connected to the proper (inlet or discharging) port according to its phase.

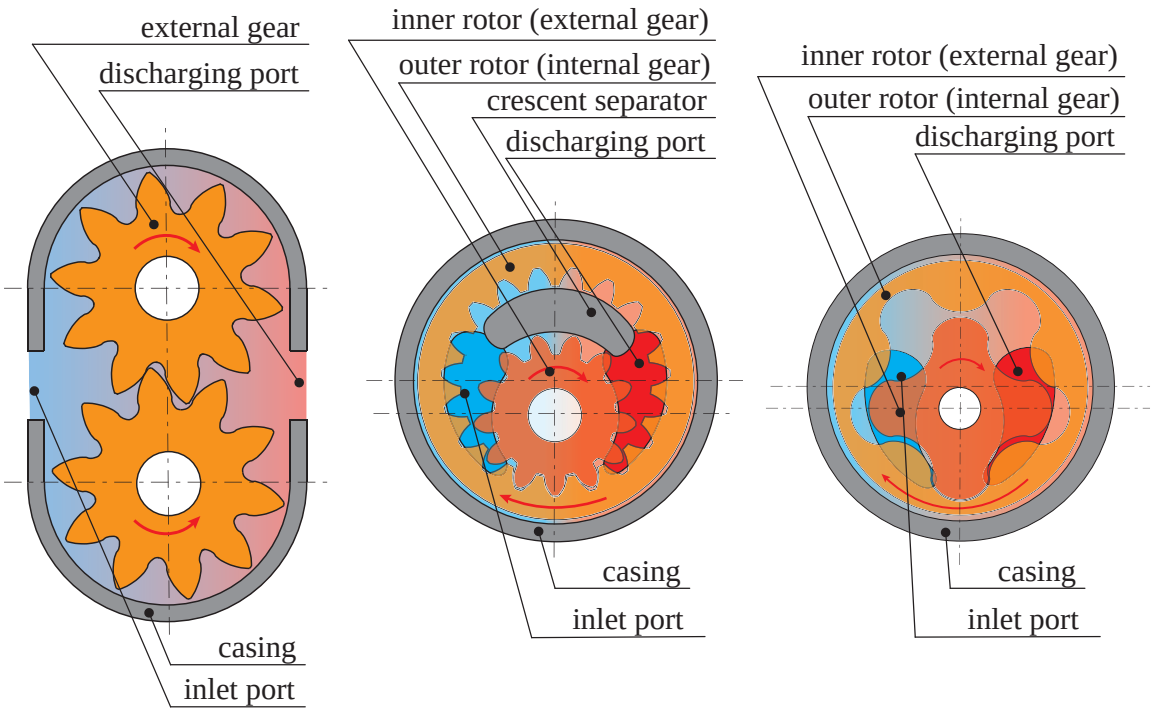

Figure 4.2: Three types of gear pumps. External gear pumps (left) are the most common type of gear pumps. They consist of two external spur gears. The fluid is captured between the tooth and the sidewall. While they have a simpler structure and higher discharging pressure, they tend to have larger outer size compared to the two following other types. Internal gear pumps (middle) have a pair of an external and internal spur gear. The fluid is captured between the teeth and a crescent separator. They have smaller outer size than external gear pumps, while they need high machining accuracy. Trochoid pumps (right) have trochoid gears and the internal gear (outer rotor) has exactly one more teeth than the external gear (inner rotor). This configuration can trap the fluid and convey them without help of the crescent separator.

from the low-pressure side to the high side. Since the fluid cannot go back to the low-pressure side through the meshing part of the gears, it is discharged from the discharging port at last. While their discharging pressure is not as high as piston pumps, they have advantages in the simple structure (therefore small size and light weight), low inertia and low friction. With the high accuracy manufacturing, the sliding contact can be limited to only the gear meshing part. Fig.4.2 shows three major type of gear pumps, which is an external gear pump, an internal gear pump, and a trochoid pump. Trochoid pumps are a variation of the internal gear pumps. The difference is that they have trochoid gears and the internal gear (outer rotor) has exactly one more teeth than the external gear (inner rotor). This configuration can trap the fluid and convey them without the help of the crescent separator, which means simpler structure and ease of maintenance. The advantage is that since the meshing of a pair of trochoid gears has a rolling contact, rather than sliding contact in the case of common involute tooth gear, the mechanical friction is low.

Among the pumps above, trochoid pumps are most advantageous in friction, then followed by involute gear pumps, then piston pumps. Their drawback, though, is the largest internal gap and therefore lowest pressure capability. To overcome the tradeoff, we adopted the discussion in chapter 3: to improve the force of EHA, improvement in the pump stiffness and the proper cooling is effective. Based on the initial design for lower capacity [52], we developed a low friction lightweight trochoid pump with reinforced structure and water cooling mechanism. Fig.4.3 shows a comparison of the original design on the left and our modified design on the right. The electric motor is also modified to be cooled by a water jacket. The rotary encoder on the motor is

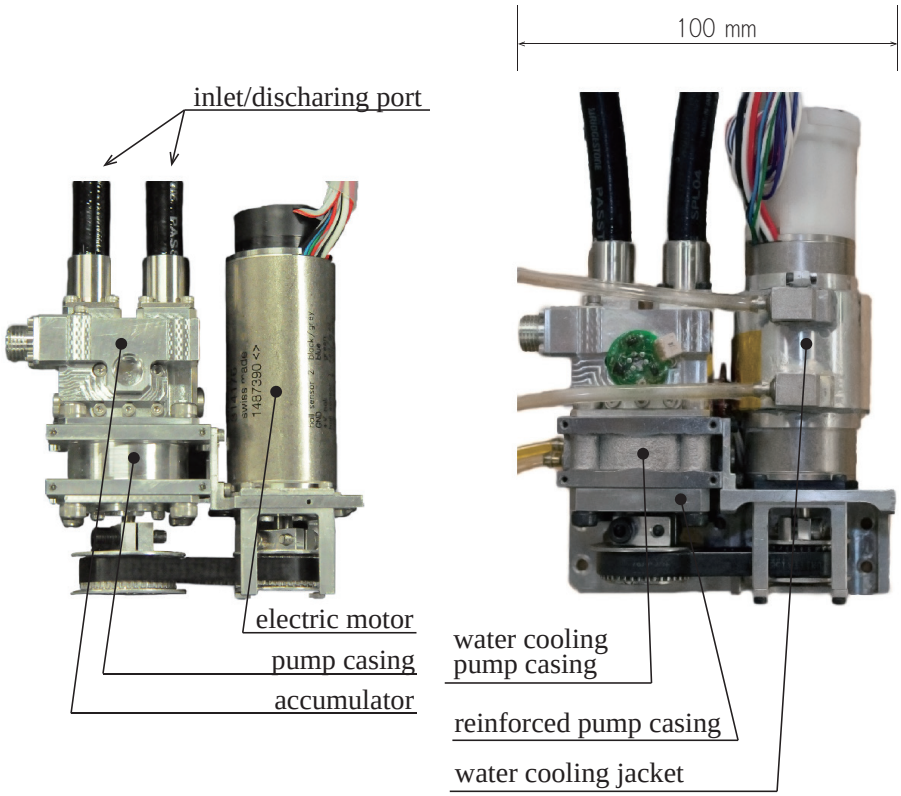

Figure 4.3: Comparison of the original design (left) and our modified design (right) of the pump. The pump casing is integrated with the 3D printed water cooling jacket. The pulley side casing is also reinforced to have higher stiffness. The electric motor is also modified to be cooled by a water jacket.

replaced from the original incremental one to an absolute one to simplify the initial process for the brushless DC motor. The specification of the pump is shown in Table 4.1.

Table 4.1: Specification of the Developed Trochoid Pump

weight (including motor)	620 g
motor power	200 W
maximum discharge pressure	5.3 MPa
displacement	418 mm^3/rev
maximum discharge flow	57000 mm^3/s

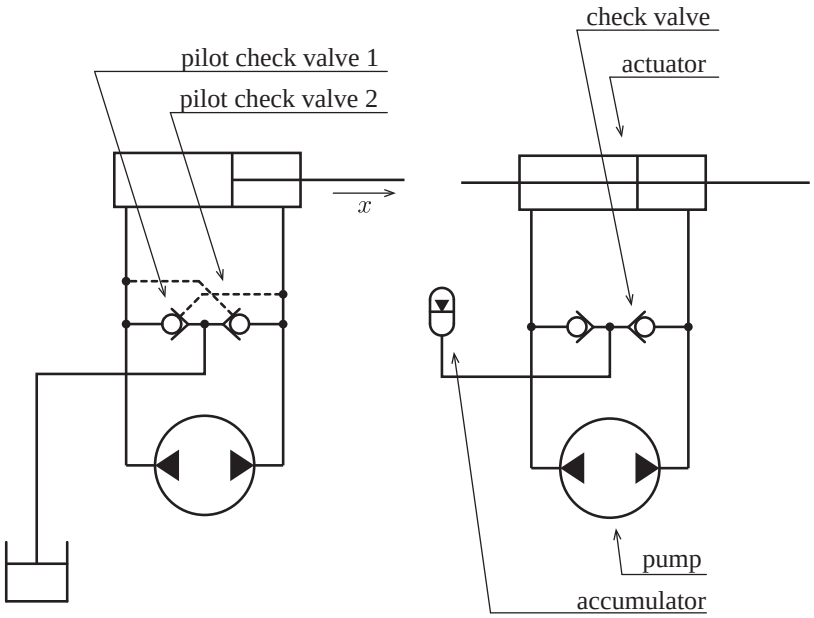

Figure 4.4: Comparison of an EHA hydraulic circuit with a single rod cylinder (left) and with a symmetric double rod cylinder (right). In the case of double rod cylinders, only a small capacity accumulator and simple check valves are needed since they work only to compensate the small amount of external leakage and avoid cavitation. In the case of single rod cylinders for closed circuits, the accumulator need to have at least larger capacity than the volume of the piston rod. The check valves need be pilot check valves. When the cylinder retracts, larger volume of the fluid moves out from the cylinder than the volume moves in. The differential volume need to be stored in the accumulator through the force cracked pilot check valve. When the cylinder extends, more fluid need to be sent to the cylinder than the fluid moves out. The differential volume is supplied from the accumulator. While in such case the check valve does not necessary to be a pilot one, a pilot check valve is advantageous in smooth operation and avoidance of cavitation.

4.3 A Double Rod Cylinder with the Beam Structure

To improve the backdrivability, a special friction reduction effort also need to be paid on the actuator. Single rod cylinders are used in most of the hydraulic systems. Advantages of single rod cylinders compared to double rod ones is that they have shorter size, lighter weight, larger pressure receiving surface, and easy to implement a magnetostrictive sensor to measure the piston position. Their asymmetric characteristic, though, is a problem for a system with a closed hydraulic circuit. This is because the total chamber volume of the circuit varies according to the piston position or the amount of the piston rod volume inside the cylinder. A proper valve system is needed to compensate this variation, which results in a complex system and large viscous friction. Fig.4.4 shows the comparison of an EHA hydraulic circuit with a single rod cylinder and with a symmetric double rod cylinder. In the case of double rod cylinders, only a small capacity accumulator and simple check valves are needed since they work only to compensate the small amount of external leakage and avoid cavitation. In the case of single rod cylinders for closed circuits, the accumulator need to have at least larger capacity than the volume of the piston rod. The check valves need be pilot check valves. When the cylinder retracts, larger volume of the fluid moves out from the cylinder than the volume moves in. The differential volume need to be stored in the accumulator through the force cracked pilot check valve. When the cylinder extends, more fluid need to be sent to the cylinder than the fluid moves out. The differential volume is supplied from the accumulator. While in such case the

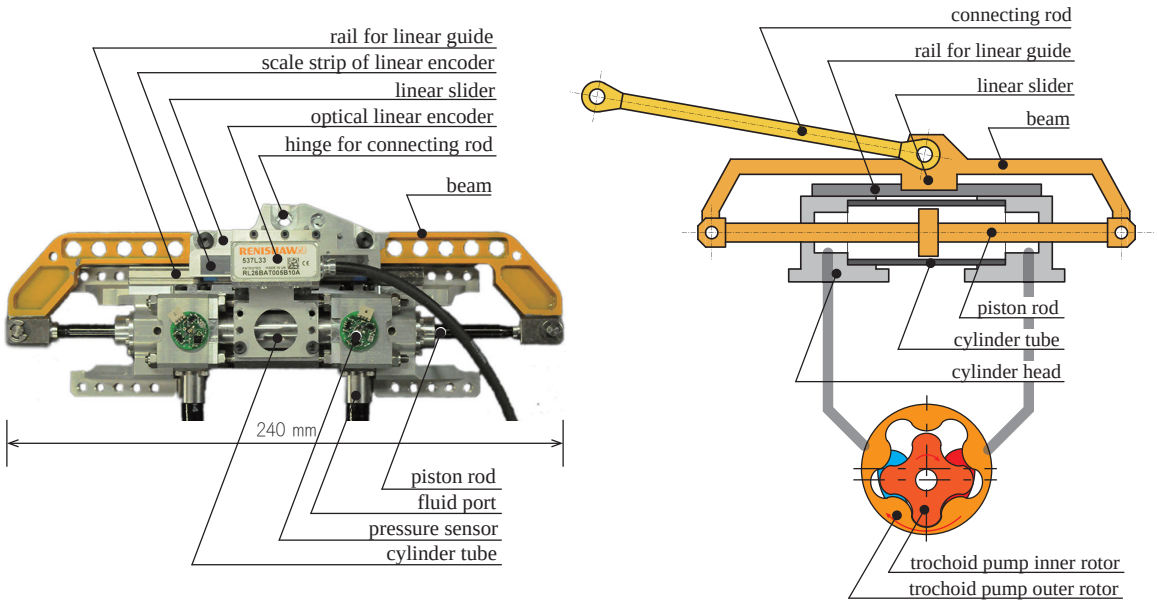

Figure 4.5: Low friction double rod cylinder with the beam structure.

check valve does not necessary to be a pilot one, a pilot check valve is advantageous in smooth operation and avoidance of cavitation. Habibi et al. [47] proposed the "symmetric linear actuator" structure where the single-rod cylinder sized actuator has the symmetric pressure receiving surface so that additional valves are not necessary. However, its complexity and large friction is problematic for force-sensitive application in a human size robot.

While double rod cylinders are advantageous in the system simplicity and friction due to the valve, the second piston rod results in two times larger friction due to the oil seal on the piston rod. With our special beam structure, however, the total oil seal friction can be even less than a single rod cylinder. Fig.4.5 illustrates the idea. In common hydraulic cylinders, the piston rod diameter is decided by the buckling strength. In our design, both ends of the piston rod is held by a beam structure, while

the external load is applied on the beam side, rather than the piston rod directly. The beam is held by a linear guide and only transfer the axial force to the piston rod. This removes the possibility of buckling and we can minimize the rod diameter as small as that the tensile strength of one rod is the half of the designed maximum force, since we can now use both of the piston rods to transfer the force.

4.4 Active Seal Friction Compensation with a Strain Gauge

EHA can measure the force/torque with high reliability by measuring the differential hydraulic pressure. The limitation is that with the pressure sensors, the oil seal friction on the actuator cannot be measured. An external torque sensor is effective to compensate the friction on the actuator [57]. The difficulty for the rotary torque sensors is that special attention need to be paid to avoid the crosstalk [2] [71]. They also have a complex structure and high cost. In the case of linear actuators, a force sensor or strain gauge attached on the connecting rod can accurately measure the force (therefore joint torque) without crosstalk, since the spherical rod end bearings do not transfer torque and non-axial force. The sensors are also easier to install and relatively cheaper.

To see the effect of friction compensation by the strain gauge, we conducted a series of experiments on the testbed shown in Fig.4.6. The actuator was under a low gain position control: a simple proportional feedback controller with the gain of 10

[2]The effect of non-actuated direction constraint force on the torque measurement.

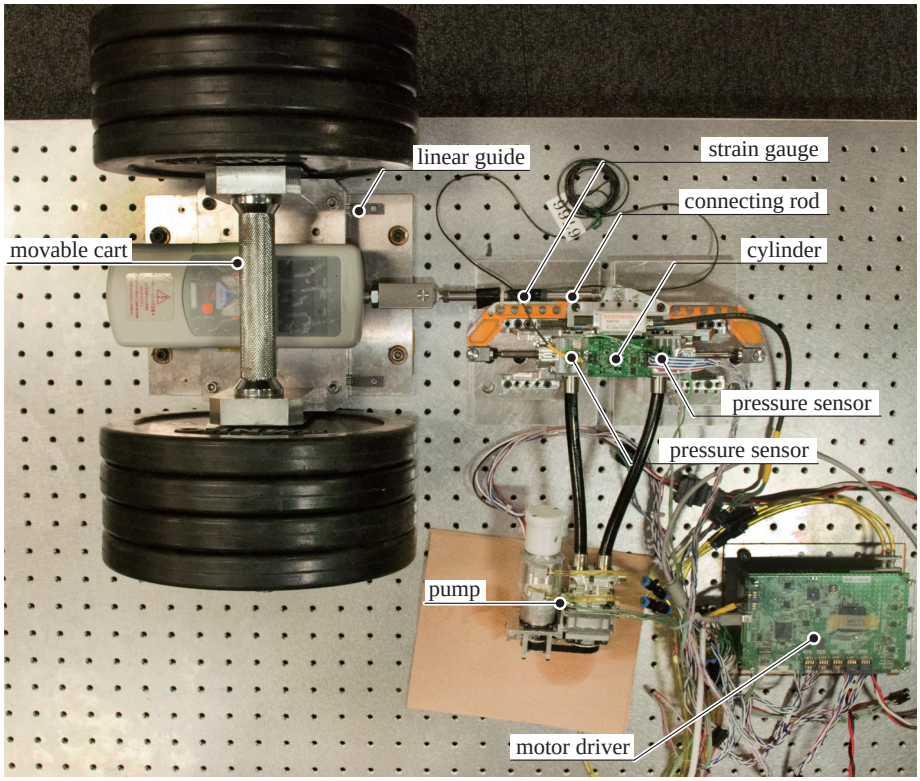

Figure 4.6: Common setup of the testbed experiment (Same figure as Fig.2.5). The actuator is placed horizontally. A movable cart supported with a pair of linear guides is aligned with the actuator. The cart and the actuator can be connected with a connecting rod, on which a strain gauge is attached. On the connection between the connecting rod and the cart, a force gauge is attached. The cart can be either fixed on the basement, free to move, or disconnected from the actuator so that the actuator has no load.

Nm/mm. The movable cart was driven externally by human hand. The position of the piston, command piston force, piston force estimated from the pressure sensors, and the force estimated from the strain gauge were recorded. The first experiment was done without the strain gauge feedback. As shown in Fig.4.7, what tracked the command force was the pressure sensor signal, therefore the actual force (strain gauge) had a constant offset depending on the direction of piston motion. With the strain gauge feedback, which is shown in Fig.4.8, we can see that the pressure was adjusted according to the direction of friction therefore the force tracking error was small. The relation between the piston position and the piston force in the two cases are plotted in Fig.4.9. Without the strain gauge feedback, the force tracking error was 12.1 N RMS, which is as small as 0.81% of the 1500 N maximum piston force, showing the effect of friction reduction efforts in the previous section. With the strain gauge information, the error was reduced to be 1.3 N, which is 0.087% of the maximum force.

A common drawback of force measurement by strain gauge based sensors is its sensitivity to the temperature. Even though the four arms method is effective in the temperature compensation, the effect is still not negligible, especially in the case that the flexure element is stiff and the deformation is small. In the case of rotary actuators, there are approaches with optical encoders [72], while it is difficult to adopt for a linear actuator. Fundamentally, pressure sensors have the same problem, since in most case they actually measure the force generated by the pressure. The difference is that the strain gauge is attached on the connecting rod, which is floating from the other parts and has a small thermal capacity. The pressure sensor is attached on the

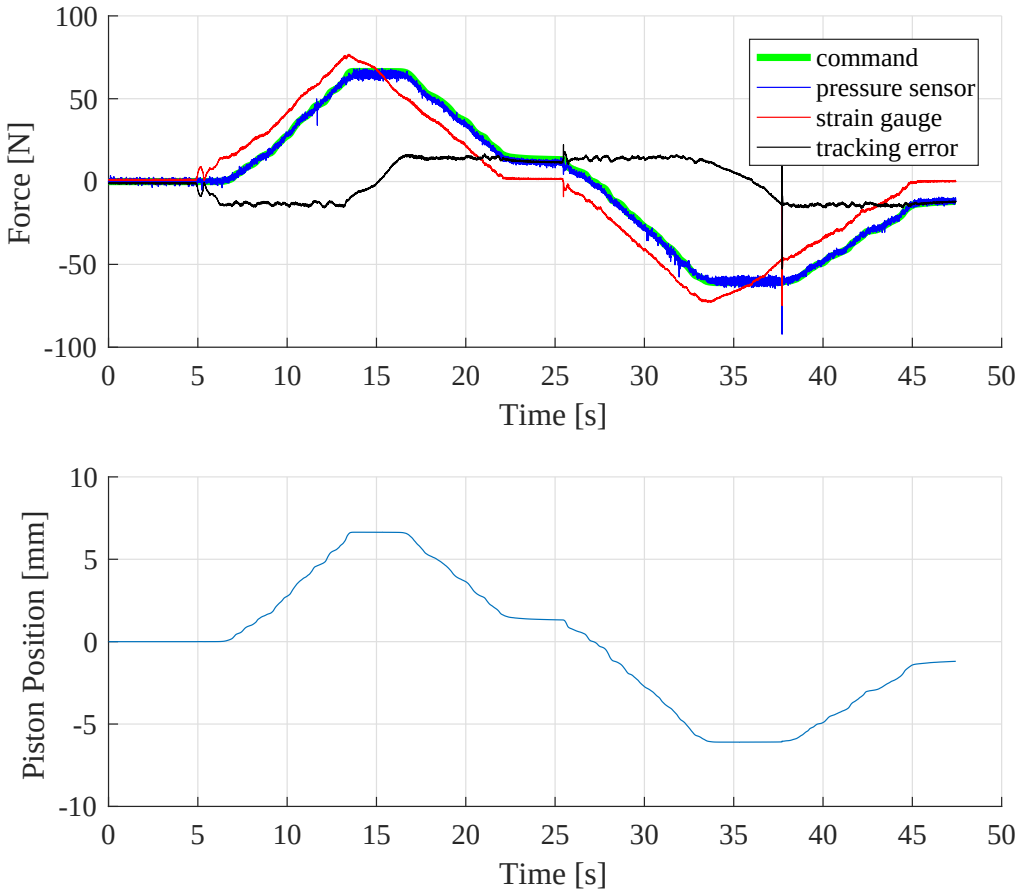

Figure 4.7: Time transition of the parameters in the experiment to confirm the quasi-static force controllability of the EHA without strain gauge feedback. The actuator is under a low gain control and the piston is manually moved by human. The red line shows the force acquired from the strain gauge on the connecting rod, which we treat as the actually exerted force by the actuator. The black line shows the error between the measured force (red line) and the desired force generated by the measured piston position (green line). The blue line shows the force estimated from the pressure sensors.

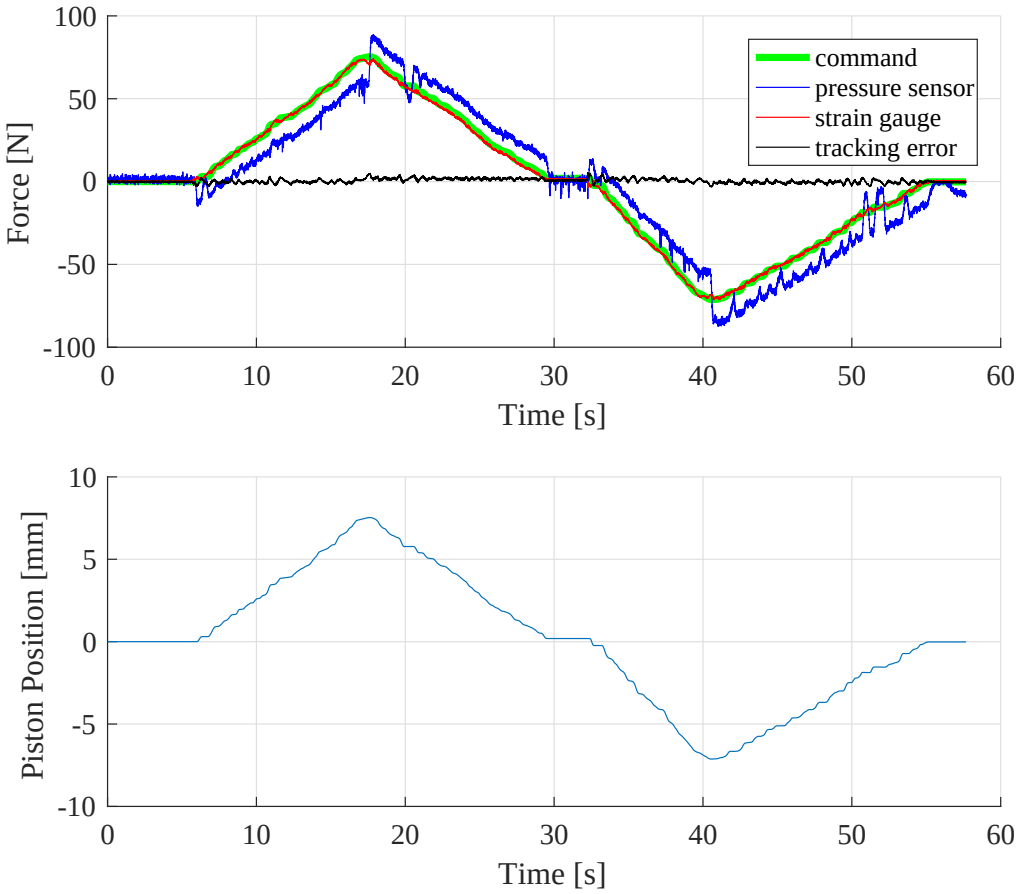

Figure 4.8: Time transition of the parameters in the experiment to confirm the quasi-static force controllability of the EHA with the strain gauge feedback. The actuator is under a low gain control and the piston is manually moved by human. The red line shows the force acquired from the strain gauge on the connecting rod, which we treat as the actually exerted force by the actuator. The black line shows the error between the measured force (red line) and the desired force generated by the measured piston position (green line). The blue line shows the force estimated from the pressure sensors.

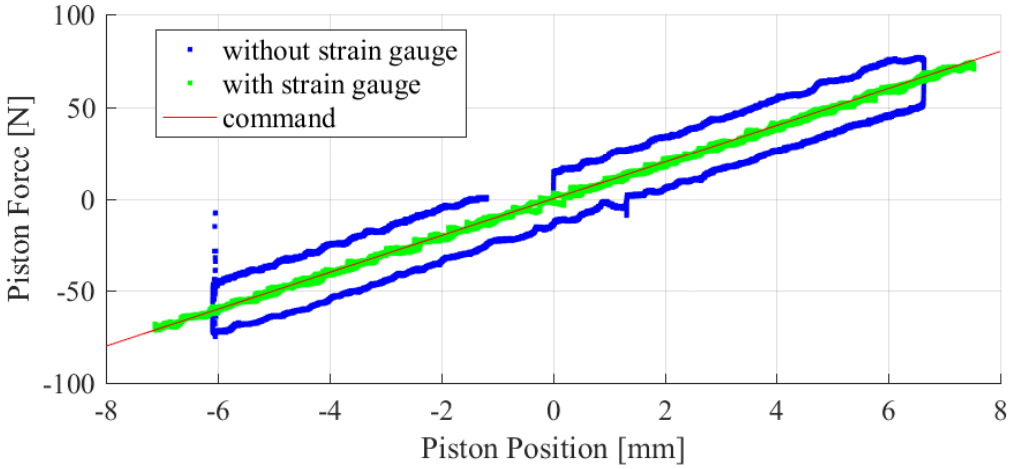

Figure 4.9: Relationship between the piston position and actuator force, when the actuator is under a low gain position control and the piston is manually moved by human. The red line shows the desired relationship between the two. The blue markers represent the case without strain gauge feedback and the green markers show the case with. The time transition of the value is shown in Fig.4.7, Fig.4.8 respectively. The RMS force tracking error of the former case was 12.1 N and 1.3 N for the latter.

cylinder, which is fixed on the robot frame, therefore it is thermodynamically more stable. Another advantage of the pressure sensors is that the differential pressure is acquired from the difference of the two gauge-pressure sensors, therefore the common mode offset is canceled. To experimentally examine the temperature effect on the sensors, we conducted a thermal disturbance experiment. The system, which is the same one as the previous discussions, is left as it is, therefore the measured force should keep zero value. We externally heat the system by a blower, making sure that the system is heated uniformly. We also attached a temperature sensor on the system. Fig.4.10 shows the relationship between the system temperature and the estimated force from the sensor. The red markers represent sensor values from the pressure sensor. We can see that the thermal effect is small. The strain gauge, which is shown in blue markers, shows a clear relationship with the temperature. The gradient is quite linear with the gain of 2.5 N/°C.

While the thermal drift of the strain gauge is as high as 2.5 N/°C, this value is already a compensated value by a careful four gauge method. The connecting rod is made of a chromium-molybdenum steel pipe with the inner diameter of 5 mm and outer diameter 0f 8 mm. The linear expansion coefficient of the material is around 10×10^{-6}/°C. To generate the same strain with 1 °C temperature variation, the axial force need to be as high as 83 N. This means that the four gauge system compensates the thermal drift by 97%. The still high variation compared with the pressure sensor is due to the high stiffness of the connecting rod, which is difficult to change the shape for the strain gauge.

One solution to compensate the variation of the strain gauge is to attach a tem-

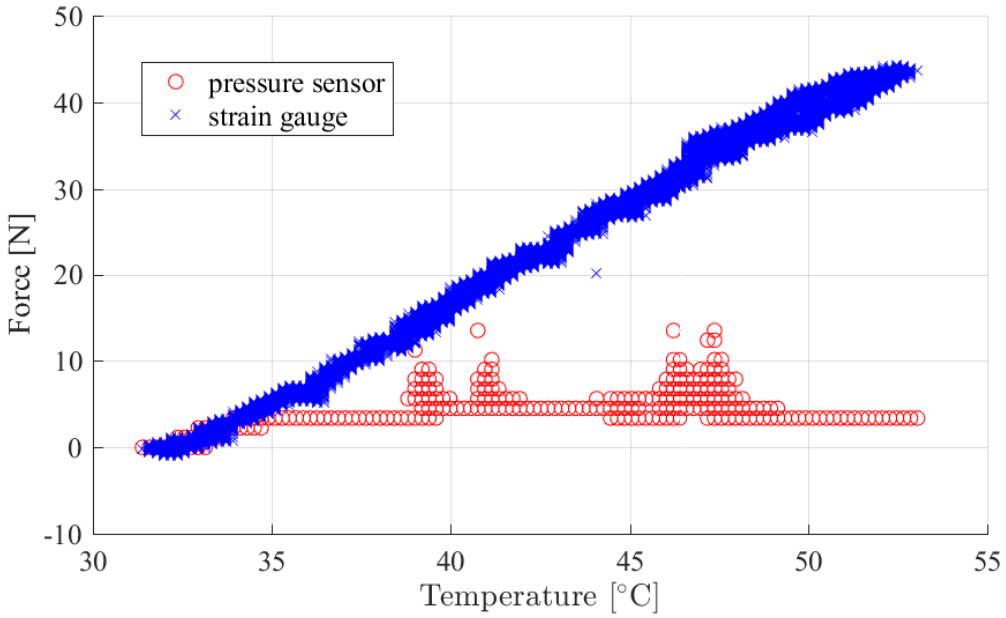

Figure 4.10: Variation the force value acquired from the pressure sensor (red markers) and the strain gauge (blue markers) against temperature variation. While the thermal effect on the pressure sensor is small, the one on the strain gauge is as high as 2.5 N/°C gradient.

perature sensor on the connecting rod, utilizing the linear relationship between the temperature and the drift. The problem is a more complex system and need of calibration for each actuator. To mix the stable but not sensitive pressure sensor signal and the precise but drifted strain gauge signal, complementary filters can be effective. A complementary filter is a set of filters with the relationship

$$\sum_i \mathrm{H}(z) = 1 \tag{4.1}$$

With a complementary filter, we can mix different signals utilizing the preferable frequency zone of each signal, while keeping the total gain as one through all of the frequency range. In this case, the piston force can be estimated by the summation of a low-pass filtered pressure sensor information and a high-pass filtered strain gauge

information:

$$f_{\text{fil}} = \text{H}_{\text{lowpass}}(z) f_{\text{pres}} + \text{H}_{\text{highpass}}(z) f_{\text{strain}} \tag{4.2}$$

$$\text{H}_{\text{lowpass}}(z) + \text{H}_{\text{highpass}}(z) = 1 \tag{4.3}$$

where f_{fil}, f_{pres}, f_{strain} represents estimated force with the complementary filter, force measured by the pressure sensor, and force measured from the strain gauge respectively. $\text{H}_{\text{lowpass}}$, $\text{H}_{\text{highpass}}$ represents a low-pass and high-pass filter. Here, we ignore the effect of the piston acceleration due to its small inertia. Since the effect of the temperature drift is slow, the cutoff frequency of the filters can be set as a very low value.

When implementing the filter on the microcontroller, we can make a simple transformation of Eq.(4.2) to reduce the computational cost as:

$$f_{\text{fil}} = f_{\text{pres}} + \text{H}_{\text{highpass}}(z)(f_{\text{strain}} - f_{\text{pres}}) \tag{4.4}$$

This means that we only need to apply a high-pass filter to the non-compensated friction. The constraint of Eq.(4.3) is automatically fulfilled so that the parameters of $\text{H}_{\text{highpass}}$ are free to adjust.

To see the force measurement performance of the pressure sensor, strain gauge, and the complementary filtered value, we conducted an experiment with the configuration that the output side of the connecting rod was attached on a fixed force gauge. The actuator was under the force control, pushing and pulling the force gauge. The value acquired from the external force gauge is treated as the ground truth. To see the effect of thermal drift, we heated up the system by an external heat gun. The result is shown in Fig.4.11. The orange dot line represents the temperature of the system,

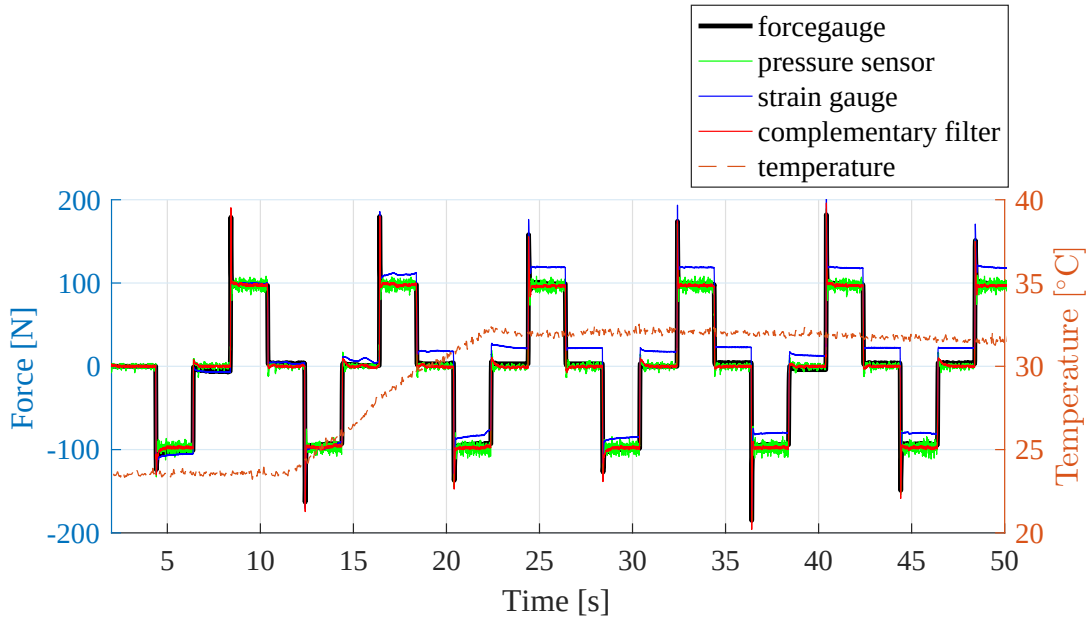

Figure 4.11: Time transition of the actuator force measured by the external force gauge, the strain gauge on the connecting rod, the pressure sensor on the cylinder, and the complementary filtered value. The system is heated up by an external heat gun. The temperature is represented by the orange dot line. The black thick line is the force gauge value, which is the grand truth. The blue line represents the force measured from the strain gauge. While it has the best accuracy at the beginning, a clear drift can be seen when the temperature rises. The RMS force measurement error is around 15.1 N. The green line represents the force estimated from the pressure sensor. While there is no clear drift, it has a constant offset error. The RMS error is around 6.58 N. This is 0.46% of the maximum actuator force 1500 N. With the complementary filter, which is represented by the red line, the error is smaller to be 4.18 N, which is 0.28% of the maximum force.

acquired from a temperature sensor attached on the cylinder. The black thick line is the grand truth. The blue line represents the force measured from the strain gauge. While it has the best accuracy at the beginning, a clear drift can be seen when the temperature rises. The RMS force measurement error is around 15.1 N. The green line represents the force estimated from the pressure sensor. While there is no clear drift, it has a constant offset error. The RMS error is around 6.58 N. This is as low as 0.46% of the maximum actuator force 1500 N, thanks to the low friction design with the beam structure. With the complementary filter, which is represented by the red line, the error is smaller to be 4.18 N, which is 0.28% of the maximum force.

4.5 Conclusion

In this chapter, we presented the way to improve the force-sensitivity of EHA from both the mechanical backdrivability aspect and the measurement aspect. The conclusion is as follows:

1. Trochoid pumps are suitable to reduce the friction and improve backdrivability of EHA, while they have limited high-pressure performance. To attain both the high backdrivability and high pressure, we developed a low friction lightweight trochoid pump with the reinforced structure and water cooling mechanism. The developed pump has 620 g weight including the 200 W electric motor and 5.3 MPa discharging pressure. The maximum discharging flow rate is 57000 mm^3/s.

2. To minimize the viscous friction, double rod cylinders are more suitable since the closed circuit volume is invariant. We proposed a double rod cylinder design

with the beam structure to minimize the piston rod diameter, therefore minimize the friction due to the piston rod oil seal. The developed cylinder had a effective friction of 6.58 N, which is 0.46% of the 1500 N maximum piston force.

3. The friction on the piston rod can be actively compensated with a strain gauge attached on the connecting rod. In that case, the thermal drift of the strain gauge can be compensated by the pressure sensor information with a complementary filter. It resulted in 4.2 N measuring error, which is 0.28% of the maximum force.

Chapter5

Current-Pressure-Position Triple-Loop Feedback Control of Electro-Hydrostatic Actuators for Humanoid Robots

5.1 Introduction

For legged or biped robots, fast torque response of the actuator is critical for balancing or locomotion, since manipulation of the COM is a hard real-time task. With a joint position control based walking framework, which is the most common approach for the walking and a torque control based robot should also allow such approach as a robot platform, the requirement for the joint torque control bandwidth is even higher to achieve a high gain joint position feedback.

For the non-backdrivable actuators, the problem is less, since in the case of a geared motor, thanks to the high rigidity of the transmission, the response is governed by the fast physical behavior of electric current. Kim et al. reported that their motor

has the current control bandwidth of 400 Hz [23]. In the case of servo-valve controlled hydraulics, only the small inertia of the valve elements need to be driven. Hyon et al. reported that their servo-valve has the control bandwidth of 120 Hz [73]. In the works by Barasuol [74], the low leakage valve showed the bandwidth of 120 Hz and the high response one showed 320 Hz.

In the case of series elastic actuators or pneumatic actuators, on the contrary, the control bandwidth is limited by the elasticity. Their typical control bandwidth is less than 30 Hz (for example, 5-25 Hz bandwidth of the SEA by Pratt et al. [32], 16 Hz by Vallery et al. [75], 10 Hz by Kong et al. [76], 19 Hz by Sensinger et al. [77], and 35 Hz by Robinson et al. [78].) The exception is the work by Paine et al. [79], combining the high stiffness spring and disturbance observer to realize 70 Hz bandwidth.

The studies on the control of EHA is widely conducted in the aerospace region [80, 81]. It is difficult to directly adopt their knowledge to robotics, though, since their hardware have much larger size and weight, therefore the time constant, than those suitable for human-size robot actuation. Their target applications have limited requirement on the capability of high gain position feedback. For example, the requirement for the EHA position control bandwidth to drive the F-18 airplane ailerons was set as 7 Hz [81].

The early studies on the EHA for the robot use includes the rotary joint by Bobrow et al. [46] and the linear actuator by Habibi et al. [47]. In the former case, the analog pressure controller realized 32 Hz bandwidth while in the latter case the position control bandwidth was around 2 Hz. Recently Sakuma et al. improved the control bandwidth of their EHA from the original less than 1 Hz [82] to 7 Hz by modeling it

as a two-mass resonant system and adopting the resonance suppression control [62]. There are also approach with sliding mode control [83] and neural network [84].

While EHA should be able to have better response performance than SEAs due to the higher transmission stiffness, the actually reported values are still limited, as shown above. To fundamentally improve the performance, both approaches from the control and hardware design should be taken, which is the main target of this chapter. On the hardware side, the first major problem that makes the control difficult – high static friction, is already treated in the previous chapter therefore we discuss the second – series elasticity. On the control side, we show that a fine-tuned multilayered controller running in a distributed devices can actually achieve advantageous response property, even though each layer of the controller has a simple structure.

5.2 Reduction of the Hydraulic Elasticity to Achieve a High Control Bandwidth

To fundamentally improve the response of EHA, the approach from hardware side is inevitable. As discussed in chapter 2, in an EHA, the load side and the input side are connected through the series elasticity because of the piping expansion and fluid compressibility. From discussion in chapter 2, on the total elasticity, the piping expansion has one order smaller effect than the fluid compression, therefore the key is how to reduce the latter. Since the volume variation depends on the chamber volume (Eq.(2.23)), reduction of dead fluid volume is effective. Placing the pump close to the cylinder and minimize the piping length is one solution. Dead volumes inside the

cylinder should be minimized in the design process or filled with other materials. In our case, we carefully designed the shape of the piston and cylinder head to reduce the gap when the piston is at the end.

While the piston swept volume is impossible to be filled by the other material, Eq.(2.27) shows a simple property: larger piston surface results in higher stiffness. This can be explained intuitively: a cylinder with a larger piston has larger volume but less pressure variation from an external force, therefore the total volume variation is constant as shown in Eq.(2.23), but the piston position variation is fewer thanks to the larger piston surface. This shows that the maximization of the pressure receiving surface is not only effective in the improvement of the force-to-weight ratio as shown in chapter 3, but also advantageous in the reduction of the effective series elasticity.

Selection of a high bulk module fluid is also important. Silicone oils have the advantages in safety and adjustable viscosity, while their bulk modules are as low as around 800 MPa [85]. Mineral oil or other types of high bulk module fluid [86] is effective in the improvement of response. In our case, we chose COSMO HYDRO HV100 mineral oil.

5.3 Force Control of EHA by Fast Motor Current Feedback

The model shown in Fig.2.3 suggests that velocity controlled motor/electronic system can realize the force control of an EHA, since the input and output side of the system is decoupled with the series damper and elasticity. This is advantageous in

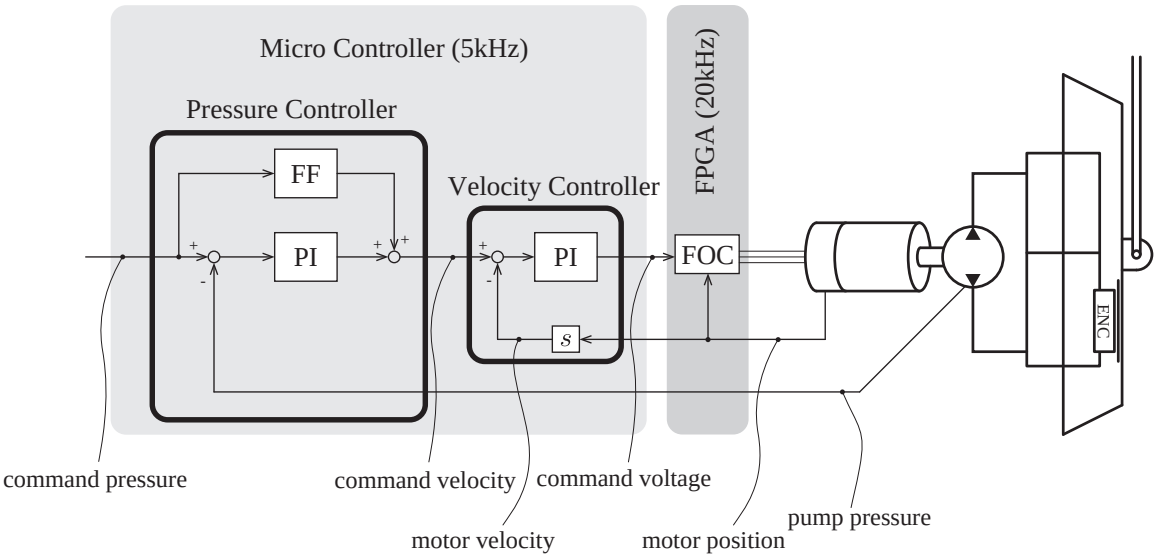

Figure 5.1: Pressure controller based on motor velocity controller. A velocity controlled motor/electronic system can realize the force control of an EHA, since the input and output side of the system is decoupled with the series damper and elasticity. This is advantageous in the cost and system simplicity since most of the industrial motor/electronic systems (even not a DC motor), especially in the low cost or small size region, support velocity command.

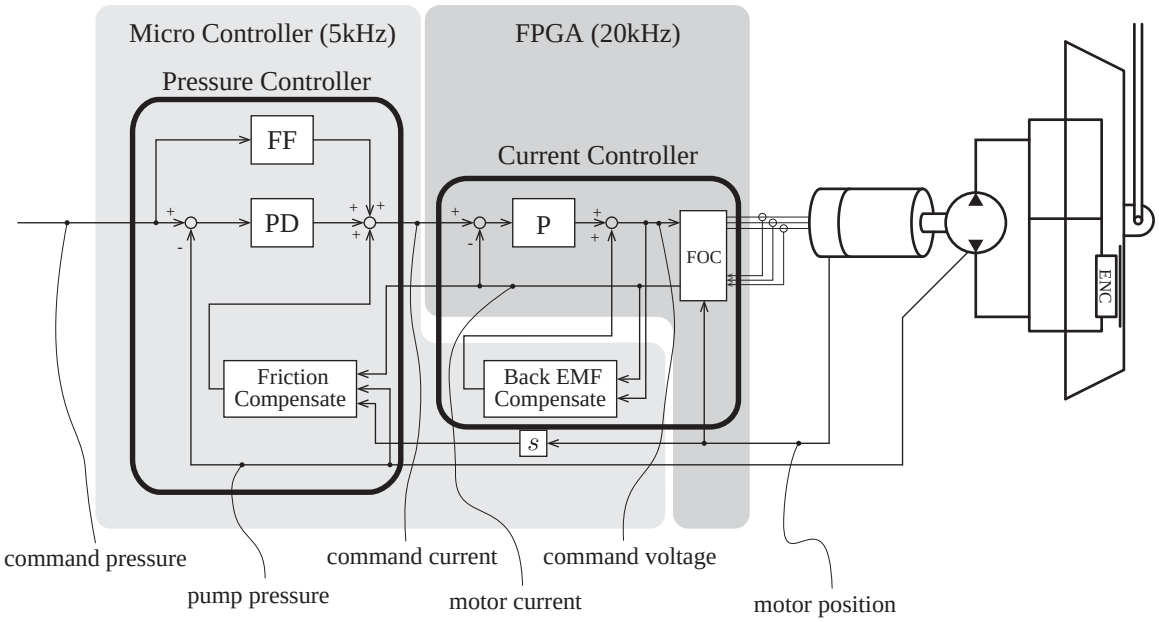

Figure 5.2: Pressure controller based on motor current controller. The motor current controller consists of a proportional feedback controller and a back EMF compensator. The former is implemented on an FPGA with 20 kHz control frequency, with the field oriented control of the brushless DC motor. The latter is implemented on a microcontroller running in 5 kHz frequency. The pressure feedback controller has a feed forward term, a PD feedback controller, and a momentum based friction observer.

the cost and system simplicity since most of the industrial motor/electronic systems (even not a DC motor), especially in the low cost or small size region, support velocity command. We implemented a PI force controller with a minor pump velocity control loop, which is shown in Fig.5.1. In that case, the effect of the pump's friction and inertia are compensated by the minor velocity loop. With a step command, we get the rise time of around 40 ms, which is shown as the blue line in Fig.5.3. The experiment is done with the setup shown in Fig.2.5 and the piston is fixed by pushing it on the end of the cylinder.

When the pump is under the pressure control, we saw a pulsation of the pressure. In Fig.5.4, the pressure tracking error is plotted against the pump rotor's angle. The

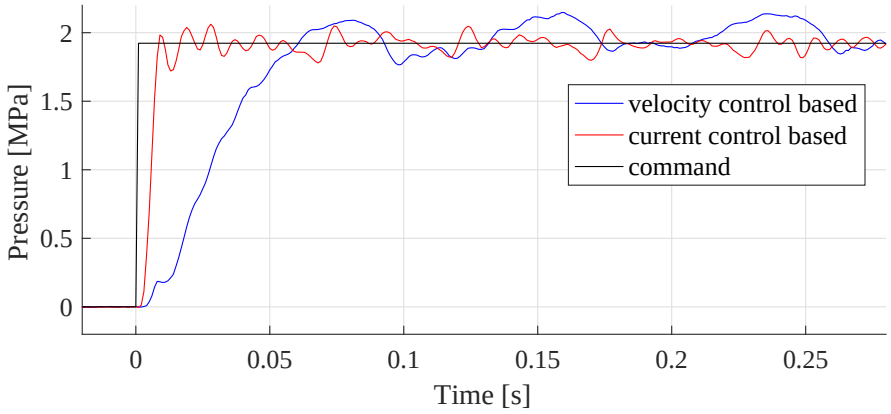

Figure 5.3: Step response of the pressure controller based on the motor velocity controller (blue) and the motor current controller (red). The command pressure is equivalent to 550 N piston force. In the former case, the rise time is 40 ms, while in the latter case the rise time is 5 ms, which is 8 times faster.

graph shows that the pulsation is dependent on the rotor angle and there are four peaks. This corresponds well to the four teeth of the inner rotor gear. (See Fig.4.2 for the structure of the trochoid pump.) While the discussion in section 2 treats the property of the pump as constant, actual gear pumps have pulsation depending on the condition of the gear meshing. It cannot be compensated by the minor velocity feedback loop since it is a modeling error between the pump velocity and the pressure.

The current control based pressure controller is more effective to compensate the pulsation. In that case, the friction is compensated by a friction observer [87, 88] and the inertia can be scaled [89] by the pressure feedback. Shown as the red line in Fig.5.4, the current control based controller can reduce the pulsation by around 74% peak-to-peak. It also improves the step response, where the rise time is around 5 ms, – 8 times faster than the velocity control based one. The step response is shown as the red line in Fig.5.3.

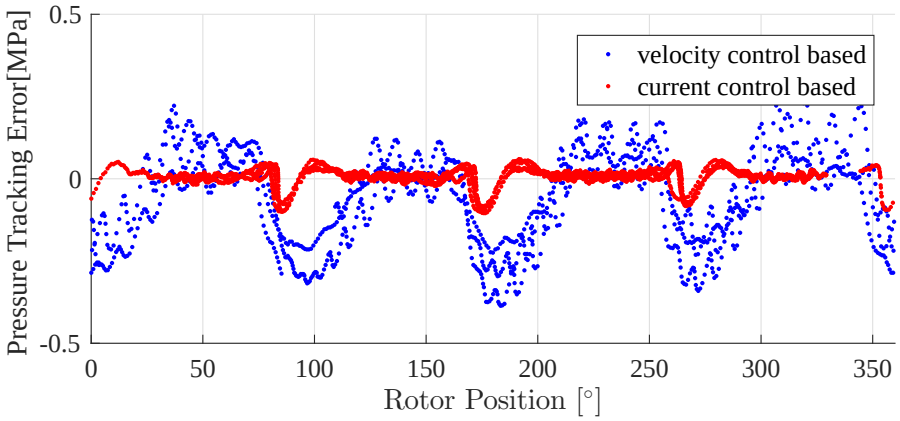

Figure 5.4: Plot of the pressure tracking error against the pump rotor's angle. Clear four pulsations per rotation can be seen in the both of the velocity control based case (blue) and current control based case (red). In the former case, the peak-to-peak tracking error is 0.63 MPa, which is 74% reduced to 0.16 MPa with the latter case.

From the perspective of control, the idea of this cascaded control is to separate the controllers in the devices with different operating frequency and handle the faster phenomenon in a faster loop. The difference between the current control based pressure controller and the velocity based one is that while current is a much faster than the behavior of pressure change, variation of the pump velocity is a slower phenomenon than the pressure variation.

Fig.5.7 shows the experimentally acquired closed-loop bode plot of the pressure controllers. The amplitude of the command pressure is 0.85 MPa, which is equivalent to 250 N piston force. The velocity control based one is shown in the blue markers and the current control based one is in the red markers. Each marker corresponds to one dataset where a constant frequency sine wave command is given. Under the fixed piston condition, the bode plot shows that the developed actuator has around 100

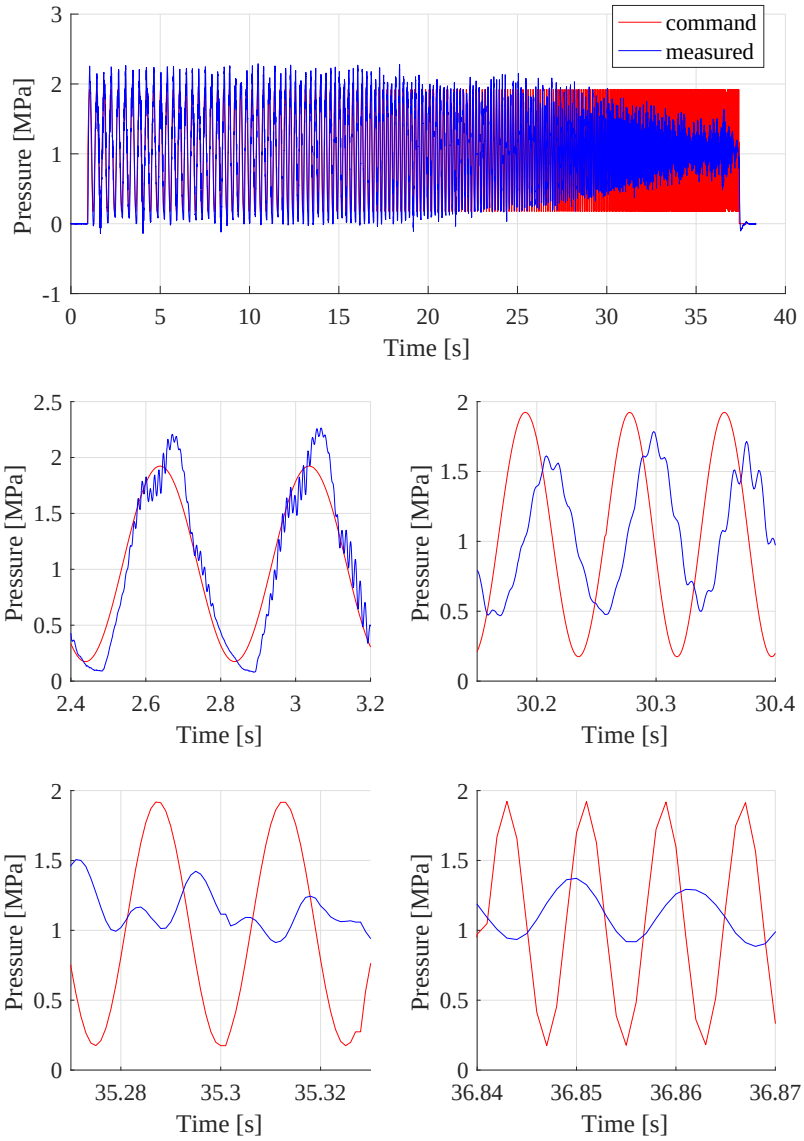

Figure 5.5: Time transition of the parameters in the experiment to acquire the frequency response between the command pressure and the measured pressure, with the pressure controller based on the motor velocity controller.

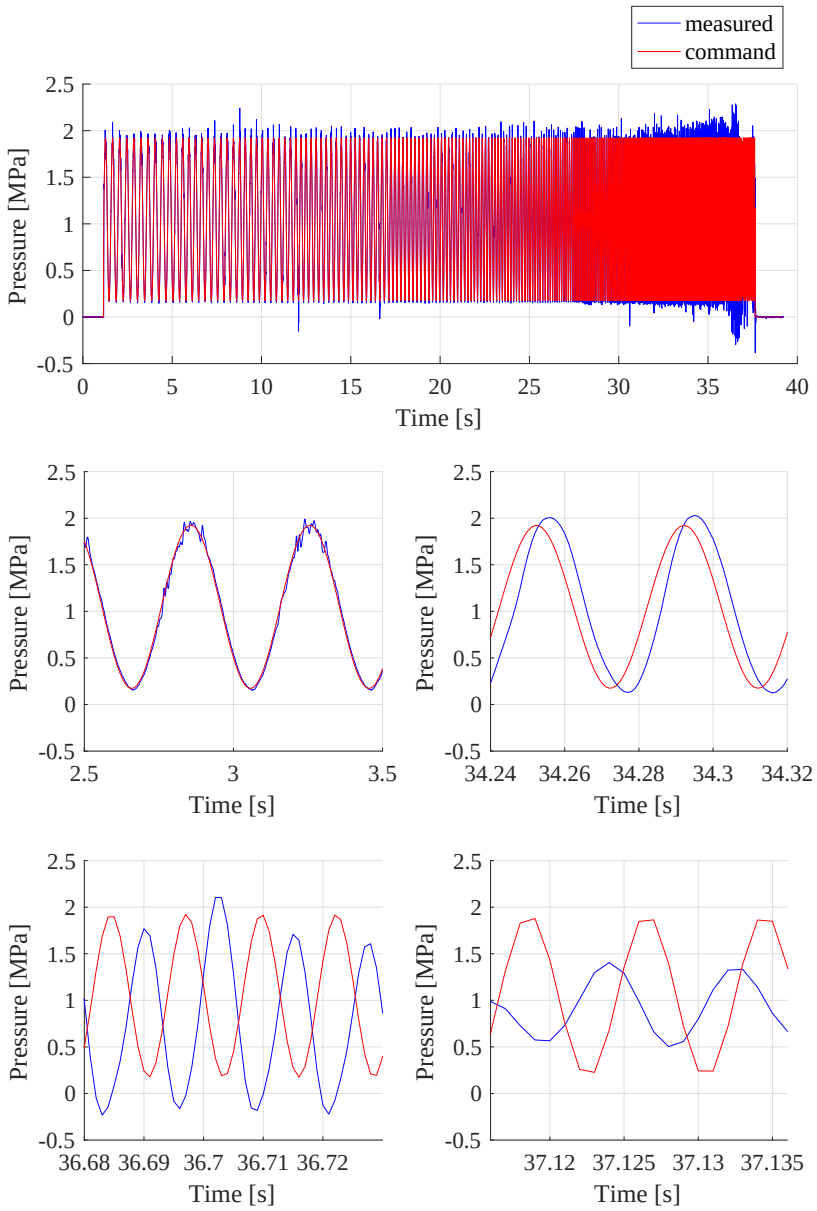

Figure 5.6: Time transition of the parameters in the experiment to acquire the frequency response between the command pressure and the measured pressure, with the pressure controller based on the motor current controller.

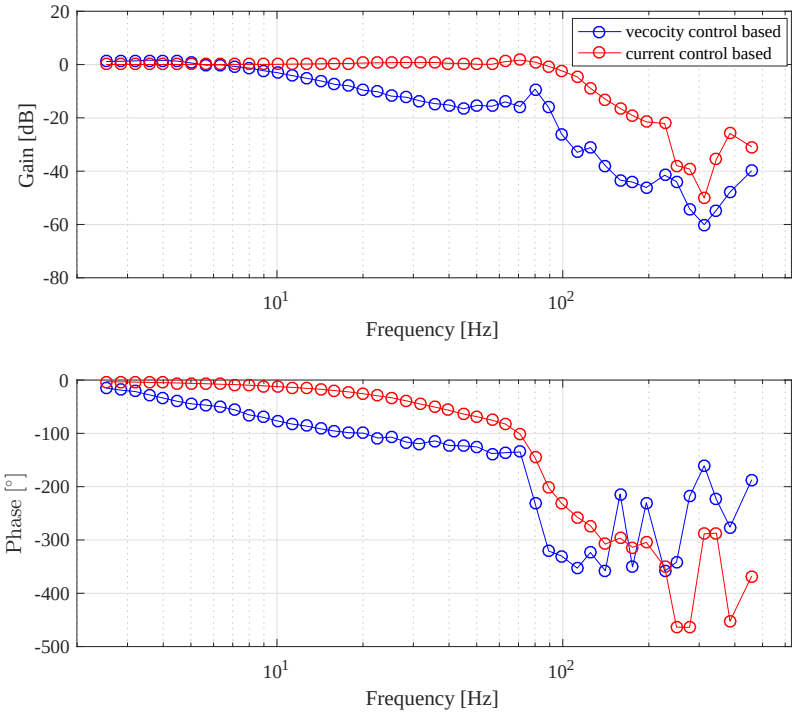

Figure 5.7: Closed-loop pressure control bode plot of the developed EHA, under the condition that the piston is fixed on the end of the cylinder. The blue markers represent the one based on the pump velocity control and the red markers represent the one based on the current control. In the latter case, the bandwidth is 100 Hz, which shows the high bandwidth property of EHAs compared with other backdrivable actuators.

Hz closed-loop pressure control bandwidth [1]. This is higher than the state-of-the-art high closed-loop bandwidth series elastic actuators such as the one by Hopkins et al. for the THOR robot [90] (30 Hz), the one by Paine et al. for the Valkyrie robot [79] (70 Hz) or the one by Hutter et al. for the ANYmal robot [91] (70 Hz), and close to the 120 Hz bandwidth of the servo valve of the hydraulic humanoid by Hyon et al. [73].

5.4 High Mechanical Stiffness Structure to Transfer the High Bandwidth Force

In addition to the stiffness of the hydraulic system discussed in section 5.2, the stiffness of the mechanical structure between the piston and the load is also important, as shown in Eq.(2.33) where we can see that the actuator force is affected by a fast motion of the piston. In Fig.5.9, the bode plot between the command force and the measured force from the strain gauge is plotted in the red color. The experiment is conducted with the same set up in chapter 2 and Fig.2.5, where the load side end of the connecting rod is fixed. While in Fig.5.7 the pressure control bandwidth was 100 Hz, this time the bandwidth is limited to 22 Hz. The bode plot between command pressure and actual pressure, and between the pressure and force is also plotted in green and blue color, respectively. From the plot, it is clear that there are few gain decrease and the delay between the pressure and strain gauge measured force, and the 22 Hz bandwidth is caused by that the pressure no longer track the command

[1]The frequency where the gain reaches -3 dB.

with 100 Hz bandwidth. The difference between the two experiments is that while in the former the piston was tightly fixed by pushing it on the end of the cylinder, in this case what was fixed is the load side end of the connecting rod. The deformation of the mechanical components between the piston and the load such as the rod end bearings, connecting rod, beam structure, linear guide, and piston rod causes motion of the piston that prevents the rise of pressure.

A large part of the deformation is caused by the deformation of the beam structure and the linear slider supporting that. A schematic of the deformation is shown in the left bottom of Fig.5.10. To confirm this, we used a laser range finder to measure the displacement of the beam in the orthogonal direction of the piston rod. The displacement when the actuator pushes the load with 500 N force is shown as black arrows in the top of Fig.5.10. On the tip of the piston rod, there is around 330 μm displacement. The arrows suggest that both the rotation of the beam due to the deformation of the linear slider, and the bending of the beam itself are the problem.

To constrain the deformation, we added additional linear guides on the tip of the piston rod, as shown in the green color parts in the middle of Fig.5.10. Its schematic is shown in the right bottom of the figure. This suppressed the displacement of the piston rod tip to 86 μm, which is 74% decrease. The distribution of the deformation is shown by the red arrows in the figure. In Fig.5.11, the red line shows the bode plot with the additional linear guide. The force control bandwidth is improved to 53 Hz, which is 2.4 times larger than original. The comparison of the bode plot is shown in Fig.5.11, where the one without reinforcement (the same plot of the red line in Fig.5.9) is shown in blue color and the one with the reinforcement is in red color.

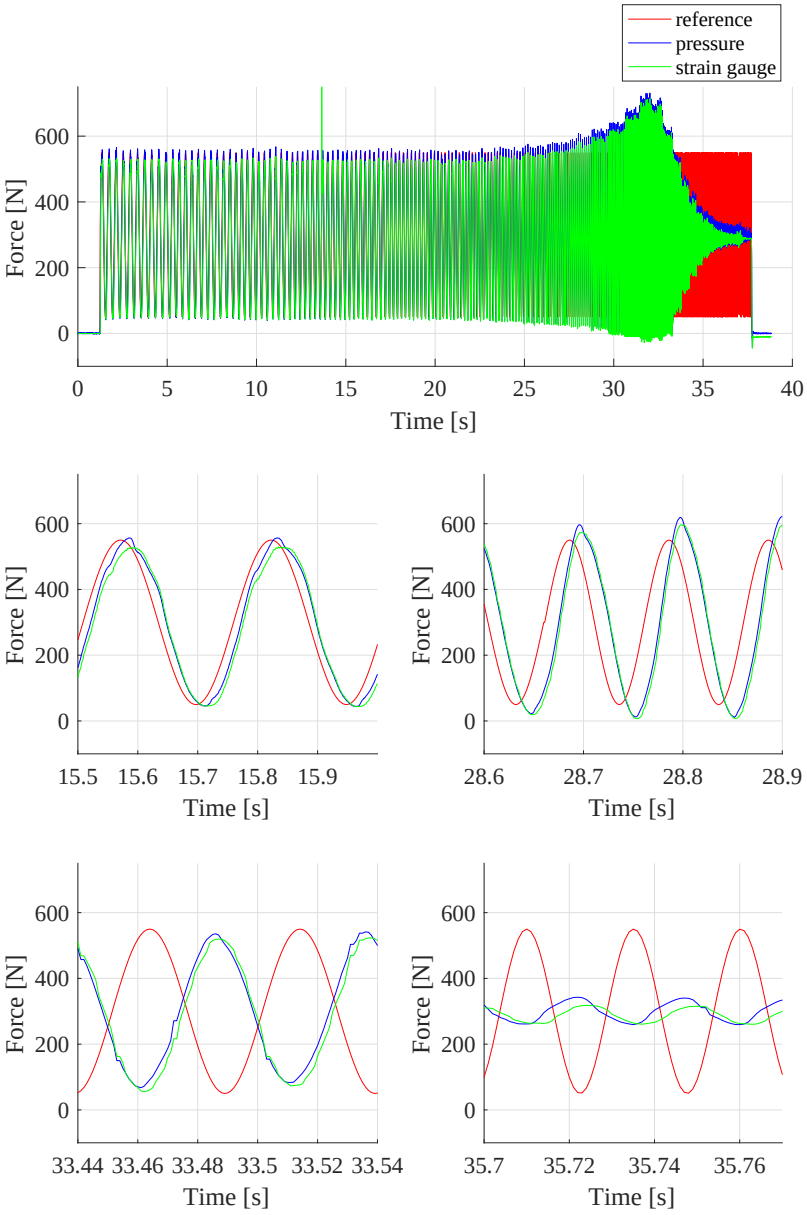

Figure 5.8: Time variation of the experiment to acquire the frequency response shown in Fig.5.9. The red line represents command force. The blue lines represent the force estimated from the pressure sensor. The green lines show the force from the strain gauge, which we treat as the force actually the actuator exerts.

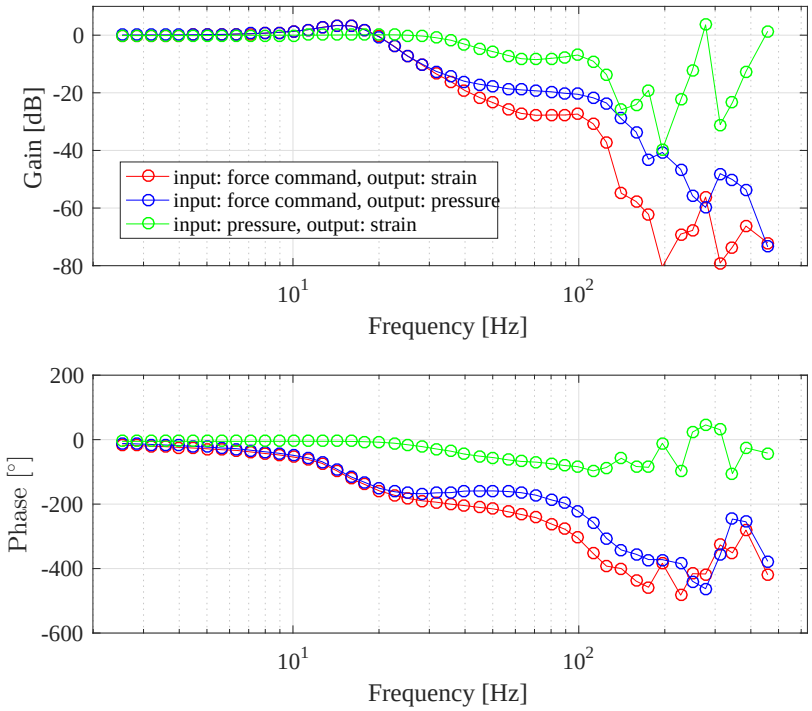

Figure 5.9: Bode plot between force command and force from strain gauge (red), between force command to the pressure (blue), and between pressure to the strain gauge force (green). The force control bandwidth is around 15 Hz. The delay between the pressure and the force is small. The dominant one is that the pressure no longer tracks the reference as fast as the case when the piston is fixed on the end of the cylinder, which is shown in Fig.5.7.

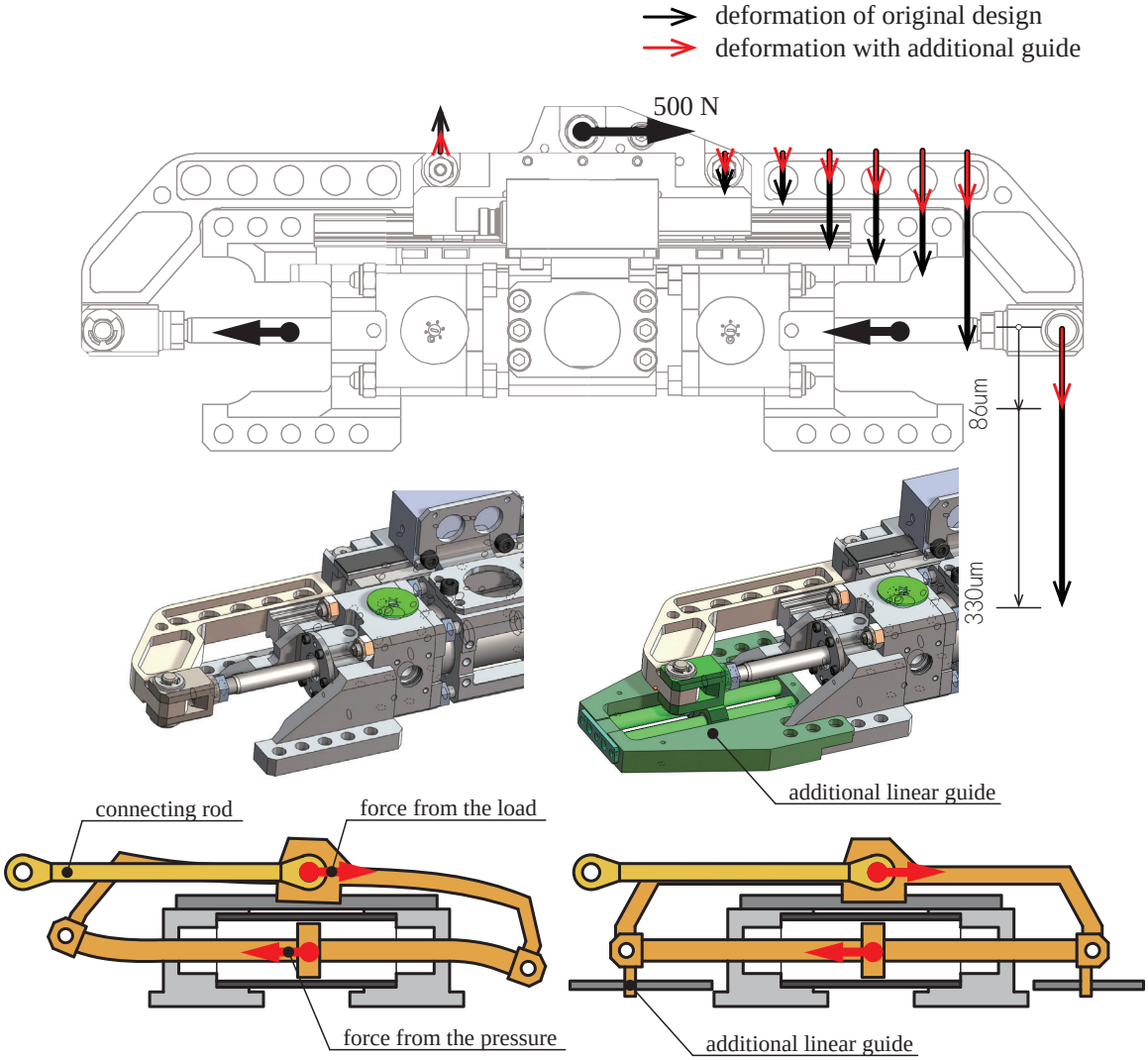

Figure 5.10: Deformation of the beam structure when 500 N piston force is applied. The arrows show that both of the linear slider deformation and the beam deformation occurs. With an additional linear guide constraining the radial direction motion of the piston rod, the deformation is suppressed from the original black arrows to the red arrows. On the tip of the piston rod, the deformation is suppressed from the original 330 μm to 86 μm, which is 74% decrease.

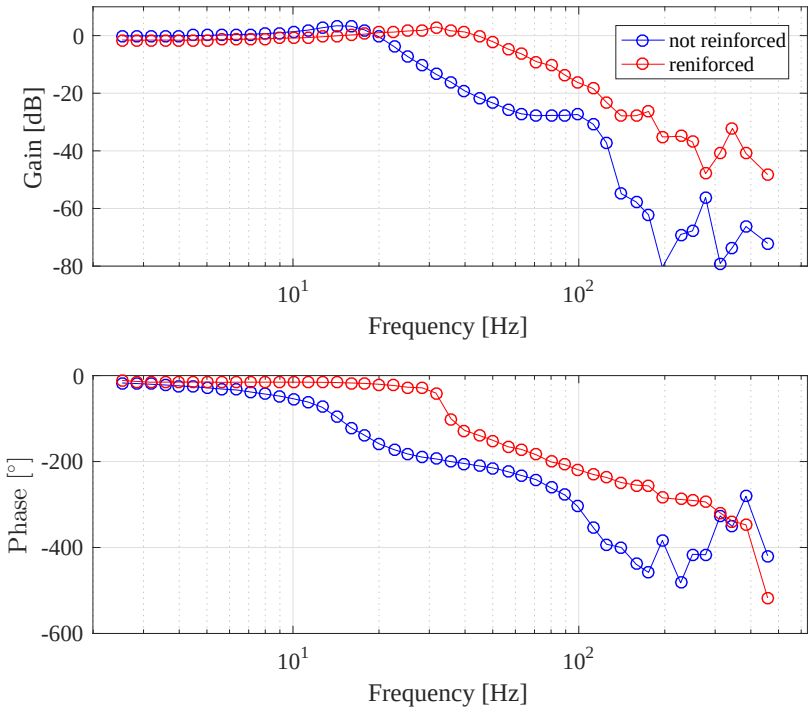

Figure 5.11: Closed-loop force control bandwidth of the developed EHA when the load side of the connecting rod is fixed. With the additional linear guide, we can improve the stiffness of the force transmission structure, resulting the improvement of the control bandwidth from the original 22 Hz to 53 Hz, which is 2.4 times larger.

5.5 Current-Pressure-Position Triple-Loop Feedback for Parallel Joints

When driving rotational robot joints with linear actuators, an advantage is that we can drive a two-DoF universal joint simultaneously by two linear actuators to fully utilize their force. In that case, the conversion between the cylinder space and joint space is costly for the local motor driver. Since the behavior of the joint position/velocity is slower than the motor current or hydraulic pressure, we can close the loop in the higher layer with lower framerate. The overall joint controller has three layers, as shown in Fig.5.12. The joint level position controller is implemented on the onboard PC with 1 kHz frequency. The conversion between cylinder position/force and joint angle/torque is also done on the onboard PC. The joint position controller outputs command joint torque, which is converted to the command cylinder force and sent to the MCU board through the EtherCAT bus. On the MCU board, the actuator level force feedback control is done in 5 kHz frequency and resulted command motor current is sent to the lower level driver board, where the current feedback loop is done in 20 kHz frequency.

The evaluation is conducted on the hydrostatically driven humanoid robot "Hydra", which will be detailed in the following chapter 6. Its hip joint has three DoF, where the pitch and roll direction are the universal joint driven by two linear EHA. The bode plot between command hip pitch joint position and actual position, and between command joint torque and actual torque are shown in Fig.5.13. The blue markers represent the position response and the red marker are the torque response. The

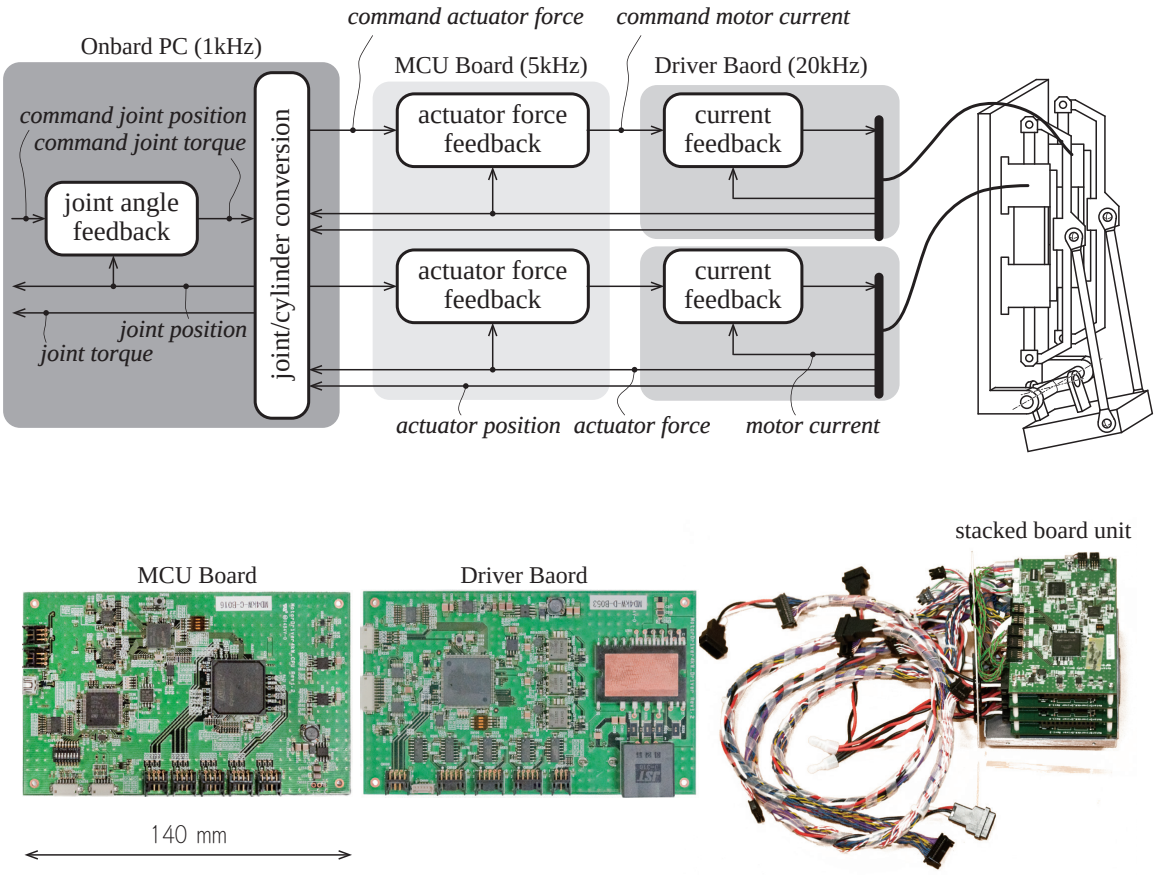

Figure 5.12: Controller architecture of the current-pressure-position triple feedback loop. The joint level position controller is implemented on the onboard PC with 1 kHz frequency. The conversion between cylinder position/force and joint angle/torque is also done on the onboard PC. The joint position controller outputs command joint torque, which is converted to the command cylinder force and sent to the MCU board through the EtherCAT bus. On the MCU board, the actuator level force feedback control is done in 5 kHz frequency and resulted command motor current is sent to the lower level driver board, where the current feedback loop is done in 20 kHz frequency.

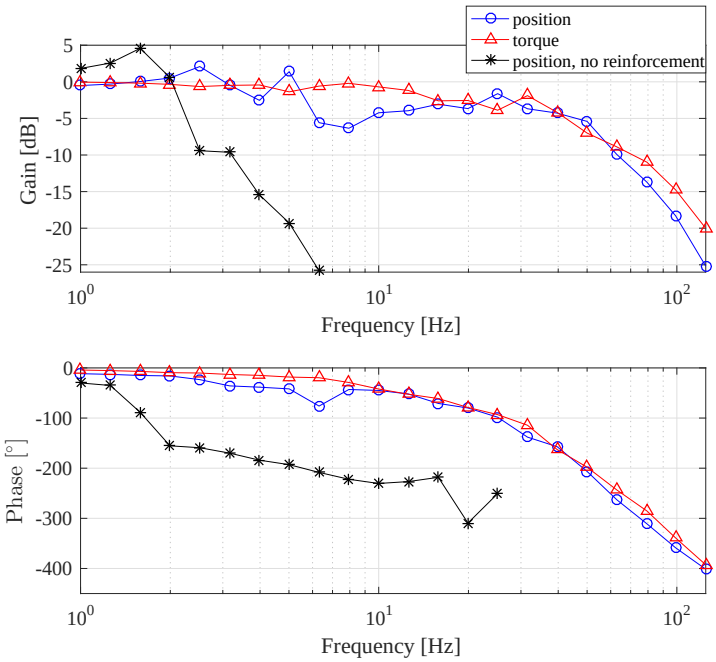

Figure 5.13: Bode plot between command joint position of the hip pitch joint of Hydra and actual position (blue markers), and between command joint torque and actual torque (red markers). The closed-loop control bandwidth in both of the position and torque control was around 30-40 Hz. For the reference, the case without the reinforcement shown in the previous section is overlaid, which proves the effectiveness of the reinforcement.

difference between the experiment shown in Fig.5.11 is that while the former one was done on the testbed with the fixed load and the actuator level response was examined, this experiment shows the joint level behavior on the actual robot joint. As shown in the plot in Fig.5.13, both of the joint position and torque control bandwidth is around 30-40 Hz. While this is lower than the one in Fig.5.11 due to the non-constrained leg motion and elasticity of the link, this is still a high value as a torque-control based robot. For the reference, the case without the reinforcement shown in the previous section is overlaid as black markers. It proves the effectiveness of the reinforcement.

5.6 Conclusion

In this chapter, we showed the evaluation and analysis on the dynamical force control performance of electro-hydrostatic actuators for a humanoid application. The conclusion is as follows:

1. To mechanically improve the response of EHA, reduction of series elasticity between the pump and the load is the key. The series elasticity in the hydraulic system mainly comes from the fluid compressibility. To reduce the total fluid volume, the pump should be placed close to the actuator and the dead volume inside the system should be filled with other material. Our proposed cylinder design with the beam structure is advantageous in this sense since it can reduce the length of the pipeline. High bulk-modulus fluid should be selected, therefore instead of the previous silicone oil, we adopted mineral oil with around two times larger bulk-modulus.

2. Based on the simplified EHA model, we derived that a larger pressure receiving surface results in lower effective series elasticity due to the fluid compressibility. Our approach of maximizing the pressure receiving surface to improve the torque density was also effective in the enhancement of response.

3. We experimentally showed that EHA can be torque controlled with low cost velocity-controlled motor/electronics systems. However, we found that it is weak against pump pulsation. With a current-controlled system, our developed EHA had a pressure control bandwidth of 100 Hz in the fixed piston configuration. This is more than 40% higher value than state-of-the-art high-response

series elastic actuators. The difference between the velocity based and the current based control approach can be interpreted as that while current is a much faster phenomenon than the behavior of pressure change, variation of the pump velocity is a slower phenomenon than the pressure variation therefore the cascaded control framework does not work properly.

4. We derived and experimentally confirmed that the force control bandwidth of an EHA is impaired when the mechanical connection between the piston and load is insufficient. Our reinforcement improved the bandwidth from 22 Hz to 53 Hz, which is 2.4 times larger value.

5. To attain high response control performance of the hydrostatically driven multi-DoF joint with a complex internal state, we introduced a current-pressure-position triple-loop feedback controller. The idea is to distribute the controller in three layers with different framerate processing device and control faster behavior in a faster device. The controller has the current feedback on 20 kHz FPGA, pressure feedback on 5 kHz micro-controller, and joint level position/torque control on 1 kHz onboard PC. It resulted in 30-40 Hz closed-loop joint position and torque control bandwidth on the hip joint of a hydrostatically driven humanoid robot.

Chapter6

Integration of Electro-Hydrostatic Actuators to a Humanoid Robot and its Whole-Body Motion Control Performance Evaluation

6.1 Introduction

In the past decades, there has been a significant improvement in the field of humanoid robots since the early works such as WABOT-1 [92] by Kato et al. Honda made an important breakthrough on the system integration and reliability by P2 [93] [94], P3, and then ASIMO [65]. Forked form P3, the humanoid robotics platform project [95] created the series of HRP2 [96], HRP3 [97], and HRP4 [98]. Recently Kojima et al. developed the humanoid JAXON [99] as the latest version of the series of the high-power robot [67, 100]. Hydraulic robots are regaining the interests after their original dominance were taken place by the motor-gear robots, thanks to the improvement on the servo-valves and emerging needs for mechanically robust robots.

The examples of the hydraulic humanoid robots are CB [17], Petman [15], Atlas [16], and a hydraulic humanoid by Hyon et al. [73].

Most of the humanoid robots have the position based walking controller, even though fundamentally walking or balancing is to control the reaction force. One reason is on their actuator: their large friction makes it difficult to control the joint torque without a complex and costly external torque sensor, while the high precision and high bandwidth joint position control is relatively easy with a simple position sensor. To utilize the joint torque information for the whole-body control, Englsberger et al. [101] developed the torque-controlled humanoid TORO. TALOS is a recent commercially available torque-controlled humanoid [102]. Nagamatsu et al. [103] proposed the joint torque estimation without additional torque sensors. While the active joint compliance with the sensor feedback has a considerable performance, it is still lack of impact resistance since the intrinsically stiff joints can realize low impedance in only lower frequency than their torque control bandwidth. To realize intrinsically compliant actuation, an increasing number of humanoids are driven by series elastic actuators. The examples are the cCub by Tsagarakis et al. [104] which is the series elastic version of the iCub [105], the series of COMAN [33] and Walk-man [34], and the series of THOR [35] and ESCHER [106] by Knabe et al. The difficulty with the elastic actuators, though, is the lack of position/torque control bandwidth, which can be critical for dynamic motions.

Electro-hydrostatic actuators(EHA) have the possibility to realize both of the intrinsically compliant actuation and high closed-loop control bandwidth. In the previous chapters, we proposed the approaches to realize small size but high torque density

EHAs for robot applications. In this chapter, we detail the integration of our developed EHA into the whole-body actuation system of the fully EHA driven humanoid robot "Hydra". The kinematic design approach, electronics and control systems, and preliminary evaluation results are shown.

6.2 Joint Actuation by Electro-Hydrostatic Actuators

6.2.1 Parallel Joint Driving Mechanism with Slider Cranks

In this subsection we describe the implementation of the joint driving mechanism for Hydra. As described in the previous chapters, linear EHAs are more suitable to drive the robot joints in the sense of no internal leakage, light weight and slim external shape. Another advantage of joints driven by linear actuators is the separation of constraint force and driving force. A free joint holds all direction of the constraint force and is only movable in the direction of actuation. The actuator only exerts force in the driving direction and do not support any constraint and structure force. This separation makes it easier for a robot to keep its shape even when the actuators are removed for maintenance. This feature is extraordinary important for a robot which need frequent maintenance.

To convert linear motions of the cylinders to revolute one of the joints, a parallel link mechanism is needed. A simple lever arm is the simplest solution. Its drawback is the limited range of motion and the large variation of the torque/force ratio, since when the joint moves the moment arm drastically changes. Four-bar mechanism enable this

transformation with a larger range of motion and smooth torque profile, which means the relation between joint torque and cylinder force are less dependent on the joint angle. The drawback is its bulkier size and large number of interconnections, which is a source of backlash and lack of stiffness. In the case of humanoid robots, we assume the simple lever arm structure is more suitable, since the variation of torque profile, or the variation of reduction ratio can be properly designed to be even advantageous to fit the requirements of variable reduction ratio for a legged robot ; the limited range of motion is still enough to exceed a normal human; and in a complex and closely packed system such as a humanoid robot a simple mechanism is especially important.

As the case of human, humanoid robots also have many orthogonal crossed multi-DOF joints, such as wrist, shoulder, waist, hip and ankle joints. We implement these joints as orthogonal universal joints, which are driven by two linear EHAs. Fig.6.1 express the idea. When the two cylinders move in the same direction, the first joint is driven. When the two cylinders move in the opposite direction, the second joint is driven. The advantage of this implementation is that we can use the force of two cylinders to drive one joint, in addition to the compact actuator arrangement. The drawback is the limited range of motion and difficulty of the conversion from the piston position to the joint position, which is described in the following paragraph.

The joint angle of the joints driven by linear EHA is calculated from the piston position, which is obtained by the linear encoder mounted on the cylinder. Here, we discuss a quasi-static interconversion between the joint angles and the cylinder positions, joint torque and cylinder force, and rod force to cylinder force, since the inertia of the connecting rod and piston rod is much smaller than the rest of the

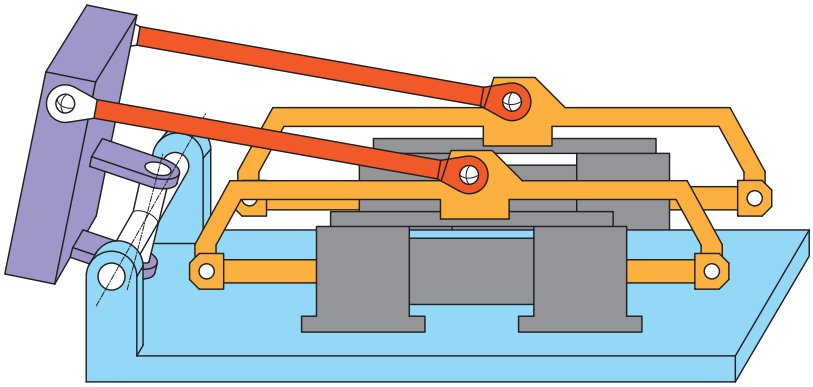

Figure 6.1: Schematic of a two DOF universal joint driven by two linear EHAs.

system to be ignored. Fig.6.2 shows the definition of parameters. This is a simplified schematic of the joint described in Fig.6.1. The orthogonal universal joint is aligned on the origin of the coordinate. The pitch joint is coaxed with y axis and the roll joint is coaxed with x. The intermediate universal joint link is connected to the parent link through the pitch joint and it is connected with the child link through the roll joint. The red lines represent the connecting rods with the length of l. $\boldsymbol{P}_i (i = 1, 2)$ is the spherical joint connecting the child link and the connecting rod. The yellow vertical lines represent the linear guides of the cylinder, which are fixed on the parent link. $\boldsymbol{z}_i$ is the other end of the connecting rod. They are also spherical joints. Due to the linear sliders, they are constrained on the yellow lines and only their z component is changeable. α_i is the angle between the connecting rod and the linear guide. Notice that the plane including both the connecting rod and the linear guide does not necessarily parallel to any other planes such as xz or yz plane. We define the joint angle vector $\boldsymbol{\theta} = [\theta_p, \theta_r]^T$. The initial position $\boldsymbol{p}_{i0} = [p_{i0x}, p_{i0y}, p_{i0z}]^T$ is the position of $\boldsymbol{p}_i$ when $\boldsymbol{\theta} = [0, 0]^T$, which is constant depend on the mechanical geometry. We set the

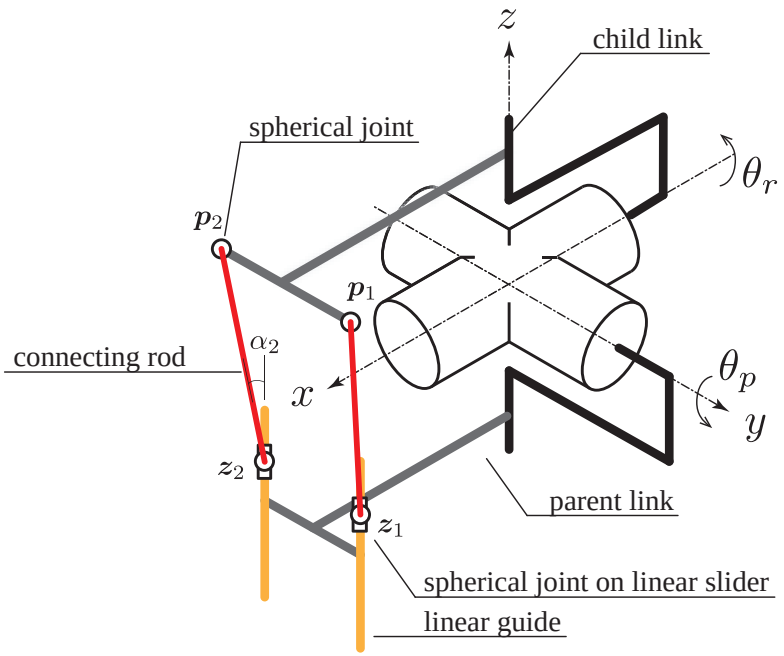

Figure 6.2: Parameter definition of the two DOF universal joint driven by two linear EHAs.

positions of pistons as $\boldsymbol{z}_i = [z_{i0x}, z_{i0y}, z_{iz}]^T$, where z_{i0x}, z_{i0y} are also constants decided by the mechanical geometry. We define the cylinder position vector as $\boldsymbol{z} = [z_{1z}, z_{2z}]^T$.

When $\boldsymbol{\theta} = [\theta_p, \theta_r]^T$, the position $\boldsymbol{p}_i$ can be written as follows:

$$\boldsymbol{p}_i = R_y(\theta_p) R_x(\theta_r) \boldsymbol{p}_{i0} \tag{6.1}$$

where $R_y(\theta_p)$ represents a rotation matrix around y axis for an angle of θ_p and $R_x(\theta_r)$ represents a rotation matrix around x axis for an angle of θ_r. With the constraint that the distance between $\boldsymbol{p}_i$ and $\boldsymbol{z}_i$ is the constant l

$$\|\boldsymbol{p}_i - \boldsymbol{z}_i\| = l \tag{6.2}$$

we can get z_{iz} described by $\boldsymbol{\theta}$.

The forward conversion, which is to convert $\boldsymbol{z}$ to $\boldsymbol{\theta}$, is hard to be expressed in a closed form. As the case of inverse kinematics, though, we can solve it iteratively by

expressing the jacobian matrix $G(\boldsymbol{\theta}) = \partial \boldsymbol{z}/\partial \boldsymbol{\theta}$. In the range of motion of Hydra's two DOF joints, there is no singular point in the mechanism. We can calculate the differential relationship between $\boldsymbol{\theta}$ and $\boldsymbol{z}$ as follows:

$$\dot{\boldsymbol{\theta}} = G(\boldsymbol{\theta})^{-1}\dot{\boldsymbol{z}} \tag{6.3}$$

With the jacobian matrix $G(\boldsymbol{\theta})$, we can convert from the cylinder force $\boldsymbol{f} = [f_1, f_2]^T$ to the joint torque $\boldsymbol{\tau} = [\tau_p, \tau_r]^T$ as the same case of serial link robot as follows:

$$\boldsymbol{\tau} = G(\boldsymbol{\theta})^T \boldsymbol{f} \tag{6.4}$$

Unlike traditional joints driven by linear actuators, in the case of Hydra the connecting rod and the piston rod is not in coaxes. The force measured by the strain gauge, therefore, is different from the piston force since it also contains the constraint force of the linear guide and slider, which is perpendicular to the direction of the piston rod. Once we calculate the position of $\boldsymbol{p}_i$ and $\boldsymbol{z}_i$, we can get $\cos\alpha_i$ from their z direction distance and the connecting rod length l, where α_i denotes the angle between the connecting rod and the piston rod. If we denote the force on the connecting rod as f_i^{strain}, we can write them as follows:

$$f_i = \cos\alpha_i \, f_i^{strain} \tag{6.5}$$

$$= \frac{p_{iz} - z_{iz}}{l} f_i^{strain} \tag{6.6}$$

6.2.2 Modular Designed Kinematic Structure of the Humanoid Hydra

In this subsection, we describe the implementation of each link and joint of Hydra with their arrangement in the whole body. Fig.6.3 shows a schematic of the whole

body joint arrangement. The basic structure of each link is a box-shaped frame composed of uniform thickness aluminum plates. The actuators are basically mounted on the outside of the frame for the ease of maintenance.

The body has two DoF on the waist: pitch and roll. They have a structure of the universal joint driven by two linear EHAs, which is described in the previous subsection. The difference from the other joints is that the cylinders are tilted to save the vertical length. Fig.6.4 shows a CAD model of the waist joint, with the torso link and the waist link. The thin purple colored structure is the frame of the torso link. It is composed of simple shaped aluminum plates. The pink colored cylinders and pumps are those to drive the waist joint. With the maximum piston force of 1500 N, the two actuators can generate 94 Nm joint torque in the pitch direction and 147 Nm torque in the roll direction, with a -20°+60° and ± 22.5° range of motion respectively. The waist link structure is shown in blue color, which is basically a single piece machined from an aluminum block. This costly design is due to the high stiffness requirement to enable walking locomotion. An IMU, which is shown in green color, is packed inside the box-shaped frame of the torso link. A backpack containing electric and cooling components is also attached on the link.

The base link of Hydra is set as the waist link. It also contains two vane motor type EHAs to drive the foot, which are shown in orange color in the Fig.6.4. The weight of the link is 5.03 kg. The torso link consists of the frame in purple, the two linear EHAs in pink, the backpack in thin gray and also two vane motor type EHAs to drive the arm, which are shown in yellow color. As the total, the link has the heaviest weight of 16.8 kg. The specification of the joints and links including those

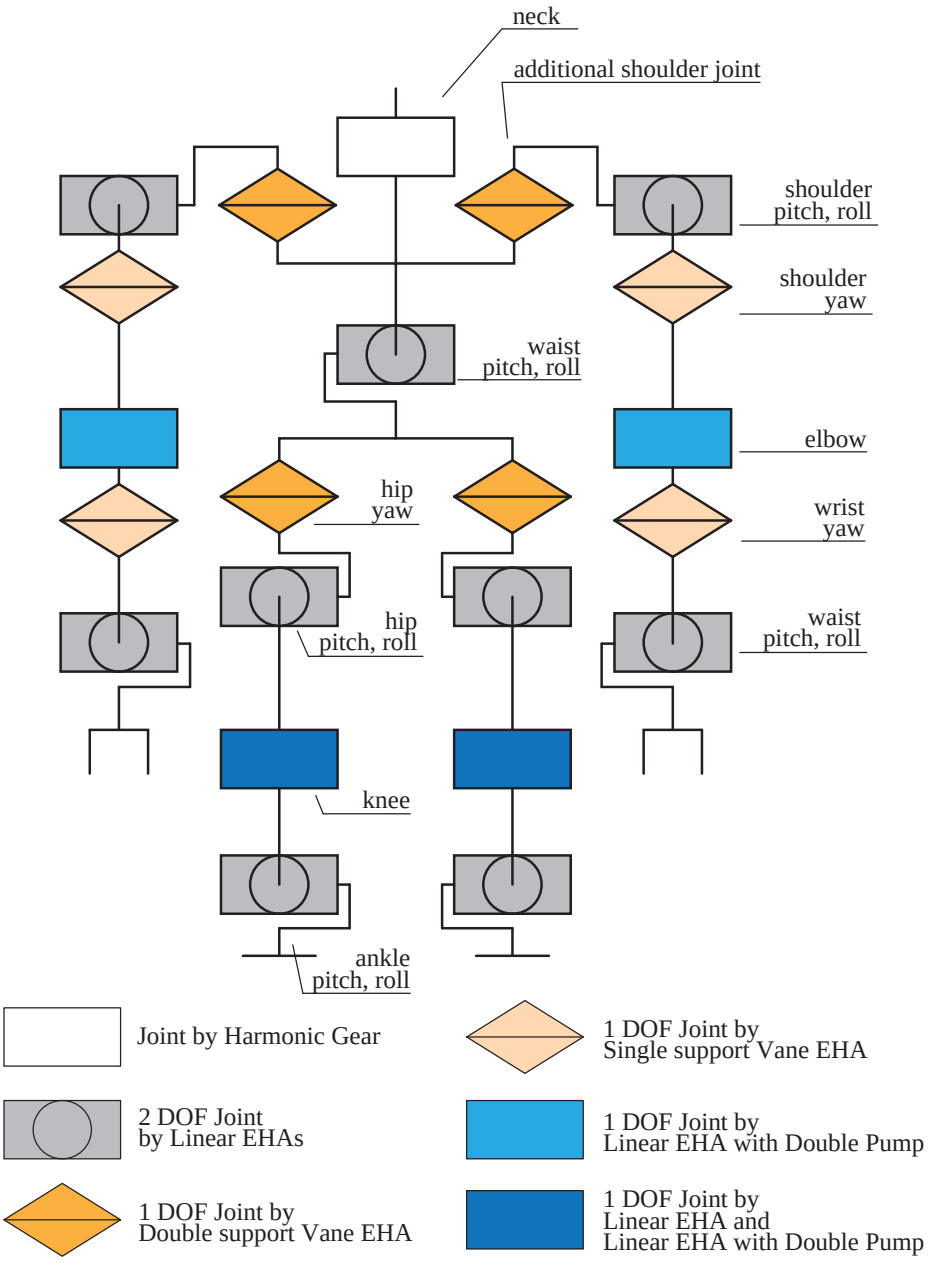

Figure 6.3: Joint arrangement of the humanoid robot Hydra.

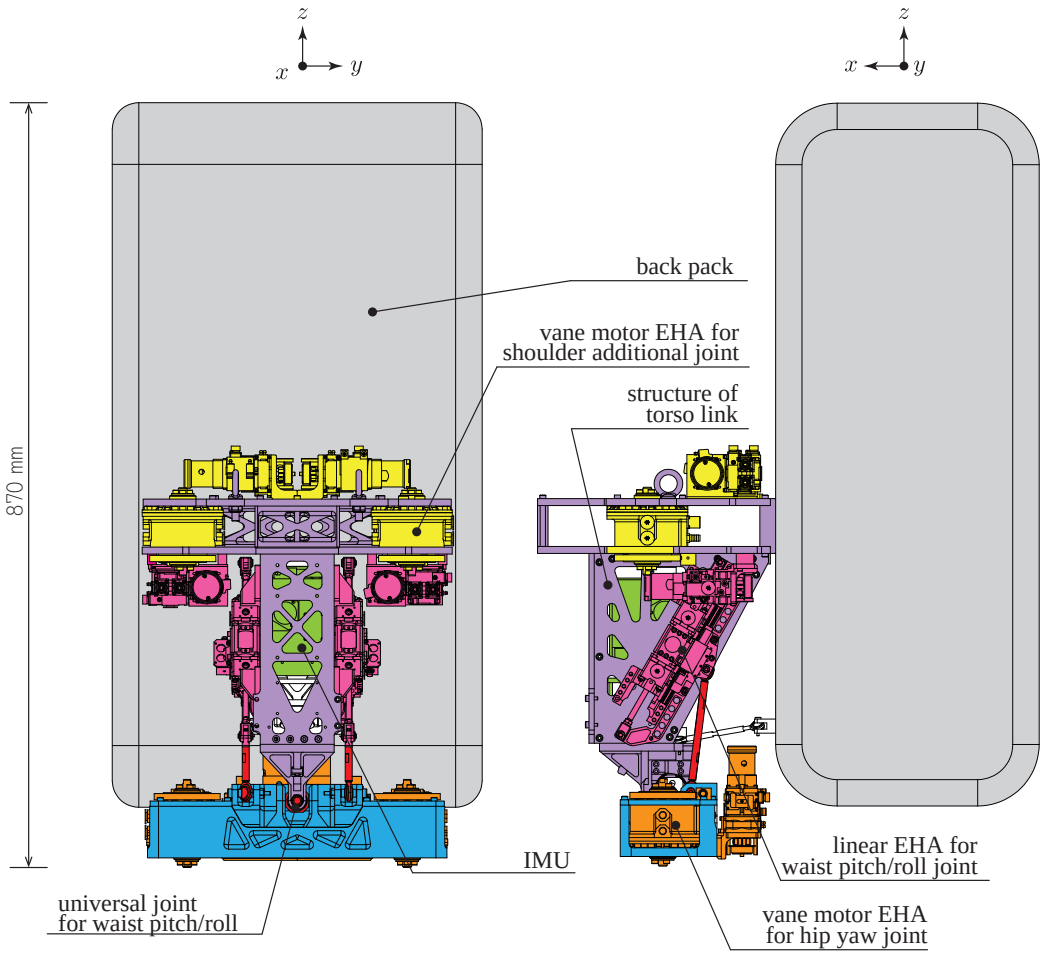

Figure 6.4: CAD model of the body of Hydra. Thin grey color shows backpack, yellow color shows vane motor EHA for the shoulder additional joint, purple color shows torso link structure, pink color shows linear EHA for the waist pitch and roll joint, blue color shows the waist link frame and the orange color shows vane motor EHA for hip yaw joint.

explained in the following paragraphs are shown in Table 6.1, Table 6.2.

Each leg of Hydra has six DOF, where the hip joint has three for yaw, pitch and roll; the knee joint has one for pitch; and the ankle has two for roll and pitch. The joint closest to the body is the yaw of the hip, which is driven by a double support type vane motor EHA. It is shown in orange color in the Fig.6.4. The joint has the maximum torque of 60 Nm and $\pm 60^\circ$ range of motion. The pitch and roll joint of the hip takes the universal joint structure driven by two linear EHAs. When the two actuators exert 1500 N force, the joint has 80 Nm torque in the pitch direction and 135 Nm torque in the roll direction, with a $-13+105^\circ$ and $\pm 22.5^\circ$ range of motion respectively. Fig.6.5 shows a CAD model of the thing link. The thigh link structure is shown in purple color. As same with the other links, it is composed with simple aluminum plates. The green link on the top is the intermediate link connecting the universal joint to the output of the hip yaw vane motor. The two pink linear EHA is those to drive the hip universal joint. On the lower side, the blue colored link is the one connected to the shank link, rotating against the thigh link around the red knee axis. Linear EHAs driving the knee joint is packed inside the box-shaped thigh link.

To improve the modularity, we use the same type of cylinder and pump for the whole body. For the knee joint, however, one cylinder driven by one pump is not enough to support the body weight. Taking account of the limitation of space and weight, we assign two cylinders and three pumps for the knee joint. One of them is the normal linear EHA: one cylinder driven by one pump. For the other, we call it "stage pump EHA", where one cylinder is driven by two serially connected pump. With this configuration, we expect three times larger knee torque compared with the

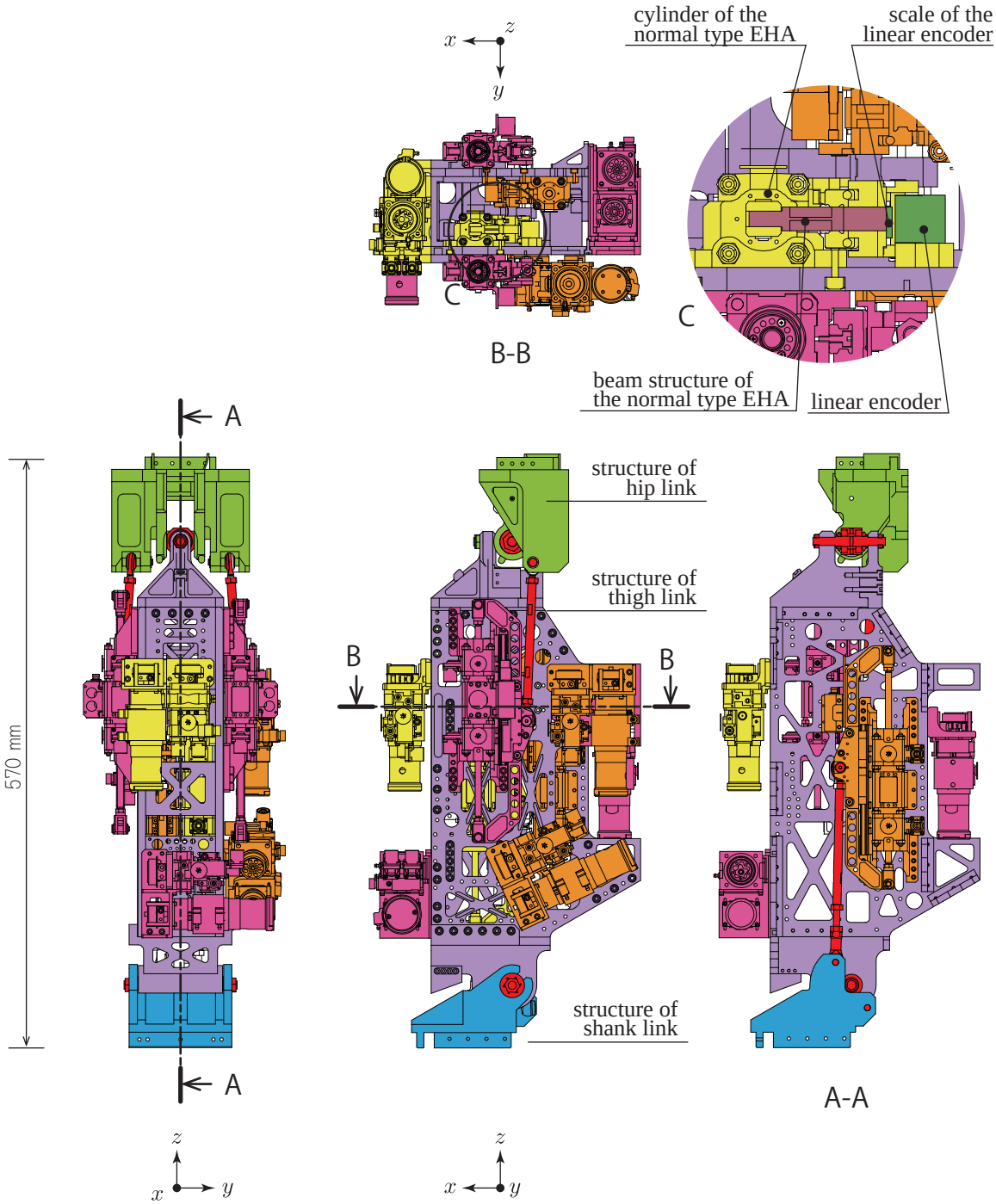

Figure 6.5: CAD model of the left thigh link. Green color shows the intermediate hip link connecting the output flange of the hip yaw vane motor. Purple color shows the link structure of the thigh. Hip joint pitch/roll universal joint is driven by pink colored linear EHAs. Shank link in blue color is driven by one standard linear EHA in yellow and one stage pump EHA in orange.

case of a standard linear EHA. In Fig.6.5, the yellow colored EHA is the standard one, while the orange colored one is the stage pump EHA. When the standard EHA exerts 1500 N and the stage pump EHA exerts 3000 N force, the joint has 120 Nm maximum torque with -10+120° range of motion.

The thigh link contains the frame, two linear EHAs to drive the hip joint, and one standard plus one stage pump EHA to drive the knee. As the total, the link weights 8.50 kg. While the weight of the intermediate link of the universal joints are small and negligible, the one between the universal joint and the output flange of the yaw direction vane motor need to be considered. The link, which is shown in green color, weights 1.59 kg.

A CAD model of the shank link and foot is shown in Fig.6.6. The link structure is shown in purple, the actuators are shown in orange, and the foot is shown in blue color. A six-axis force-torque sensor is attached on the foot to measure the contact force redundantly, in addition to joint torque measurement by pressure sensors and strain gauges on the actuators. The two linear EHAs drive the roll and pitch direction of the universal joint, with ±27° and -44+34° range of motion. The 1500 N piston force can generate 80 Nm and 135 Nm joint torque respectively.

The arm has eight DOF each. This is to increase the working range in front of the body, where both of the arms can cooperate, and also to cover the limited range of motion of the two DOF universal joint. In addition to a three DOF orthogonal shoulder joint, which is by a combination of the two DOF universal joint and vane motor EHA, a joint which plays a similar role of the human's acromioclavicular joint is inserted between the shoulder link and torso. A similar approach was taken in the

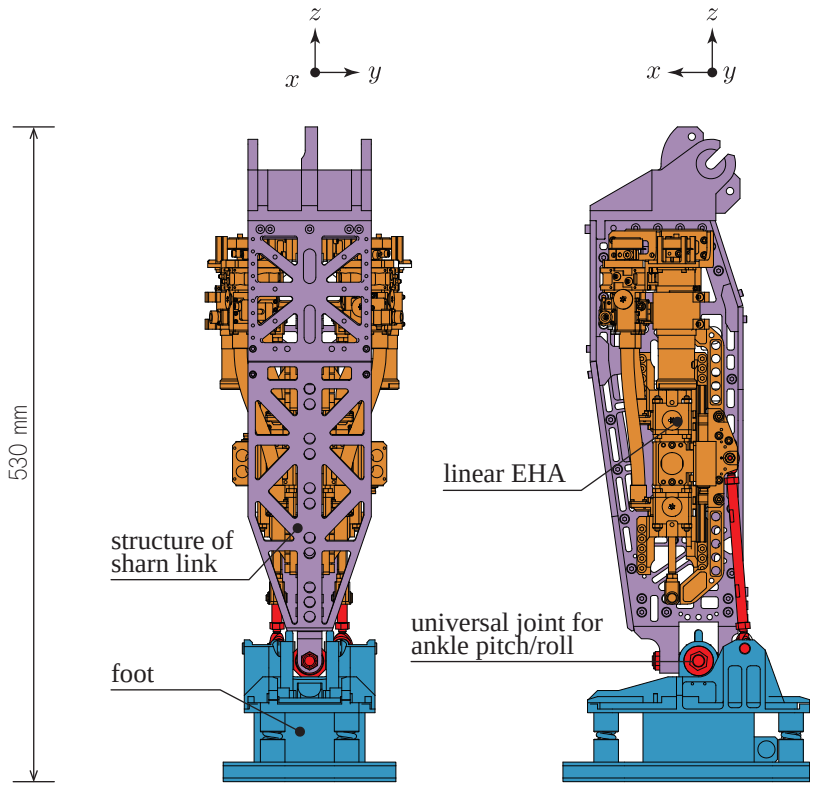

Figure 6.6: CAD model of the thigh link. Purple color shows the structure of shank link. Orange color linear EHAs drive blue colored fool link.

case of H6 [107]. The additional joint is driven by a vane motor type EHA, which is shown in yellow color in the Fig.6.4. The double support type vane motor generates 60 Nm maximum joint torque, with -30+90° range of motion (in the case of the right shoulder. For the left side, it is opposite. The following discussion is all for the right side.) A CAD model of the shoulder link and shoulder joint is shown in Fig.6.7. In the figure, the shoulder link is shown in purple, the liner EHA is shown in orange, the universal joint for pitch and roll is shown in red, the vane motor EHA for yaw is shown in yellow, and the intermediate link connecting the vane motor EHA and the universal joint is shown in blue color. The two linear EHAs drives the pitch direction

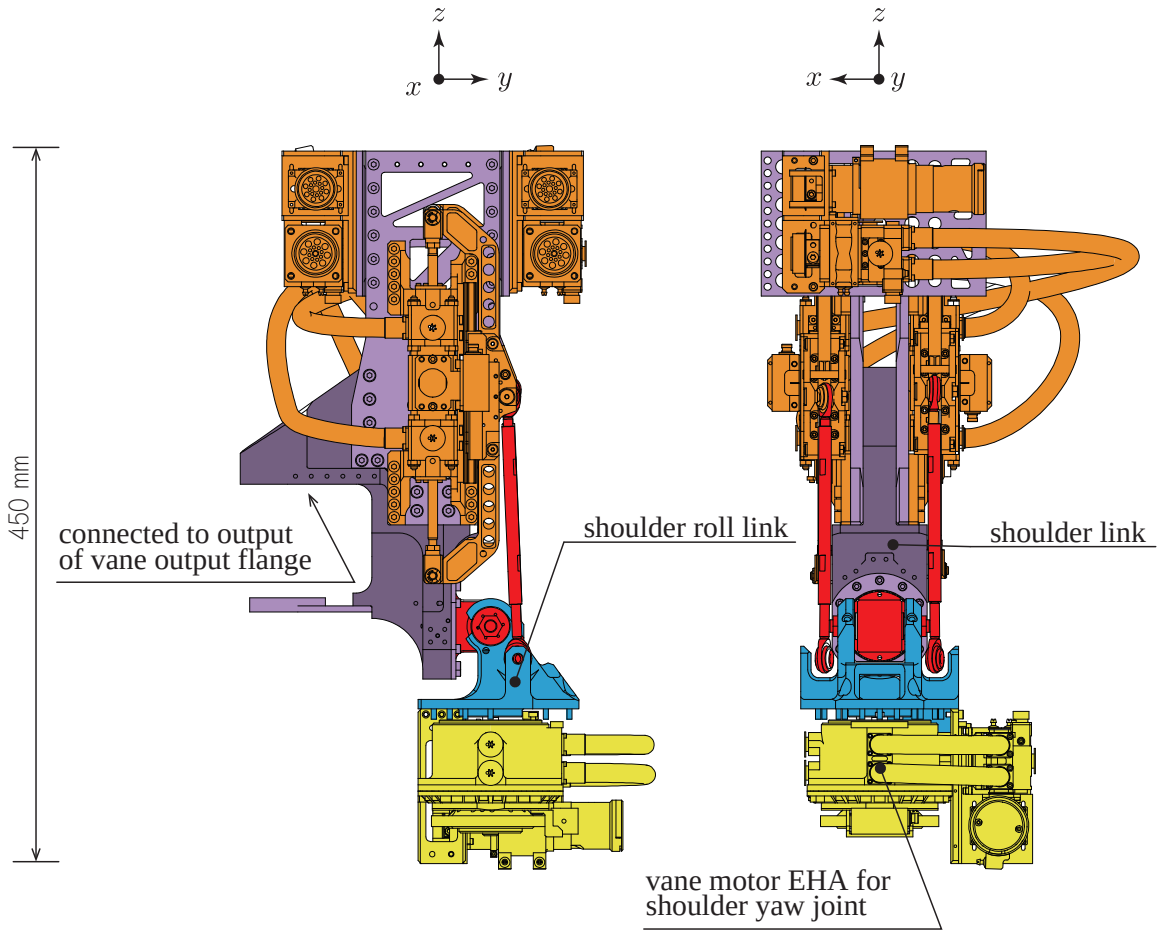

Figure 6.7: CAD model of the left shoulder link. Structure of shoulder link is shown in purple. The shoulder link is fixed on the output flange of the additional joint, which is not shown in this figure. Orange colored linear EHAs drive blue intermediate shoulder roll link. The link rotates around the red colored universal joint to pitch/roll direction. Yellow colored vane motor drives yaw direction of shoulder.

with ±30° range of motion and roll direction with -117.5+17.5° range of motion. The 1500 N piston force can generate 83 Nm and 80 Nm joint torque respectively. The yaw direction has -30+90° range of motion and 40 Nm torque with the single support type vane motor EHA.

The shoulder link has an overhang structure from its supporting area, which is the output flange of the additional shoulder joint vane motor. To attain high stiffness, the shoulder link is machined from a single piece aluminum block, with plate-shaped attachments for the fixture of the linear EHAs. In Fig.6.7, the single piece link is shown in thicker purple color compared to the other components. The shoulder link, with the frame in purple and two linear EHAs, weights 4.59 kg in total. The intermediate link, consisting of the blue structure and the yellow vane motor EHA weights 1.88 kg.

The elbow has one DOF driven by one stage pump EHA. Fig.6.8 shows the CAD model of the upper arm link with the elbow joint. In the figure, the link is shown in purple, the actuator is shown in orange, and the link connected to the lower arm is shown in blue color. The joint has -117+9° range of motion and 82.5 Nm maximum torque. The upper arm link has a weight of 6.16 kg. The elbow intermediate link in the blue color weights 0.29 kg. This light weight is because the following vane motor EHA is fixed on the child link side due to the space problem.

The wrist joint has three DOF. The lower arm link has a single supported vane motor type EHA between the intermediate link to the elbow joint to drive the yaw direction. It has ±60° range of motion and 40 Nm torque. On the other side of the link, it has a two DOF universal joint for roll and pitch direction. The roll direction

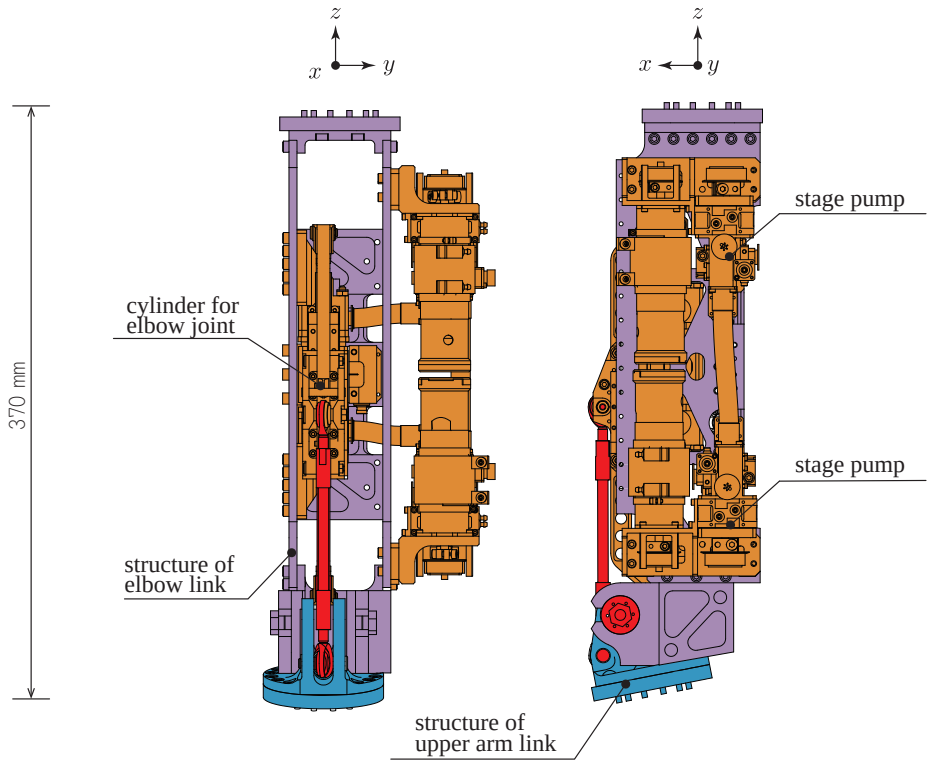

Figure 6.8: CAD model of the left upper arm link. The link is attached on the output flange of the shoulder yaw vane motor. Orange colored stage pump EHA fixed on the purple link structure drives blue colored intermediate elbow link.

has ±29° range of motion while the pitch direction has -66+85° range of motion. The maximum joint torque is 142 Nm and 77 Nm respectively. The axes of the three DOF is orthogonal to each other and crossing at a single point. The CAD model of the lower arm is shown in Fig.6.9. The structure of the lower arm has a simple box-shape, which is shown in purple color. The yellow colored vane motor EHA drive the yaw direction. The universal joint in red color is driven by linear EHAs in orange color. The hand, which is in blue color, is a tendon-driven under-actuated hand with five DOF. The hand is driven by the miniature cluster tie rod EHA which is described in 3.5. The cluster EHA, which is shown in thin green color, is packed inside the box

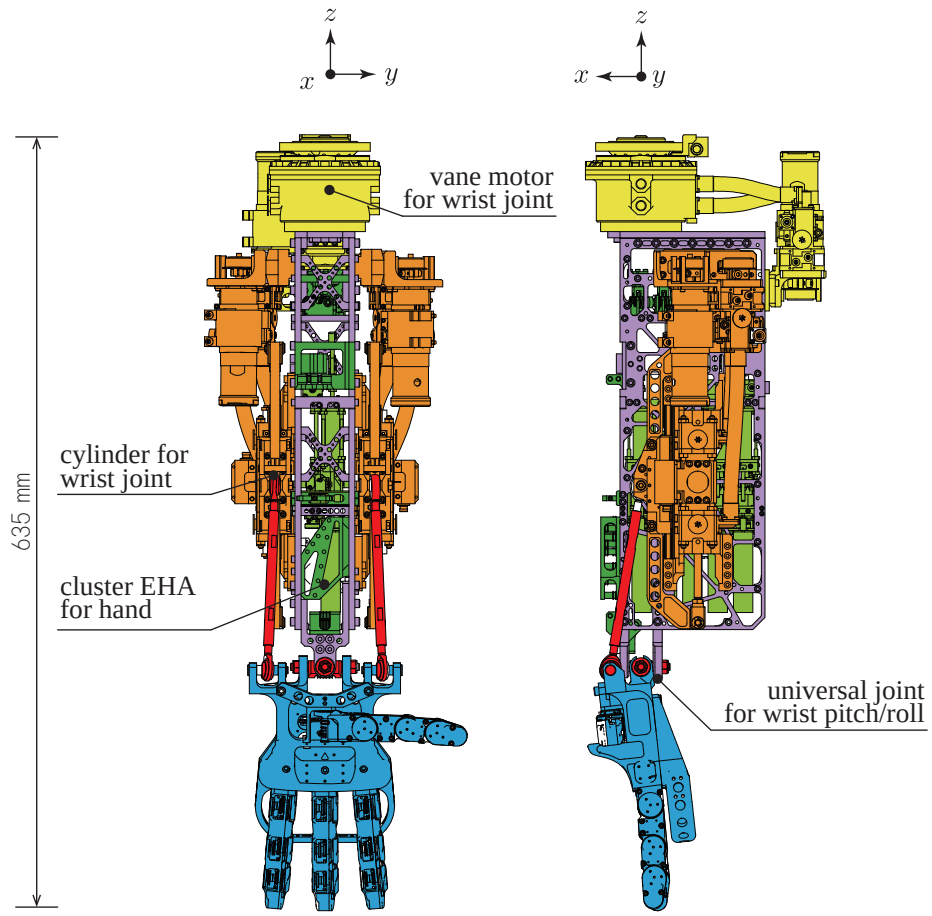

Figure 6.9: CAD model of the left lower arm link with hand. Yellow colored vane motor EHA is to drive yaw joint of the wrist. Its output flange is attached on the elbow intermediate link, which is not shown here. Orange colored linear EHAs fixed on the purple link structure drive the blue colored hand. Green colored cluster EHA to tendon drive the hand is packed inside the arm link structure. Thin green color shows the actuator itself while thick green shows tendon guiding structures.

Table 6.1: Mechanical specification of Hydra (lower body). The link name is of the link whose parent joint has the ID and name.

ID	Joint Name	Link Name	Range of Motion [°]	Joint Torque [Nm]	Link Weight [kg]
0	-	waist	-	-	5.03
1	r_hip_y[1]	r_hip	±60	60	1.59
2	r_hip_p	-	-13+105	80	-
3	r_hip_r	r_thigh	±22.5	135	8.50
4	r_knee	r_ankle	-10+120	120	4.67
5	r_ankle_r	-	±27	80	-
6	r_ankle_p	r_foot	-44+34	117	2.11
7	l_hip_y	l_hip	±60	60	1.59
8	l_hip_p	-	-13+105	80	-
9	l_hip_r	l_thigh	±22.5	135	8.50
10	l_knee	l_ankle	-10+120	120	4.67
11	l_ankle_r	-	±27	80	-
12	l_ankle_p	l_foot	-44+34	117	2.11
13	waist_p	-	-20+60	94	-
14	waist_r	torso	±22.5	147	16.8
15	neck_p	head	-	-	-

structure of the link. The thick green colored parts are tendon guiding structures. A detailed discussion on the hand is done in the following subsection. The lower arm link, with one vane type EHA, two linear EHA and one cluster EHA for the hand weights 6.16 kg. The hand link weights 0.5 kg including fingers.

A picture of the assembled whole body Hydra is shown in Fig.6.10. The total body weight is and the height is around 180 cm. The arm is longer than a human. This is advantageous in taking objects from the ground or use the arms to help its locomotion as monkeys do. Table 6.1, Table 6.1 summarize the mechanical specification of Hydra, where the former table is of the lower body and the latter table is of the upper body.

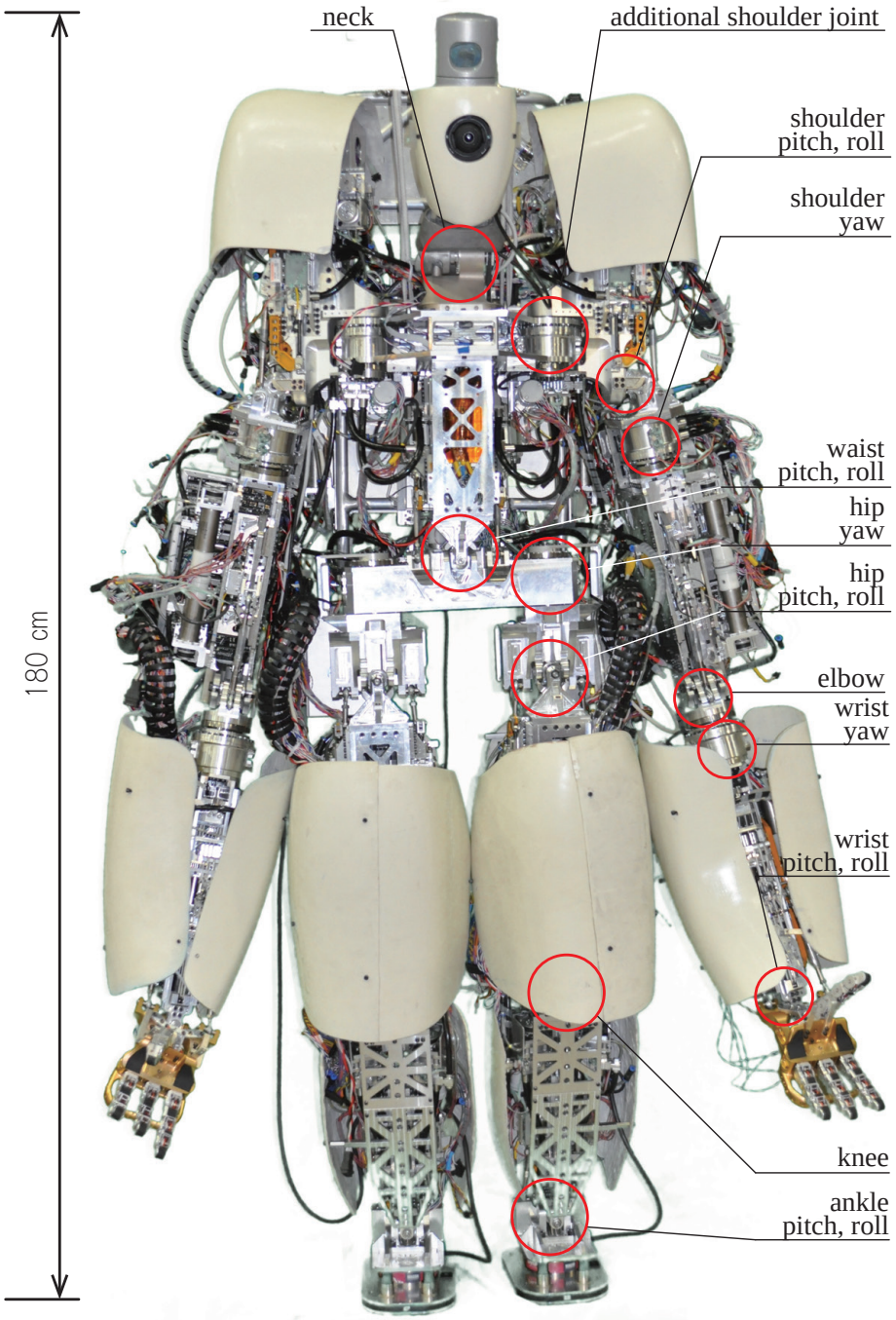

Figure 6.10: Whole body picture of the humanoid robot Hydra. The outer cover (in white color) is designed by Professor Satoru Kitagou, Tokyo University of the Arts.

6.2.3 Underactuated Four-fingered Hand with Five EHA in Cluster

Anthropomorphic hands enable robots to use the same tools and handle the same environments that are designed to maximize the efficiency of a human worker. The problem is that the more the fingers, joints, and DoF a hand has, the more fragile it tends to be. Unlike a hand on a testbed that is designed and used for pure manipulation researches, hands for a humanoid robot need to be mechanically robust enough to avoid damage due to unexpected contact with the environment, falling down of the robot, or a whole body locomotion utilizing grasping of the environment with the hand. Poor robustness of mechanical transmissions, especially those of miniature ones for hands, led us to develop miniature EHAs for hand use. While discussions on the actuator was done in the 3.5, the design of the hand itself is described in this subsection.

The hand has four fingers, which correspond to human's thumb, index, middle and ring finger. To improve modularity, all of the fingers, for both left hand and right hand, have the same structure. In power grasps of a human, the thumb, or especially thenar part exerts a large force and play an important role. In our approach, instead

---

[1]abbreviation of "right hip yaw"

[2]abbreviation of "right shoulder additional joint"

[3]abbreviation of "adduction/abduction"

[4]Three joints underactuated by one active tendon are treated as a single joint here. The values shown in the table is the one that the actuator can control: The equally distributed finger joint torque governed by tendon tension and the summation of the three joints' angle governed by the tendon position.

[5]abbreviation of "flexion/extension"

Table 6.2: Mechanical specification of Hydra (upper body).

ID	Joint Name	Link Name	Range of Motion [°]	Joint Torque [Nm]	Link Weight [kg]
16	r_shoulder_a[2]	r_shoulder	-30+90	60	4.59
17	r_shoulder_p	-	±30	83	-
18	r_shoulder_r	r_shoulder_r	-117.5+17.5	80	1.88
19	r_shoulder_y	r_upperarm	-30+90	40	6.16
20	r_elbow	r_elbow	-117+9	82.5	0.291
21	r_wrist_y	r_lowerarm	±60	40	6.16
22	r_wrist_r	-	±29.1	142.5	-
23	r_wrist_p	r_hand	-66+85	77	0.489
24	l_shoulder_a	l_shoulder	-90+30	60	4.59
25	l_shoulder_p	-	±30	83	-
26	l_shoulder_r	l_shoulder_r	-17.5+117.5	40	1.88
27	l_shoulder_y	l_upperarm	-90+30	40	6.16
28	l_elbow	l_elbow	-117+9	82.5	0.291
29	l_wrist_y	l_lowerarm	±60	40	6.16
30	l_wrist_r	-	±29.1	142.5	-
31	l_wrist_p	l_hand	-66+85	77	0.489
32	r_thumb_AA[3]	-	-0+110	1.5	-
33[4]	r_thumb_FE[5]	-	-0+270	1.5	-
34	r_finger_idx	-	-270+0	1.5	-
35	r_finger_mid	-	-270+0	1.5	-
36	r_finger_rng	-	-270+0	1.5	-
37	l_thumb_AA	-	-110+0	1.5	-
38	l_thumb_FE	-	-0+270	1.5	-
39	l_finger_idx	-	-270+0	1.5	-
40	l_finger_mid	-	-270+0	1.5	-
41	l_finger_rng	-	-270+0	1.5	-

of creating a special forceful thumb, we merge the thenar to the palm as a single piece. In other words, we omit the DoF for thenar and fixed it in the power grasp configuration. As the tradeoff, the hand is not able to be totally opened as a flat surface, therefore it is impossible to stably support the body weight by the palm in the same way that a human does. To overcome this drawback, we introduce a protector on the back of the hand. The protector is designed to guard the fingers when the hand is closed, with enough strength to support the whole body weight of the robot. The protector is easy to be changed to attach a camera, light or any other tools without disassembling or removing the hand form the arm.

The finger is based on the work by Treratanakulwong et al. [108]. It has four joints: DIP, PIP, MP1, and MP2. The axis of DIP, PIP and MP1 are parallel and they are underactuated by a single tendon. The MP2 joint has an axis orthogonal to the others. When the finger is assigned as the thumb, its MP2 joint is arranged to the direction of opposition/reposition and it is driven by another active tendon. When the finger is for the index, middle or ring finger the MP2 joint works as adduction/abduction. The adduction/abduction of the three fingers is not actively driven, but still supported by ball bearings. A set of pressurized rubber blocks holds those joints to absorb external impact force on this direction. Flexion/extension of the four fingers and adduction/abduction of the thumb consist five active DoF, whose five tendons to through the wrist and driven by the five DoF cluster EHA placed inside the lower arm structure.

While underactuation of a robot finger enable the finger to passively adapt the shape of the target object therefore is advantageous in power grasping, it lacks the

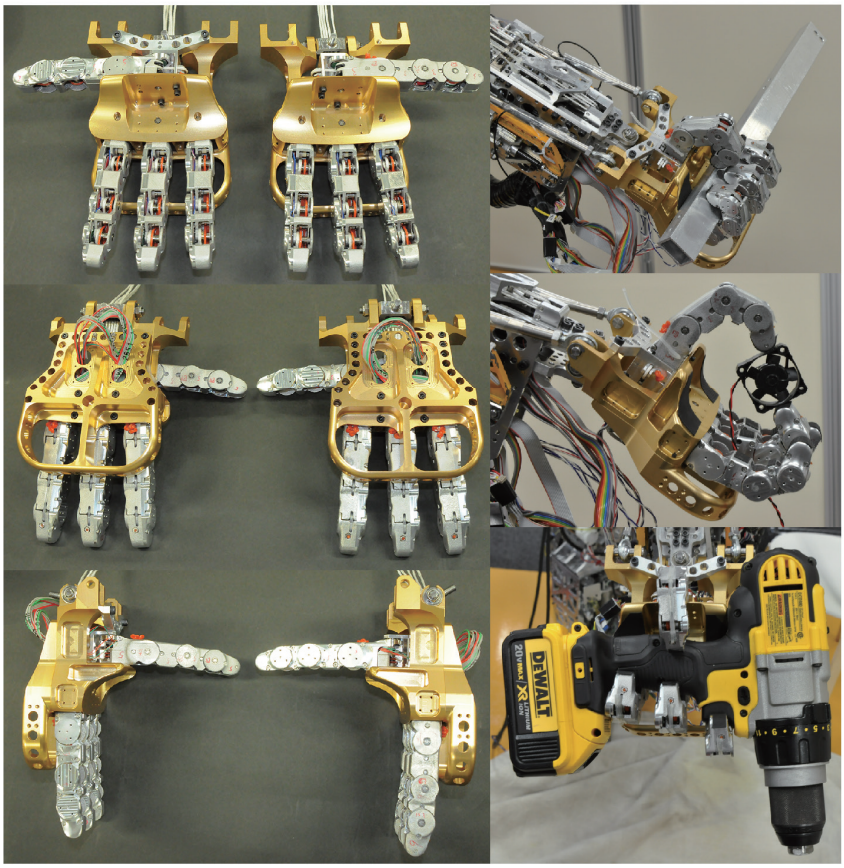

Figure 6.11: Picture of the developed four-fingered hand. The thumb has two DoF and each of the index, middle, and ring finger has one underactuated DoF.

ability in precise manipulation such as pinching. To enable pinching of small objects, elastic coupling tendons are introduced in the finger. All joints of the finger have the same pulley with 10 mm diameter, converting the 300 N actuator force to 1.5 Nm joint torque. The links of the finger take a monocoque structure, which is manufactured by 3D printing with aluminum alloy. Each joint and pulley is supported by ball bearings to reduce the friction. The tendon is Dyneema strand with 1.5 mm diameter, which has high strength, low friction and low bending resistance. Each joint has a magnetic rotary encoder to obtain the joint angle. The joint torque is measured by tension sensor mounted on the actuator. Fig.6.11 shows pictures of the developed hand.

To confirm the ability of the hand, we did an experiment of grasping an electric power drill. The hand could stably hold the handle of the drill with the thumb, middle and ring finger, while the index finger could control the trigger of the drill. Fig.6.12 shows the time transition of the joint angles of each finger during the experiment. The vertical axis shows the joint angles where 0 means fully extended condition and 90 ° means fully closed. In spite of the successful demonstration, we can see some factors to improve. In the graphs of the thumb, middle and ring finger, which were to tightly hold the handle, we can see a fast increase of the DIP angles and drop of PIP angles. The angle decrease of the PIP joint may result in object ejection, which is a common problem of underactuated hands. The reason for this is the same pulley diameter of the joints, even though the effective moment arm of the external force is larger for the PIP joint compared to the one of DIP joint. An optimization of the pulley diameter will improve the grasping quality.

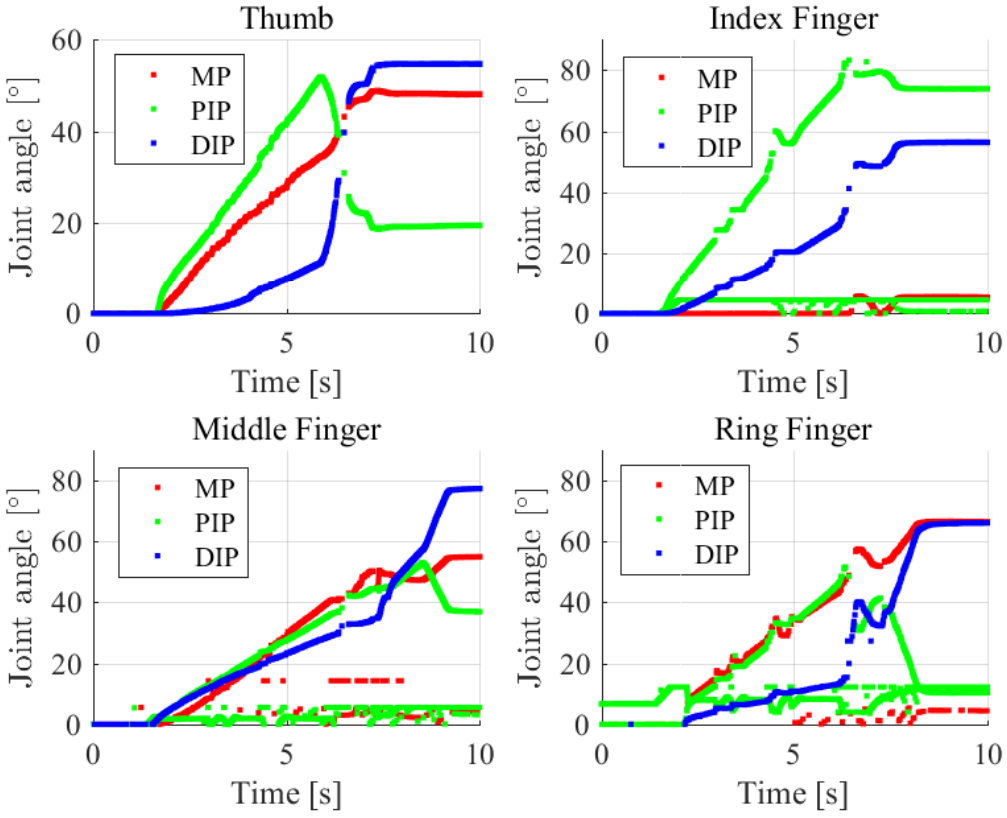

Figure 6.12: Time transition of the finger joint angles during the drill grasping experiment. Four graphs correspond to four fingers and the three lines represents the three joints on each finger.

6.3 Distributed Multilayered System of the Humanoid Hydra

6.3.1 Sensory and Electronics Architecture

Integration of a large number of electronic components as a whole system is a challenging engineering work. In the case of a humanoid robot, high performance actuators with a large number of sensors are placed in limited space, under severe mechanical disturbance due to the locomotion and electrical disturbance due to high capacity motors. Stable and reliable communication between those components are crucial. In the case of Hydra, its sensor-rich EHAs need more considerations since a single unit of EHA has as many sensors as a hole effect sensor, two encoders, five pressure sensors and a strain gauge. Table 6.3 summarized sensors on an EHA.

The hole effect sensor is to acquire the magnetic position of the brushless DC motor. It is a built-in sensor of the MAXON EC-4pole 30 motor. It needs five wires which are a 5 V power line, ground line, and three single end digital signal wires corresponding to the three electric phase. Since it only has a resolution of six per rotation, we use the sensor only in debug and calibration scenes. The first encoder is an absolute rotary encoder attached on the end of the motor. To omit initial calibration process when each time they are powered on, which is to calibrate the offset between the electric position of the rotor and the mechanical position acquired from the encoder, we attached an external RLS RMB30SI absolute encoder, instead of the built-in incremental one. It has a resolution of 2048 per rotation, which is output by both SSI serial interface and simple ABI count. The calibration between

the mechanical position and the magnet position is done once the encoder is attached on the motor. The offset is saved in a file on the onboard PC, which is sent to the motor driver when the system is booted up. The ABI incremental output information is used to simplify the calculation of the motor velocity since the value does not wind up unlike the case of absolute value. The SSI signal (clock and data) and ABI signal (A and B, I is not used) are transferred by the RS422 differential manner, which needs 10 cables including the 5 V power and ground line.

Piston position is acquired by a Renishaw RESOLUTE optical encoder. It outputs the absolute position between the read head and linear scale with a resolution of 5 nm. The data is sent out with an RS422 differential BiSS protocol, though six cables in total (MA±, SLO±, power and ground). The stainless steel linear scale is attached on the beam/slider structure while the read head is fixed on the cylinder body. In a case of vane motor, the same series read head can be used to read a ring-shaped rotary scale. In that case the resolution is 26 bit per rev.

Hydraulic pressure information is acquired via Measurement Specialties Model 89 PCB mount sensor. The pressure sensor can measure a pressure up to 7 MPa in standard type EHA, while in the case of stage pump EHA we use the 21 MPa version. An amplifier board is directly soldered on the sensor. The board include an instrumentation bridge amplifier (AD8290) and a voltage follower, which converts the small differential voltage to a 1-3.3V analogue signal. A bridge based sensor tends to have a large variation of the gain. To adjust this variation on the amplifier board, the board has a pre-set resistor whose value is decided by the individual data sheet of each sensor. To protect the board from mechanical damage, the whole board is

laminated with epoxy plastic. Five sensors are attached on the cylinder: one to measure the pressure in the accumulator, two to measure the differential pressure on the pump, and two to measure the differential pressure on the cylinder.

In the case of a cylinder type EHA, a strain gauge is attached on the connecting rod. A custom-made bridge amplifier board is mounted on the cylinder. The combination of the 24-bit digital output bridge amplifier IC (AD7195) and line driver outputs the force information with an SPI interface in the differential way. The number of the wires is 10: 5 V power, ground, MISO±, MOSI±, chip select± and clock±. The diameter of the connecting rod is designed to generate full span strain under 3000 N force.

To handle the large number of the sensors listed above, we took a distributed processing approach. Apart from the amplifier boards for pressure sensors and strain gauges, motor driver boards compose the lowest level of the system. The higher level is MCU boards, then the onboard PC. The motor driver and motor controller is custom made by Brains Inc., which are specially designed to control high capacity EHAs. The processing unit of the motor driver board is a Lattice Semiconductor's MachXO2 FPGA. The FPGA handles all of the serial communications between each sensor, in addition to the field oriented control of the brushless DC motor. A PI motor current feedback control loop is also implemented on the FPGA. The motor current is regulated by Mitsubishi Electrics' PS219 hybrid SiC IGBT. It has a rated maximum of 600 V collector-emitter voltage and 15 A collector current. Its recommended PWM frequency is 20 kHz with 1μs switching dead time. The motor control loop frequency,

[6]Number of wires to transfer the sensor data, excluding the power and ground line.

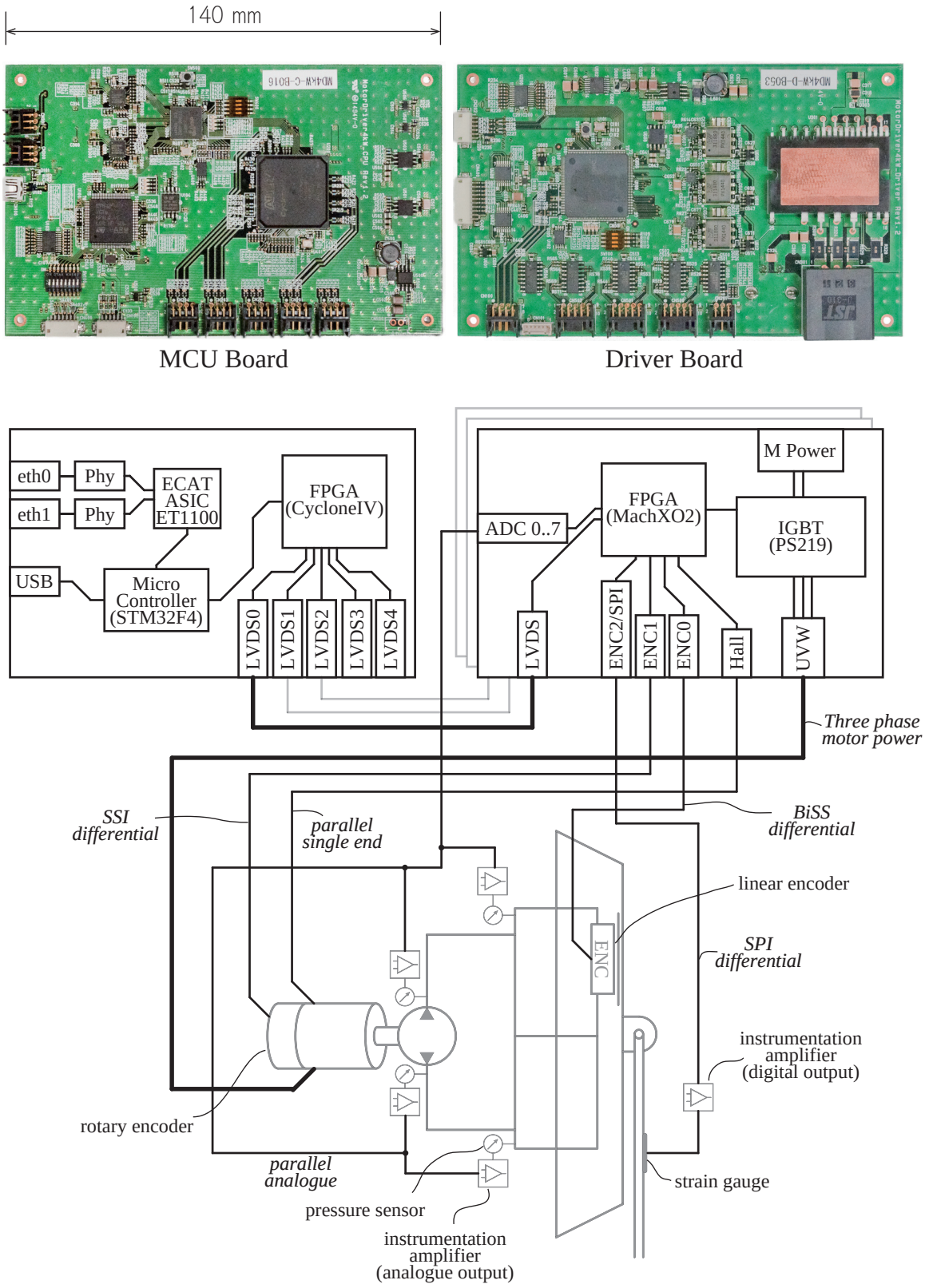

Figure 6.13: Picture and block diagram a MCU board and a driver board.

Table 6.3: Sensors on a single developed EHA unit.

ID	Sensor Type	Output Type	Wires[6]	Value to Measure
1	hall sensor	Digital, Single end Parallel	3	absolute motor magnetic position
2	encoder	Digital, Differential SSI + ABI	8	absolute motor mechanical position
3	encoder	Digital, Differential BiSS	4	absolute piston/vane position
4	pressure sensor	Analogue Single end	1	gauge pressure on accumulator
5	pressure sensor	Analogue Single end	1	gauge pressure on pump
6	pressure sensor	Analogue Single end	1	gauge pressure on pump
7	pressure sensor	Analogue Single end	1	gauge pressure on cylinder
8	pressure sensor	Analogue Single end	1	gauge pressure on cylinder
9	strain gauge	Digital, Differential SPI	8	force on con-rod (only for cylinder)

therefore, is also set as 20 kHz. The driver board also contains an 8-ch AD converter for the pressure sensor.

The MCU board has a STMicroelectronics' STM32F4 microcontroller and an Altera's CycloneIV FPGA. The MCU board is designed to supervise up to five motor driver boards. The MCU board and the motor driver boards communicate through a full duplex synchronous LVDS signal. On the motor controller side, the LVDS communications through the five channels are handled by the FPGA. The communication protocol is a custom one with a start word, address, data, and CRC error check code. In particular, the motor controller FPGA and the motor driver FPGA

have two shared memory spaces for upstream communication (from driver to controller) and downstream communication (from controller to driver.) Synchronizing with the clock signal sent from the controller, the controller keeps sending the content in its downstream memory space one by one, while receiving the upstream data, decode, and store into the upstream memory space. The driver side is the opposite: it keeps sending the data in the upstream memory while receiving and storing data into downstream memory based on an internal state machine. A corrupted data with CRC inconsistency is discarded.

Communication between the microcontroller and the FPGA on the controller board is implemented as an external SRAM memory access. Instead of an external SRAM IC, the memory access bus from the microcontroller is connected to a dual-port memory IP core in the FPGA. Thanks to a state machine copying the data between the memory for LVDS communication and the one for microcontroller memory access, the microcontroller can access any value in the driver board via standard variable access in its program code. Fig.6.13 shows a picture of an MCU board and a driver board, with their schematic shown below. The information flow is illustrated in Fig.6.16.

Communication between the MCU boards and the onboard PC is done through the EtherCAT bus [109]. The communication is handled by an ASIC (ET1100), whose information is accessible from the microcontroller through the hardware abstraction layer.

An MCU board and typically three driver boards consist a joint driver box. Each multi-DOF joints, such as hip's pitch, roll, yaw, is driven by a single joint driver box.

The boards are packed in an aluminum container to be protected against mechanical damage. Fig.6.15 shows external views of a joint driver box. Due to the rich number of I/O ports on the driver board, we also use them as sensor interface board for the foot six-axes sensors and IMU. Since EtherCAT bus takes daisy chain structure, each joint box has two EtherCAT ports for input and output. The first box on the bus is the one for the right hip joint, driving the yaw direction vane motor type EHA and two linear EHAs for the pitch and roll direction. The following box is for the right knee. As described in 6.2.2, the knee joint is driven by one normal type EHA and one driven by two pumps. These are driven by one joint driver box. For the ankle, there are only two EHAs needed. A third driver board, though, is placed as the interface between the six-axes force-torque sensor on the foot. The I/O port for the encoders is diverted to handle the RS422 communication between the foot sensor in ASCII. The EtherCAT bus then goes through the left leg. to the torso.

The first box in the torso is the one to handle the IMU. For high accuracy, we built the IMU with three independent fiber-optical gyroscopes and three servo accelerometers, instead of standard MEMS type integrated IMU. The output from the gyro scopes is the pulse corresponding CW/CCW angular velocity, therefore it is easy to be handled by the three I/O interfaces for encoders on the driver board. The output from the accelerometers is analog. The signals are adjusted to fit the analog input range of the driver board by an intermediate amplifier board. The signals are processed in the MCU and sent out through the EtherCAT bus. Fig.6.14 shows the outlook of the IMU.

A box driving two EHAs for the waist and one electric motor for the neck follows

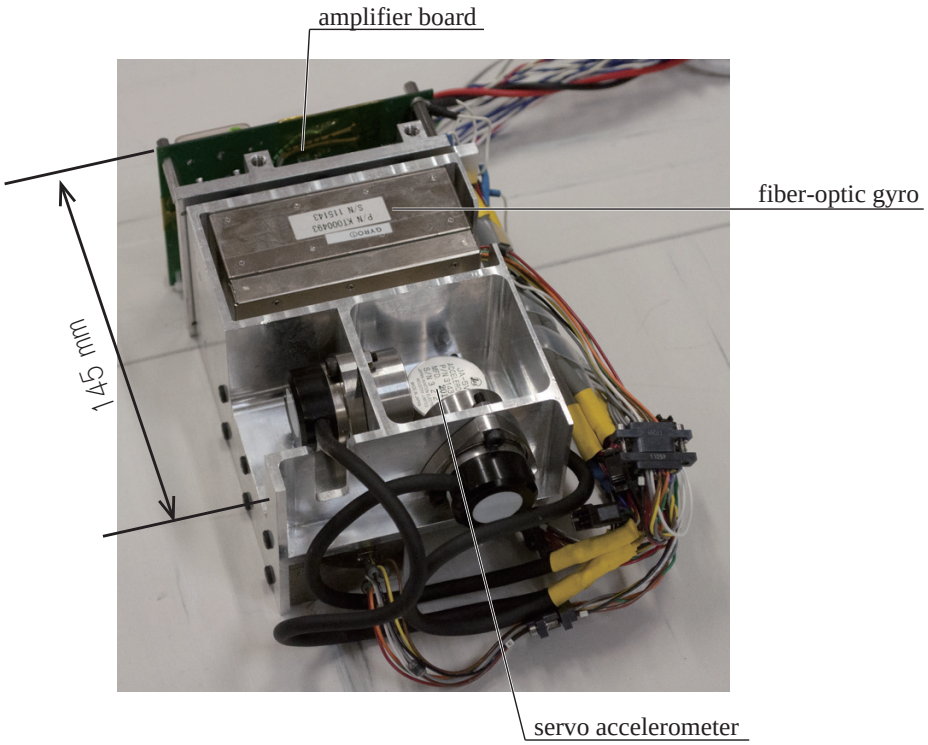

Figure 6.14: Outlook of the IMU, consisted with three independent fiber-optical gyroscopes and three servo accelerometers.

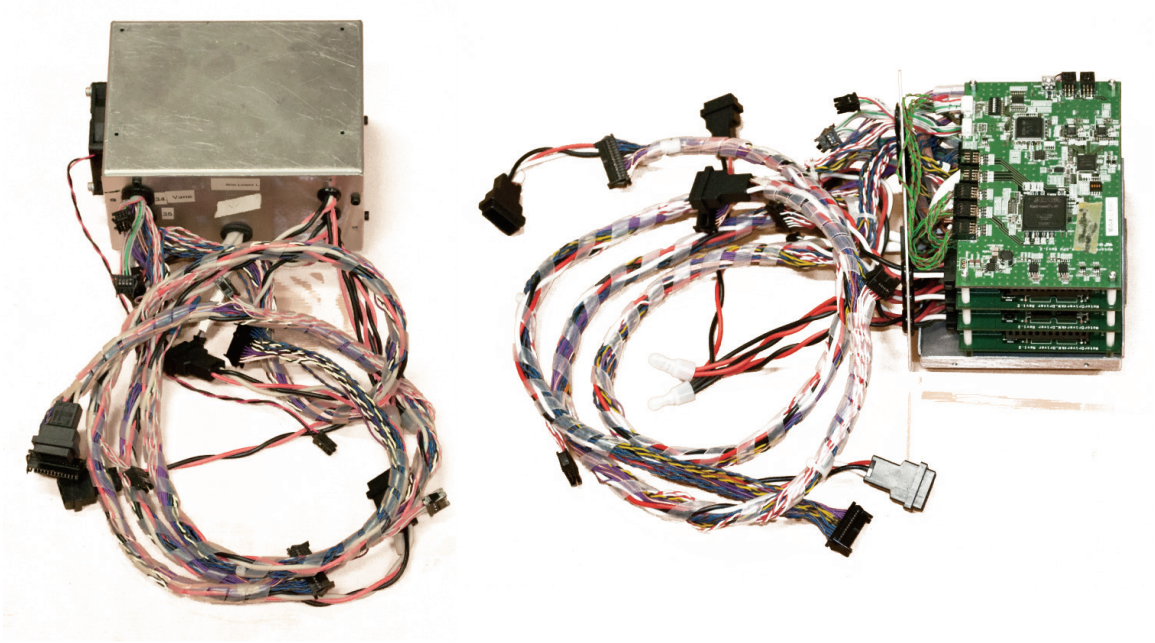

Figure 6.15: Outlook of a joint driver box. A box typically consists of an MCU board and three driver boards, which can drive three joints simultaneously. The boards are packed in an aluminum box to be protected against mechanical damage.

the box for the IMU. The bus then goes through the right arm. The first box on the arm drives the vane motor EHA for the shoulder additional joint and two linear EHAs for the pitch and roll direction. As described in 6.2.2, the elbow joint is driven by a linear EHA driven by two pumps. These two pumps and one vane motor type EHA for the yaw direction of the shoulder joint consists the second box, which is followed by the third box driving the yaw direction vane motor EHA and the two linear EHAs for the pitch, roll of the wrist joint. The last box is for the hand. While the driver board is over spec to drive the 60 W motor, we prioritized uniformity of the system. The arrangement of the joint driver boxed is summarized in Table 6.4.

Table 6.4: Arrangement of the joint driver box.

Box ID	Driver boards	Box ID	Driver boards
0	r_hip yaw	8	r_shoulder additional
	r_hip pitch, roll		r_shoulder pitch, roll
	r_hip pitch, roll		r_shoulder pitch, roll
1	r_knee normal	9	r_shoulder yaw
	r_knee double pump		r_elbow
	r_knee double pump		r_elbow
2	r_ankle pitch, roll	10	r_wrist yaw
	r_ankle pitch, roll		r_wrist pitch, roll
	right foot sensor		r_wrist pitch, roll
3	l_hip yaw	11	r_hand thumb_AA
	l_hip pitch, roll		r_hand thumb_FE
	l_hip pitch, roll		r_hand index finger
4	l_knee normal		r_hand middle finger
	l_knee double pump		r_hand ring finger
	l_knee double pump	12	l_shoulder additional
5	l_ankle pitch, roll		l_shoulder pitch, roll
	l_ankle pitch, roll		l_shoulder picth, roll
	left foot sensor	13	l_shoulder yaw
6	IMU		l_elbow
7	waist pitch, roll		l_elbow
	waist pitch, roll	14	l_wrist yaw
	neck		l_wrist pitch, roll
			l_wrist pitch, roll
		15	l_hand thumb_AA
			l_hand thumb_FE
			l_hand index finger
			l_hand middle finger
			l_hand ring finger

6.3.2 Software Architecture

An advantage with the EtherCAT is that any computer with a compatible ethernet adapter can serve the role of the whole body controller. This makes it easy to introduce the newest computational power to the system. The whole body controller runs on an RT-Preempted patched Ubuntu 14.04 system. A real-time process called "EC-Master", which is a commercially available EtherCAT master stack, handles the EtherCAT communication. It communicates with the whole body controller via a shared memory. All of the mutual conversions between EHA values and the rotational joint values are implemented in the EC-Master. The controller process is not a real-time one, but it is synchronized with the EC-Master with a semaphore. The controller has a main thread which conducts the whole body control and takes logs, a user interface thread with a simple "curses" based text user interface, and a ROS [110] thread publishing the current state and also available to receive commands from external user interfaces.

A choreonoid simulator [111] with a custom plug-in can be used as an emulator of the physical robot. The plug-in is based on the "Simple Controller" of the choreonoid, and it has the same interface to the shared memory and semaphore that the EC-Master and the controller communicates. With this setup, a real experiment and a simulation can be done with totally the same controller. In the case of simulation, the controller can be synchronized with the simulation time thanks to the semaphore. Fig.6.16 summarizes the architecture of the system.

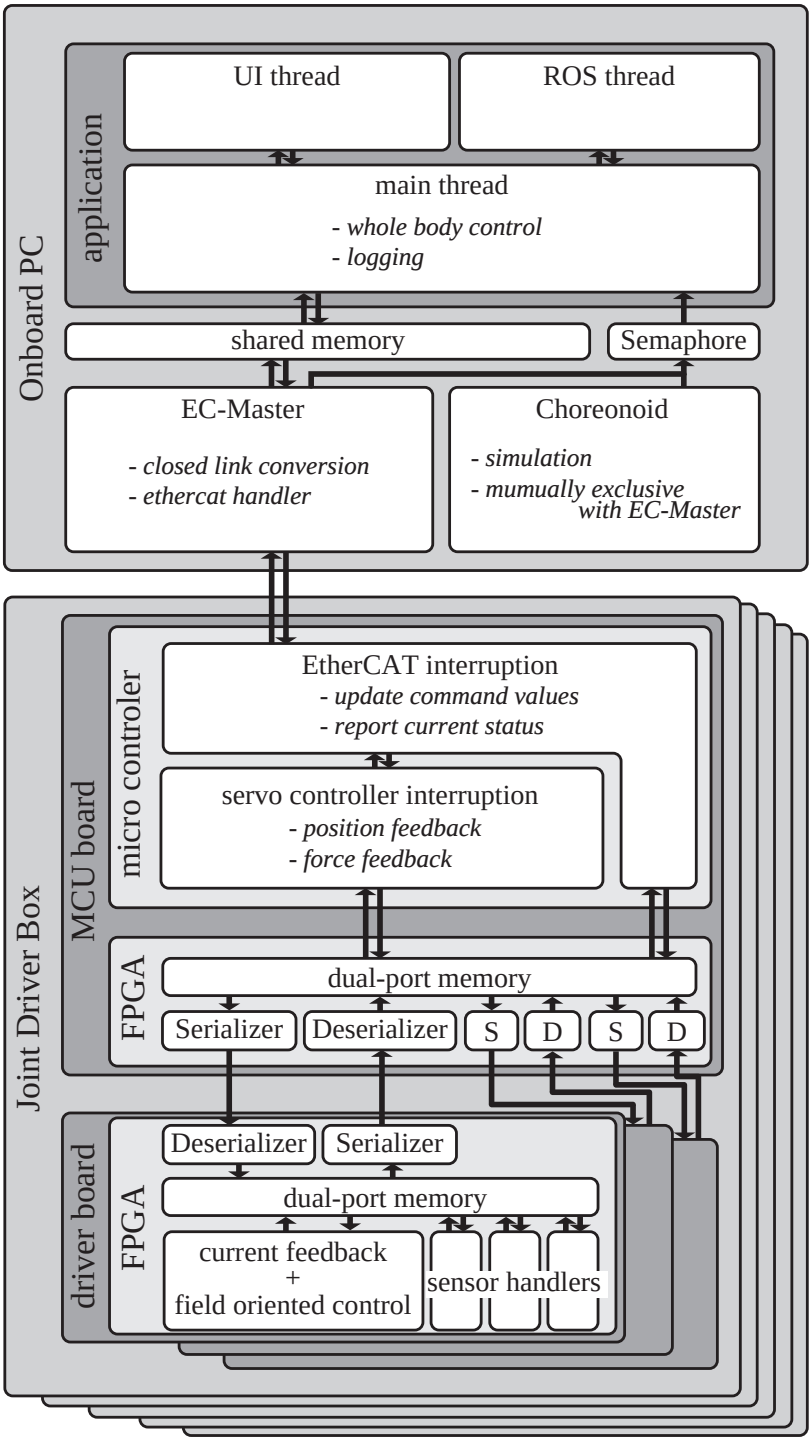

Figure 6.16: Software architecture of Hydra.

6.4 Compliant Whole-Body Locomotion Evaluation

6.4.1 Independent Joint Control Bandwidth Evaluation

For a humanoid robot, the closed loop position/torque control bandwidth of the joints is critical to precisely manipulate the center of mass and conduct a balancing or walking motion. An EHA driven robot is advantageous than the series elastically driven ones in this sense due to its fast response property, as shown in the previous chapter. In this subsection, we examine the joint level position/torque control bandwidth of Hydra. The experiment was done in a condition that the robot is hanged on the crane and one of the leg is servo-on. The joints were under the position control and a sine-wave shape signal with 0.25 ° amplitude was given to the target joint. The position bandwidth is acquired from the command and measured joint angle. Since the position controller is based on the minor joint level torque controller, the command and actual joint torque could be also acquired, with which we get the torque bandwidth.

The pitch and roll direction of the hip joint were tested, whose Bode plots are shown in Fig.6.19 and Fig.6.22 respectively. The time transition of the command/measured joint position and torque for the two joints are shown in Fig.6.17, Fig.6.18, Fig.6.20, Fig.6.21. For the pitch direction, both of the position and torque control bandwidth were around 30 to 40 Hz. This well matches the result of the single actuator on the testbed, which had around 50 Hz force control bandwidth with a totally fixed load, as shown in 5.4. For the roll direction, the torque gain decreased before 30 Hz,

unlike the case of the pitch direction. However, the delay property was almost the same. This means that the stability margin was still kept, therefore we can increase the position feedback gain. As the result, the torque gain drop was covered by the higher level position feedback loop and the position control bandwidth was around 30-40 Hz, similarly as the case of the pitch direction. The difference of the torque response between the pitch and roll direction is regarded as the result of the different command torque amplitude, since the torque controller is the minor loop receiving the command from the higher position feedback loop. This can be seen comparing the command and measured joint torque in Fig.6.18 and Fig.6.21. Indeed, the position feedback gain was different: 3000 Nm/rad for the pitch and 6000 Nm/rad for the roll direction.

6.4.2 While-body Joint Torque Control Performance Evaluation with a Gravity Compensation Experiment

To evaluate joint torque control performance of the developed robot, we conducted a gravity compensation experiment. One leg of the robot was under the torque control and the gravity torque was calculated on the on-board PC, transformed to the actuator force and commanded to each actuator. The leg was externally moved by human hand, therefore the command joint torque varies according to the varying joint angle. Fig.6.23 shows the experiment scene. The backdrivable joints were easy to be moved by human hand and kept the same position when there was no external force, showing their high torque control performance. The time transition of the joint angle and joint command/measured torque is shown in Fig.6.24. From the graph, the

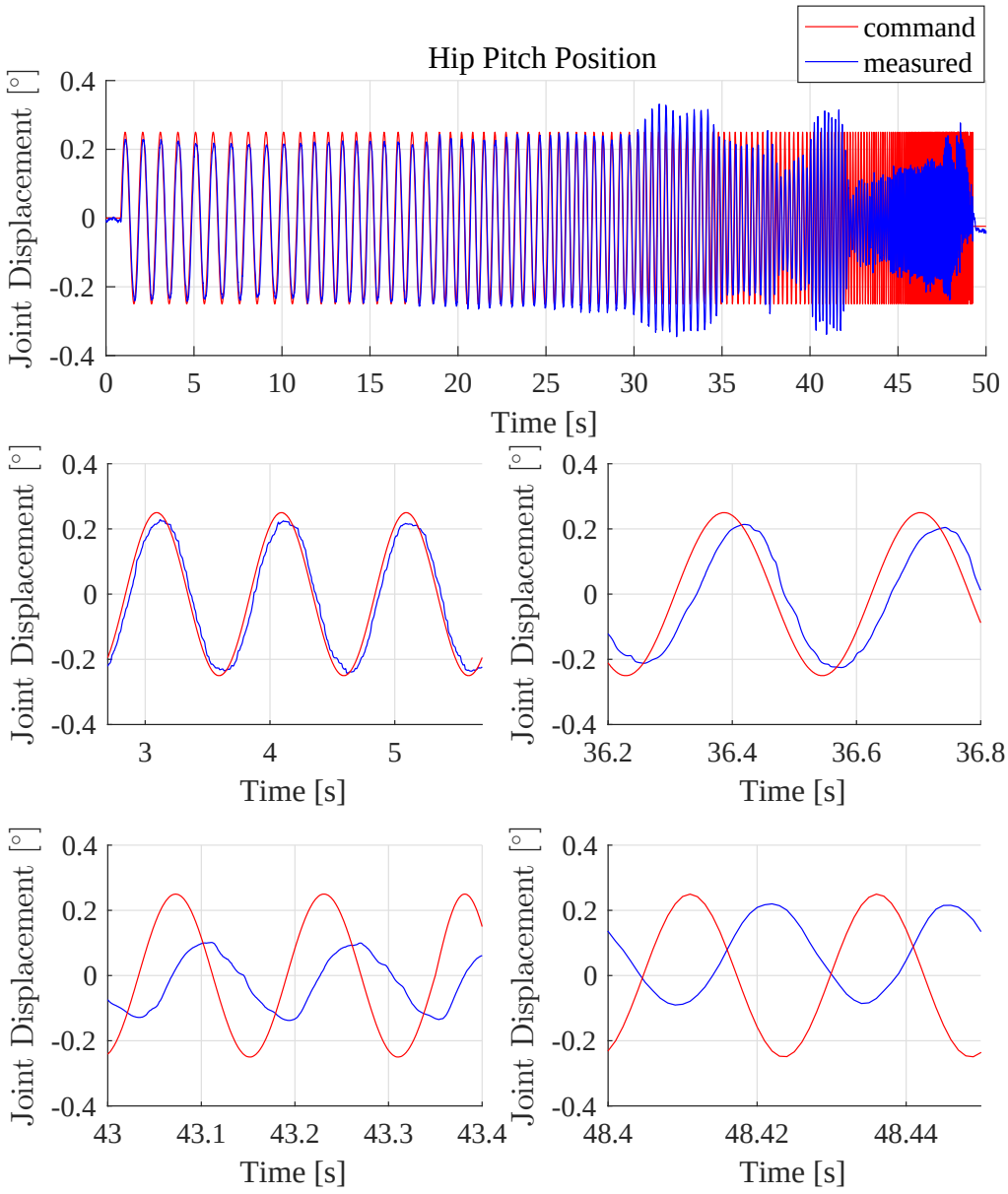

Figure 6.17: Time transition of the command(red) and measured(blue) joint position of the hip pitch joint to acquire the bode plot shown as the blue line in Fig.6.19.

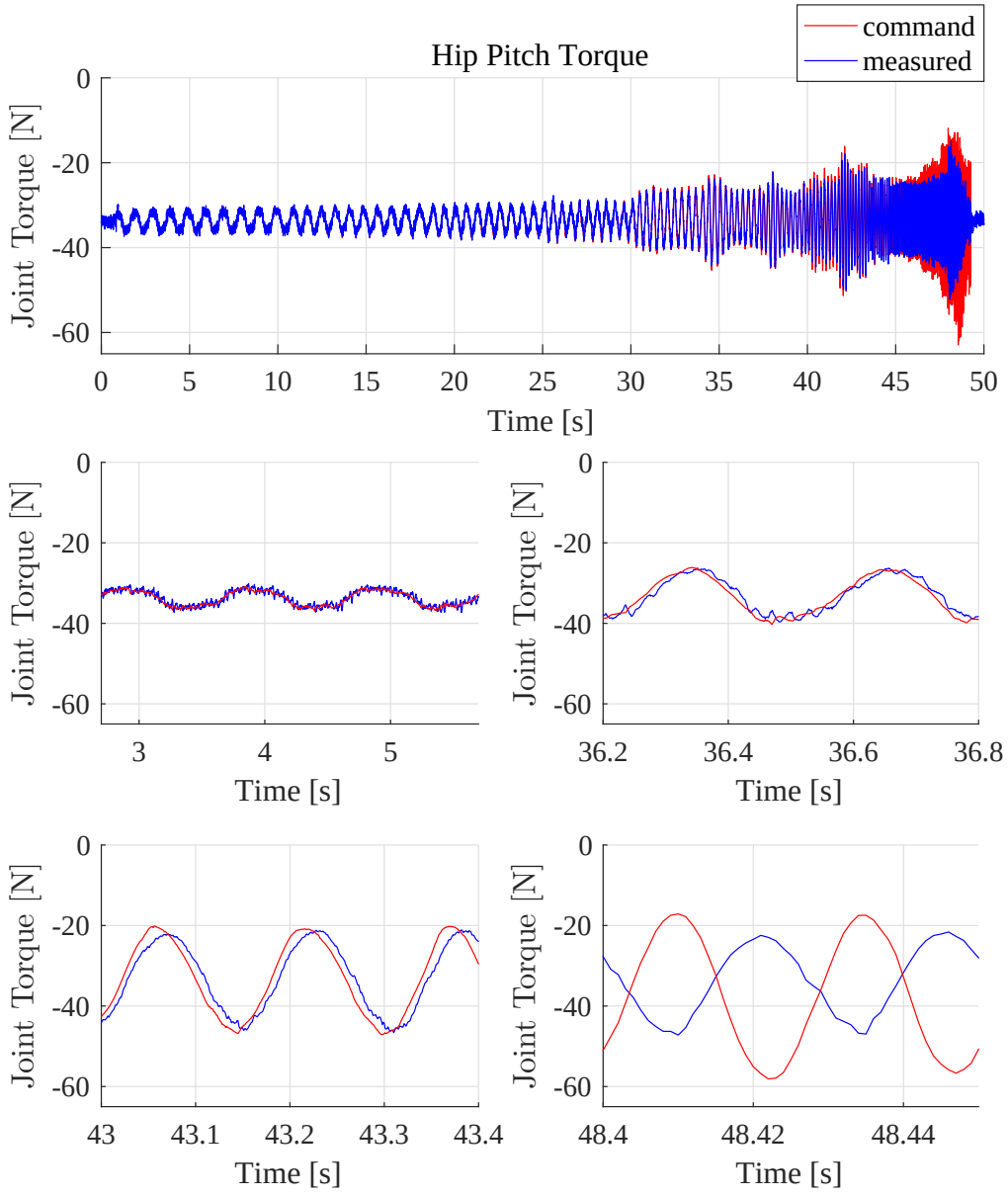

Figure 6.18: Time transition of the command(red) and measured(blue) joint torque of the hip pitch joint to acquire the bode plot shown as the red line in Fig.6.19.

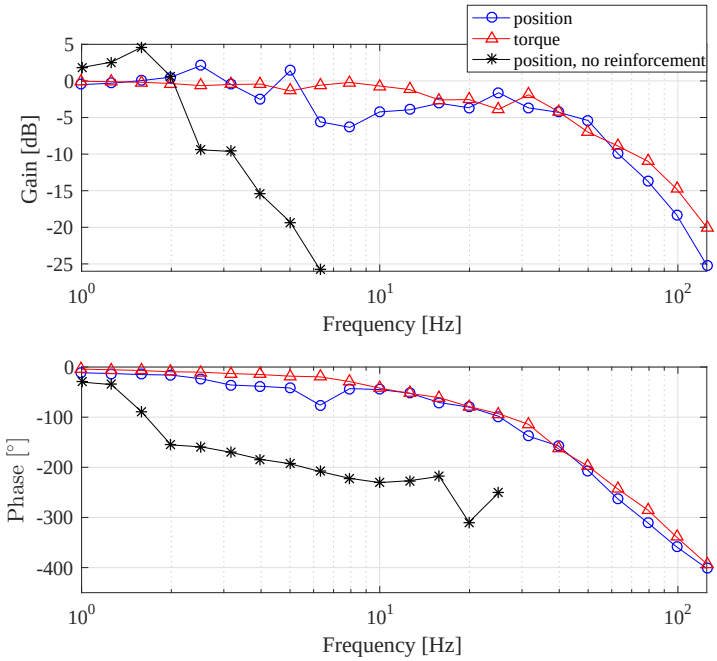

Figure 6.19: Bode plot between command joint position of the hip pitch joint of Hydra and actual position (blue markers), and between command joint torque and actual torque (red markers) (same figure with Fig.5.13). The joints were under the position control and a sine-wave shape signal with 0.25 ° amplitude was given to the target joint. The position bandwidth is acquired from the command and measured joint angle. Since the position controller is based on the minor joint level torque controller, the command and actual joint torque could be also acquired, with which we get the torque bandwidth. The closed-loop control bandwidth in both of the position and torque control was around 30-40 Hz. For the reference, the case without the reinforcement shown in the previous section is overlaid, which proves the effectiveness of the reinforcement.

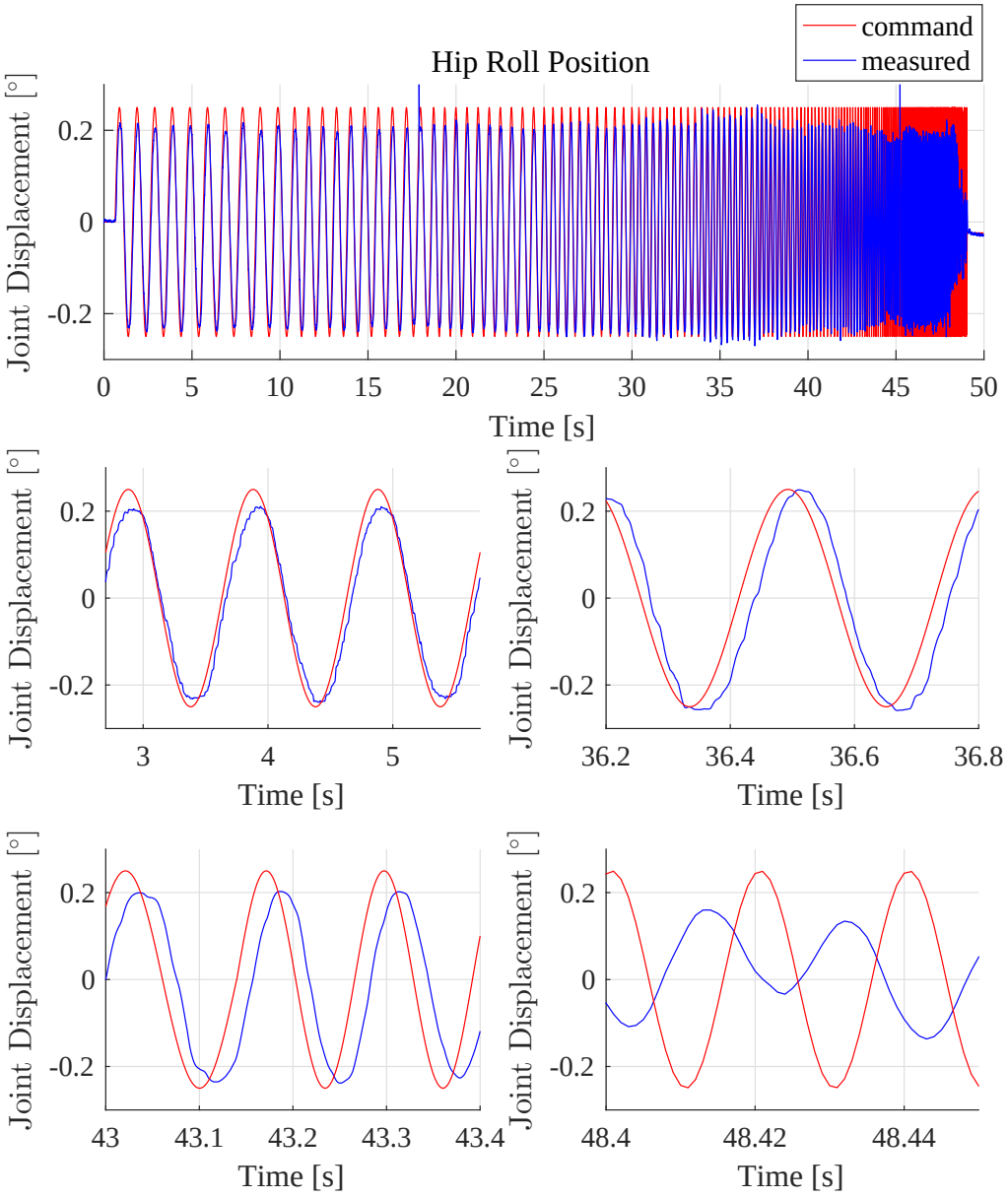

Figure 6.20: Time transition of the command(red) and measured(blue) joint position of the hip roll joint to acquire the bode plot shown as the blue line in Fig.6.22.

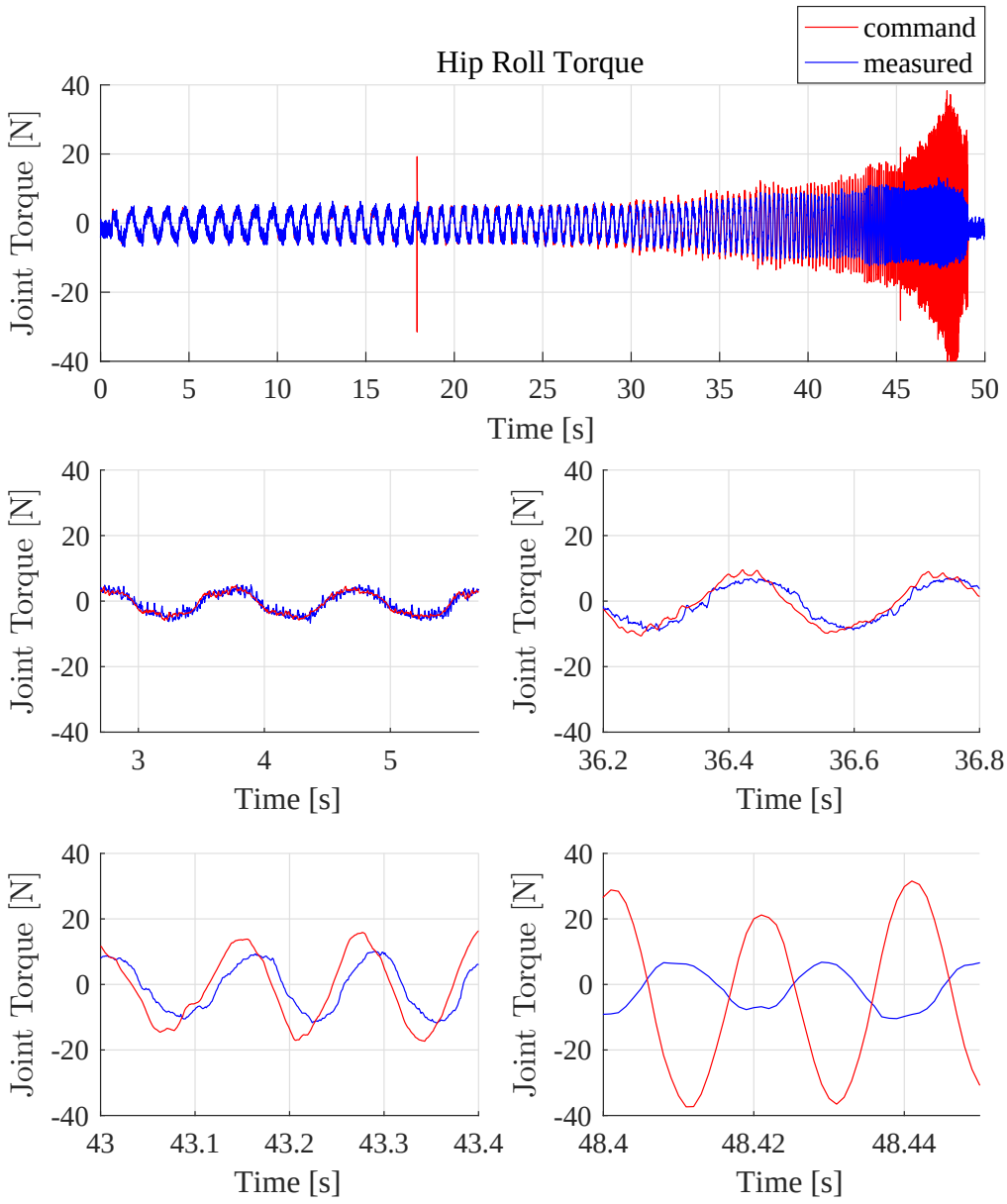

Figure 6.21: Time transition of the command(red) and measured(blue) joint torque of the hip roll joint to acquire the bode plot shown as the red line in Fig.6.22.

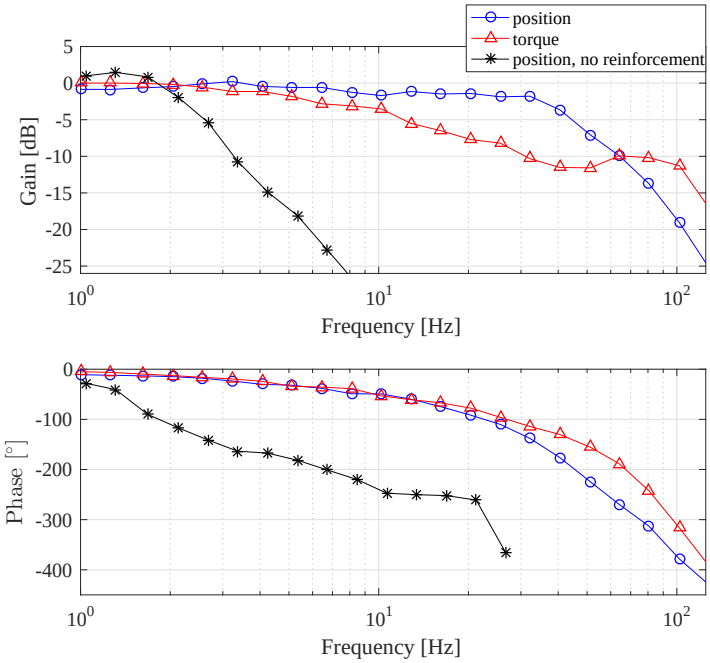

Figure 6.22: Bode plot between command joint position of the hip roll joint of Hydra and actual position (blue markers), and between command joint torque and actual torque (red markers). The joints were under the position control and a sine-wave shape signal with 0.25 ° amplitude was given to the target joint. The position bandwidth is acquired from the command and measured joint angle. Since the position controller is based on the minor joint level torque controller, the command and actual joint torque could be also acquired, with which we get the torque bandwidth. The torque gain decreased before 30 Hz, unlike the case of the pitch direction. However, the delay property was almost the same. This means that the stability margin was still kept, therefore we can increase the position feedback gain. As the result, the torque gain drop was covered by the higher level position feedback loop and the position control bandwidth was around 30-40 Hz, similarly as the case of the pitch direction. For the reference, the case without the reinforcement shown in the previous section is overlaid, which proves the effectiveness of the reinforcement.

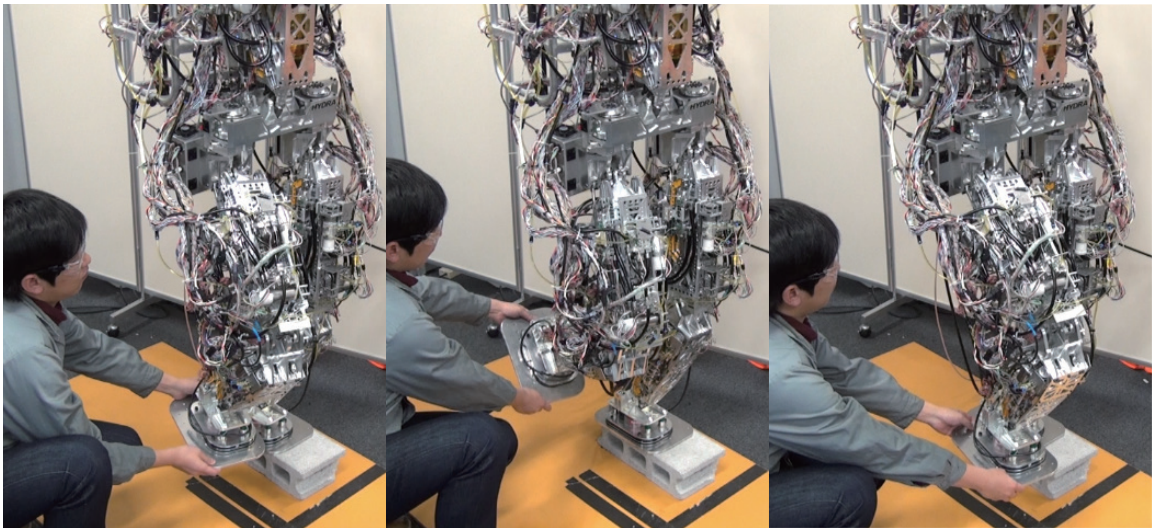

Figure 6.23: Gravity compensation experiment to evaluate joint torque control performance of the developed robot. The gravity torque was calculated on the on-board PC, converted to the actuator force, and then commanded to each actuator. The joints were easy to be moved by human hand and kept the same position when there were no external force, showing their high torque control performance.

joint torque tracks the command value rapidly and smoothly, with the RMS error of 0.73 Nm.

6.4.3 Stiff Control Realized by the High Control Bandwidth

Joint position control based walking frameworks are widely studied for the position controlled robots since they are robust against joint torque error and mass parameters error. While Hydra is a torque control based robot, it needs the capability to support those control framework as a robot platform. In this subsection, we construct an independent joint level position feedback controller on the local torque controller and treat Hydra as a position control based robot, therefore evaluate its locomotion performance based on the position control. As the whole-body controller, we

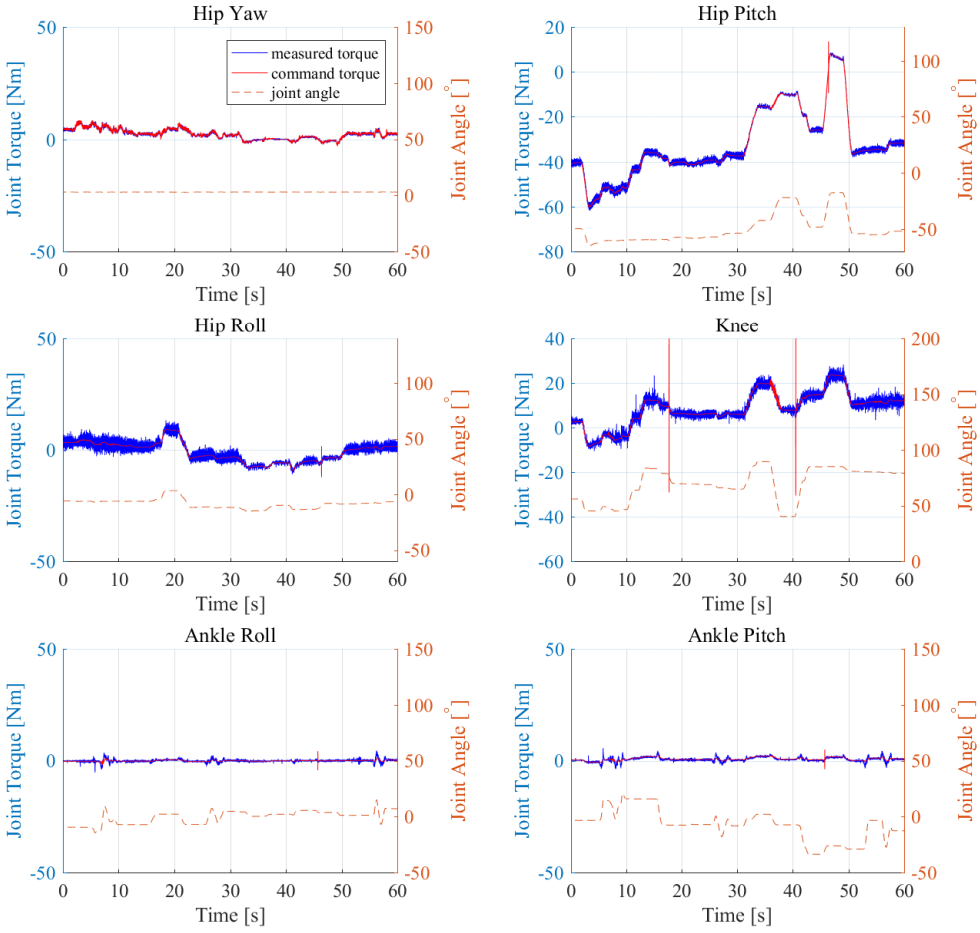

Figure 6.24: Time transition of the joint angle and command/measured joint torque during the gravity compensation experiment. The graph shows that the joint torque tracks the command value rapidly and smoothly. The RMS tracking error was 0.73 Nm.

implemented the Capture Point Tracking controller by Englsberger et al. [112, 113].

The LIP [114] based Capture Point [115] is the point on the ground on which if the robot step, it can bring itself to a complete rest. The CP can be written as

$$\boldsymbol{\xi} = \boldsymbol{x} + \frac{\dot{\boldsymbol{x}}}{\omega} \tag{6.7}$$

where $\boldsymbol{\xi} = [\xi_x, \xi_y]^T$ is the CP on the ground, $\boldsymbol{x} = [x_x, x_y]^T$ is the sagittal and frontal position of the COM, and $\omega = \sqrt{g/z}$ where z is the height of the COM and g is the acceleration of gravity. The CP cannot only be used to bring the robot to the rest, but also to control the balancing and walking, by treating it as a value that represents the state of the robot. Substituting Eq.(6.7) to the dynamics of the LIP, which is

$$\ddot{\boldsymbol{x}} = \omega^2(\boldsymbol{x} - \boldsymbol{p}), \tag{6.8}$$

where $\boldsymbol{p} = [p_x, p_y]^T$ is the ZMP [116], the second order unstable system can be decomposed to a stable component and divergent component [117] as follows:

$$\dot{\boldsymbol{x}} = -\omega(\boldsymbol{x} - \boldsymbol{\xi}) \tag{6.9}$$

$$\dot{\boldsymbol{\xi}} = \omega(\boldsymbol{\xi} - \boldsymbol{p}). \tag{6.10}$$

The first equation shows that the COM automatically follows the CP with a stable first order system therefore only the CP needs to be considered to find the control law. The second equation shows that the CP is propelled from the ZMP with an unstable first order system, and for a given initial CP $\boldsymbol{\xi}_0$ and a constant ZMP $\boldsymbol{p}$, the future CP after the time t, which is $\boldsymbol{\xi}(t)$, can be written as

$$\boldsymbol{\xi}(t) = \boldsymbol{p} + e^{wt}(\boldsymbol{\xi}_0 - \boldsymbol{p}). \tag{6.11}$$

To make the current CP $\boldsymbol{\xi}$ to reach the desired one $\boldsymbol{\xi}_d$ after the time dT, therefore, the desired ZMP $\boldsymbol{p}_d$ can be written as follows:

$$\boldsymbol{p}_d = \frac{\boldsymbol{\xi}_d - e^{\omega dT}\boldsymbol{\xi}}{1 - e^{\omega dT}}. \tag{6.12}$$

In the CP Tracking control [112, 113], dT is fixed while $\boldsymbol{\xi}_d$ has a predefined trajectory $\boldsymbol{\xi}_d(t)$, therefore the control law becomes

$$\boldsymbol{p}_d = \frac{\boldsymbol{\xi}_d(t + dT) - e^{\omega dT}\boldsymbol{\xi}}{1 - e^{\omega dT}}. \tag{6.13}$$

To produce the desired ZMP, the desired COM acceleration $\ddot{\boldsymbol{x}}_d$ is generated [118]:

$$\ddot{\boldsymbol{x}}_d = k_f \frac{F_z}{z}(\boldsymbol{p} - \boldsymbol{p}_d). \tag{6.14}$$

The desired COM acceleration is integrated as the desired COM velocity and projected to the joint space velocity with the task priority [119, 120], in addition to other tasks such as the moving leg position/attitude. The projection to the joint space can done recursively [121] with the initial condition of $\dot{\boldsymbol{\theta}}_0 = 0, \boldsymbol{P}_0 = \boldsymbol{E}$:

$$\hat{\boldsymbol{J}}_i = \boldsymbol{J}_i \boldsymbol{P}_{i-1} \tag{6.15}$$

$$\dot{\boldsymbol{\theta}}_i = \dot{\boldsymbol{\theta}}_{i-1} + \hat{\boldsymbol{J}}_i^{\#}(\dot{\boldsymbol{r}}_i - \boldsymbol{J}_i \dot{\boldsymbol{\theta}}_{i-1}) \tag{6.16}$$

$$\boldsymbol{P}_i = \boldsymbol{P}_{i-1}(\boldsymbol{E} - \hat{\boldsymbol{J}}_i^{\#}\hat{\boldsymbol{J}}_i) \tag{6.17}$$

where $\dot{\boldsymbol{r}}_i$ is the ith task, $\boldsymbol{J}_i$ is the jacobian for the task, $\boldsymbol{J}_i^{\#}$ is the pseudo-inverse of $\boldsymbol{J}_i$, $\dot{\boldsymbol{\theta}}_i$ is the generated command joint velocity to fill the tasks from the first one to the ith one with the priority, $\boldsymbol{P}_i$ is the null space of the tasks from the first one to the ith one, and $\boldsymbol{E}$ is proper-sized identity matrix. Finally, the command joint velocity is integrated as the command joint position and sent to the joint level feedback controller. Fig.6.25 summarizes the controller.

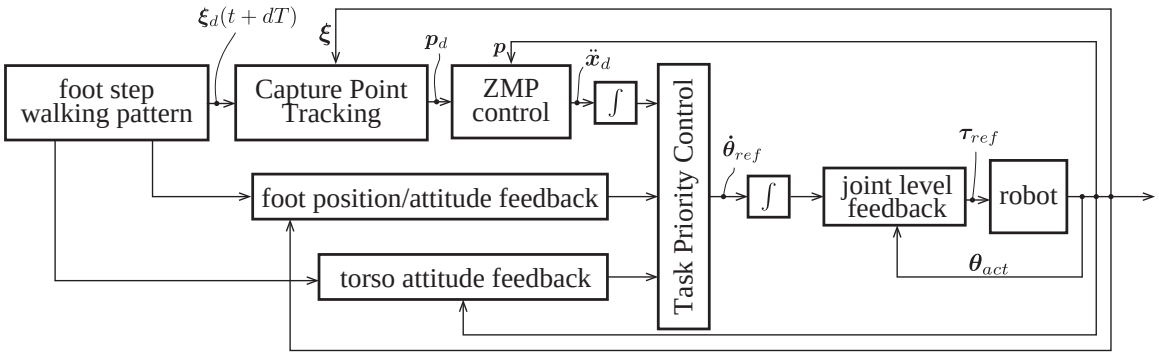

Figure 6.25: Block diagram of the Capture Point Tracking controller. The footstep and CP trajectory are pre-planned. To drive the actual CP to converge to the preferred trajectory, the CP Tracking controller generates the desired ZMP. The command COM acceleration is then generated for the actual ZMP to track the desired one. The command COM acceleration is integrated to be the command COM velocity and projected to the command joint velocity, with the task priority. The command joint velocity is integrated as the command joint position and sent to the joint level position feedback controller.

We first conducted the balancing experiment. Instead of stepping, a constant command CP is given to the robot and we manually applied disturbance on the body. Fig.6.26 shows the view of experiment. Horizontal disturbance, both pushing and pulling, in both x and y direction, was given. The robot could successfully move its body in the direction to avoid the disturbance. The time transition of the command/measured CP, command/measured ZMP, and position of the COM is shown in Fig.6.27. As the disturbance is given, the actual CP shifts from the desired position. The command ZMP, therefore, varies to push the CP back. The graph in the middle shows that the actual ZMP successfully tracks the command one. The RMS tracking error is 8.7 mm.

The following experiment is to evaluate the walking performance, as shown in Fig.6.28. The stride was 0.2 m with 30 mm height and the step time was set

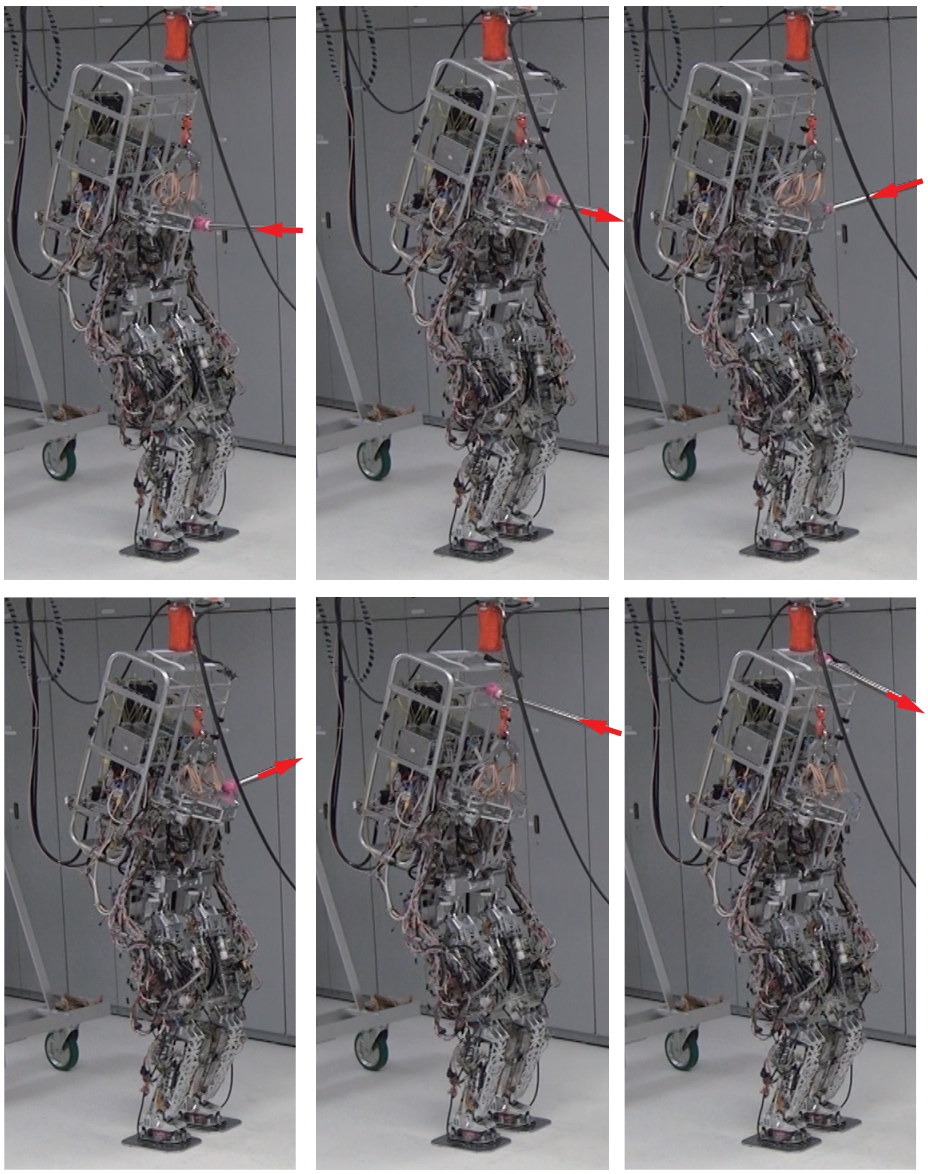

Figure 6.26: The balancing experiment based on the capture point tracking control. Horizontal disturbance, both pushing and pulling, in both x and y direction, was given. The robot could successfully move its body to the direction to avoid the disturbance.

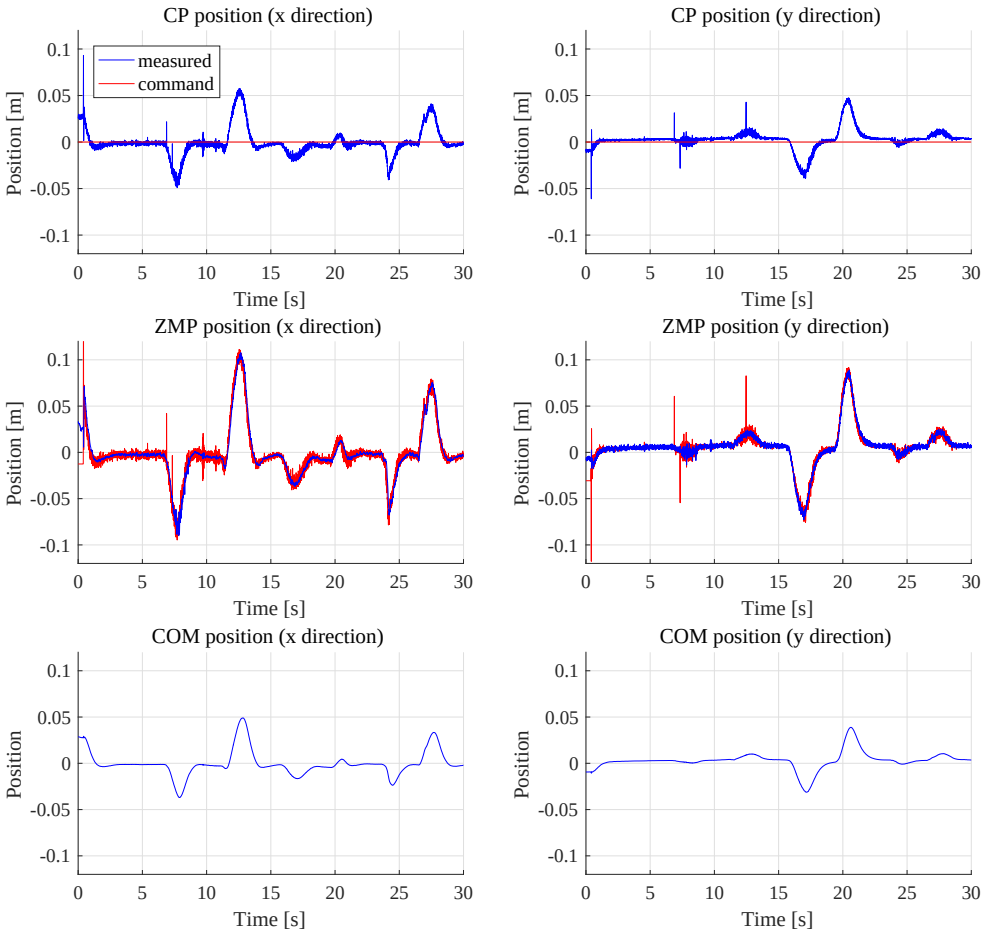

Figure 6.27: The time transition of the command/measured CP, command/measured ZMP, and position of the COM during the balancing experiment. As the disturbance is given, the actual CP shifts from the desired position. The command ZMP, therefore, varies to push the CP back. The middle graph shows that the actual ZMP successfully tracks the command one. The RMS tracking error is 8.7 mm.

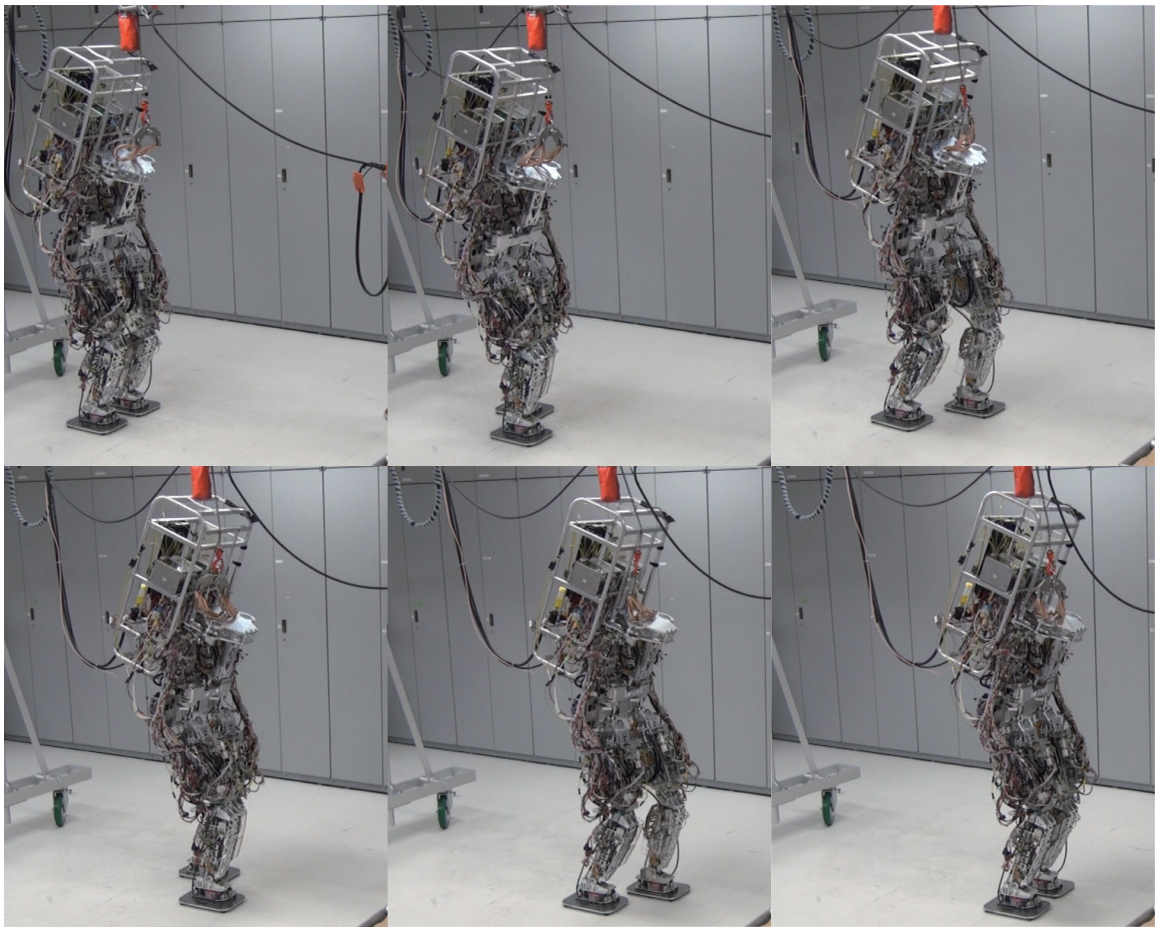

Figure 6.28: Outlook of the walking experiment based on the Capture Point Tracking control. The robot could successfully conduct the walking motion with 20 cm stride and 30 mm step height. The step time was set as 1 second.

as 1 second. The robot could successfully conduct the walking motion without falling. Fig.6.29 shows the time transition of the command/measured CP, command/measured ZMP, and the COM position. The actual CP varies earlier than the command one since the controller tries to follow the dT time future point. In this case dT is set as 0.2 second. The actual ZMP follows the command one with 47 mm RMS error. This is larger than the case of the stand balancing experiment, since the motion is much more dynamic and the disturbance was large.

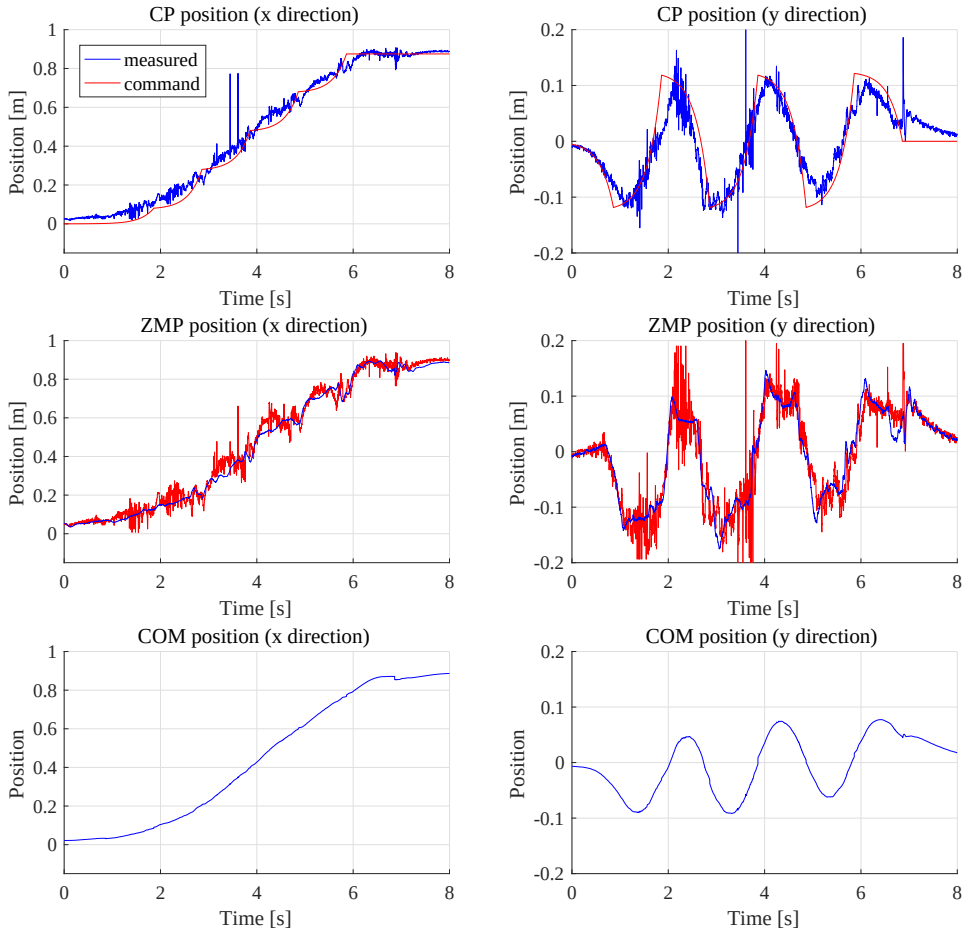

Figure 6.29: Time transition of the command/measured CP, command/measured ZMP, and the COM position. The actual CP varies earlier than the command one since the controller tries to follow the dT time future point. In this case dT is set as 0.2 second. The actual ZMP follows the command one with 47 mm RMS error.

6.4.4 Compliant Control Realized by the Backdrivability

Resolved Viscoelasticity Control [123, 122]

An advantage of robots with backdrivable joints it that if an external force is applied to the distal parts of the body, the local joints can absorb it without harming the overall locomotion. In other words, even if the robot is disturbed in the configuration space, it should not react on it as long as the tasks in the operational space such as COM motion is not disturbed. This is difficult for the position control based robot, which has high gain configuration space level position feedback.

The Resolved Viscoelasticity Control (RVC) [122] provides a control framework to separate the task space viscoelasticity and the nullspace one by the interconversions of the stiffness (or viscosity) in the task space and joint space. The joint viscoelasticity and task viscoelasticity can be written as follows:

$$\boldsymbol{\tau} = {}^{ref}\boldsymbol{\tau} + \boldsymbol{K}_\theta({}^{ref}\boldsymbol{\theta} - \boldsymbol{\theta}) + \boldsymbol{D}_\theta({}^{ref}\dot{\boldsymbol{\theta}} - \dot{\boldsymbol{\theta}}) \tag{6.18}$$

$$\boldsymbol{f}_i = {}^{ref}\boldsymbol{f}_i + \boldsymbol{K}_i({}^{ref}\boldsymbol{p}_i - \boldsymbol{p}_i) + \boldsymbol{D}_i({}^{ref}\dot{\boldsymbol{p}}_i - \dot{\boldsymbol{p}}_i) \tag{6.19}$$

where $\boldsymbol{\theta}, \boldsymbol{\tau} \in \mathbb{R}^n$ denotes joint position and torque, $\boldsymbol{p}_i, \boldsymbol{f}_i \in \mathbb{R}^3$ denotes a feature quantity in the task space and the force acting on it, and $\boldsymbol{K}_\theta, \boldsymbol{D}_\theta \in \mathbb{R}^{n\times n}$, $\boldsymbol{K}_i, \boldsymbol{D}_i \in \mathbb{R}^{3\times 3}$ denotes the viscoelasticity in the configuration space and task space. For the simplicity, we focus on the compliance, which is the inverse of stiffness $\boldsymbol{C}_i = \boldsymbol{K}_i^{-1}, \boldsymbol{C}_\theta = \boldsymbol{K}_\theta^{-1}$. Their relationship is given as:

$$\boldsymbol{C}_i = \boldsymbol{J}_i \boldsymbol{C}_\theta \boldsymbol{J}_i^T \tag{6.20}$$

where $\boldsymbol{J}_i \in \mathbb{R}^{3\times n}$ is the Jacobian matrix for the task $\boldsymbol{p}_i$.

With redundant DoF, Eq.(6.20) is solved as

$$\boldsymbol{C}_\theta = \boldsymbol{J}_i^{\#}\boldsymbol{C}_i\boldsymbol{J}_i^{\#T} + ({}^d\boldsymbol{C}_\theta - \boldsymbol{J}_i^{\#}\boldsymbol{J}_i\ {}^d\boldsymbol{C}_\theta\boldsymbol{J}_i^T\boldsymbol{J}_i^{\#T}) \tag{6.21}$$

where $\boldsymbol{J}_i^{\#}$ is the pseudo-inverse of $\boldsymbol{J}_i$ and ${}^d\boldsymbol{C}_\theta \in \mathbb{R}^n$ is an arbitrary desired joint compliance[122]. The desired joint compliance ${}^d\boldsymbol{C}_\theta$ is fulfilled by $\boldsymbol{C}_\theta$ with a least square error under the condition that Eq.(6.20) is fulfilled. Setting ${}^d\boldsymbol{C}_\theta$ as a high value, we can realize highly compliant motion in the direction that the task is not affected.

For balancing or locomotion, two approaches are possible for the task space or the COM viscoelasticity. One is to make $\boldsymbol{K}_i$ as stiff as possible and change the target COM position according to the ground reaction force. It results in a simpler controller, however, if we can adjust $\boldsymbol{K}_i$ to a proper value that realize the same property of the former case. In fact, it is shown in the literature [123] that the COM viscoelasticity can be identically converted from the PD gain of a linear feedback controller manipulating the ZMP to maintain the COM position. When the control law is given as:

$$\boldsymbol{u} =^{ref} \boldsymbol{u} + \boldsymbol{F}({}^{ref}\boldsymbol{x} - \boldsymbol{x}) \tag{6.22}$$

where $\boldsymbol{u} = [x_z\ y_z]^T$ is the position of ZMP, $\boldsymbol{F} = [\boldsymbol{F}_k\ \boldsymbol{F}_d]$ is the state feedback gain, $\boldsymbol{x} = [x_G\ y_G\ \dot{x}_G\ \dot{y}_G]^T$ is the robot state containing the COM position and velocity, the

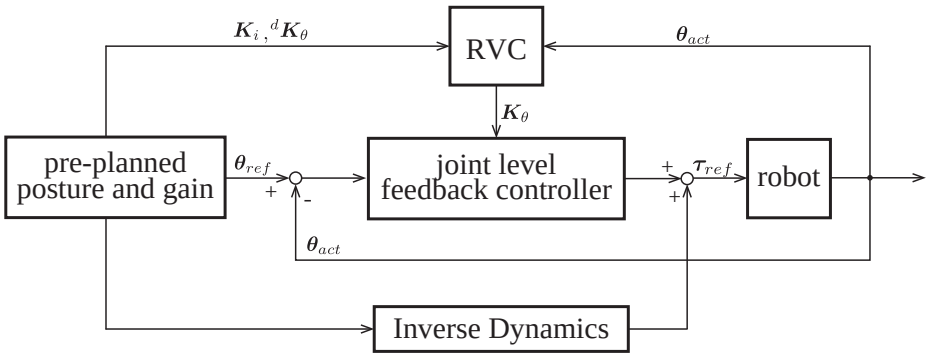

Figure 6.30: Block diagram of hydra's resolved viscoelasticity controller. The RVC module updates the gain matrix, according to the current joint position. The joint position feedback controller receives the gain matrix and conduct position control. Since the joint gain matrix is not diagonal, this feedback is done as the whole body and the resulted whole body torque is sent to the robot. To achieve dynamic motions with low feedback gain, feed forward torque calculated from the inverse dynamics plays an important role.

equivalent COM viscoelasticity $\boldsymbol{K}_G, \boldsymbol{D}_G$ is given as:

$$\boldsymbol{K}_G = \begin{bmatrix} -m\omega^2(\boldsymbol{E} + \boldsymbol{F}_k) & \boldsymbol{0} \\ \boldsymbol{0} & k_z \end{bmatrix} \tag{6.23}$$

$$\boldsymbol{D}_G = \begin{bmatrix} -m\omega^2\boldsymbol{F}_d & \boldsymbol{0} \\ \boldsymbol{0} & d_z \end{bmatrix} \tag{6.24}$$

where $\boldsymbol{E}$ is identity matrix, m is the weight of the robot, and $\omega = \sqrt{g/z}$ with g, z denoting the acceleration of gravity and height of the COM.

Fig.6.30 shows the structure of the RVC controller. In addition to the footstep, the joint trajectory is also preplanned. The RVC module updates the joint stiffness, in other words the gain matrix, according to the current joint position. The joint position feedback controller receives the gain matrix and conduct position control. Since the joint gain matrix is not diagonal, this feedback is done as the whole body and the resulted whole body torque is sent to the robot. To achieve dynamic motions with

low feedback gain, feed forward torque calculated from the inverse dynamics plays an important role. The controller shown in Fig.6.30 is much simpler than the one in Fig.6.25. This is because the RVC framework does not have an explicit ground force feedback with the CP and ZMP. Instead, the force feedback is implicitly conducted by the joint torque feedback.

A practical advantage of the RVC is that since the task space feedback is not directly done in the task space but realized through the projected joint level feedback, we can explicitly examine the gain matrix. Even though the EHA developed for Hydra has an enhanced response property, the control bandwidth is still limited. This leads the limitation of the task space level or joint level feedback gain. While the output joint gain matrix from the RVC is not diagonal, the diagonal elements still have a relatively dominant value. Comparing it with the fine-tuned gains for the individual joints, we can roughly estimate whether the task space feedback gain is affordable for the real hardware. This is a strong tool since the multiple task space gains such as COM, moving leg or body attitude result in a large DoF of gain tuning, which requires numerous try and error.

Disturbance Rejection with the High Backdrivability

To evaluate the disturbance rejection performance of Hydra, we first conducted an experiment shown in Fig.6.31. The robot was standing by the left leg and a disturbance was manually applied on the right foot. The robot was under a joint level position control, without the whole-body feedback. Two experiments were conducted: one with high joint stiffness and another with low joint feedback gain on the right leg

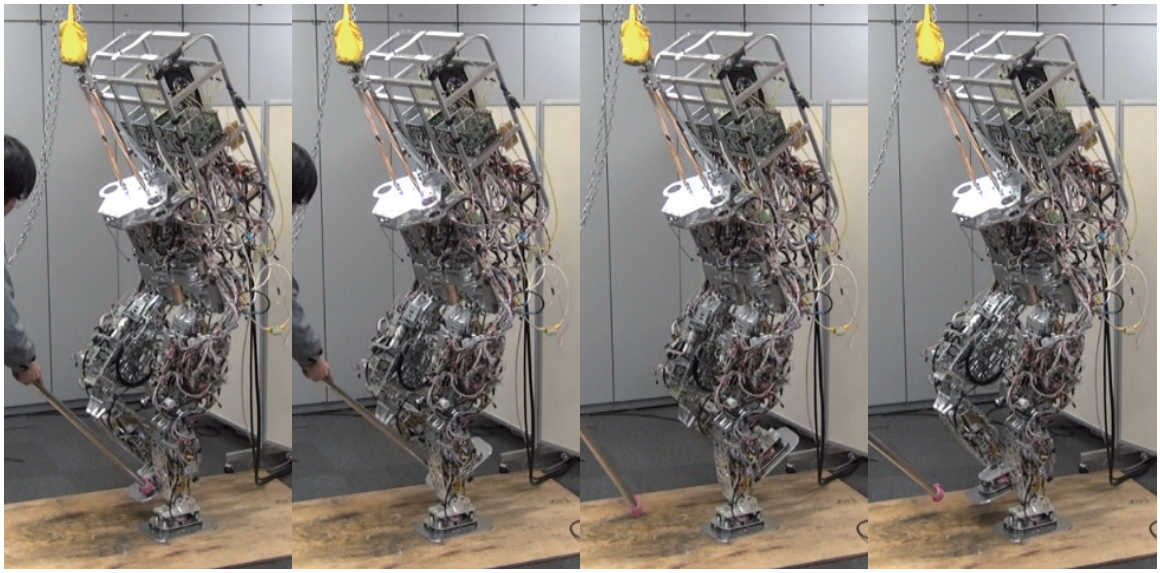

Figure 6.31: Experiment to examine the disturbance rejection performance of the backdrivable joints. The robot is standing by the left leg and a disturbance is manually applied on the right foot. The robot is under a joint level position control, without whole-body feedback. Two experiments were conducted: one with high joint stiffness and another with low joint feedback gain on the right leg therefore it can absorb disturbance.

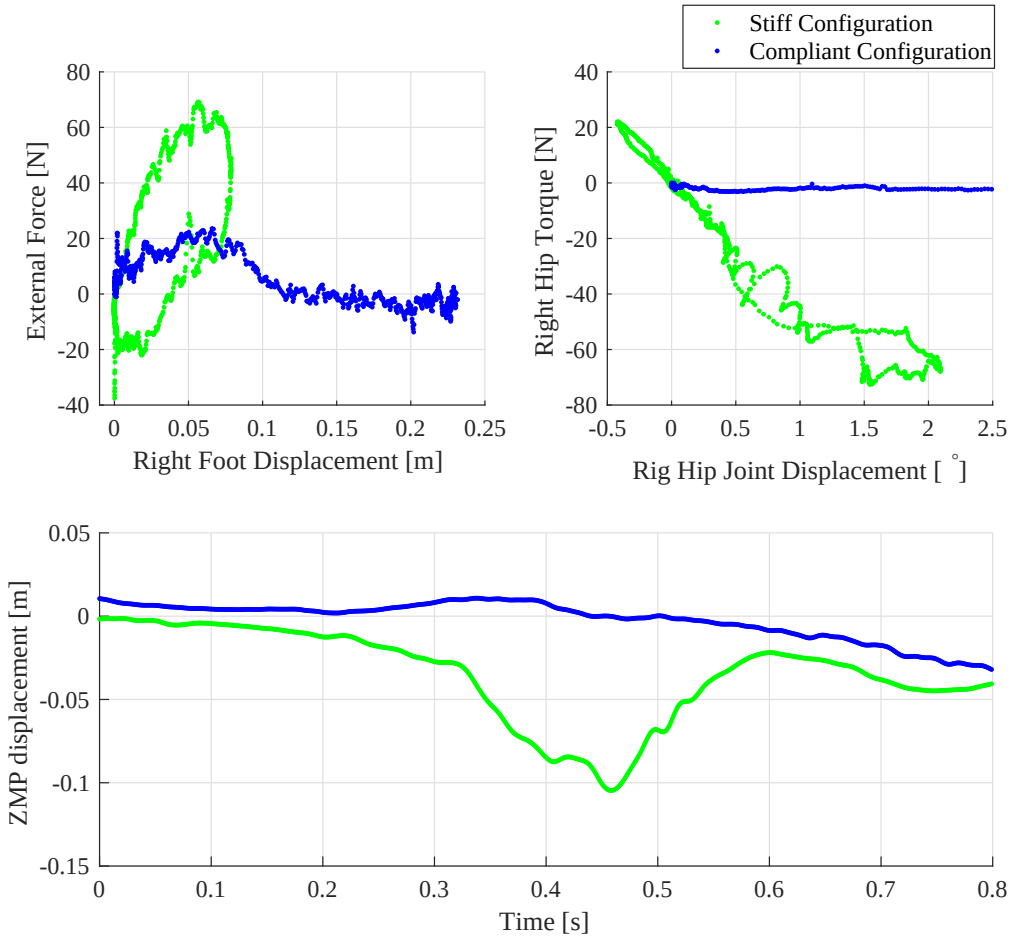

Figure 6.32: Displacement against the disturbance in the operational space and configuration space, and variation of ZMP during the initial 0.8 second after the disturbance happens. The green makers show the case with high gain (stiff configuration) and the blue markers show the case with the low gain (compliant configuration). On the top left is the right foot displacement against the force in the x (sagittal) direction. On the top right is the relationship between the joint angle displacement and joint torque of the right hip pitch joint. On the bottom of the figure, the time transition of the ZMP on the left foot is shown.

therefore it can absorb the disturbance by the local joints. The figure shows the one with the compliant configuration. With the disturbance, the right leg moved rapidly and the external force was absorbed as the acceleration of the right leg. The rest of the body therefore did not receive an impulsive effect and the robot could keep standing.

In Fig.6.32, the values of the initial 0.8 second after the disturbance is shown. On the top left is the right foot displacement against the force in the x (sagittal) direction. The displacement is calculated from the joint angles and forward kinematics. The force is measured by the foot force sensor on the right foot, which is not used in the control in this experiment. The green makers show the case with high gain (stiff configuration) and the blue markers show the case with the low gain (compliant configuration). While the stiff case showed a high operational space impedance, in the compliant case it was largely reduced. The relatively high impedance at the beginning of the compliant case is due to the acceleration of the foot, since the impedance cannot be seen when the displacement is large. On the top right is the relationship between the joint angle displacement and joint torque of the right hip pitch joint. This graph shows that the disturbance force is not transferred to the COM, thanks to the high joint backdrivability. This results in slower disturbance on the ZMP. On the bottom of the figure, the time transition of the ZMP on the left foot is shown. Unlike the stiff case where it varies rapidly, in the compliant case the velocity was suppressed to around 30% value.

To quantitatively evaluate the nullspace compliance with the whole-body controller, we conducted the evaluation with the setup shown in Fig.6.33. A horizontal impulsive

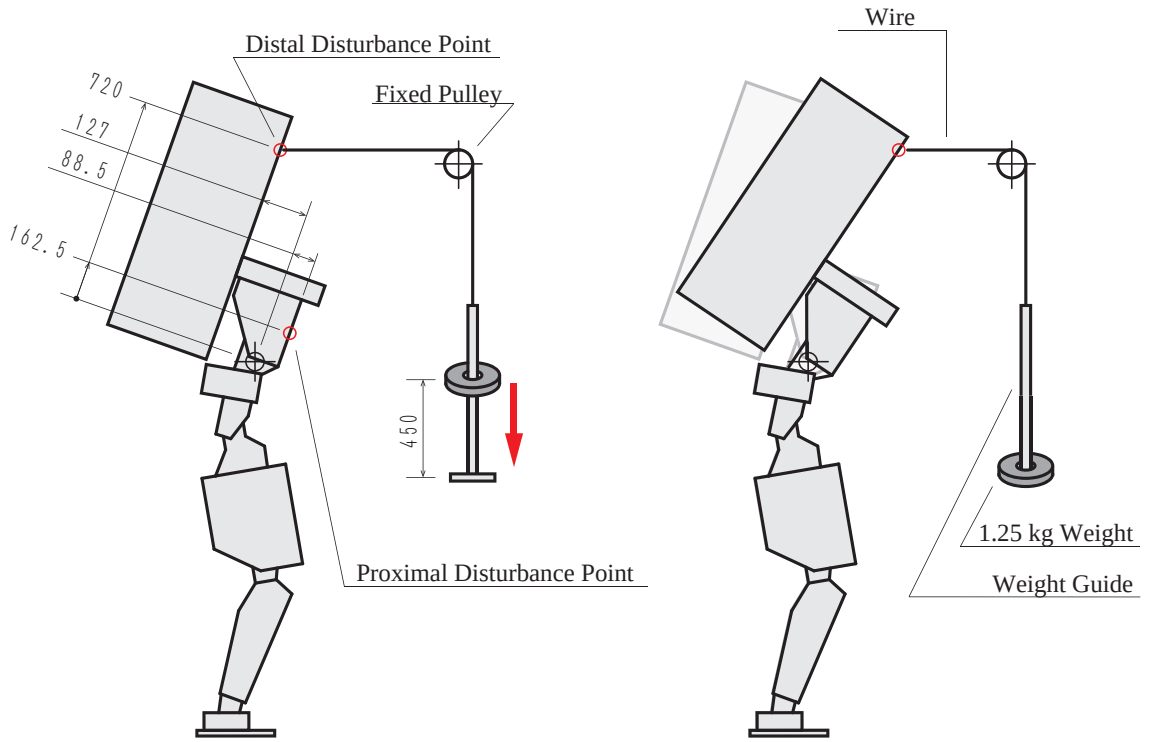

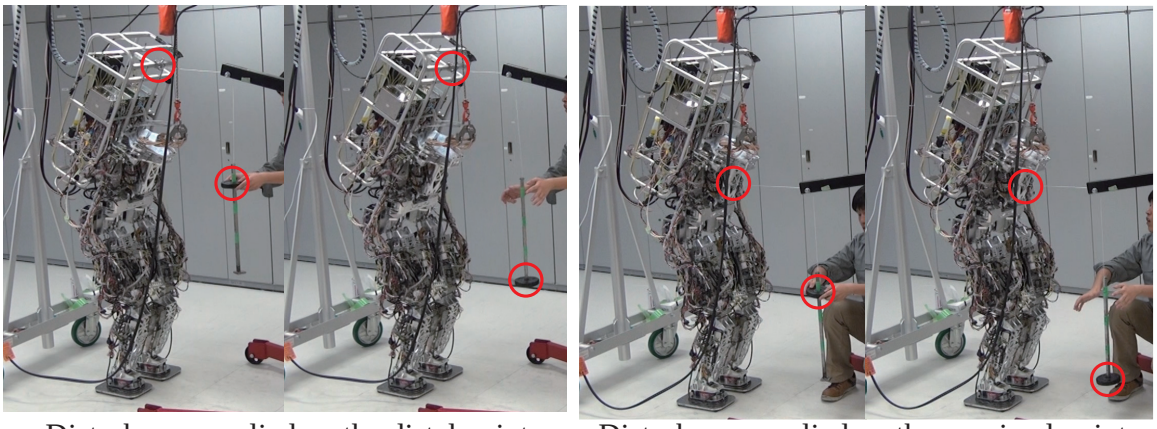

Disturbance applied on the distal point

Disturbance applied on the proximal point

Figure 6.33: Setup of the impulsive experiment to quantitatively evaluate that the robot is more compliant in the distal part. The robot is pulled by a horizontal wire, which is guided by a pulley to the vertical direction. On the other side of the wire from the robot, a linear guide with a stopper is attached. A weight, constrained by the linear guide, is dropped from a constant height from the stopper. When the weight falls by the gravity and collide with the stopper, we can apply a constant momentum to the robot. The impact was applied on two points on the robot, namely the distal disturbance point and the proximal disturbance point, as shown in the figure. The mass of the weight was 1.25 kg and the drop height was set as 45 cm, resulting in 3.71 kg·m/s momentum.

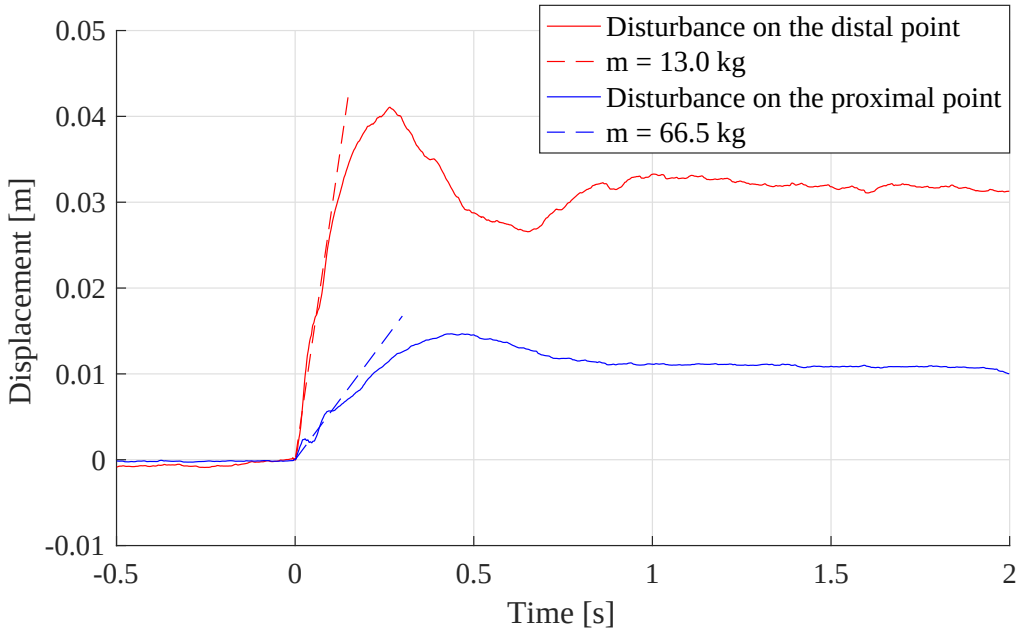

Figure 6.34: Time transition of the X direction displacement of the two points. The apparent operational space stiffness, which can be estimated from the constant displacement due to the gravity on the weight after the impact, was 378 N/m for the distal point. This is 34% value of the 1110 N/m stiffness for the proximal point. The apparent operational space mass, which can be estimated from the conservation of the momentum, taking the average velocity during the initial 80 ms after the impact, was 11.8 kg for the distal point. This is 18% of the value of the 65.5 kg of the proximal point.

disturbance is applied to the robot through a wire. The wire is guided to the vertical direction and connected with a structure with a guide and stopper. A 1.25 kg weight, constrained by the guide, is dropped from a constant 45 cm height from the stopper. We applied the same disturbance to two points on the robot: one is close to the center of the torso and another on the top of the backpack. When the weight collide with the stopper, we could see that in the latter case the body moved larger and faster. The time transition of the horizontal displacement of the point that the wire is attached is shown in Fig.6.34. As the previous case, the position is acquired from the forward kinematics. In the graph, the constant displacement represents the equivalent stiffness seen from the wire. From the graph, we can calculate 1110 N/m stiffness for the proximal point and 378 N/m for the distal point, which is 34% reduced value. For the apparent inertia, we tread the collision as a perfectly inelastic one. The apparent inertia is then calculated from the conservation of the momentum, taking the average velocity during the first 80 ms after the impact. For the proximal point, the apparent mass was 65.5 kg. Taking into account that the total body weight of the robot is 74 kg, we can regard that this estimation method has fine accuracy. For the distal point, the mass appeared to be 11.8 kg, which is 18% value of the proximal point.

Coexistence of a Proper COM Stabilization and Nullspace Compliance

With the RVC, both of the COM stabilization and nullspace compliance can be achieved simultaneously. To quantitatively evaluate the the realization of the COM stiffness we manually applied a horizontal external force to the standing robot in a quasi-static manner. The displacement of the COM is then acquired from the forward

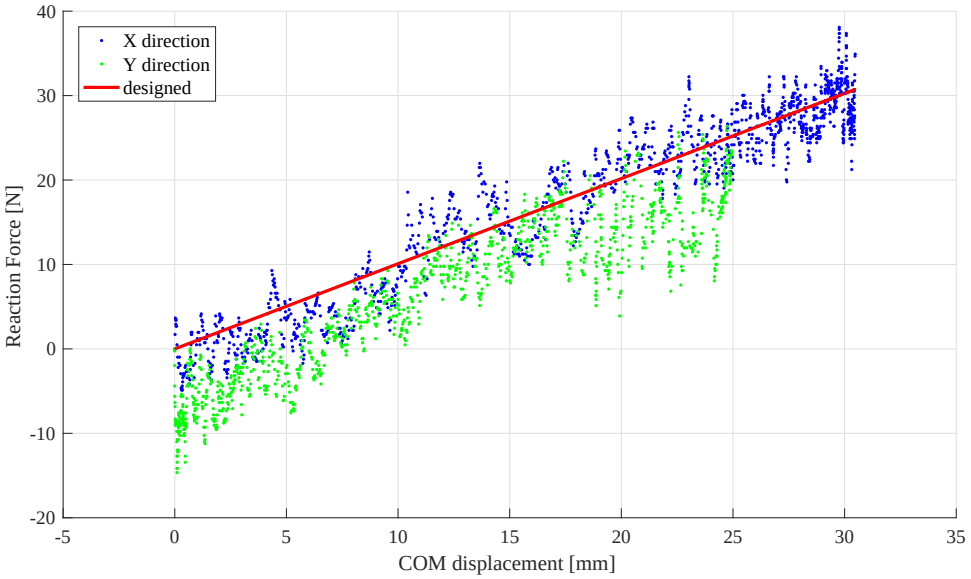

Figure 6.35: Relationship between the disturbance and displacement of the COM when a quasi-static external force was applied. The graph shows that the measured relation between the COM displacement and external force, which is shown in the blue markers, is actually linear and close to the predefined property which is shown as the red line.

kinematics. The COM reaction force is estimated from the foot force torque sensor. The relation between the COM displacement and reaction force is shown in Fig.6.35. In the graph, the blue markers show the measured data and the red line represents the predefined COM stiffness. The two value corresponds well, with the RMS error of 3.1 N. This is 10% of the maximum force in this experiment. It is worth to note that there is no task space level force feedback and the resulted task space force is due to the joint level torque feedback. The accurate task space force means the joint level force controller has a fine accuracy.

Fig.6.36 shows a demonstration where different parts of Hydra are manually moved in different directions. When the robot was moved in the direction that COM also moves, as shown in the left of the figure, the reaction force was relatively high. When the robot was moved in the yawing direction, as shown in the middle of the figure, the reaction force was low and it was observed that the joints cooperate to maintain the COM position while allowing yawing direction displacement. When the force was applied on the top of the backpack, as shown in the right of the figure, the robot bent the waist compliantly while actively moving the pelvis link to the opposite direction to maintain the COM position.

Fig.6.38 shows the time transition of the COM, ZMP, and waist joint angle during the same experiment setup, while this time the disturbance is simpler, as shown in Fig.6.37. The top two graphs show that the ZMP properly moved to push the COM to the initial position, similar to the case with an explicit balancer with the ZMP manipulation. Notice that the ZMP is measured for the evaluation and not used in the controller. The motion of ZMP is implicitly achieved by the COM viscoelasticity.

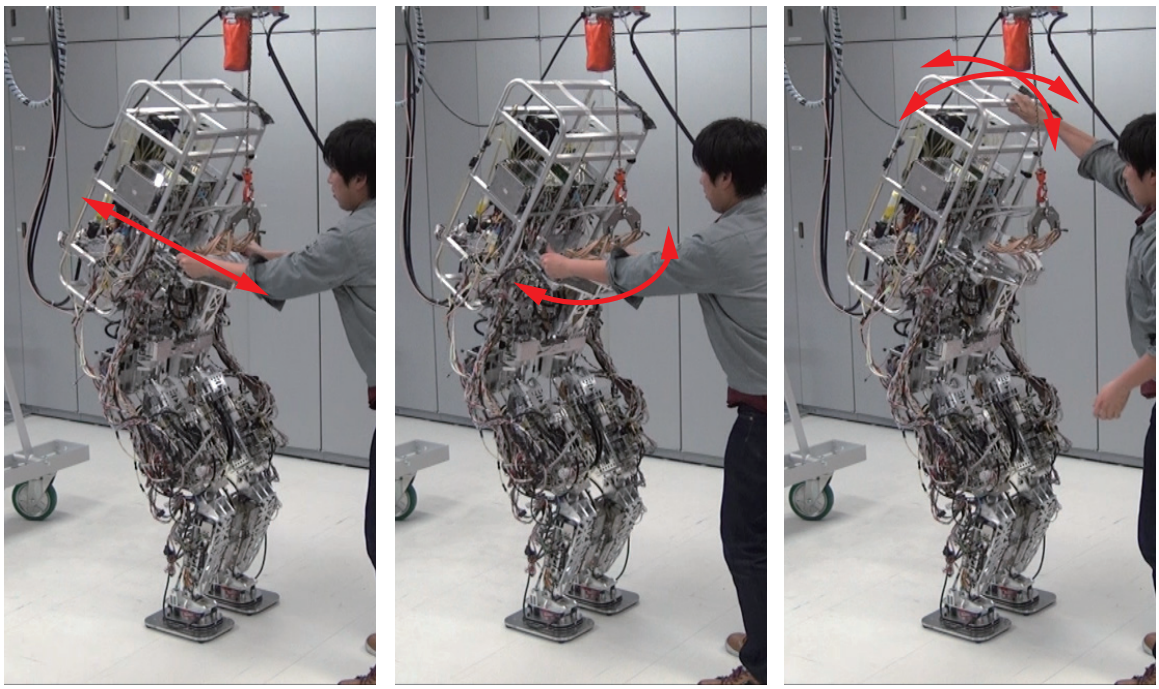

Figure 6.36: Different parts of Hydra are manually moved in different directions. When the robot was moved in the direction that COM also moves (left figure), the reaction force was relatively high. When the robot was moved in the yawing direction (middle), the reaction force was low and it was observed that the joints cooperate to maintain the COM position while allowing yawing direction displacement. When the force was applied on the top of the backpack (right), the robot bent the waist compliantly while moving the pelvis link to the opposite direction to maintain the COM position.

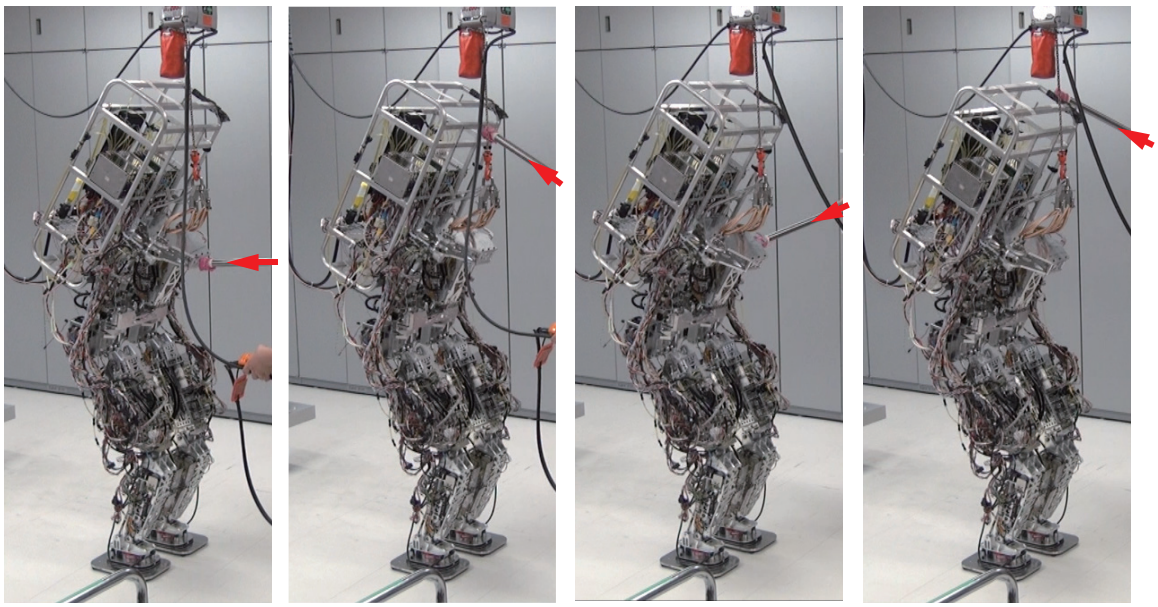

Figure 6.37: Outlook of the balancing experiment with the Resolved Viscoelasticity Control. It was observed that when the disturbance was applied close to the COM, the robot behaved similarly to a stiff robot with a stabilizer, while when the disturbance was on the edge of the body, the robot tries to absorb it compliantly moving the whole body in the direction that does not affect the COM position.

In the timing of around 13 seconds and 27 seconds, the disturbance was given on the highest part of the backpack attached on the torso. The third graph shows that while the waist joint largely moved, the motion of the COM and ZMP were kept as the same as the other cases. This can be interpreted as that the robot absorbed disturbance in the nullspace therefore minimize the effect on the COM motion.

Fig.6.39 shows the view of the walking experiment based on the RVC. During the walking it kept compliant in the nullspace therefore even though a disturbance force was manually applied on the top of the backpack, its effect on the locomotion was suppressed by the compliant motion of the waist joints. Fig.6.40 shows the time transition of the command/actual COM position (estimated from the forward

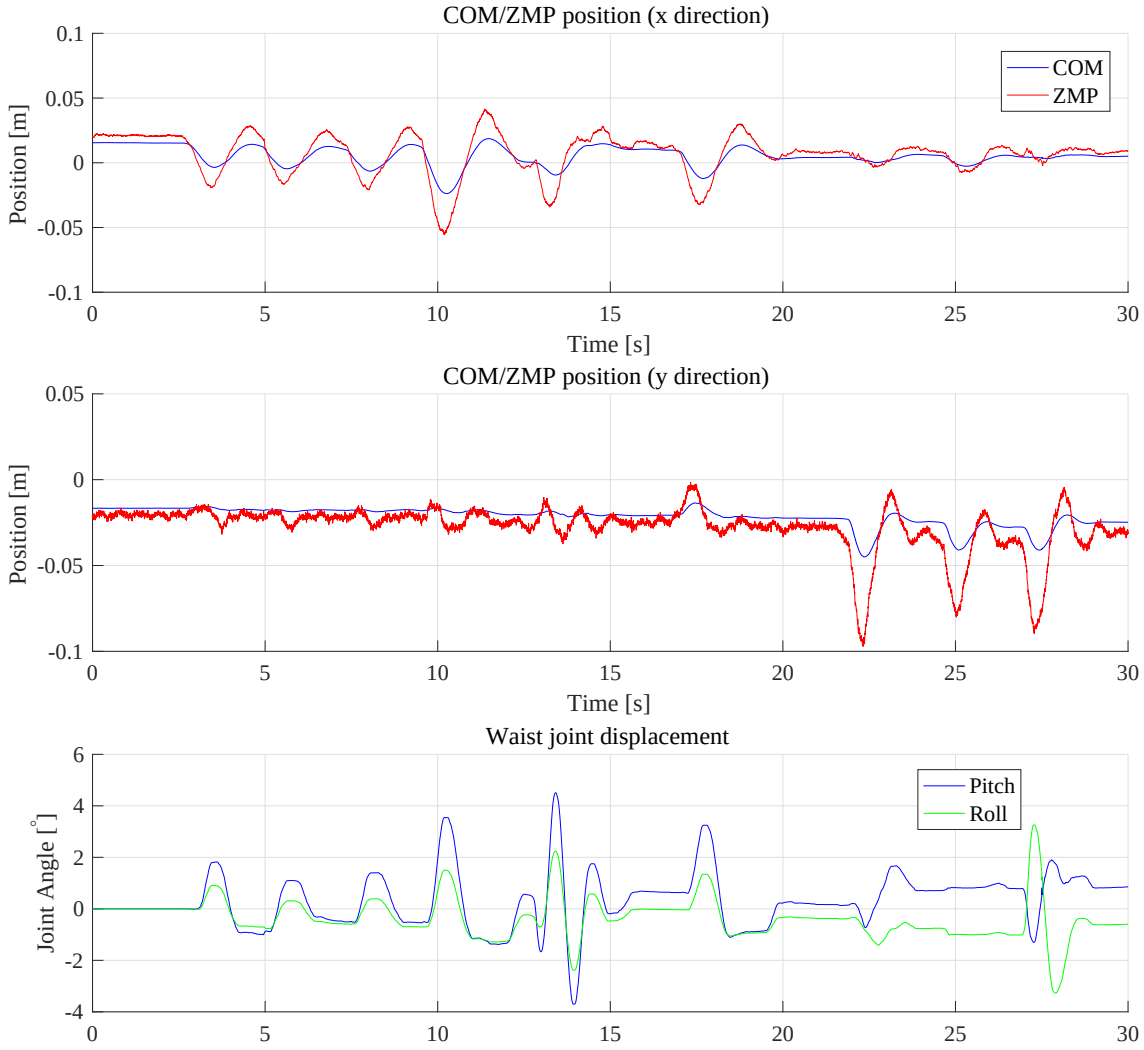

Figure 6.38: Time transition of the COM and ZMP in the X and Y direction, and the joint angle of the waist joint when an impulsive disturbance was given on the different part of the body. The top two graphs show that the ZMP properly moved to push the COM to the initial position, similar to the case with an explicit balancer with the ZMP manipulation. In the timing of around 13 seconds and 27 seconds, the disturbance was given on the highest part of the backpack attached on the torso. The third graph shows that while the waist joint largely moved, the motion of the COM and ZMP were kept as the same as the other cases. This can be interpreted as that the robot absorbed disturbance in the nullspace therefore minimize the effect on the COM motion.

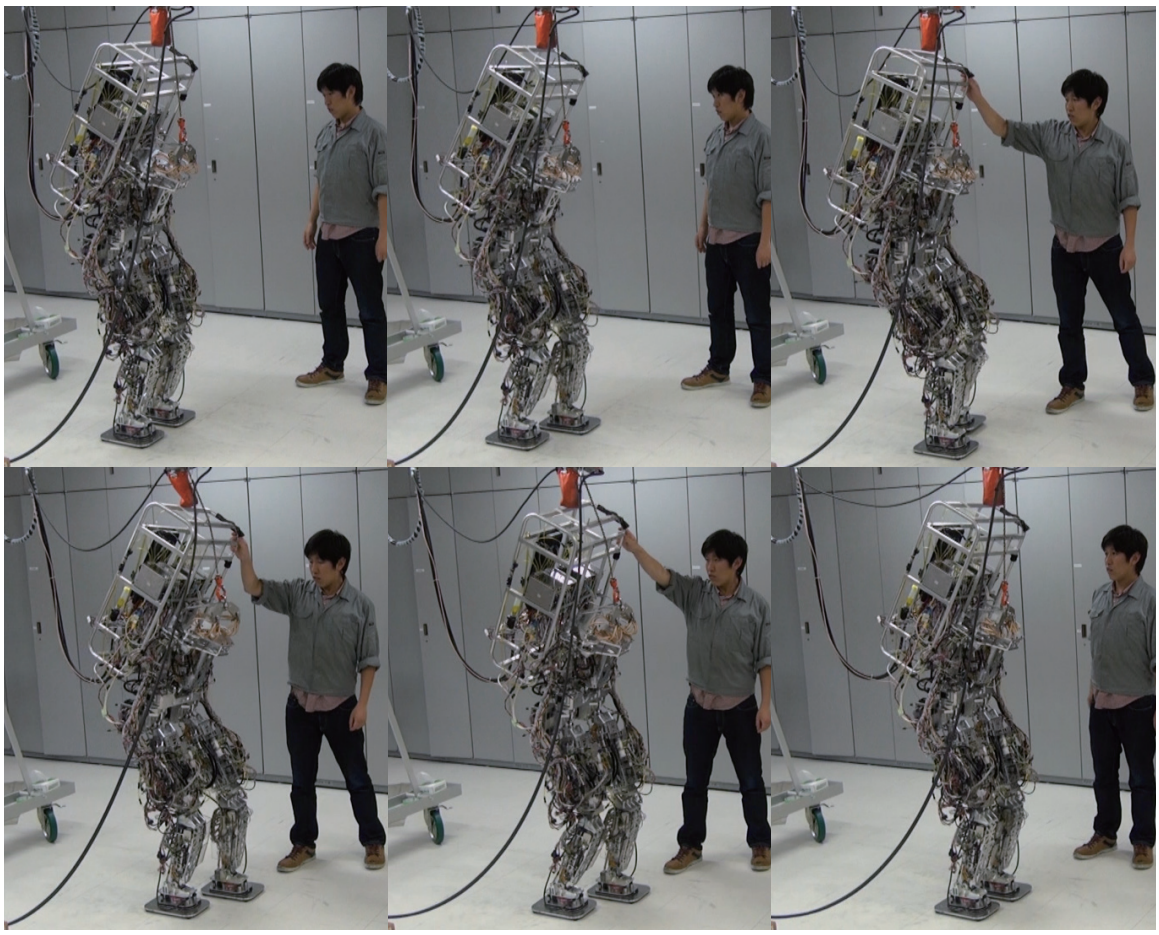

Figure 6.39: Outlook of the walking experiment based on the resolved viscoelasticity control. During the walking it kept compliant in the nullspace therefore even though a disturbance force was manually applied on the top of the backpack, its effect on the locomotion was suppressed by the compliant motion of the waist joints.

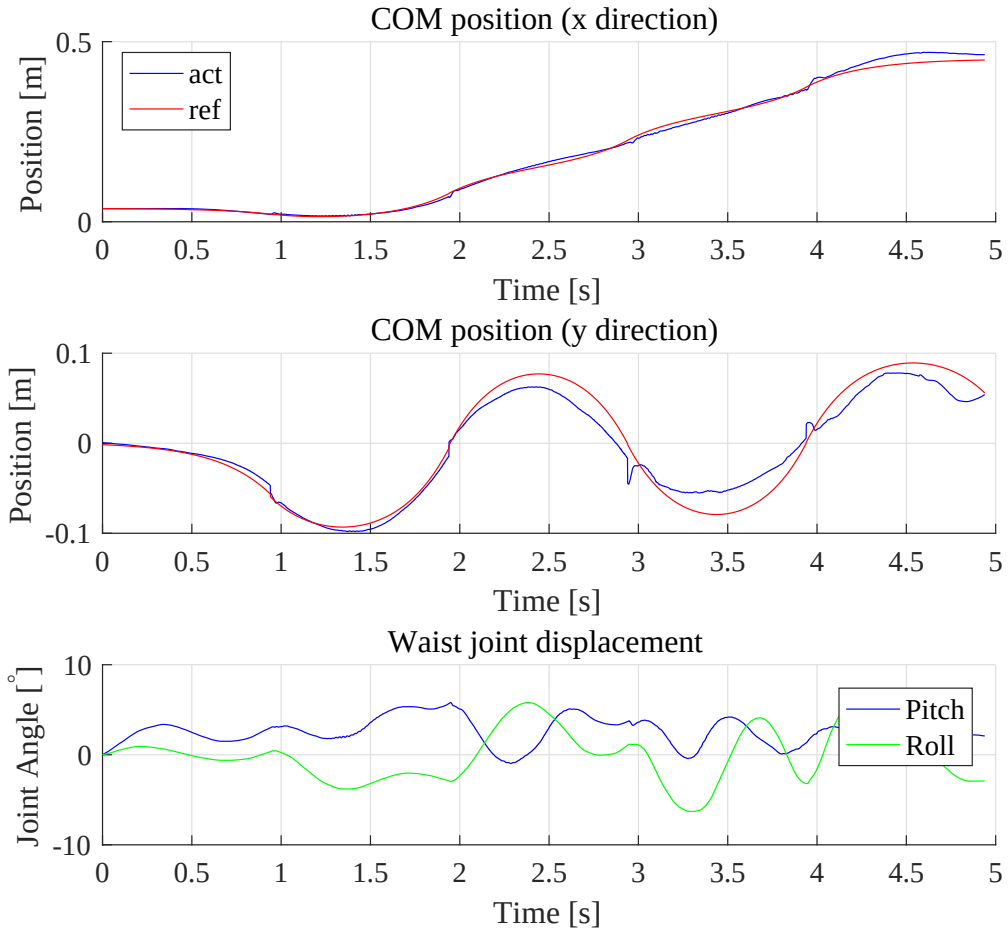

Figure 6.40: Time transition of the command/actual COM position and the joint displacement of the waist joint. A large disturbance was applied on the top of the backpack when the time was 2 - 2.5 second. The bottom graph shows that the waist joint largely moved according to the disturbance. From the COM trajectory, however, it is difficult to see its effect. This shows that the controller successfully separated the motion of the COM and nullspace and absorbed the disturbance by the nullspace compliance.

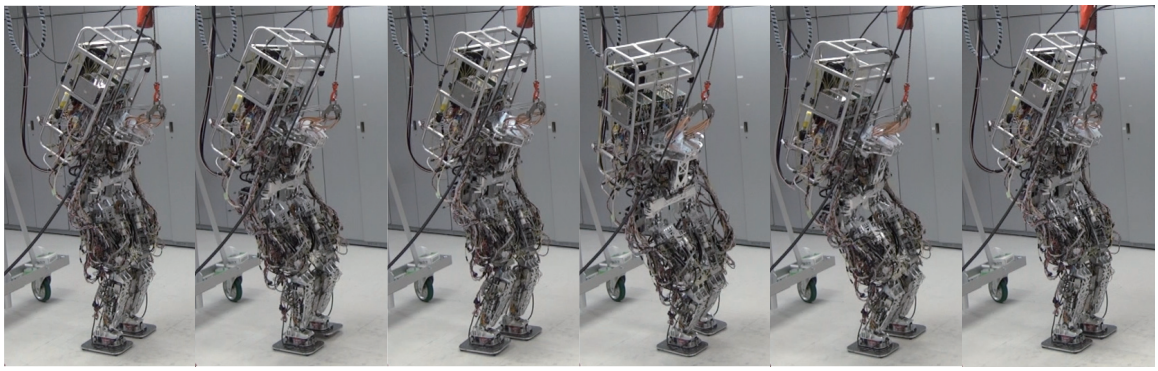

Figure 6.41: Since the whole-body stabilization is realized by the joint compliance, the failure mode is a stable and compliant one. In this figure case the robot failed to step forward due to uncleaned oil on the floor. Nevertheless, it still kept stability and did not fall down.

kinematics from the joint angles) and the joint displacement of the waist joint. Unlike the case with the position control based walking, no CP or ZMP information is used in the control therefore it is now shown in the graph. The command COM position, on the other hand, is available from the preplanned joint trajectory. A large disturbance was applied on the top of the backpack when the time was 2 - 2.5 second. The bottom graph shows that the waist joint largely moved according to the disturbance. From the COM trajectory, however, it is difficult to see its effect. This shows that the controller successfully separated the motion of the COM and nullspace and absorbed the disturbance by the nullspace compliance.

During the experiments, a practical advantage of RVC was seen, which is the robustness against unpredicted accidents such as falling down or slipping due to the floor with uncleaned oil. In the case with explicit ZMP feedback, when the robot fell down, it resulted in a totally unstable and dangerous motion. In the case of RVC, on the contrary, since the whole-body stabilization is realized by the joint compliance,

the failure mode is a stable and compliant one. Fig.6.41 shows an example where the robot failed to step forward due to uncleaned oil on the floor. Nevertheless, it still kept stability and did not fall down.

6.5 Conclusion

In this chapter, we presented our approach to integrate the complex EHA system into a whole-body humanoid Hydra, in each of the hardware, electronics and software level. We also examined its joint level and whole-body control performance, including the walking performance evaluation. The conclusion is as follows:

1. We showed the mechanical design of the humanoid robot "Hydra", whose 40 joints are driven by 24 double rod linear cylinders with the beam structure and eight casing-reinforced vane motor, powered by 36 water cooled trochoid pump in addition to the two five-DoF cluster EHAs for the hand. Parallel actuation was used extensively to separate the actuation force and constraint force, and maximally utilize the actuator force. To realize high modularity, the same actuator and joint structure was taken and the joint geometry parameters were adjusted to adapt different requirements of different joints. The full version robot has 130 kg weight and is 180 cm tall. The reduced lower body version for the walking experiment has 14 DoF and 74 kg.

2. We established a whole body control architecture which is suitable for an EHA driven system with complex physical behavior. The multilayered distributed control system is composed of the motor level motor current feedback loop

running in 20 kHz on the FPGAs, the actuator level force controller running in 5 kHz on the micro-controllers, and the joint level position controller running in 1 kHz on the onboard PC.

3. Due to its high position control performance realized by the high actuator bandwidth, we confirmed that Hydra could perform a position control based locomotion. With a Capture Point based balancing controller, it could keep the standing posture while avoiding external disturbance, During the experiment the ZMP could track the desired one with 8.7 mm RMS error. With the Capture Point Tracking control, Hydra could successfully conduct a walking motion with 0.2 m stride, 30 mm step height and 1 second stepping time.

4. All EHA driven joints of Hydra are highly backdrivable and torque controllable. The gravity compensation experiment showed that the joints were easy to be moved by human hand and kept the same position when there was no external force. The joint torque accurately tracked the varying command joint torque according to the varying joint angle, with the RMS error of 0.73 Nm. Hydra could also generate the COM reaction force in the task space in the range of 0 - 30 N with the RMS error of 3.1 N.

5. With its high joint backdrivability, Hydra can prevent a disturbance force applied on a distal link to be transferred to other links. By simply reducing the position feedback gain, the effect of a disturbance force on ZMP variation was suppressed to 30%. With the resolved viscoelasticity control, The apparent mass of the robot on the top tip of the torso was experimentally confirmed to

be 11.8 kg, which is 18% of the 65.5 kg value when a force was applied to the point close to the COM. Similarly, the apparent stiffness was 378 N/m for the distal point, which is 34% of the 1110 N/m for the point close to the COM.

6. Simultaneously realizing both of the moderate stiffness of the COM and compliant motion in the nullspace, it was experimentally confirmed that Hydra could conduct a stable balancing and locomotion while absorbing external force by the nullspace motion.

Chapter7

Conclusion

In this dissertation, we established a generalized hardware design, control, and system integration framework to realize a hydrostatically driven humanoid robot, and experimentally showed its performance of the joint torque control, disturbance rejection and locomotion. The challenge was the enhancement of the torque density and control bandwidth of the small and light-weight EHA. The key advantage of a hydrostatically driven robot was the coexistence of the high backdrivability and fast response, therefore enable both a high stiffness control for a target task and a highly compliant motion in the null space with the same hardware. The tackled problems were as follows:

1. To derive a simple EHA model from the complex model described with hardware design parameters, therefore connecting the mechanical design and controller design.

2. To provide a systematic mechanical design approach to enable miniature backdrivable EHA with enough torque density to drive a humanoid robot.

3. To enhance the backdrivability of the newly designed high torque EHA to realize highly backdrivable robot joints.

4. To enhance and experimentally prove the high response property of EHA to enable an EHA driven robot to precisely control the reaction force or posture to realize a balancing and walking motion.

5. To provide a system integration framework to integrate the complex EHA to the whole-body actuation system of a humanoid robot and examine its joint level and whole-body control performance, including disturbance rejection and walking performance evaluation.

In chapter 2, we derived a simplified mass-spring-damper EHA model from the fluiddynamical and material mechanical principle. This approximation was possible with the assumption that the flow inside the pump is laminar, the pump is a rotary one, and all values such as pump torque/velocity and fluid pressure/flow-rate are expressed in the equivalent value seen from the actuator. The actuator output force is affected by both the motor torque and the actuator output velocity, as the second order lag system. The output velocity of the actuator is a third order lag system from the motor torque input. We also experimentally showed that our simplified model, with parameters identified in the quasi-static conditions, had close dynamic behaviors with the one of the real actuator.

In chapter 3, we proposed a systematic mechanical design approach to improve the miniature backdrivable EHA's torque density, which is currently too low to actuate legged robots. We made it clear that miniaturization of the system size has the effect of increasing internal leakage and therefore impair the output force. To encounter it, the key was to attain small internal gap and high fluid viscosity, while maximizing the effective pressure receiving surface in the limited overall weight or size. To reduce

the gap inside the pump, we experimentally showed that the optimization of bearing arrangement or type, and reinforcement of the pump casing are effective. To reduce the gap in the actuator, we presented the design of a light weight cylinder and a vane motor with reinforced casing rigidity. To maintain the fluid viscosity, we proposed a direct pump casing water cooling approach. Lastly, we showed the integrated tie rod cluster cylinder to maximize the effective pressure receiving surface.

In chapter 4, we provided the enrichment of the backdrivability of the high torque density EHA developed in the previous chapter. To minimize the viscous friction, double rod cylinders are more suitable since the closed circuit volume is invariant. We proposed a double rod cylinder design with the beam structure to minimize the piston rod diameter, therefore minimize the friction due to the piston rod oil seal. We also presented an active friction compensation of the rod oil seal with the merged information of the pressure sensor and strain gauge by a complementary filter.

In chapter 5, from both the hardware and control perspective, we present the enhancement of the fast response property of EHA, proving their superiority over elastic actuators in the sense of the closed-loop control bandwidth. From the hardware side, to reduce the series elasticity between the pump and the load, we filled the dead volume in the chamber and selected the high bulk-modulus fluid since the fluid compressibility is a large source of elasticity. We also applied the reinforcement on the force transmission structure, with which a clear improvement in the response was seen. From the control side, we introduced the current-pressure-position triple-loop feedback controller. The idea is to distribute the controller in three layers with different framerate processing device and control faster behavior in a faster device,

instead of treating the large number of internal parameters as a single state vector. The pressure control bandwidth in the fixed piston configuration was 100 Hz, which is clearly higher than that of state-of-the-art series elastic actuators and pneumatic ones.

In chapter 6, we presented our approach to integrate the complex EHA system into a whole-body humanoid, in each of the hardware, electronics and software level. We also examined its joint level and whole-body control performance, including the walking performance evaluation. The hydrostatically driven humanoid "Hydra" has 40 joints driven by 24 double rod linear cylinders with the beam structure and eight casing-reinforced vane motor, powered by 36 water cooled trochoid pump in addition to the two five-DoF cluster EHAs for the hand. The full version robot has 130 kg weight and is 180 cm tall. The reduced lower body version for the walking experiment has 14 DoF and 60 kg.

Due to its high position control performance realized by the high actuator bandwidth, we confirmed that Hydra could perform a position control based locomotion. with 0.2 m stride, 30 mm step height and 1 second stepping time. With its high joint backdrivability, Hydra can prevent a disturbance force applied on a distal link to be transferred to other links. Simultaneously realizing both of the moderate stiffness of the COM and compliant motion in the nullspace by the resolved viscoelasticity controller, it was experimentally confirmed that Hydra could perform a stable balancing and locomotion while absorbing external force by the nullspace motion.

Acknowledgments

This dissertation was written under the supervision of Professor Yoshihiko Nakamura. He was my adviser when I was in my third year of the undergraduate, before the students were assigned to the lab. Since I entered his lab from the fourth year undergraduate, through my master course, until the doctor course, he has been by supervisor. His unconstrained ideas, clear instructions and unbounded enthusiasm to the research strongly propelled me to my goal. I express sincere gratitude to him.

I also want to express my appreciation to Professor Hiroshi Kaminaga. He was an assistant professor in our lab, who established the foundation of EHA as robot actuators. Though I could not work with him for the last years since he moved out to AIST, he established all my foundation in robotics and mechatronics. I still remember his first word in my welcome party:"Hey you, are you interested in hydraulics?" I'm also especially grateful to Professor Ko Yamamoto, who is actually an alumnus of our lab and returned as an associate professor. His return was in a great timing since he is a specialist on the humanoid walking control and I was just at the stage to finish the integration of the developing robot and trying to make it walk.

I want to express special thanks to all of the lab members, former or current. Professor Wataru Takano gave me many pieces of precious advice on my university life. Dr. Yosuke Ikegami showed me how a doctor course student should be. I still remember his help when I broke the lab's shared PC in my first week. Dr. Ko Ayusawa's precious advice, both on my research and on the lab life, was a great help. I also thanks him for the delicious one-pound hamburger steak. Dr. Akihiko Murai told me many interesting stories on his carriers, which encouraged me a lot. Dr. Stephane Caron was my role model as a researcher. His deep knowledge and

high skill was a good stimulation to me. Chattering with Jose Enrique Chen always relieved me from the stress. Thanks to Rorenzo Vannucci for his deep knowledge and instruction on the programming and computer systems. Thanks to Rohan Budhiraja for his humor, and for his kind help during my internship in France.

Special thanks to all members worked on Hydra. The huge amount of work on Hydra could not be accomplished only by my own effort. Ryo Masumura was a nice colleague and a good friend. He made the initial concept and design of the knee. Mitsuo Komagata did a large number of works on the foot design, modification of cylinder design, and assembly of the vane motors. Shunsuke Sato played an important role in the electric wiring and experiments, in addition to his large contribution to the shoulder design. Satoshi Yorita was a great mechanical engineer, who fixed many of our mistaken designed parts. He also assembled most of the hydraulic pumps with me, which was a truly tough work, in addition to his intense work on torso design. Tatsuya Ishikawa helped me a lot in assembling of fingers and designing of the arms.

Masaki Hayashi is my nice friend and was like my technical advisor on the electronics. In his one year short stay in our lab, he gave us many useful suggestions and information from the industrial perspective. He also contributed to introduce the real-time kernel to Hydra's onboard PC. Yasuhiro Ishiguro played a special role in the establishment of the software framework for Hydra. Sundermeyer Martin Bernd, Juntaro Tamura, and Seyde Tim Niklas's continuous works were essential for the development of walking controller. Kazuya Murotani's work on the walking controller was especially important, kicking the final goal to connect the walking controller in the closed simulator environment to the real robot. Thanks to Ostroumov Georgy for

his help on the maintenance of Hydra. His works were extraordinary fast. Thanks to Bryan Penin's internship work on water cooling systems. Thanks for the help by Ayaka Yamada, Takafumi Ikemoto, and Yumiko Furuhata during the hard time in Las Vegas and Los Angeles.

I also want to express my appreciation to the staffs in the lab. Ms. Eri Totsuka, the technical specialist, helped me a lot, especially in the hard re-arrangement and re-surfacing of the experiment room. Mr. Masamitsu Saito, the technical staff, actually told me many skills in the undergraduate exercise course. The large number of kind helps by Ms. Shoko Odagiri, the project academic support staff, were very important in the daily life.

The contents of this dissertation include the works by the collaboration with a large number of the members included in the project to develop the humanoid robot. Some of the developments are based on the knowledge or prototype originally developed in the lab. Therefore, here I clarify my personal contribution in the whole system development. The contents in chapter 2 is my personal work, motivated by the mismatch that while our original model did not include any elasticity, the actual behavior of the system clearly showed a behavior with a series elasticity. For chapter 3, subsection 3.3.1 and 3.5 is my individual work, as a part of the project to develop a more forceful robot hand. Subsection 3.3.2 is the result of the improvement based on a prototype cylinder by the collaboration of myself and Satoshi Otsuki. The prototype cylinder was developed right after the development of the smaller cylinder in 3.5 and it includes the experiences accumulated there. The improvement was done to improve the structure strength and match the requirement for the developing humanoid, which

is the team work by myself, Ryo Masumura, and Mitsuo Komagata. The vane motor in subsection 3.3.3 is designed by Prof. Kaminaga and assembled/tested by myself and Mitsuo Komagata. The water cooling mechanism in section 3.4 is based on the process: (1) necessity pointed by myself based on the experience in 3.3.1, (2) water cooling casing designed by Prof. Kaminaga, (3) assembled/evaluated by myself. As shown above, the contents in chapter 3 were originally developed independently and heuristically, and it was my individual work to re-organize them by extracting their common background – reduction of internal leakage. Before this work, it was already known from the experiences that we need to keep the balance between the internal leakage and viscous friction. However, it is my personal contribution to point out that there is a scale effect where the miniaturization of the system leads the internal leakage to be dominant, therefore we need to pay an extra effort to reduce it for a small-sized EHA, as shown in section 3.2.

For the contents in chapter 4, the pump in section 4.2 is based on the prototype developed by Prof. Kaminaga. I applied the technique shown in chapter 3 to improve torque density, which is the modification of the bearing type, structure stiffness, and water cooling. The specification of the pump rotor is not modified by myself. The active friction compensation of the oil seal in section 4.4 is planned by Prof. Kaminaga and implemented/evaluated by myself. For chapter 5, it is my individual contribution to firstly point that the advantage of EHA over series elastic actuators or pneumatic actuators is its possibility of high control bandwidth, and we need to focus on it to achieve a locomotion of the humanoid robot. At last, this was the last key to make the robot walk, after a long time suffering that the robot could show a walking motion

in the air but could not actually walk on the ground. The electric system, or the motor driver, is developed by the Brains Corporation, and the initial framework of the firmware was developed by Prof. Kaminaga. Its debugging, implementation of the controller, and all of the evaluations are done by myself.

For the development of the whole humanoid, which is the contents of chapter 6, the mechanical development and was done by the team including Ryo Masumura, Mitsuo Komagata, Satoshi Yorita, Shunsuke Sato, and myself. Its maintenance and upgrade were made by Yorita, Sato and me. The framework of the whole-body communication system with EtherCAT was mainly established by Prof. Kaminaga and maintained by me to match the latest updates on the hardware, embedded controller, and whole-body controller. The initial whole-body control framework is developed by Prof. Kaminaga and Yasuhiro Ishiguro, and the integration of the walking controller to the control system is done by myself and Kazuya Murotani. The experiments and evaluations on the real hardware, from the basic gain tune to the locomotion, was mostly my personal work.

Finally, I would like to gratefully acknowledge the support by the Graduate Program for Social ICT Global Creative Leaders (GCL) of The University of Tokyo by Japan society for the promotion of science, and my greatest appreciation to my family. Their precious advice and experiences strongly encouraged me. This work was totally impossible without their support in many aspects.

Bibliography

[1] Bruno Siciliano and Oussama Khatib. *Springer handbook of robotics*. Springer Science & Business Media, 2008.

[2] Ray C Goertz. Manipulator Systems Developed at ANL. In *Proc. of The 12th Conference on Remote Systems Technology*, pages 117–136, 1964.

[3] C Loucks, V Johnson, P Boissiere, G Starr, and J Steele. Modeling and control of the Stanford/JPL hand. In *Proc. of IEEE Int'l Conf. on Robotics and Automation.* , volume 4, pages 573–578, 1987.

[4] J Kenneth Salisbury and John J Craig. Articulated hands: Force control and kinematic issues. *The International journal of Robotics Research*, 1(1):4–17, 1982.

[5] Anthony R Lanfranco, Andres E Castellanos, Jaydev P Desai, and William C Meyers. Robotic surgery: a current perspective. *Annals of surgery*, 239(1):14, 2004.

[6] I. Mizuuchi, T. Yoshikai, Y. Sodeyama, Y. Nakanishi, A. Miyadera, T. Yamamoto, T. Niemela, M. Hayashi, J. Urata, Y. Namiki, T. Nishino, and M. Inaba. A musculoskeletal flexible-spine humanoid 'Kotaro' aiming at year 2020. In *Proc. of International Symposium on Robotics*, page TH1C4, 2005.

[7] Ikuo Mizuuchi, Yuto Nakanishi, Yoshinao Sodeyama, Yuta Namiki, Tamaki Nishino, Naoya Muramatsu, Junichi Urata, Kazuo Hongo, Tomoaki Yoshikai, and Masayuki Inaba. An advanced musculoskeletal humanoid kojiro. In *Humanoid Robots, 2007 7th IEEE-RAS International Conference on*, pages 294–299. IEEE, 2007.

[8] Y. Nakanishi, T. Izawa, M. Osada, N. Ito, S. Ohta, J. Urata, and M. Inaba. Development of musculoskeletal humanoid kenzoh with mechanical compliance changeable tendons by nonlinear spring unit. In *IEEE International Conference on Robotics and Biomimetics*, pages 2384–2389, 2011.

[9] Y. Nakanishi, Y. Asano, T. Kozuki, H. Mizoguchi, Y. Motegi, M. Osada, T. Shirai, J. Urata, K. Okada, and M. Inaba. Design concept of detail musculoskeletal humanoid Kenshiro-toward a real human body musculoskeletal simulator. In *Proc. of IEEE-RAS International Conference on Humanoid Robots*, pages 1–6, 2012.

[10] Y. Asano, T. Kozuki, S. Ookubo, M. Kawamura, S. Nakashima, T. Katayama, I. Yanokura, T. Hirose, K. Kawaharazuka, S. Makino, et al. Human mimetic musculoskeletal humanoid kengoro toward real world physically interactive actions. In *Proc. of IEEE-RAS Int'l Conf. on Humanoid Robots*, pages 876–883, 2016.

[11] D Gall and F Steghart. Improvements in or relating to servo systems, Patent GB620688 filled 1946.

[12] W. C. Moog. Electrohydraulic servo mechanism, Patent US2625136 filled 1950.

[13] Marc Raibert, Kevin Blankespoor, Gabriel Nelson, and Rob Playter. Bigdog, the rough-terrain quadruped robot. *IFAC Proceedings Volumes*, 41(2):10822–10825, 2008.

[14] Claudio Semini, Nikos G Tsagarakis, Emanuele Guglielmino, Michele Focchi, Ferdinando Cannella, and Darwin G Caldwell. Design of hyq–a hydraulically and electrically actuated quadruped robot. *Proc. of the Institution of Mechanical Engineers, Part I: Journal of Systems and Control Engineering*, 225(6):831–849, 2011.

[15] G. Nelson, A. Saunders, N. Neville, B. Swilling, J. Bondaryk, D. Billings, C. Lee, R. Playter, and M. Raibert. Petman: A humanoid robot for testing chemical protective clothing. *Journal of the Robotics Society of Japan*, 30(4):372–377, 2012.

[16] Boston Dynamics: Atlas The Agile Anthropomorphic Robot. `http://www.bostondynamics.com/robot_Atlas.html`.

[17] G. Cheng, Sang-Ho Hyon, J. Morimoto, A. Ude, G. Colvin, W. Scroggin, and S.C. Jacobsen. CB: A Humanoid Research Platform for Exploring NeuroScience. pages 182 –187, 2006.

[18] Gordon Cheng, Sang-Ho Hyon, Jun Morimoto, Aleš Ude, Joshua G Hale, Glenn Colvin, Wayco Scroggin, and Stephen C Jacobsen. Cb: A humanoid research platform for exploring neuroscience. *Advanced Robotics*, 21(10):1097–1114, 2007.

[19] C.W. Musser. Strain wage gearing, US2906143A filled 1957.

[20] History of Harmonic Drive Systems Inc. `http://www.hds.co.jp/english/company/statutes/`.

[21] H. Asada and T. Kanade. Design concept of direct-drive manipulators using rare-earth DC torque motors. In *Proc. of the Int'l Joint Conf. on Artificial intelligence*, pages 775–778, 1981.

[22] S. Seok, A. Wang, M.Y. Chuah, D. Otten, J. Lang, and S. Kim. Design principles for highly efficient quadrupeds and implementation on the MIT Cheetah robot. In *Proc. of IEEE Int'l Conf. on Robotics and Automation*, pages 3307–3312, 2013.

[23] S. Seok, A. Wang, D. Otten, and S. Kim. Actuator Design for High Force Proprioceptive Control in Fast Legged Locomotion. In *Proc. of IEEE/RSJ Int'l Conf. on Intelligent Robots and Systems*, pages 1970–1975, 2012.

[24] P. M. Wensing, A. Wang, S. Seok, D. Otten, J. Lang, and S. Kim. Proprioceptive Actuator Design in the MIT Cheetah: Impact Mitigation and High-Bandwidth Physical Interaction for Dynamic Legged Robots. *IEEE Transactions on Robotics*, 33(3):509–522, 2017.

[25] S. Jacobsen, E. Iversen, D. Knutti, R. Johnson, and K. Biggers. Design of the Utah/M.I.T. Dextrous Hand. In *Proc. IEEE Int'l Conf. on Robotics and Automation.*, volume 3, pages 1520 – 1532, 1986.

[26] Richard H Gaylord. Fluid actuated motor system and stroking device, Patent US2844125 filled 1955.

[27] Shadow Dexterous Hand Now available for purchase. `https://www.shadowrobot.com/products/dexteroushand`.

[28] Björn Verrelst, Bram Vanderborght, Jimmy Vermeulen, Ronald Van Ham, Joris Naudet, and Dirk Lefeber. Control architecture for the pneumatically actuated dynamic walking biped lucy. *Mechatronics*, 15(6):703–729, 2005.

[29] R. Niiyama, S. Nishikawa, and Y. Kuniyoshi. Athlete robot with applied human muscle activation patterns for bipedal running. In *IEEE-RAS International Conference on Humanoid Robots*, pages 498–503, 2010.

[30] AV Hill. The heat of shortening and the dynamic constants of muscle. *Proceedings of the Royal Society of London B: Biological Sciences*, 126(843):136–195, 1938.

[31] K. Hyodo and H. Kobayashi. A study on tendon controlled wrist mechanism with nonlinear spring tensioner. *Journal of the robotics Society of Japan*, 11(8):1244–1251, 1993.

[32] G.A. Pratt and M.M. Williamson. Series Elastic Actuators. In *Proc. of IEEE/RSJ Int'l Conf. on Intelligent Robots and Systems*, pages 399 –406, 1995.

[33] N.G. Tsagarakis, S. Morfey, G.M. Cerda, Li Zhibin, and D.G. Caldwell. COMpliant huMANoid COMAN: Optimal joint stiffness tuning for modal frequency

control. In *Proc. of IEEE Int'l Conf. on Robotics and Automation*, pages 673–678, 2013.

[34] F. Negrello, M. Garabini, M. G Catalano, P. Kryczka, W. Choi, D. G Caldwell, A. Bicchi, and N. G Tsagarakis. Walk-man humanoid lower body design optimization for enhanced physical performance. In *IEEE International Conference on Robotics and Automation*, pages 1817–1824, 2016.

[35] C. Knabe, J. Seminatore, J. Webb, M. Hopkins, T. Furukawa, A. Leonessa, and B. Lattimer. Design of a Series Elastic Humanoid for the DARPA Robotics Challenge. In *Proc. of IEEE-RAS Int'l Conf. on Humanoid Robots*, pages 738–743, 2015.

[36] B. Vanderborght, A. Albu-Schaeffer, A. Bicchi, E. Burdet, D. G. Caldwell, R. Carloni, M. Catalano, O. Eiberger, W. Friedl, G. Ganesh, M. Garabini, M. Grebenstein, G. Grioli, S. Haddadin, H. Hoppner, A. Jafari, M. Laffranchi, D. Lefeber, F. Petit, S. Stramigioli, N. Tsagarakis, M. Van Damme, R. Van Ham, L. C. Visser, and S. Wolf. Variable impedance actuators: A review. *Robotics and Autonomous Systems*, 61(12):1601–1614, 2013.

[37] M. Grebenstein, A. Albu-Schäffer, T. Bahls, M. Chalon, O. Eiberger, W. Friedl, R. Gruber, S. Haddadin, U. Hagn, R. Haslinger, H. Hoppner, S. Jorg, M. Nickl, A. Nothhelfer, F. Petit, J. Reill, N. Seitz, T. Wimbock, S. Wolf, T. Wusthoff, and G. Hirzinger. The DLR hand arm system. In *Proc. of IEEE Int'l Conf. on Robotics and Automation*, pages 3175 –3182, 2011.

[38] S. Wolf, O. Eiberger, and G. Hirzinger. The DLR FSJ: Energy based design of a variable stiffness joint. In *IEEE Int'l Conf. on Robotics and Automation*, pages 5082–5089, 2011.

[39] T. Otani, K. Hashimoto, S. Hamamoto, S. Miyamae, M. Sakaguchi, Y. Kawakami, H. Lim, and A. Takanishi. Knee joint mechanism that mimics elastic characteristics and bending in human running. In *IEEE/RSJ Int'l Conf. on Intelligent Robots and Systems*, pages 5156–5161, 2015.

[40] M. Zinn, B. Roth, O. Khatib, and J. K. Salisbury. A new actuation approach for human friendly robot design. *The International Journal of Robotics Research*, 23(4-5):379–398, 2004.

[41] Y. Fujimoto, Issam A Smadi, H. Omori, K. Suzuki, and H. Hamada. Modeling and control of a high-thrust direct-drive spiral motor. In *IEEE International Power Electronics Conference*, pages 2222–2229, 2010.

[42] Electrohydrostatic Actuators Moog. `http://www.moog.com/products/actuatorsservoactuators/actuationtechnologies/electrohydrostatic`.

[43] Compact HST Takako Industries Inc. `http://www.takakoinc.com/english/products/hst.html`.

[44] Christian Favre. Fly-by-wire for commercial aircraft: the Airbus experience. *International Journal of Control*, 59(1):139–157, 1994.

[45] Navatha Alle, Somashekhar S Hiremath, Singaperumal Makaram, Karunanidhi Subramaniam, and Apratim Talukdar. Review on electro hydrostatic actuator for flight control. *International Journal of Fluid Power*, 17(2):125–145, 2016.

[46] J. E. Bobrow and J. Desai. A high torque to weight ratio robot actuator. *Robotica*, 13(2):201–208, 1995.

[47] S. Habibi and A. Goldenberg. Design of a new high performance electrohydraulic actuator. In *Proc. of IEEE/ASME International Conference on Advanced Intelligent Mechatronics*, pages 227–232. IEEE, 1999.

[48] H. Kaminaga. Study on Electro-Hydrostatic Actuators for Force Sensitive Robot Systems. *Ph.D theis, The University of Tokyo*, 2009.

[49] H. Kaminaga, T. Yamamoto, J. Ono, and Y. Nakamura. Backdrivable miniature hydrostatic transmission for actuation of anthropomorphic robot hands. In *Proc. of IEEE-RAS Int'l Conf. on Humanoid Robots*, pages 36 –41, 2007.

[50] H. Kaminaga, J. Ono, Y. Shimoyama, T. Amari, Y. Katayama, and Y. Nakamura. Anthropomorphic robot hand with hydrostatic cluster actuator and detachable passive wire mechanism. pages 1 – 6, 2009.

[51] H. Kaminaga, J. Ono, Y. Nakashima, and Y. Nakamura. Development of backdrivable hydraulic joint mechanism for knee joint of humanoid robots. In *Proc. of IEEE Int'l Conf. on Robotics and Automation* , pages 1577–1582, 2009.

[52] H. Kaminaga, T. Amari, Y. Niwa, and Y. Nakamura. Development of knee power assist using backdrivable electro-hydrostatic actuator. In *Proc. of IEEE/RSJ Int'l Conf. on Intelligent Robots and Systems*, pages 5517–5524, 2010.

[53] H. Kaminaga, T. Amari, Y. Katayama, J. Ono, Y. Shimoyama, and Y. Nakamura. Backdrivability analysis of electro-hydrostatic actuator and series dissipative actuation model. In *Proc. of IEEE International Conference on Robotics and Automation*, pages 4204–4211, 2010.

[54] S. Alfayad, F. B Ouezdou, F. Namoun, and G. Gheng. High performance integrated electro-hydraulic actuator for robotics–Part I: Principle, prototype design and first experiments. *Sensors and Actuators A: Physical*, 169(1):115–123, 2011.

[55] S. Alfayad, F. B Ouezdou, F. Namoun, and G. Gheng. High performance Integrated Electro-Hydraulic Actuator for robotics. Part II: Theoretical modelling, simulation, control & comparison with real measurements. *Sensors and Actuators A: Physical*, 169(1):124–132, 2011.

[56] M Elasswad, A Tayba, A Abdellatif, S Alfayad, and K Khalil. Development of lightweight hydraulic cylinder for humanoid robots applications. *Proc. of the Institution of Mechanical Engineers, Part C: Journal of Mechanical Engineering Science*, page 0954406217731794, 2017.

[57] H. Kaminaga, K. Odanaka, Y. Ando, S. Otsuki, and Y. Nakamura. Evaluations on contribution of backdrivability and force measurement performance on force sensitivity of actuators. In *Proc. of IEEE/RSJ Int'l Conf. on Intelligent Robots and Systems*, pages 4472–4477, 2013.

[58] S. Alfayad, F. B Ouezdou, and F. Namoun. New 3-DOFs hybrid mechanism for ankle and wrist of humanoid robot: modeling, simulation, and experiments. *Journal of Mechanical Design*, 133(2):021005, 2011.

[59] S. Alfayad, A. M Tayba, F. B Ouezdou, and F. Namoun. Kinematic Synthesis and Modeling of a Three Degrees-of-Freedom Hybrid Mechanism for Shoulder and Hip Modules of Humanoid Robots. *Journal of Mechanisms and Robotics*, 8(4):041017, 2016.

[60] J. Watton. *Fluid power systems: modeling, simulation, analog and microcomputer control*. Prentice-Hall, Inc., 1989.

[61] W. Lee, M. J. Kim, and W. K. Chung. Joint torque servo control of electro-hydrostatic actuators for high torque-to-weight ratio robot control. In *IEEE/RSJ Int'l Conf. on Intelligent Robots and Systems*, pages 368–375. IEEE, 2016.

[62] K. Tsuda, T. Sakuma, K. Umeda, S. Sakaino, and T. Tsuji. Resonance-suppression Control for Electro-hydrostatic Actuator as Two-inertia System. *IEEJ Journal of Industry Applications*, 6(5):320–327, 2017.

[63] M. Aoki, H. Fujimoto, Y. Hori, and T. Takahashi. Robust resonance suppression control based on self resonance cancellation disturbance observer and application to humanoid robot. In *IEEE Int'l Conf. on Mechatronics*, pages 623–628. IEEE, 2013.

[64] H. Kaminaga, S. Otsuki, and Y. Nakamura. Development of High-Power and Backdrivable Linear Electro-Hydrostatic Actuator. In *Proc. of IEEE-RAS Int'l Conf. on Humanoid Robots*, pages 973–978, 2014.

[65] Masato Hirose. Development of humanoid robot asimo. In *Proc. IEEE/RSJ Int'l Conf. on Intelligent Robots and Systems*, 2001.

[66] J. Urata, T. Hirose, Y. Namiki, Y. Nakanishi, I. Mizuuchi, and M. Inaba. Thermal control of electrical motors for high-power humanoid robots. In *IEEE/RSJ Int'l Conf. on Intelligent Robots and Systems*, pages 2047–2052, 2008.

[67] J. Urata, Y. Nakanishi, K. Okada, and M. Inaba. Design of high torque and high speed leg module for high power humanoid. In *Proc. of IEEE/RSJ Int'l Conf. on Intelligent Robots and Systems*, pages 4497–4502, 2010.

[68] T. Ko, H. Kaminaga, and Y. Nakamura. Underactuated four-fingered hand with five electro hydrostatic actuators in cluster. In *Proc. of IEEE Int'l Conf. on Robotics and Automation*, pages 620–625, 2017.

[69] T. Kang, H. Kaminaga, and Y. Nakamura. A robot hand driven by hydraulic cluster actuators. In *Proc. of IEEE-RAS Int'l Conf. on Humanoid Robots*, pages 39–44, 2014.

[70] J. Whitney, M. Glisson, E. Brockmeyer, and J. Hodgins. A low-friction passive fluid transmission and fluid-tendon soft actuator. In *IEEE/RSJ Int'l Conf. on Intelligent Robots and Systems*, pages 2801–2808. IEEE, 2014.

[71] N. Kashiri, J. Malzahn, and N. Tsagarakis. On the Sensor Design of Torque Controlled Actuators: A Comparison Study of Strain Gauge and Encoder-Based Principles. *IEEE Robotics and Automation Letters*, 2(2):1186–1194, 2017.

[72] T. Kawakami, K. Ayusawa, H. Kaminaga, and Y. Nakamura. High-fidelity joint drive system by torque feedback control using high precision linear encoder. In *Proc. of IEEE Int'l Conf. on Robotics and Automation*, pages 3904–3909, 2010.

[73] S. H. Hyon, D. Suewaka, Y. Torii, and N. Oku. Design and Experimental Evaluation of a Fast Torque-Controlled Hydraulic Humanoid Robot. *IEEE/ASME Transactions on Mechatronics*, 22(2):623–634, 2017.

[74] V. Barasuol, O. Villarreal-Magana, D. Sangiah, M. Frigerio, M. Baker, R. Morgan, G. A Medrano-Cerda, D. G. Caldwell, and C. Semini. Highly-integrated hydraulic smart actuators and smart manifolds for high-bandwidth force control. *Frontiers in Robotics and AI*, 5:51, 2018.

[75] H. Vallery, R. Ekkelenkamp, H. van der Kooij, and M. Buss. Passive and accurate torque control of series elastic actuators. In *Proc. of IEEE/RSJ Int'l Conf. on Intelligent Robots and Systems*, pages 3534–3538, 2007.

[76] K. Kong, J. Bae, and M. Tomizuka. Control of rotary series elastic actuator for ideal force-mode actuation in human–robot interaction applications. *IEEE/ASME transactions on mechatronics*, 14(1):105–118, 2009.

[77] J. W. Sensinger and R. F. Weir. Design and analysis of a non-backdrivable series elastic actuator. In *Proc. of Int'l Conf. on Rehabilitation Robotics*, pages 390–393, 2005.

[78] D. W. Robinson, J. E. Pratt, D. J. Paluska, and G. A. Pratt. Series elastic actuator development for a biomimetic walking robot. In *Proc of IEEE/ASME Int'l Conf. on Advanced Intelligent Mechatronics*, pages 561–568, 1999.

[79] N. Paine, J.S. Mehling, J. Holley, N.A. Radford, G. Johnson, C.L. Fok, and L. Sentis. Actuator control for the NASA-JSC valkyrie humanoid robot: A decoupled dynamics approach for torque control of series elastic robots. *Journal of Field Robotics*, 32(3), 2015.

[80] JA Rosero, JA Ortega, E Aldabas, and LARL Romeral. Moving towards a more electric aircraft. *IEEE Aerospace and Electronic Systems Magazine*, 22(3):3–9, 2007.

[81] R. Navarro. Performance of an electro-hydrostatic actuator on the f-18 systems research aircraft. 1997.

[82] Sho Sakaino and Toshiaki Tsuji. Development of friction free controller for electro-hydrostatic actuator using feedback modulator and disturbance observer. *ROBOMECH Journal*, 4(1):1, 2017.

[83] Y. Lin, Y. Shi, and R. Burton. Modeling and robust discrete-time sliding-mode control design for a fluid power electrohydraulic actuator (eha) system. *IEEE/ASME Transactions on Mechatronics*, 18(1):1–10, 2013.

[84] I. S. Seo, J. M. Shin, H. M. Kim, and J. S. Kim. Adaptive position control scheme with neural networks for electro-hydrostatic actuator systems. In *Int'l Conf. on Mechatronics and Automation*, pages 501–506. IEEE, 2010.

[85] Shin-Etsu Silicone. The uniquie properties of silicone `http://www.silicone.jp/e/products/type/oil/detail/about/index2.shtml`. .

[86] C. Liu, J. Lu, T. Tsubouchi, K. Osaka, K. Oba, and A. Kitagawa. Performance improvement of hydraulic servo system using high bulk modulus oil. *Transactions of the Japan Fluid Power System Society*, 42(2):7–12, 2011.

[87] A. De Luca and R. Mattone. Actuator failure detection and isolation using generalized momenta. In *Proc. of IEEE Int'l Conf. on Robotics and Automation*, pages 634–639, 2003.

[88] L. Le Tien, A. Albu-Schäffer, A. De Luca, and G. Hirzinger. Friction observer and compensation for control of robots with joint torque measurement. In *Proc. of IEEE/RSJ Int'l Conf. on Intelligent Robots and Systems*, pages 3789–3795, 2008.

[89] A. Albu-Schäffer, C. Ott, and G. Hirzinger. A unified passivity-based control framework for position, torque and impedance control of flexible joint robots. *The International Journal of Robotics Research*, 26(1):23–39, 2007.

[90] Michael A Hopkins, Stephen A Ressler, Derek F Lahr, Alexander Leonessa, and Dennis W Hong. Embedded joint-space control of a series elastic humanoid. In *Proc. of IEEE/RSJ Int'l Conf. on Intelligent Robots and Systems*, pages 3358–3365. IEEE, 2015.

[91] M Hutter, C Gehring, A Lauber, F Gunther, CD Bellicoso, V Tsounis, P Fankhauser, R Diethelm, S Bachmann, M Bloesch, et al. ANYmal-toward legged robots for harsh environments. *Advanced Robotics*, 31(17):918–931, 2017.

[92] I. Kato. Development of biped walking robot(wabot-1). *Biomechanism 2, The University of Tokyo Press*, pages 173–184, 1973(in Japanese).

[93] K. Hirai. Current and future perspective of honda humamoid robot. In *Proc. of IEEE/RSJ Int'l Conf. on Intelligent Robots and Systems*, volume 2, pages 500–508, 1997.

[94] K. Hirai, M. Hirose, Y. Haikawa, and T. Takenaka. The development of Honda humanoid robot. In *Proc. of IEEE Int'l Conf. on Robotics and Automation*, volume 2, pages 1321–1326, 1998.

[95] Hirohisa Hirukawa, Fumio Kanehiro, Kenji Kaneko, Shuuji Kajita, Kiyoshi Fujiwara, Yoshihiro Kawai, Fumiaki Tomita, Shigeoki Hirai, Kazuo Tanie, Takakatsu Isozumi, Kazuhiko Akachi, Toshikazu Kawasaki, Shigehiko Ota, Kazuhiko Yokoyama, Hiroyuki Handa, Yutaro Fukase, Jun ichiro Maeda, Yoshihiko Nakamura, Susumu Tachi, and Hirochika Inoue. Humanoid robotics platforms developed in hrp. *Robotics and Autonomous Systems*, 48(4):165 – 175, 2004. Humanoids 2003.

[96] K. Kaneko, F. Kanehiro, S. Kajita, H. Hirukawa, T. Kawasaki, M. Hirata, K. Akachi, and T. Isozumi. Humanoid robot HRP-2. In *Proc. of IEEE Int'l Conf. on Robotics and Automation*, volume 2, pages 1083 – 1090, 2004.

[97] K. Kaneko, K. Harada, F. Kanehiro, G. Miyamori, and K. Akachi. Humanoid robot HRP-3. In *Int'l Conf. on Intelligent Robots and Systems*, pages 2471–2478, 2008.

[98] K. Kaneko, F. Kanehiro, M. Morisawa, K. Akachi, G. Miyamori, A. Hayashi, and N. Kanehira. Humanoid robot HRP-4 - Humanoid robotics platform with lightweight and slim body. In *IEEE/RSJ Int'l Conf. on Intelligent Robots and Systems*, pages 4400–4407, 2011.

[99] K. Kojima, T. Karasawa, T. Kozuki, E. Kuroiwa, S. Yukizaki, S. Iwaishi, T. Ishikawa, R. Koyama, S. Noda, F. Sugai, et al. Development of life-sized high-power humanoid robot jaxon for real-world use. In *Proc. of IEEE-RAS 15th International Conference on Humanoid Robots*, pages 838–843, 2015.

[100] Y. Ito, S. Nozawa, J. Urata, T. Nakaoka, K. Kobayashi, Y. Nakanishi, K. Okada, and M. Inaba. Development and verification of life-size humanoid with high-output actuation system. In *Proc. of IEEE International Conference on Robotics and Automation*, pages 3433–3438, 2014.

[101] J. Englsberger, A. Werner, C. Ott, B. Henze, M. A Roa, G. Garofalo, R. Burger, A. Beyer, O. Eiberger, K. Schmid, et al. Overview of the torque-controlled humanoid robot toro. In *IEEE-RAS Int'l Conf. on Humanoid Robots*, pages 916–923, 2014.

[102] O. Stasse, T. Flayols, R. Budhiraja, K. Giraud-Esclasse, J. Carpentier, A. Del Prete, P. Soueres, N. Mansard, F. Lamiraux, J. P. Laumond, et al. Talos: A new humanoid research platform targeted for industrial applications. 2017.

[103] Y. Nagamatsu, T. Shirai, H. Suzuki, Y. Kakiuchi, K. Okada, and M. Inaba. Distributed torque estimation toward low-latency variable stiffness control for gear-driven torque sensorless humanoid. In *IEEE/RSJ International Conference on Intelligent Robots and Systems*, pages 5239–5244, 2017.

[104] Nikos G Tsagarakis, Zhibin Li, Jody Saglia, and Darwin G Caldwell. The design of the lower body of the compliant humanoid robot ccub. In *IEEE International Conference on Robotics and Automation*, pages 2035–2040, 2011.

[105] N. G. Tsagarakis, G. Metta, G. Sandini, D. Vernon, R. Beira, F. Becchi, L. Righetti, J. Santos-Victor, a. J. Ijspeert, M. C. Carrozza, and D. G. Caldwell. iCub: the design and realization of an open humanoid platform for cognitive and neuroscience research. *Advanced Robotics*, 21(10):1151–1175, 2007.

[106] C. Knabe, J. Seminatore, J. Webb, M. Hopkins, T. Furukawa, A. Leonessa, and B. Lattimer. Design of a series elastic humanoid for the darpa robotics challenge. In *IEEE-RAS 15th International Conference on Humanoid Robots*, pages 738–743, 2015.

[107] Satoshi Kagami, Koichi Nishiwaki, James J Kuffner, Tomomichi Sugihara, Masayuki Inaba, and Inoue Hirochika. Design, implementation, and remote operation of the humanoid h6. In *Experimental Robotics VII*, pages 41–50. Springer, 2001.

[108] T. Treratanakulwong, H. Kaminaga, and Y. Nakamura. Low-friction tendon-driven robot hand with carpal tunnel mechanism in the palm by optimal 3D allocation of pulleys. In *Proc. of IEEE Int'l Conf. on Robotics and Automation*, pages 6739–6744, 2014.

[109] Ethercat technology group. *http://www.ethercat.org/*.

[110] M. Quigley, K. Conley, B. Gerkey, J. Faust, T. Foote, J. Leibs, R. Wheeler, and Andrew Y Ng. Ros: an open-source robot operating system. In *ICRA workshop on open source software*, volume 3, page 5, 2009.

[111] S. Nakaoka. Choreonoid: Extensible virtual robot environment built on an integrated gui framework. In *Proc. of IEEE/SICE International Symposium on System Integration*, pages 79–85, 2012.

[112] J. Englsberger, C. Ott, M. Roa, A. Albu-Schäffer, and G. Hirzinger. Bipedal walking control based on capture point dynamics. In *IEEE/RSJ International Conference on Intelligent Robots and Systems*, pages 4420–4427. IEEE, 2011.

[113] J. Englsberger and C. Ott. Integration of vertical COM motion and angular momentum in an extended Capture Point tracking controller for bipedal walking. In *Proc. of IEEE-RAS Int'l Conf. on Humanoid Robots*, pages 183–189, 2012.

[114] S. Kajita, F. Kanehiro, K. Kaneko, K. Yokoi, and H. Hirukawa. The 3d linear inverted pendulum mode: A simple modeling for a biped walking pattern generation. In *IEEE/RSJ International Conference on Intelligent Robots and Systems*, volume 1, pages 239–246. IEEE, 2001.

[115] J. Pratt, J. Carff, S. Drakunov, and A. Goswami. Capture point: A step toward humanoid push recovery. In *Proc. of IEEE-RAS International Conference on Humanoid Robots*, pages 200–207, 2006.

[116] Miomir Vukobratović and J Stepanenko. On the stability of anthropomorphic systems. *Mathematical biosciences*, 15(1-2):1–37, 1972.

[117] T. Takenaka, T. Matsumoto, and T. Yoshiike. Real time motion generation and control for biped robot-1 st report: Walking gait pattern generation. In *IEEE/RSJ International Conference on Intelligent Robots and Systems*, pages 1084–1091, 2009.

[118] J. Roy and L. L. Whitcomb. Adaptive force control of position/velocity controlled robots: theory and experiment. *IEEE Transactions on Robotics and Automation*, 18(2):121–137, 2002.

[119] Y. Nakamura, H. Hanafusa, and T. Yoshikawa. Task-priority based redundancy control of robot manipulators. *The International Journal of Robotics Research*, 6(2):3–15, 1987.

[120] Y. Nakamura. *Advanced robotics: redundancy and optimization*. Addison-Wesley Longman Publishing Co., Inc., 1990.

[121] Bruno Siciliano and Jean-Jacques Slotine. A general framework for managing multiple tasks in highly redundant robotic systems. *Advanced Robotics*, pages 1211–1216, 1991.

[122] Ko Yamamoto. Resolved multiple viscoelasticity control for a humanoid. *IEEE Robotics and Automation Letters*, 3(1):44–51, 2018.

[123] K Yamamoto. Humanoid motion analysis and control based on cog viscoelasticity. *Advanced Robotics*, 31(7):341–354, 2017.

List of Publications

Journal

[1] Tianyi Ko, Hiroshi Kaminaga, Yoshihiko Nakamura, "Key Design Parameters of a Few Types of Electro-Hydrostatic Actuators for Humanoid Robots" Advanced Robotics (Under Review).

[2] Tianyi Ko, Hiroshi Kaminaga, Yoshihiko Nakamura, "Current-Pressure-Position Triple-Loop Feedback Control of Electro-Hydrostatic Actuators for Humanoid Robots" Advanced Robotics (Under Review).

Reviewed Conference Proceedings

[1] Tianyi Ko, Ko Yamamoto, Kazuya Murotani, Yoshihiko Nakamura "Compliant Biped Locomotion of Hydra, an Electro-Hydrostatically Driven Humanoid." Proceedings of IEEE-RAS International Conference on Humanoid Robots, 2018 (Under Review).

[2] Mitsuo Komagata, Tianyi Ko, Yoshihiko Nakamura "Small Size Hydraulic Pumps with Low Heat Generation for Electro Hydrostatic Actuation of Humanoid Robots." Proceedings of IEEE-RAS International Conference on Humanoid Robots, 2018 (Under Review).

[3] Ko Yamamoto, Tianyi Ko, Kazuya Murotani, Yoshihiko Nakamura "Experimental Validation of Resolved Viscoelasticity Control on Hydrostatically Driven Humanoid Hydra." International Symposium on Experimental Robotics, 2018 (Accepted).

[4] Tianyi Ko, Hiroshi Kaminaga, Yoshihiko Nakamura, "Underactuated Four-fingered Hand with Five Electro Hydrostatic Actuators in Cluster." Proceedings of IEEE International Conference on Robotics and Automation, pp.620-625, 2017.

[5] Hiroshi Kaminaga, Tianyi Ko, Ryo Masumura, Mitsuo Komagata, Shunsuke Sato, Satoshi Yorita, and Yoshihiko Nakamura, "Mechanism and Control of Whole-Body Electro-Hydrostatic Actuator Driven Humanoid Robot Hydra." International Symposium on Experimental Robotics, 2016.

[6] Hiroshi Kaminaga, Tianyi Ko, Satoshi Yorita, Shunsuke Sato, Ryo Masumura, Mitsuo Komagata, Tatsuya Ishikawa, Taira Miyatake, and Yoshihiko Nakamura, "Enhancement of Mechanical Strength, Computational Power, and Heat Management for Fieldwork Humanoid Robots." Proceedings of IEEE-RAS International Conference on Humanoid Robots, pp.786-793, 2016.

[7] Tianyi Kang, Hiroshi Kaminaga, Yoshihiko Nakamura, "A Robot Hand Driven By Hydraulic Cluster Actuators." Proceedings of IEEE-RAS International Conference on Humanoid Robots, pp.39-44, 2014.

Oral Presentations (all in Japanese)

[1] 康天毅, 山本江, 室谷和哉, 中村仁彦, (Tianyi Ko, Ko Yamamoto, Kazuya Murotani, Yoshihiko Nakamura) “静油圧駆動ヒューマノイド Hydra の粘弾性分解制御による全身柔軟運動の実現.” (Realization of a Compliant Whole-Body Motion of the Hydrostatically Driven Humanoid Hydra with Resolved Viscoelasticity Control *) 日本ロボット学会学術講演会, 2018 (発表予定).

[2] 室谷和哉, 康天毅, 山本江, 中村仁彦, (Kazuya Murotani, Tianyi Ko, Ko Yamamoto, Yoshihiko Nakamura) “ヒューマノイドの全身トルク制御と ZMP 外乱オブザーバによる高精度 ZMP 制御.” (High Accuracy ZMP Control of Humanoid Robots with Whole-Body Torque Control and ZMP Disturbance Observer *) 日本ロボット学会学術講演会, 2018 (発表予定).

[3] 鈴木亮矢, 康天毅, 駒形光夫, 山本江, 中村仁彦, (Ryoya Suzuki, Tianyi Ko, Mitsuo Komagata, Ko Yamamoto, Yoshihiko Nakamura) “短ストローク油圧シリンダによる高トルク広可動域ロボット関節の開発.” (Development of a High Torque and Large Range of Motion Robot Joint with Short-Stroke Hydraulic Cylinders *) 日本ロボット学会学術講演会, 2018 (発表予定).

[4] 康天毅, 室谷和哉, 山本江, 中村仁彦, (Tianyi Ko, Kazuya Murotani, Ko Yamamoto, Yoshihiko Nakamura) “静油圧駆動ヒューマノイド Hydra の全身運動制御性能評価.” (Whole-Body Motor Control Performance Evaluation of the Hydrostatically Driven Humanoid Hydra.) 日本 IFToMM 会議シンポジウム, 2018.

[5] 室谷和哉, 康天毅, 山本江, 中村仁彦, (Kazuya Murotani, Tianyi Ko, Ko Yamamoto, Yoshihiko Nakamura) “油圧駆動ヒューマノイドロボット HYDRA の歩行制御.” (Walking Control of EHA Driven Humanoid Robot Hydra) 日本 IFToMM 会議シンポジウム, 2018.

[6] 駒形光夫, 康天毅, 中村仁彦, (Mitsuo Komagata, Tianyi Ko, Yoshihiko Nakamura) “EHA のためのインボリュート外接歯車ポンプの小型高圧設計.” (Compact and High Pressure Design of Involute External Gear Pump for EHA) ロボティクス・メカトロニクス講演会, 2P1-E15, 2018.

[7] 康天毅, 神永拓, 佐藤駿輔, 依田聡, 中村仁彦, (Tianyi Ko, Hiroshi Kaminaga, Shunsuke Sato, Satoshi Yorita, Yoshihiko Nakamura) “静油圧駆動ヒューマノイド Hydra のアクチュエータ評価.” (Actuator Evaluation of the Hydrostatically Driven Humanoid Hydra *) 日本ロボット学会学術講演会, 2F1-05, 2017.

[8] 康天毅, 神永拓, 佐藤駿輔, 依田聡, 中村仁彦, (Tianyi Ko, Hiroshi Kaminaga, Shunsuke Sato, Satoshi Yorita, Yoshihiko Nakamura) “ロボット用電気静油圧駆

*The english title is for reference and not official.

動系の電流・圧力・力覚・位置の多重フィードバック系の性能評価.” (Evaluation of Current-Force-Position Feedback Loop of Electro-Hydrostatic Actuators for Robot Application *) 日本ロボット学会学術講演会, 1X1-07, 2016.

[9] 依田聡, 神永拓, 康天毅, 中村仁彦, (Satoshi Yorita, Hiroshi Kaminaga, Tianyi Ko, Yoshihiko Nakamura) “換気孔付きフィンを有した通風筒を持つ水冷ヒートシンク.” (Water-Cooled Heat Sink with Air Channels on the Fines *) 日本ロボット学会学術講演会, 1X2-07, 2016

[10] 神永拓, 康天毅, 堀慎太郎, 中村仁彦, (Hiroshi Kaminaga, Tianyi Ko, Shintaro Hori, Yoshihiko Nakamura) “相補フィルタを用いた電気静油圧アクチュエータの外力測定センサフュージョン”, (Force Measurement Sensor Fusion of EHA with a Complementary Filter *) 日本ロボット学会学術講演会，1X1-06, 2016.

[11] 北島克将, 神永拓, 康天毅, 増村諒, 駒形光夫, 佐藤駿輔, 依田聡, 中村仁彦, (Katsumasa Kitajima, Hiroshi Kaminaga, Tianyi Ko, Ryo Masumura, Mitsuo Komagata, Shunsuke Sato, Satoshi Yorita, Yoshihiko Nakamura) “電気静油圧アクチュエータによる関節駆動系の出力トルク制御のための伝達機構中の力計測.” (Force Measurement in Kinematic Transmission for Output Torque Control of Joint Drive System by Electro-Hydrostatic Cylinders) 日本機械学会関東支部第 23 期総会・講演会, GS0103-02, 2016.

[12] 康天毅, 神永拓, Bryan Penin, 中村仁彦, (Tianyi Ko, Hiroshi Kaminaga, Bryan Penin, Yoshihiko Nakamura) “三次元造形による EHA ポンプと駆動モータの水冷系流路の開発.” (Development of a 3D-Printed Water-Cooling System for EHA Pumps and their Driving Motors *) 日本ロボット学会学術講演会, 3J2-04, 2015.

[13] 康天毅, 神永拓, 中村仁彦, (Tianyi Ko, Hiroshi Kaminaga, Yoshihiko Nakamura) “5 自由度油圧駆動 Hydra ハンドの開発.” (Development of Hydrostatically Driven 5-DoF Hydra Hand *) 日本ロボット学会学術講演会, 1A2-01, 2015.

[14] 神永拓, 康天毅, 中村仁彦, (Hiroshi Kaminaga, Tianyi Kang, Yoshihiko Nakamura) “慣性負荷を用いた電気静油圧アクチュエータのセンサキャリブレーション.” (Sensor Calibration of Electro-Hydrostatic Actuators with Using Reaction Mass *) 日本ロボット学会学術講演会, 2O1-05, 2014.

[15] 康天毅, 神永拓, 中村仁彦, (Tianyi Kang, Hiroshi Kaminaga, Yoshihiko Nakamura) “油圧トロコイドポンプ付シリンダブロックアクチュエータの特性評価.” (Evaluation of Cylinder Block Actuator with Hydraulic Trochoid Pump) ロボティクス・メカトロニクス講演会, 1P1-I07, 2014.

[16] 神永拓, 康天毅, 大月智史, 中村仁彦, (Hiroshi Kaminaga, Tianyi Kang, Satoshi Otsuki, Yoshihiko Nakamura) “質量負荷を用いた小型直動電気静油圧アクチュエー

タの動特性評価." (Dynamic Property Evaluation of a Miniature Linear Electro-Hydrostatic Actuator Using Reaction Mass) ロボティクス・メカトロニクス講演会, 1A1-I03, 2014.

[17] 神永拓, 康天毅, 中村仁彦, (Hiroshi Kaminaga, Tianyi Kang, Yoshihiko Nakamura) "モータの速度制御を用いた電気静油圧アクチュエータの力制御," (Force Control of an Electro-Hydrostatic Actuator Using Motor Velocity Control) ロボティクス・メカトロニクス講演会, 1A1-I04, 2014.

[18] 康天毅, 神永拓, 中村仁彦, (Tianyi Kang, Hiroshi Kaminaga, Yoshihiko Nakamura) "鋳造シリンダマニフォールドと三日月仕切付トロコイドポンプを用いたハンド用集合アクチュエータの開発." (Development of a Cluster Actuator with a Casted Cylinder Manifold and Crescent Trochoid Pump for Hand Application *) 日本ロボット学会学術講演会, 2E1-08, 2013.

[19] 康天毅, 神永拓, 中村仁彦, (Tianyi Kang, Hiroshi Kaminaga, Yoshihiko Nakamura) "三日月仕切付トロコイド歯車ポンプと油圧シリンダによるロボットハンド駆動系の開発." (Development of Robot Hand Actuating System with Trochoid Gear Pump with Crescent Separator and Hydraulic Cylinder) ロボティクス・メカトロニクス講演会, 2P1-D10, 2013.

Award

[1] 2017 IEEE Robotics and Automation Society Japan Joint Chapter Young Award (ICRA2017), for the paper "Underactuated Four-fingered Hand with Five Electro Hydrostatic Actuators in Cluster", May 2017.

[2] Young Investigator Fund Best Paper Award in the 24-th Jc-IFToMM Symposium on Theory of Machines and Mechanisms, for the paper "Whole-Body Motor Control Performance Evaluation of the Hydrostatically Driven Humanoid Hydra (in Japanese) ", June 2018.

Patent (Japan)

[1] 神永拓，中村仁彦，康天毅. (Hiroshi Kaminaga, Yoshihiko Nakamura, Tianyi Ko) 電気静油圧アクチュエータおよび電気静油圧アクチュエータにおけるパラメータ推定方法，(Electro-Hydrostatic Actuators and Parameter Estimation for Electro-Hydrostatic Actuators *) 出願番号 2014-225449, 公開番号 2016-089961.（公開中）(Published)

[2] 中村仁彦，神永拓，康天毅. (Yoshihiko Nakamura, Hiroshi Kaminaga, Tianyi Ko) 歯車ポンプの冷却構造 (Cooling Structure of Gear Pumps *，出願番号 2015-172792, 公開番号 2017-048728. （公開中）(Published)

東京大学知的財産登録 (Intellectual Property Registration of the University of Tokyo)

[1] 中村仁彦，神永拓，康天毅. (Yoshihiko Nakamura, Hiroshi Kaminaga, Tianyi Ko) モータ制御用コントロール基板の組込みソフトウェア. (Embedded Software for Motor Control Circuit Board) 知的財産部管理番号 C23181001, 2018.